THE FABRICATION AND CHARACTERISATION OF QUANTUM DOTS, WIRES AND WIRE NET WORKS

BY

QI ZHANG, B.Sc, M.Sc

A thesis submitted to the CNAA in partial fulfilment of the requirements for the degree of Doctor of Philosophy

Department of Applied Physics

School of Applied Science

De Montfort University

Leicester LE1 9BH, UK

July 1996

ACKNOWLEDGEMENT

First of all, I would like to express my sincere gratitude to my supervisors, Dr. S.C. Bayliss, Dr. R.G. Pritchard for their guidance and encouragement throughout my research project.

Thanks are also to Dr. D.A. Hutt, Dr. J. Bates, Mr. A. Al-Ajili and Mr. D. Bazeley for their help and technical assistance.

I would like to thank The Committee of Vice-Chancellors and Principals of The Universities of The UK, The School of Applied Sciences of De Montfort University and The Department of Physics of Loughborough University of Technology for supporting my study. Special thanks to Professor R. Linford for awarding me a Student Bursary.

No doubt, the Student Bursaries and support for The 1st European Conference on Synchrotron Radiation in Materials Science (UK, 3-8 July 1994) and The 188th Meeting of Electrochemical Society of USA from the conference organisations and from Dr. S.C. Bayliss and Dr. R.G. Pritchard, and the travelling and registration fee from Dr. S. C. Bayliss for the Chelsea Amorphous And Organic Semiconductors Meeting (London, April 1995) are great encouragements to me and my study.

DECLARATION

The work presented in this thesis has been carried out entirely by the candidate, under the supervision from Dr. S.C. Bayliss and Dr. R.G. Pritchard. No part of this work has been submitted for any other degree by the candidate, or by any other person.

Candidate: Qi Zhang

Director of Studies: Dr. S. C. Bayliss

ABSTRACT

The work in this thesis includes two aspects as described below:

1. Freshly produced red, yellow and green emitting porous Si have been fabricated and studied by NEXAFS and EXAFS. The emission peaks are at 690, 580 and 520 nm, which almost covers the full visible range that direct anodization can achieve. The correlation between the co-ordination numbers of the first, second and third Si neighbour shells from Fourier transform fitting of EXAFS and both emission peak energies and optical bandgaps estimated by PLE (photoluminescence excitation dependence) suggests that the nanostructures of the PS are nanowires, rather than nanoclusters. Two types of quantum nanowire with one and one-plus-a-fraction dimensionality are proposed to interpret the correlation. The order factors of the theoretical fits suggest the nanowires of the freshly produced PS have crystalline cores.

2. Strong and stable blue photoluminescence (PL), visible to the naked eye under 0.4 μW of 300 nm and 2.7 μW of 370 nm excitation, has been observed for samples of Si and C clusters embedded in SiO_2 matrices, prepared by rf co-sputtering followed by N_2 annealing at 800°C. Firstly for the Si clusters, Si K-edge EXAFS and NEXAFS strongly suggest the existence of Si nanoclusters with crystalline cores in the efficient emitting material. On the other hand for the carbon clusters, silicon, carbon and oxygen K-edge XAFS suggest that 1) the nanoclusters present are C-based materials, 2) the luminescent materials probably involves π bonded carbon. The size distributions of both kinds of the nanoclusters obtained by TEM suggest that a quantum-confined size effect can also apply to the blue PL. The strong blue emission is related with the crystallisation of the nanodots by annealing. The PL excitation dependence is explained by an increase in the conduction band density of states deep in the band, and the formation of a band tail.

CONTENTS

of freshly produced porous silicon, Q. Zhang, and S.C. Bayliss, **J. Appl. Phys.** 79, 1351(1996).

C. The blue and UV photoluminescence of Si and C nanoclusters embedded in SiO_2 matrices, Qi Zhang, S.C. Bayliss and R.G. Pritchard, **Proceeding Volume of 3rd International Symposium of Quantum Confinement : Quantum Wires and Dots, 188th Meeting of The Electrochemical Society, Inc.** Chicago, USA, October, 1995.

D. The dimensions and sizes of as-anodised red, yellow and green emitting porous silicon and blue emitting clusters, Qi Zhang and S.C. Bayliss, **Proceeding Volume of 1st International Symposium of Advanced Luminescent Materials, 188th Meeting of The Electrochemical Society, Inc.** Chicago, USA, October, 1995.

E. The blue photoluminescence and local structure of Si nanostructures embedded in SiO_2 matrices. Q. Zhang, S.C. Bayliss, and D.A. Hutt, **Appl. Phys. Lett. 68,** 1977 (1995).

F. The blue photoluminescence and nanostructure of Si and C clusters embedded in SiO_2 matrices, Q. Zhang, S.C. Bayliss, D.A. Hutt, A. Al-Ajili and P. Harris, **Nucl. Inst. & Meth. in Phys. Res. B 97,** 329 (1995).

G. The optical responce of porous silicon under different excitation energies, Q. Zhang, S.C. Bayliss, D. A. Hutt and A. Al-Ajili, **Nucl. Inst. & Meth. in Phys. Res. B 97,** 326 (1995).

CHAPTER 1 INTRODUCTION

This Chapter reviews all types of nanostructures from quantum well to nanodot and from experimental set up to achievements. The very basic concept of quantum confinement or size effect is given in conjunction with the topic of this thesis. The necessary connections between other published works and this thesis are presented. The last section of this Chapter introduces the work in this thesis.

1.1 Porous Silicon and Other Nanomaterials with Optoeletronics

Silicon has been the dominant material for microelectronics for several decades. The technology and fabrication of Si-based electronic devices have been developed and refined in many ways and commercial applications now exist in a vast variety. However, in the past crystalline Si has never been a good candidate for active optoelectronic devices. The indirect energy gap of crystalline Si requires the participation of phonons for recombination of electrons and holes below 3.3 eV to satisfy wave vector conservation, which makes optical recombinations in the visible spectrum rather weak.

In order to realise optoelectronic applications within the well-known Si technology, the main approach has been to utilise the optical properties of III-V compounds such as GaAs or InP, leading to the wide field of heteroepitaxy on Si. Nevertheless, there still

are efforts to overcome in Si the constraints imposed by wave vector conservation, e.g. by introducing point defects as radiative recombination centres, producing small Si crystallites with diameters small enough for significant quantum confinement (2-5 nm), or the fabrication of strained Si/Ge superlattices. As a simple guideline, the success which can be expected from such approaches depends critically on the overlap of the electronic wave functions of the states between which the optical transitions should occur. Even if the electronic wave function was localised within less than about ten lattice constants in two dimensions, the selection rules of the matrix elements would not be violated by more than 20 percent of the typical allowed matrix element, leading to transition probabilities of less than 4 percent of that of dipole-allowed transitions. However, the photoluminescence efficiency of small crystallites may be enhanced with respect to the bulk due to a reduction of nonradiative recombination centres.

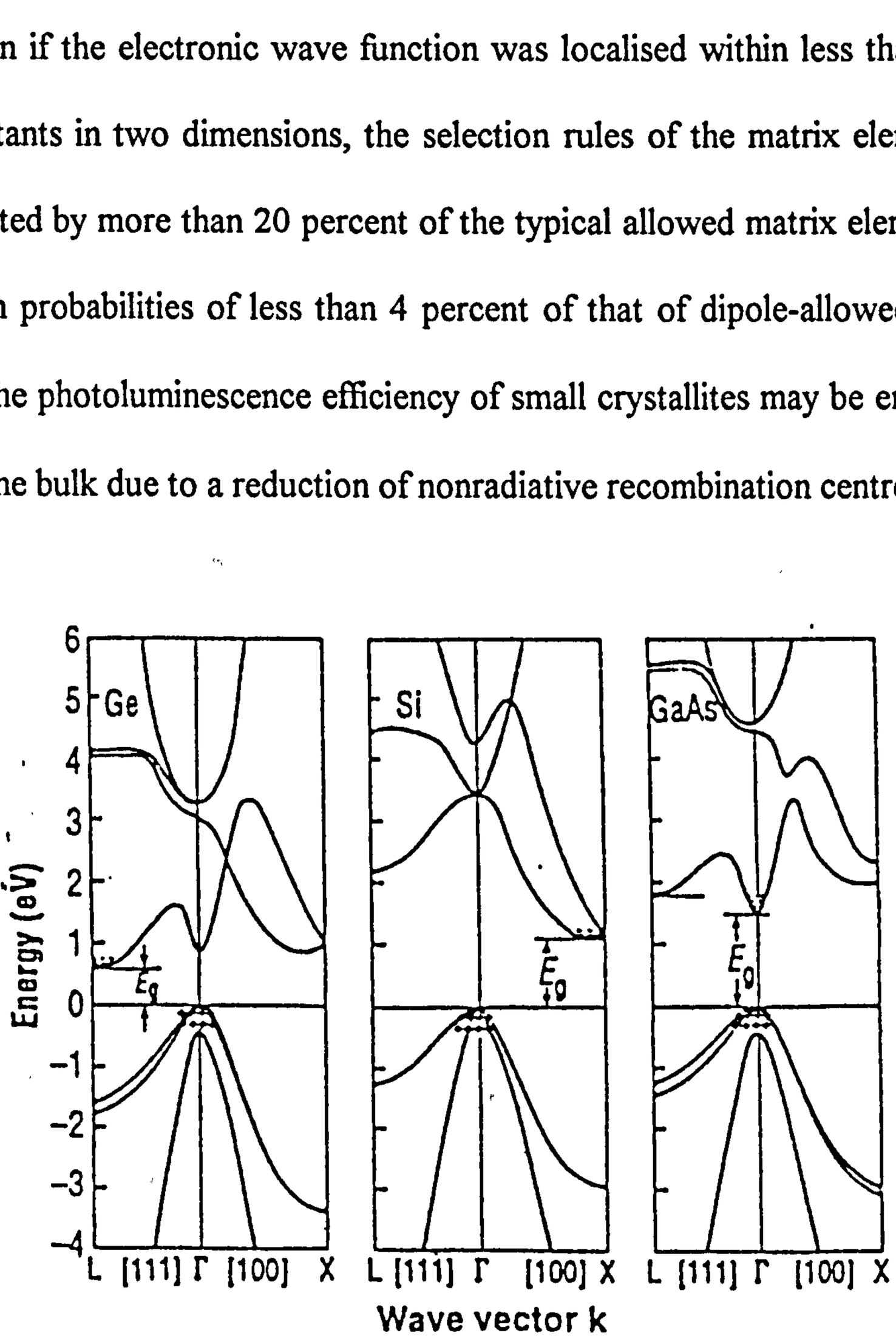

Figure 1.1. The band structures of Ge, Si and GaAs. The direct

gap of GaAs and indirect gap of Ge and Si. Electron at the conduction band minimum in an indirect semiconductor need the assistance of a phonon to relax into the hole state filled with hole at the maximum of the valence band. (after Lyer and Xie, 1993).

In general, nonradiative recombination centres at the surfaces or heterointerfaces are a persistent problem in all approaches mentioned above. There are several alloys of silicon with hydrogen, oxygen, and other elements which are known to exhibit a strong luminescence only below 100K, e.g. hydrogenated amorphous Si, a-Si:H, or its wide-bandgap alloys a-Si:O:H, a-Si:N:O:H and a-Si:C:H. Unfortunately, the luminescence in most cases is not strong enough for any practical applications and would not challenge the III-V materials.

Above all, bulk silicon, with a 1.1 eV indirect band gap, is a poor material for optoelectronic applications. Presently, popular solid-state light emitters such as LEDs and lasers are made from direct and large bandgap compound semiconductors within the confines of technology of III-V materials and their hybridisation with Si chips, such as GaAs/AlGaAs and InGaAs/InP. As a comparison, the band structures of Ge, Si and GaAs are shown in Figure 1.1 in k-space. The rapidly expanding field of optoelectronics has until now had to rely on the III-V materials, which are more complex and much more expensive semiconductors. However, direct integration of

these materials with silicon electronics is extremely difficult because of major differences in materials characteristics and processing requirements (Collins and Tischler, 1993). And, from a commercial point of view, it will be extremely expensive for applications such as true large-scale optoelectronic integration. Nevertheless, it has long been perceived that integrated optical and electronic devices within one "chip" can be applied to optical communications systems, display technology, and other related areas.

In 1990, L. Canham (1990) reported the observation of a strong photoluminescence (PL) in porous (PS) under illumination at room temperature. Then, independently, Lehmann and Gösele (1990) reported a pronounced shift of fundamental absorption edge of self-supporting porous Si layers. This discovery has stimulated intensive studies and interests in porous silicon and other nanomaterials, such as nanoclusters and nanopowders, due to the possibility that these materials may provide a substantial advantage for optoelectonic materials and integrations. Besides the integration dream, porous Si can be relatively easily produced and has external PL efficiencies from 1 to 10 percent at room temperature, which rivals that of III-V materials and is the basis for the great deal of excitement about these materials. Within 6 years, that more than two thousands papers have been published based on porous silicon, nanopowders and nanoclusters, as Canham stated, is a good description of the intensive attention.

Research in porous Si and other nanostructures can be divided into two basic areas: (1) fully understanding the origin of the luminescence; and (2) fabrication of

electroluminescent (EL) and other devices. The fundamental mechanism of luminescence is among the most-discussed topics in this field. An understanding of the mechanism is important not only from the standpoint of basic science, but also to determine whether porous silicon can be used in practical applications.

1.2 Porous Silicon (PS)

It was 1956, the beginning of the silicon age, when I. Uhlir and her husband were trying to develop a technique for polishing and shaping the surfaces of two elemental semiconducting materials, Ge and Si, at Bell Laboratories. Theses materials were being tried out in new electronic devices; the shaped surfaces were needed for attaching wires and contacts. But though the electropolishing method worked well most of the time, their samples were sometimes ruined by a thick black, red or brown film which appeared on the surface of the material. Then, they found a way of adjusting the experimental conditions to stop this happening: when the current density was high enough the surface of this anode was etched away by the electrolyte, hydrofluoric acid (HF), leaving a smooth, reflective surface. The coloured film was call porous silicon. Then, about ten years ago, visible luminescence from this material was reported although only at low temperature (Pickering, et al., 1984). After 34 years, knowledge about the coloured film, PS, was only that when the current density was low, the silicon surface became riddled with an array of small holes or pores, and

between these pores the material remained crystalline and was largely covered with hydrogen by the etching anodisation process.

In 1989, Canham began studying porous Si. By using the most concentrated HF acid available, he tried to reduce the size of the pores to as small as one to two nanometers wide, but many micrometers long. The resulting silicon skeleton between the pores was of similar dimensions, following the idea that if the pores were widened they would eventually meet and overlap, reducing the silicon separating them to mass of tiny columns. These columns emitted light efficiently (Canham, 1993). Since the first strong visible PL (peaks at about 780 nm) was reported by Canham (1990), efficient luminescence at room temperature covering the full visible range of wavelengths has been obtained, from red to green PL directly from anodisation, blue PL only coming from further treatments (such as rapid thermal oxidation (RTO)(Mimura, et al., 1993, Loni, et al., 1995) or boiling in water (Hou, et al., 1993).

Porous Si is itself fabricated by an anodic dissolution process that is usually done in a HF based electrolyte. Although the microscopic details of pore formation are complex and as yet incompletely understood, a labyrinth of interconnected Si is created. The microstructure of PS depends on the composition of the electrolyte, the type and resistivity of the initial Si wafer/substrate, the current density during anodization, and the post-anodization treatment. Under the right conditions, a large pore structure is created, in which as much as 85% to 90% of the Si is etched off leaving filaments as thin as a few nanometers across. The principal feature of PS is extremely fine

structures, either wires or dots, which are small enough to exhibit quantum confinement effects - blue shift. Structural analysis has confirmed that the filaments are crystalline, by TEM, x-ray diffraction and Raman spectroscopy. The material is fragile and by nature has a very large surface area. Immediately after anodization, this surface is usually hydrogen-passivated with little evidence of oxygen or other impurities. One can widen the pores or, equivalently, make the filaments thinner, by leaching in HF solution.

Different from the PL from GaAs or a defect level in Si, the line shape of any PL spectra from porous Si is broad, and a typical half width of the PL is from 0.3 to 0.45 eV. Although the peak intensity is smaller than that of a direct-gap semiconductor, the integrated intensity is comparable. Furthermore, by changing the anodization conditions to obtain a finer filamentary network, one can shift the peak to shorter wavelengths. This leads most of researchers to believe that quantum confinement plays a significant role in the light generation mechanism, as was suggested in the first report. The broadening of the peak can be ascribed to the size distribution in PS.

Research has been done in almost every aspect of the properties of PS, such as structural, electronic states, defects, transition behaviour and life time, by means of TEM, AFM, PL, Raman, SAS, time resolved PL, ESR, EXAFS, and theoretical calculations (tight binding and LCAO), although the origin of the strong luminescence is still not very clear. The details will be given in section 1.5.

1.3 Nanoclusters Embedded in SiO_2 Matrices

Nanoclustered films, clusters embedded in matrices (also called semiconductor nanocrystallites or quantum dots, and semiconductor doped glasses), also have attracted much attention, because they exhibit new quantum phenomena and have potentials for beckoning novel and future photonic devices. Some work has been on nanocrystallites or quantum dots made from direct-gap semiconductors such as CdS, CdSe, CuCl, etc., both experimental and theoretical (Hanamura, 1988, Kayanuma, 1988, and Alivisatos, 1995). In very recent years, optical properties of nanodots or nanoclusters made from indirect-gap semiconductors such as Si (Dimaria, et al., 1994, Ito, et al., 1992), Ge (Maeda, 1991 and Maeda, et al.,1995, Kanemitsu, et al, 1992), and C (Hayashi, et al., 1993) have been reported. The discovery of luminescence in nanocrystallites of Si and Ge is an extremely important scientific breakthrough with enormous technological implications, since it opens a new possibility for group IV semiconductors as materials for optoelectronic applications. The origin and mechanism of strong visible luminescence in the nanocrystallites at room temperature are currently under discussion.

Normally, clustered films are made by the rf co-sputtering technique. After being annealed in an inert atmosphere, the films exhibit visible luminescence under the excitation by blue or UV light. Until now, the photoluminescence from nanoclusters can be achieved in the visible range of dark red, red, orange, yellow and green (from

800 nm to 530 nm) by other groups using nanomaterials of Ge, C and Si. Strong blue PL (420 nm - 500 nm) from both Si and C clustered films have been observed and reported from our recent study (Zhang, et al, 1995). Electroluminescence has been obtained from the LED structure made by these nanoclusters.

Since the peak energies of luminescence from clustered films are closely related to the size distribution of the clusters, and the intensities of PL are related to the densities of clusters in the films, the common understanding about the widening band gaps is also in terms of the size effect, as applied to porous silicon. However, the transition behaviour is not clear at this stage. That the life time of carriers in the quantum dots is less than a few ns lead researchers to suggest the transition is likely to be more direct.

1.4 Other Nano-sized Materials

1.4.1 Three dimensional confined nanostructures

In recent years besides porous silicon and nanoclusters, nanopowders (also called nano-particles or nano-spheres) have also been intensively studied. Nanopowder can be produced by plasma enhanced chemical vapour deposition using silane, SiH_4. The rf power generator can be modulated by a square-wave signal with different frequencies and periods of duty cycle, which allows the powder production inside the

plasma to be controlled. Thus, the powder could have nanometer size, a large presence of silicon-hydride groups, and a peak emission wavelength of 700 nm to 800 nm (Costa, et al., 1994, Zhang, et al. 1994). Nanocrystalline powder can be made by laser breakdowned silane (SiH_4) gas (Kanemitsu, et al.,1993, Kawaguchi and Miyazima, 1992). Nanodots also can be fabricated by spark-erosion of silicon surfaces, which could produce blue and green PL (Rüter, et al., 1994). When amorphous Si thin films were annealed in dry nitrogen by so-called RTA (rapid thermal annealing), photoluminescence was also observed under UV laser excitation: normally, the PL shows different peaks within a large visible range from red to violet. The origin PL of the response was believed to be from nanodots with a size distribution from 3 to 7 nm (Zhao, et al. 1994).

Strong PL has also been observed from Si^+-implanted and thermally annealed SiO_2 films, and it is believed that nanocrstallines of Si formed during annealing at temperatures from 900°C to 1100°C (Tsutomu, et al.,1994). The PL peaks can be tuned from 1.5 eV to 2.6 eV when annealed in forming gas (N_2+H_2) for different times and temperatures (Koch, et al., 1995).

Furthermore, semiconductor nanocrystals have been made by a special chemical-physics way--- starting with an organic fluid (Alivisatos, 1995, Steigerwald, et al., 1988). To create this kind of crystallite, a set of precursors are injected into a very hot organic liquid and upon injection the temperature immediately rises above the nucleation limit so that nucleation occurs and then the temperature quickly drops. The

concentration drops quickly because dilution occurs, resulting in crystallites in a fluid. The crystallites will be encapsulated in a layer of organic material so that they do not run into each other and fuse. Using this method, Si, Au, especially cadmium selenide (CdSe) nanoparticles are made.

1.4.2 One or two dimensional confined nanostructures

Lithography technology has been developed to deal with microfabrication of sizes from 10 nm to sub-μm from the conventional sub-μm scale. This technology includes lithography (photo, holographic electron beam, ion beam and x-ray), and etching (plasma, reactive-ion and chemical). When the size-scale becomes close to 10 nm or less, the quantum effect begins to appear in relevant properties because of the size effect. Therefore, quantum-effect electronic and optoelectronic devices would have to be fabricated by a novel lithography technology. Silicon pillars of diameter below 10 nm and with an aspect ratio of height to diameter as high as 50:1 are a example of two dimensional confined quantum structures which have been produced using lithography fabrication (Nassiopoulos, 1995). The process for the fabrication was: (1) patterning definition by optical lithography; (2) reactive ion etching by a mixture of SF_6 and CHF_3 gases; (3) reducing the thickness of the pillars further by thermal oxidation to form the nanostructures with a strong size effect. The recorded PL peaks can reach 580-650 nm in the visible range.

Furthermore, atomic force microscope (AFM) based lithography has been employed to write down quantum wires using an AFM to oxidize H-passivated Si surface with 10-30 nm oxide patterns on the surface. The oxide patterns are extremely uniform and serve as robust masks for pattern transfer into the substrate by liquid etching (Snow and Campbell, 1994).

One dimensionally confined structures -quantum wells, superlattices of III-V compounds (e.g. GaAs/AlGaAs) and elementary semiconductors (e.g. Si/Ge) - are normally constructed by MBE (molecular beam epitaxy) with a monolayer thickness of a few atomic layers. MBE was developed in the early 1970s as a means of growing epitaxial layers of compound semiconductors. It offers the advantage of higher quality crystalline layers with good thickness control. Since then, quantum well structures have been recognised as one of the promising candidates for novel optical devices for both communication and computing, such as modulators, self-electro-optical effect devices and optical emitters (Haug, 1988).

1.5 Mechanisms on The Understanding of Nanostructures

1.5.1 General concept of quantum size effect

Luminescence from porous silicon was proposed in the very first reports (Canham, 1990, and Lehmann, 1991), and is most frequently discussed in terms of a quantum

confinement model. As the characteristic size of a semiconductor is reduced to the nanometer regime, confinement of the electron and hole wavefunctions effectively increases the bandgap of the materials and hence the luminescence energy.

An example of a particle in a rectangular potential well can give the basic concept of the size effect. In quantum theory, the problem of determining the stationary states of the motion of a particle of mass μ in an external potential field reduces to finding the values of the energy operator, that is, to solving the linear second-order differential equation:

$$\left[\nabla^2 + \frac{2\mu}{\hbar^2}\{E - U(r)\}\right]\psi = 0 \qquad (1.1)$$

Exact analytical solutions of the equation can be found in the condition which refer to systems for which the potential energy is constant in the whole of space, changing discontinuously on the surfaces which separate these regions. The wave function must be continuous on the discontinuity surface of the potential, since the probability density must be continuous. If the energy of the particle is bounded and the jump in the potential energy on the discontinuity-surfaces finite, it follows from (1.1) the $\nabla\varphi$ must necessarily be continuous on the discontinuity surfaces. The boundary conditions on the surfaces σ where the potential undergoes a jump reduce thus to the requirement that: φ and $\nabla\varphi$ must be continuous on σ.

Let us now consider a particle moving in a potential as shown in Figure 1.2:

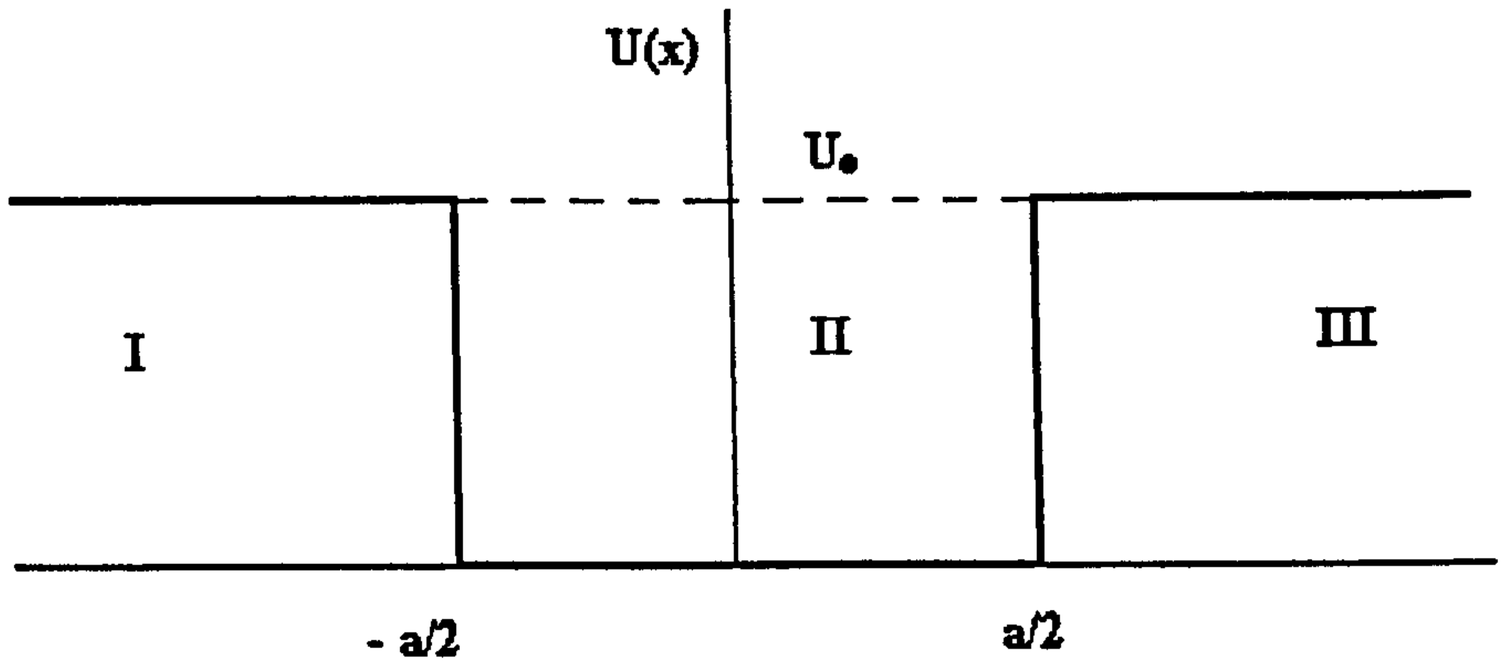

Figure 2. Rectangular form of potential energy

i.e.

$$U(x) = 0, \text{ if } -a/2 \le x \le a/2; \quad U(x) = U_0, \text{ if } x < -a/2 \text{ or } x > a/2,$$

in that case equation (1.1) reduces to the one-dimensional equation

$$\left[\frac{d^2}{dx^2} + \frac{2\mu}{\hbar^2}[\varepsilon - U(x)]\right]\psi(x) = 0 \qquad (1.2)$$

Let

$$k^2 = 2\mu\varepsilon/\hbar^2, \text{ and } \gamma^2 = 2\mu(U_o - \varepsilon)/\hbar^2$$

We can thus write equation (1.2) in the form

$$(\frac{d^2}{dx^2}+k^2)\psi_I = 0, \qquad 0 \leq x \leq a/2$$

$$(\frac{d^2}{dx^2}-\gamma^2)\psi_{II} = 0, \qquad x \geq a/2$$

The solution φ_{II} which is finite as $x \to \infty$ can be written in the form

$$\varphi_{II} = Ae^{-\gamma x} \tag{1.3}$$

The solution φ_I corresponding to states of even parity will be

$$\varphi_I^{(+)} = B \cos kx$$

For odd parity we have

$$\varphi_I^{(-)} = C \sin kx \tag{1.4}$$

Let us first of all consider states of even parity. From the requirement that φ and $d\varphi/dx$ be continuous at $x = a/2$ it follows that we have the following two equations for A and B

$$B \cos ka/2 = A\, e^{-\gamma a/2}$$

$$B \sin ka/2 = (\gamma/k)\, A\, e^{-\gamma a/2} \tag{1.5}$$

This set of equations has a non-vanishing solution only if

$$k \tan(ka/2) = \gamma = \sqrt{\frac{2\mu U_0}{\hbar^2} - k^2}$$

As the tangent is a periodic function with period π we can rewrite this equation as follows

$$ka = n\pi - 2 \arcsin \frac{\hbar k}{\sqrt{2\mu U_0}} \qquad (1.6)$$

where n = 1,3,5 ... ..., and where the values of the arcsin must be taken to lie in the 0, $\pi/2$ interval. As we calculate the energy from the bottom of the potential well, the energy ε is positive. As the argument of the arcsin cannot exceed 1, the values of k can lie only in the range $0 \leq k \leq 2\mu U_0/\hbar$. The values ka satisfying (1.6) for n=1,3.5 ... ... correspond to the points of intersection of the straight line ka and the monotonically decreasing curves

$$\zeta_n(k) = n\pi - 2 \arcsin \frac{\hbar k}{\sqrt{2\mu U_0}} \qquad (1.7)$$

The solutions of equation (1.6) have a particularly simple form for very large values of Uo ($U >> \varepsilon$). In that case

$$\arcsin \frac{\hbar k}{\sqrt{2\mu U_0}} \cong 0$$

and $k_n = n\pi/a$, with n = 1, 3, ... We then get for the energy of the particle

$$\varepsilon_n^{(+)} = \frac{\pi^2\hbar^2}{2\mu a^2} n^2, \quad \text{n odd.} \tag{1.8}$$

So, to a particle with and without quantum confinement, the energy difference is

$$\Delta E = \frac{\pi^2 \hbar^2}{2\mu a^2} \tag{1.9}$$

In the same way, to a quantum wire with a square cross section of side length a

$$\Delta E = \frac{h^2}{4m^* a^2} \tag{1.10}$$

here, m* denotes the effective hole or electron mass m_h^* or m_e^* for ΔE_v or ΔE_c, respectively. For the given range of quantum wire diameters a, an increase ($\Delta E_v + \Delta E_c$) in the band-gap energy of approximately 0.3-3.2 eV results, following the equation above.

As the size of the nanocolumns of porous silicon has a distribution, the growth of the columns is a stochastic process and it appears reasonable to assume columns of silicon with a Gaussian distribution of diameters centred around a mean diameter d_o. The distribution is written as

$$P_d = \frac{1}{\sqrt{2\pi}\sigma} \exp\left[-\frac{(d-d_0)^2}{2\sigma^2}\right] \tag{1.11}$$

The number of electrons in a column of diameter d participating in the PL process is proportional to d_0. The heights of the columns depend only on the growth time and are approximately the same. Hence

$$N_e = N_e(d) = ad^2 \tag{1.12}$$

where a is a constant.

For a porous silicon sample consisting of varying column diameters the probability distribution of electrons participating in the PL process is given by a product of the above two expressions:

$$P_{ed} = \frac{1}{\sqrt{2\pi}\sigma} \exp\left[-\frac{(d-d_0)^2}{2\sigma^2}\right] \tag{1.13}$$

where b is a suitable normalisation constant.

In the quantum confinement model, the PL process is attributed to the energy upshift of the electrons and is proportional to $1/d^2$.

The PL energy $\hbar\omega$ is given by

$$\hbar\omega = E_g - E_b + \frac{c}{d^2} \tag{1.14}$$

where E_g is the bulk silicon gap(1.17 eV), E_b the excitation binding energy, and c an appropriately dimensioned constant. The energy upshift (or energy difference) due to confinement ΔE is

$$\Delta E = \hbar\omega - (E_g - E_b) \tag{1.15}$$

$$\Delta E_0 = \frac{c}{d_o^2} \tag{1.16}$$

where we have also paused to define a mean upshift ΔE_0 related to the mean column diameter d_o. This is a model of quantum confinement when size distribution is concerned (John and Singh, 1994).

1.5.2 Special characteristics for porous Si and clusters

For these nanostructure systems, nanoclusters, particles and porous silicon, there are different models/calculations using different approximations for understanding these systems in detail. Fishman, et al. (1993) took into account the finite potential confining the carriers in silicon crystallites embedded in SiO_2 and found an electron-hole confinement energy proportional to $L^{1.64}$ using an effective-mass approximation with statistical-description. Here L is the diameter of the crystallites, assumed to be spherical. With first-principles analysis, Hybertsen and Needels (1993) found that the

electronic states near the fundamental gap (substantially blue-shifted from that of bulk Si) could have a direct gap between bulk-Si-derived states when the Si nano quantum wires are (a) fully relaxed within the local-density approach showing bulk-like co-ordination of the Si atoms, (b) hydrogen-terminated, (c) about 10 nm or less in cross-section. Using a second-neighbour empirical tight-binding model which includes d orbitals and spin-orbit interaction, Sanders and Chang (1992) found that for narrow Si quantum wires with widths around 8 Å, the averaged exciton oscillator strength is comparable to that of bulk GaAs, i.e. the carrier's life time of a Si nanostructure with a size of 8 Å can be as fast as in bulk GaAs. However, the average exciton oscillator strength decreases dramatically (faster than $1/L^5$) as the quantum-wire width L increases. The life-time of the shortest-lived exciton ranges from 57 ns to 170 μs for wire widths from 7.7 to 31 Å.

Delerue, et al., (1992-1994) used the linear combination of atomic orbitals (LCAO) technique and obtained the bandgap energies of nanostructures as a function of that their diameters and dimensionalities (Si crystallites and wires) and orientations. In that work, the electronic structure was calculated of crystallites and wires with a diameter up to 4.3 nm (2049 atoms in the crystallite), with the dangling bonds at surface saturated by hydrogen atoms to avoid localised states in the bandgaps. Figure 1.3 shows some main results of their work and experimental results by Furukawa and Miyasato (1988) for comparison. As shown, the

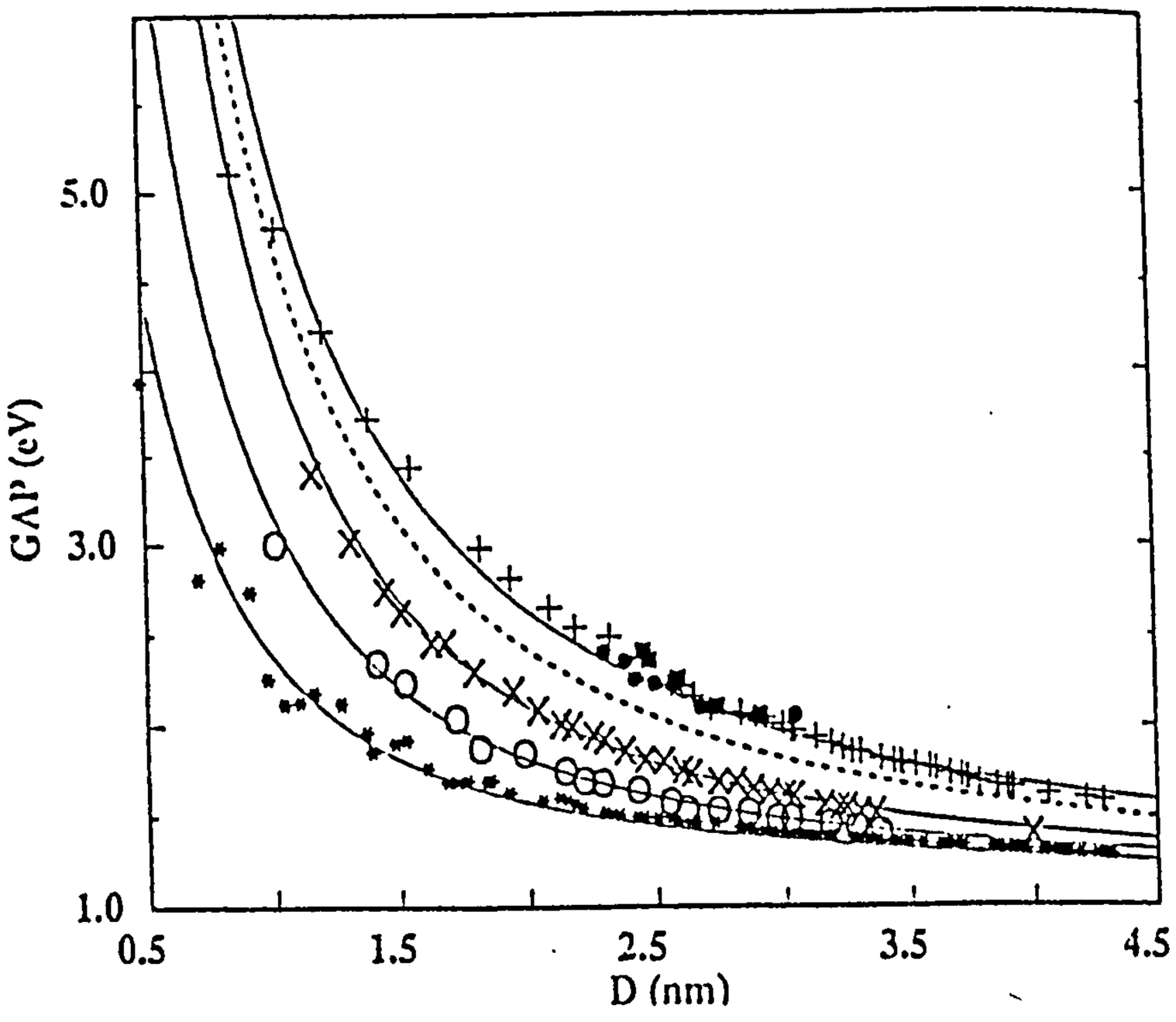

Figure 1.3 Calculated optical band gap energies for various silicon crystallites(+) or wires (100: ×, 110: ∗, 111: o) as a function of their diameter d. The continuous lines are an interpolation and an extrapolation of these results by a d^{-n} law. The black dots and squares are the experimental results of Furukawa and Miyasato (1988) for comparison. The dashed line is the band gap energy for the crystallites including the Coulomb interaction between the electron and the hole. After Delerue, et al.,(1993).

confinement is obviously more important in crystallites but a strong anisotropy exists between the different directions of the wires. They found that the confinement is more

important for holes than for electrons in accordance with other calculations. The observed bandwidth of the red emission of porous Si (1.4 and 2.2 eV) is compatible with crystallites with diameters between 2.5 and 4.5 nm. Similar confinement energies are possible for wires with smaller dimensions. In particular, bandgap energies higher that 2.0 eV can only be obtained with very thin wires (diameters less than 2.3 nm). These calculations will be used together with modelling developed in this project to understand the information given by EXAFS (extended x-ray absorption fine structure).

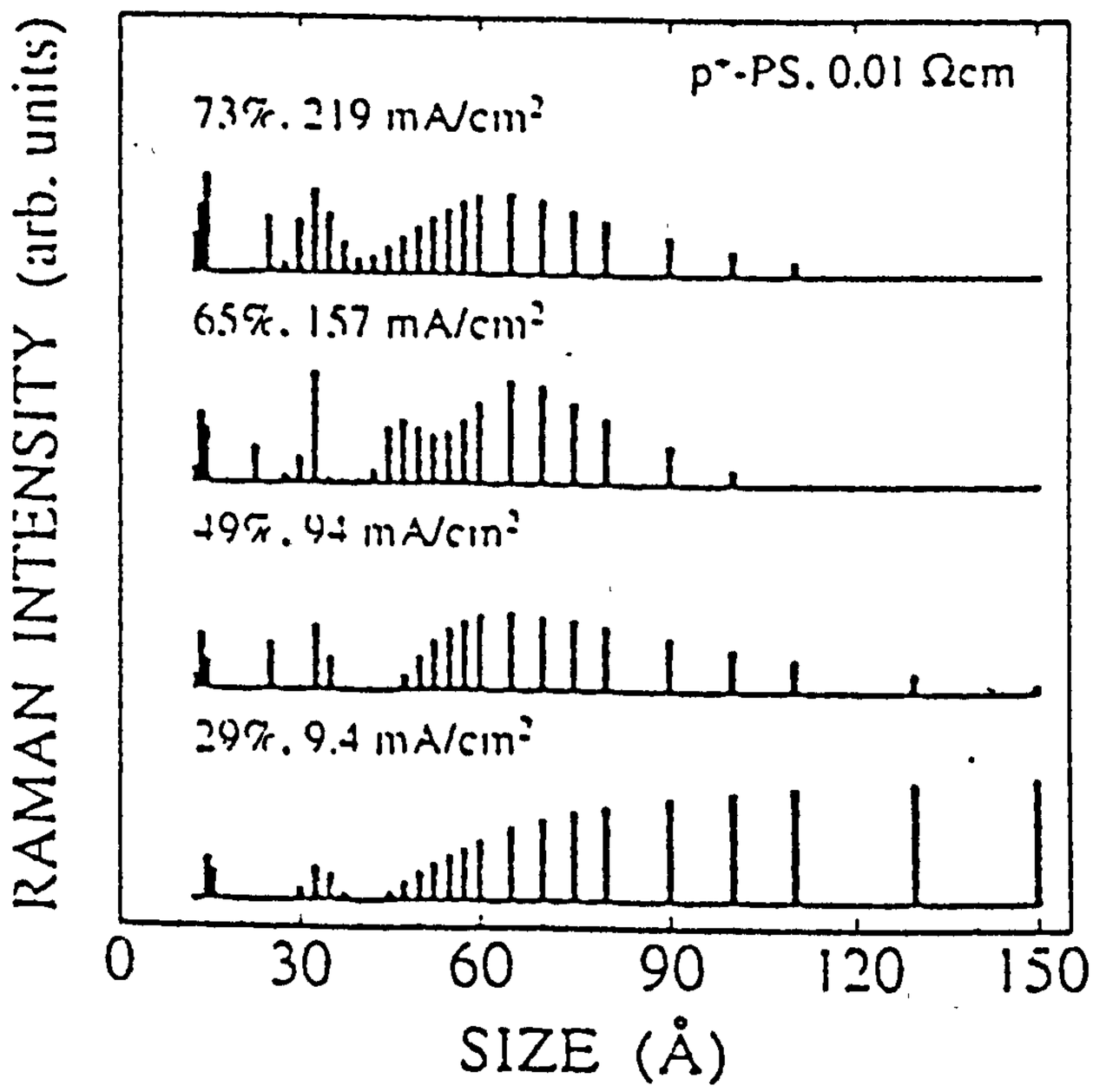

Figure 1.4 Size distribution from PS by Raman spectroscopy. Nanocrystal size distribution for porous Si layer formed with different current densities and therefore exhibiting different porosities. The PS layer thickness is 5 μm and the substrate is p-type doped (0.001 cm). After H. Münder, et al., (1993).

As a comparison, Figures 1.4 and 1.5 show the size distributions of nanowires/crystallites from porous silicon obtained using Raman spectroscopy (Münder, et al. 1993) and from clusters by high resolution TEM (Kanemitsu, et al., 1992) respectively.

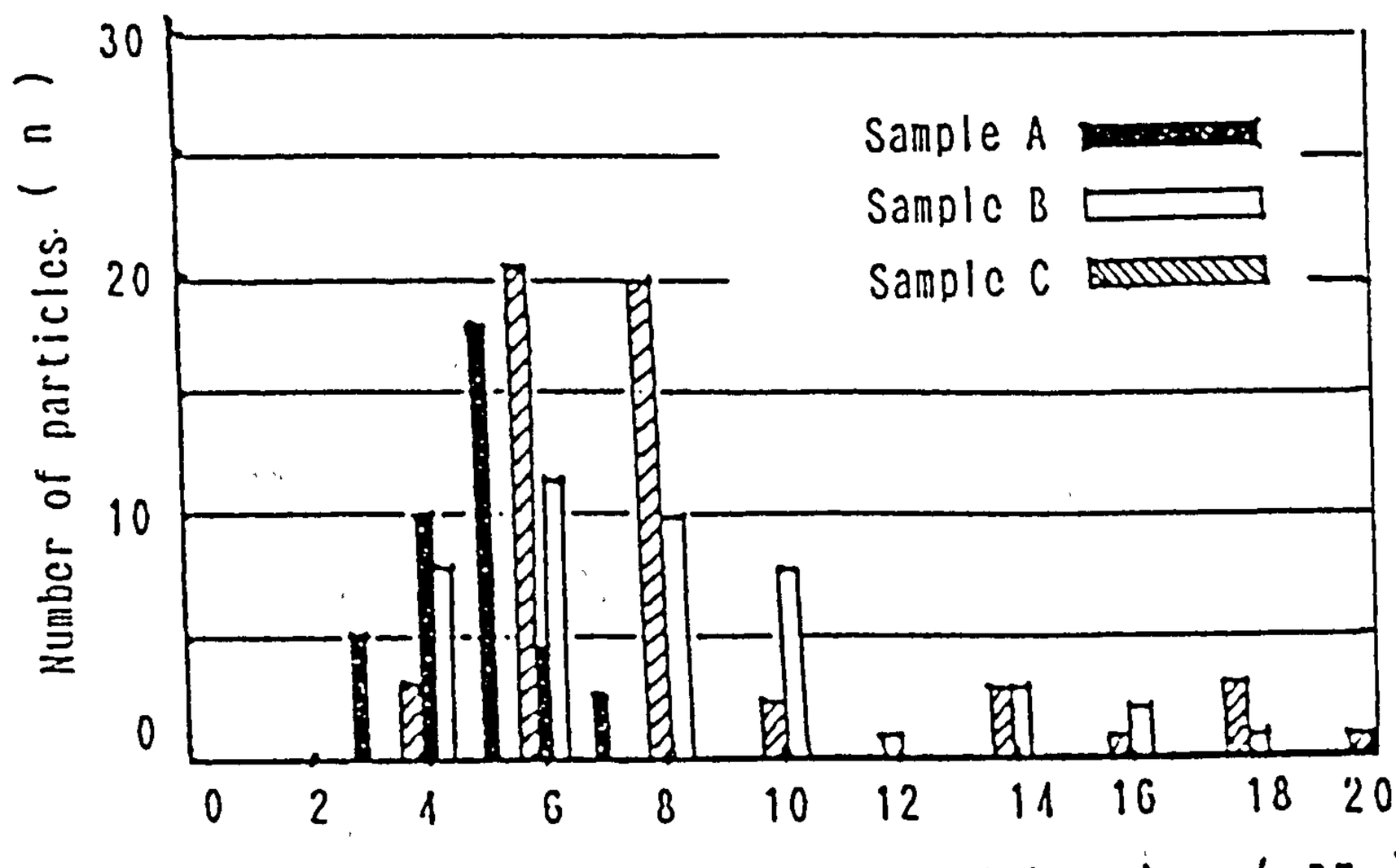

Figure 1.5 Size distribution for clusters by HRTEM. The size distribution of Si nanocrystals in SiO_2 matrices. The distributions correspond to PL peaks at 710 nm (sample A) and 720 nm (sample B). After Kawaguchi and Miyazima, (1992).

Both calculations of size effect and experimental measurements of nanosized crystalline cores appear to correlate as shown above. Unfortunately, porous silicon tends to be

inhomogeneous, its luminescence spectrum is broad, and microscopy on highly porous material is difficult. High resolution TEM can do much less for this kind of system, while Raman spectroscopy is only sensitive to three dimensionally confined materials rather than two or one dimensionally confined. Therefore, a direct comparison of particle size with luminescence energy, which would provide a stringent test of the quantum confinement model, has not been achieved (Collins and Tischler, 1993).

Furthermore, there has not been universal agreement about the applicability of the quantum confinement model, and other explanations have been proposed. Most of these proposals are based on similarities between the properties of porous silicon and other silicon-based materials that exhibit visible luminescence: that from HOMOCVD-deposited a-Si:H was attributed to a Si-H alloy effect in which high concentrations of hydrogen in the a-Si effectively increase the bandgap of the material (Wolford et al., 1993). In the case of porous silicon, the hydrogen termination and large surface-to-volume ratio in the small features making up the porous layer imply that the ratio of hydrogen to silicon is also large for this material. Several groups (Prokes et al., 1992, Tessler, et al., 1993) have investigated the possibility that an alloy effect may apply to porous silicon. On the other hand, recent results show that efficient luminescence can be obtained from oxidised PS in which hydrogen is absent from the surface, which is inconsistent with the model.

Another interesting explanation that has received much attention attributes the luminescence to the polymer silioxene ($Si_6O_3H_6$), which is produced in the porous layer

during anodization (Brandt et al., 1992, and Fuchs, et al., 1993). In those studies, they compared the optical and structural properties of anodically oxidized silicon with those of siloxene and its related compounds, and concluded that the entity causing the luminescence in porous silicon layers is identical to that in siloxene. It was said that the full agreement had been found between the vibrational properties and the behaviour of the luminescence (life-time, intensities, position, blue shifts) in both materials. The main conclusion was that visible light emission from porous silicon layer is not an intrinsic property of crystalline silicon (i.e. not due to quantum confinement effects) but depends on specific chemical reactions of silicon with hydrogen and oxygen. However, many means (e.g. infrared measurements and XPS) have been used to show that oxygen is essentially absent from freshly prepared, optically efficient porous silicon. This observation is inconsistent with the anticipated chemical and structural properties of siloxene.

It is natural to wonder if a common explanation for visible luminescence applies to some or all of these materials (porous silicon, nanocrystallite, nanopowder and nanocluster). At present, most researchers agree that quantum confinement is probably at least partly responsible for luminescence in nanostructures, but a definitive experiment has yet to be reported.

1.6 The Work in This Thesis

1.6.1 About porous silicon

It was suggested in the very first reports on porous silicon (Canham, 1990, and, Lehmann, 1991) that the strong blue shift of the photoluminescence (PL) was caused by a quantum size effect, mainly due to the presence of quantum wires. This strong blue shift results in the originally infrared band-gap material emitting at room temperature over the entire visible region from red to blue (Mimura, 1994). Much research has supported the model of band-gap widening by confinement: (1) details of the PL spectra, of which about 3%-5% show small extrema that superimpose on the larger main peak. Spacing between these smaller maxima is reproducible and independent of the main peak energy and sample history, while energy steps between them correlate with differences in the exciton energies due to changing the sizes of the quantum wires by a complete monolayer of atoms (Behrensmeier et al., 1993); (2) soft x-ray absorption, for which measurements of x-ray absorption in the vicinity of the silicon L-edge in PS show a blueshift and a broadening of the conduction band edge, consistent with a distribution of quantum confinement energies (Buuren, et al., 1992); (3) synchrotron-light-induced optical luminescence, for which both luminescence spectra and the absorption edge shifts of total electron yield K-edge XAFS (x-ray absorption fine structure) under the excitation energy of around 1,839 eV, suggested that the luminescence was due to the size effect (Sham, et al., 1993); (4) x-ray small-angle scattering (Naudon, et al., 1994), by which it is shown that when the oxidation

level increases, the size of the crystalline Si domains, which constitute the PS layer, decreases. This size reduction correlates with the blue-shift observed in the PL spectra when the oxidation level is increased, and with conventional optical-absorption (Kanemitsu, et al., 1993), and high resolution TEM (Berbezier, and Halimaoui, 1993). In addition other species could also be the cause of the bandgap widening depending on the sample conditions, e.g. amorphous or disordered phases and siloxene or similar complexes, as mentioned before.

Two types of carrier transition models have been proposed to interpret the transition behaviours based on the confinement effect : firstly the band-to-band transition model (Canham, 1990) and secondly the recombination-centre-related transition model, involving surface states and disorder (tail) states (Koch, et al., 1993, and Lavine, et al. 1993) Although, it is not clear which transition type takes the major part in luminescence it is more likely to be via recombination centres as the slow band of the broad PL spectra has a much longer life-time in the range of 20-200μs.

The cores of PS are generally described as crystalline Si wires (for example, Canham, 1990, Lehmann, and Gösele, 1991, Sanders and Chang, 1992, and Xia and Chang, 1993), see Figure 1.6 (after Teschke, et al., 1993) or dots (Vial, et al., 1992, Nishida, et al., 1992). Both of the individual nanostructures, wires and dots, have been shown to exist by high resolution TEM.

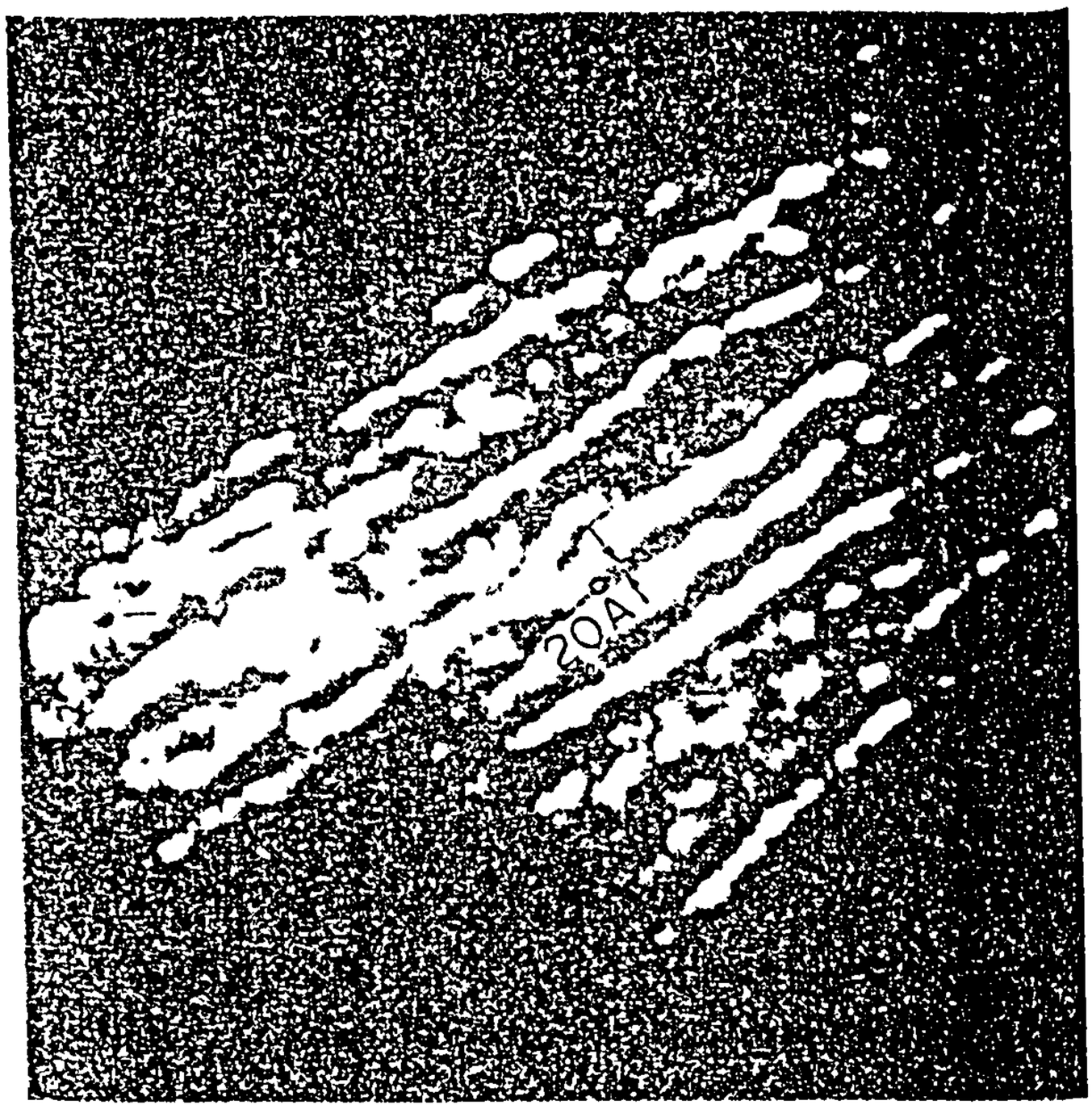

Figure 1.6 Wire-shaped-nanostructure microphotograph of porous silicon obtained by HRTEM, after Teschke, et al., (1993).

However, there remains a basic lack of knowledge of regarding (a) the average dimension and size dependence of these cores for visible emission from red to green (as blue emission from PS can only be obtained by post-anodization treatments) within a sampling depth of hundreds of nm, and (b) the ordering of the cores of freshly produced PS (which can lead us to understand at what stage other mechanisms, rather than quantum confinement, start to take part in the bandgap widening). This is mainly because (i) the size and shape of the PS framework is inhomogeneous, (ii) little structural information can be obtained by standard microscopy or diffraction techniques within the depth of the photo-exciting radiation, (iii) the average size of the cores from as-anodised PS is beyond practical detection limits. The technique of extended x-ray absorption fine structure (EXAFS) provides a useful way to estimate

the dimensions and average size, and even the ordering, on a scale of a few nanometers, within a reasonable effective sample depth (~2500Å for 80% porosity Si (Eroil, et al., 1988).

A previous report (Schuppler, et al., 1994) on deducing core effective dimensionality and sizes by EXAFS, where only orange to infrared PS (PL peaks at ~640-840 nm) was measured, suggested a figure of three-dimensional confined nanodots with sizes from 1.5-8 nm in diameter. Two dimensionally confined nanowires were ruled out by this study. This nanodot conclusion of PS is quite negative to the applications of PS, such as in electroluminescent (EL) devices, as lower carrier transportation through nanodots rather than nanowires would strongly affect the efficiency of EL. Studies of EL from PS however claim lower voltage and higher current than expected from a dot-based system.

As part of this project, a study is presented of PS nanostructure from a series of as-anodised PS emitting in the red, yellow and green (PL peaks at 690, 580 and 520 nm respectively). This almost covers all of the visible luminescence region that has so far been obtained from as-anodised material : blue luminescence is only observed after further processing such as rapid thermal oxidation (RTO) (Loni, et al., 1995, and Twybeskov, et al., 1994) or boiling in water (Hou, et al., 1993). As we are interested in the nanostructure of PS from the most type of wafers used most by researchers, the resistance used in this study is 1-3 Ωcm. About 40% of researchers use 1-5 Ωcm in both PL and EL research, rather than >50 Ωcm as used in the work of Schuppler, et al.,

(1994) and on which only a few percent work. We emphasise the resistance here because it plays an important part in the PL peak energy of PS as well as in the nanostructure: it is very difficult to make very efficient green PL from very higher resistance wafers. NEXAFS shows the near K-edge absorption of Si-Si and Si-O bonds. From Fourier transform of the fits to the EXAFS data, combined with the widening of the bandgap from both PL peak energy (suitable for the band-to-band model) and estimated optical bandgap from PLE (suitable for the transition centre model), the nanostructure shape, one dimension nanowire, is deduced. The dependencies of structural dimensionality and sizes are predicted for differently emitting PS.

1.6.2 About blue emitting clusters

As mentioned above, visible light emission from elemental semiconductor nanodots/crystallites, such as, Si, C, Ge clusters embedded in SiO_2, is one of the areas of extensive research in quantum physics and applications in recent years. Previous reports on silicon (Dimaria, et al., 1984, and Ito, et al., 1992), carbon (Hayashi, et al., 1993), and germanium (Maeda, et al., 1991, Kanemitsu, et al., 1992, and Maeda, 1995) clusters embedded in SiO_2 matrices suggested that optical transitions associated with the fundamental absorption edge of the nanostructured material had direct rather than indirect character, (e.g. the life time is only a few ns or less), and there was evidence for the presence of nanocrystals in high-resolution TEM real-space images,

see Figure 1.7. Similarly to porous silicon, there are broad distributions in the cluster sizes and broad PL spectra. It is believed that the strong blue-shifted visible emission is mainly due to the size effect, as the PL peak energies increase when the mean sizes of the clusters decrease. The reported PL peak wavelengths are >800 nm for Si clusters excited by 325 nm, 540-570 nm for C when excited by 514 nm, and ~ 530-700 nm for Ge clusters when excited by 488 nm. In other words, intense visible photoluminescence (PL), from red to green, have been observed from annealed Si, Ge or C nanoclusters (nanocrystallite) - three dimensional confined quantum dots - embedded in SiO_2 matrices. Weak UV and blue PL were also detected from as-deposited samples (Maeda, 1995). For flat panel display, the three basic colours red, yellow and blue are essential. So higher energy emission from nanostructures, i.e. blue PL, is a basic requirement.

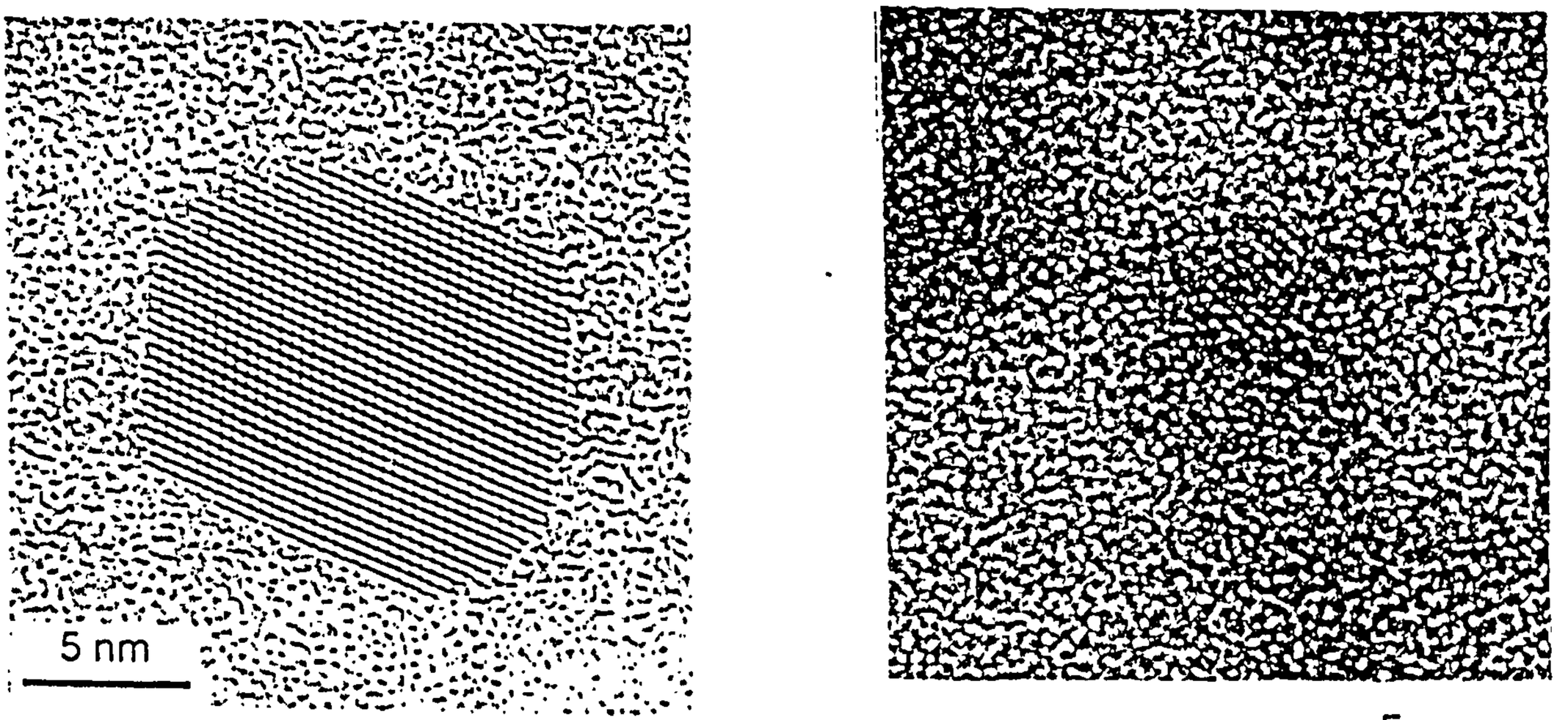

(a) Lattice image with the size of 15 nm (b) The clusters of green PL

Figure 1.7 The TEM real-space image of nanocrystal of

Ge nanoclusters, after Maeda, (1995).

The other part of the work in this thesis is the presentation of strong and stable blue (420-490 nm) PL from both silicon and carbon clusters embedded in SiO_2. Silicon, carbon and oxygen K-edge EXAFS have been used to determine the emitting related materials and relevant chemical environment of the sputtered clusters. The local structure information from both as-sputtered and annealed clustered films will be compared to understand the relation between annealing and radiative transition. The size distributions of the clusters will be given from TEM and will again suggest the origin of the blue PL is due to quantum confinement. The reason for obtaining the higher energy emission is discussed in term of size control by N_2 annealing. Unstable UV emission was also observed from some of the carbon clustered films, and the possible origin of this is also given attention.

CHAPTER 2 METHODS OF MAKING NANOSTRUCTURES AND CHARACTERIZATIONS IN THIS PROJECT

This Chapter gives some detailed experimental layouts and conditions of both preparation of porous silicon and nanoclustered films, and characterization by PL, TEM, EXAFS, NEXAFS. The theory of EXAFS and NEXAFS is given as well, since XAFS techniques played an important part in the nanostructure related characterizations.

2.1 Anodisation and Stain Etching

Despite the discovery of porous silicon as long ago as 1956 by Uhlir (1956), the morphology and structures achievable with partial electrochemical dissolution of Si have only received detailed study over the last decade (Beale, et al., 1985, Earwaker, et al., 1985, and Bomchil, et al., 1988). The anodisation of Si wafers at low current densities in HF-based solutions can be used to generate an array of extremely small holes that run orthogonal to the surface. Bulk Si can be made microporous (pore $\leq$ 20 Å), mesoporous (pore width 20-500 Å), or macroporous (pore width $\rangle$ 500 Å) depending upon substrate resistivity and anodization conditions (Gregg and Sing, 1982).

Figure 2.1 shows the basic process of anodization - the main method for making porous silicon. The solutions which have been used to fabricate porous Si are (1) hydrofluoric acid (HF) with pure water and (2) hydrofluoric acid with ethanol (C_2H_5OH)and water, although

other solutions have also been used. In the very first reports on the strong photoluminescence from porous Si, both types of solutions were used to obtain porous Si. These solutions were (1) HF, concentrations from 20% to 48% (Canham, 1990), and (2) 1:1 of 98 wt. % ethanol and 48 wt. % HF (Lehmann and Gösele, 1991). Since then, the two studies have become the main electrochemical etches for PS. Very different concentrations of HF have been employed for adjusting the size of nanopores to obtain a range of PL response (Zhang, et al., 1993). A very popular solution, up to now, is 1:1:2 of HF:H_2O:ethanol, e.g. in the reports by Grosman, et al., 1993, and Lee, et al. 1994.

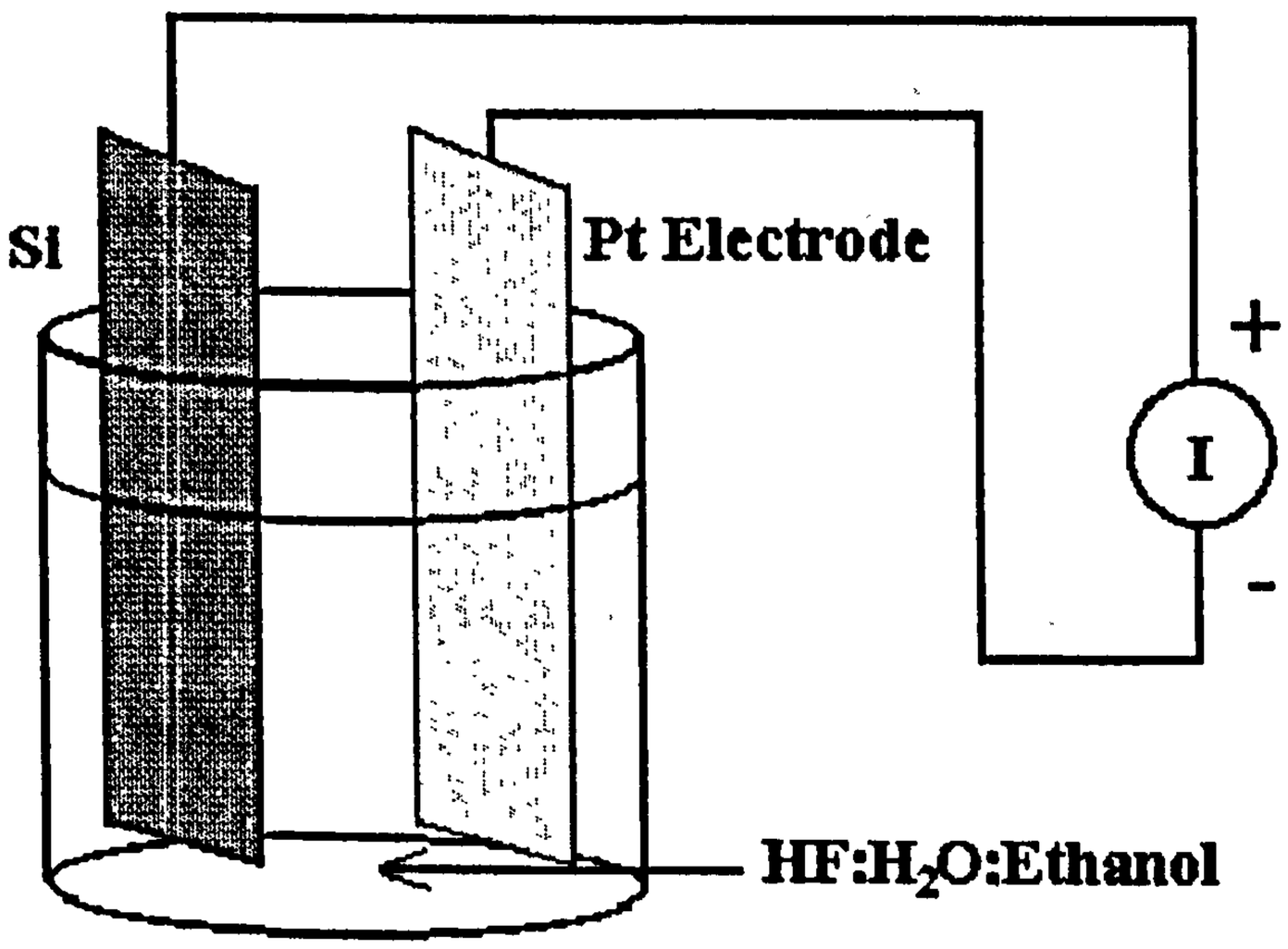

Figure 2.1 Anodization process for making porous silicon.

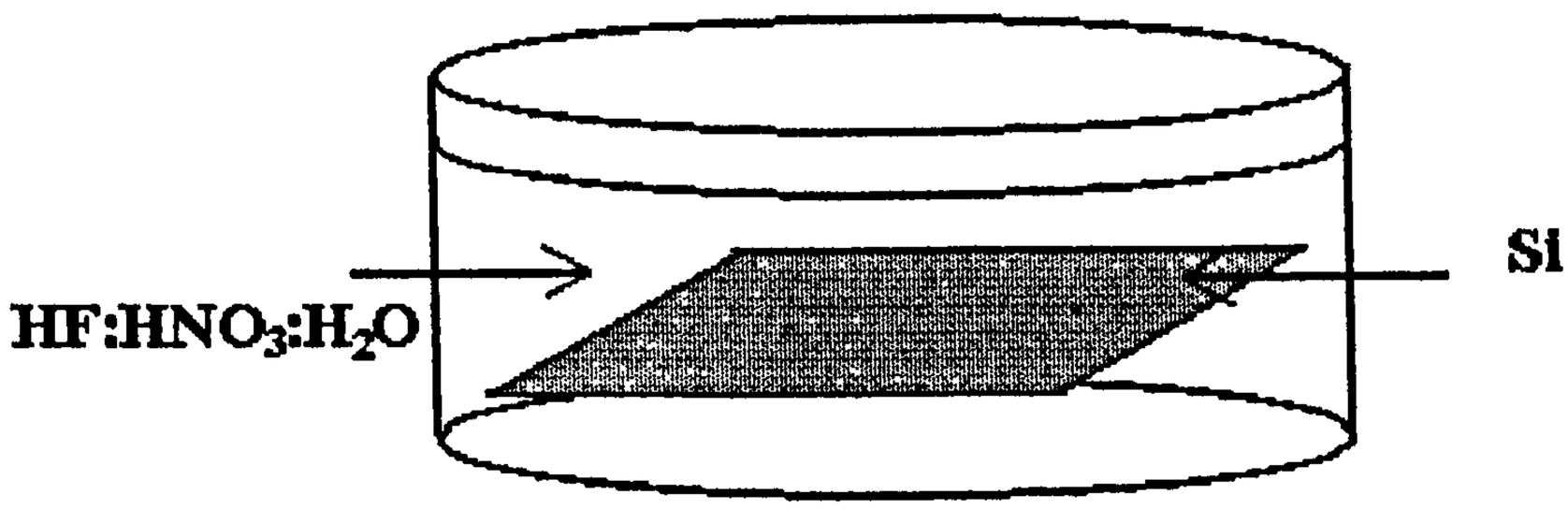

Figure 2.2 Chemical stain etching of porous Si.

Instead of anodization, chemical stain etching (or chemical etching) can be used to fabricate porous Si, especially for PS from deposited polycrystalline Si (poly-Si) (Dubbelday, et al., 1993, and Steckl, et al., 1994) or from poly-Si from annealed amorphous Si. Stain etching, unlike anodization, has the advantage that the formation of porous-Si-film is not affected by the impurities concentration of doping very much. Since poly-Si or amorphous Si can be deposited at low temperatures, this opens the door for many optoelectronic applications of poly-Si which integrate photoemissive poly-Si thin film with existing device structures. For example, poly-Si photoemitters can be deposited on Si very large scale integrated (VLSI) circuits for inter- and intrachip optical communications and on glass substrates for flat panel displays.

A typical chemical stain etch uses a solution of HF:HNO_3:deionized H_2O (1:3:5) or (1:5:10), see Figure 2.2. The formation of porous Si by this way is a result of hole injection from the HNO_3 oxidant in to the silicon substrate via the following net reaction:

$$Si + HNO_3 + 6HF \rightarrow H_2SiF_6 + HNO_2 + H_2O + H_2$$

The reaction is catalyzed by the presence of NO_2^- ions, and so there is usually an induction period observed for the etching process. Typical etch times range from 2 to 15 min.

Porous silicon in the work of this thesis was mainly prepared by electrochemical anodisation of (100) p-type, boron-doped, 1-3 Ωcm Si wafers in a solution of HF(48%):H_2O:ethanol=1:1:2, resulting in PS film thickness of >1 μm. Different anodization conditions were used to make porous Si with different PL peak wavelengths, such as peaks in the dark red, red, orange, yellow and green. The anodising conditions for red, yellow and green samples are: (1) 8 min, current density 30 mA/cm², (2) 20 min, 20 mA/cm², + 5 min without current, (3) 20 min, 20 mA/cm², + 30 min without current, respectively. Furthermore, for dark red and orange PL peaks, they are (1) 4-5 min., current density 20-30 mA/cm², and (2) 10-13 min, current density 20-30 mA/cm². The wafers for yellow and green PL were coated on the back with aluminum and wax to produce a very uniform emission area. After rinsing in de-ionized water and blow-drying with N_2, the samples (1) were put in a vacuum storage chamber and kept at 10^{-6} torr to keep them "fresh", as native oxidization would furtherly oxidise the top layer and affect the mean nanostructure to be investigated, or (2) kept in air to enable oxidation to proceed for different purposes.

2.2 RF - Sputtering

The semiconductor-doped glasses (sometimes called glassy-matric films) including nonstoichometric Si and C oxide were deposited by rf-sputtering, see Figure 2.3, onto Si (100)substrates with thicknesses of $\rangle$ 1 μm. The mixed targets were set up as following: (1) on the pure SiO_2 8" target between 3 and 20 pieces of Si wafer (10×10×0.3 mm^3) were placed in an area of ~4" in diameter; (2) on the pure SiO_2 8" target, between 5 and 16 pieces of pure graphite rod of 6 mm diameter were placed in an area of ~4" in diameter, to produce Si and C cluster samples of various PL response, respectively. The base pressure of the system was $3x10^{-6}$ mbar before sputtering. The deposition conditions were: $3×10^{-4}$ - $6×10^{-3}$ mbar Ar, 400W rf power for Si doped glasses, and, $6×10^{-4}$ - $1×10^{-2}$ mbar Ar, 500 - 1250W rf power for C doped glasses, respectively. After deposition the samples were isothermally annealed to get large amount of nc- Si and C in the matrix. The isothermal annealing was carried out in an electrical furnace at 600°C and 800°C for 20 min and 30 min in a N_2 atmosphere flowing at a rate of 3 l min^{-1}.

Compared with other reports on glassy-matrix films, the main difference in the method for producing luminescence clusters presented here is that the annealing was carried out here in N_2 atmosphere, rather than in an Ar atmosphere (as described by e.g. Maeda, 1995, and Hayashi et al, 1993).

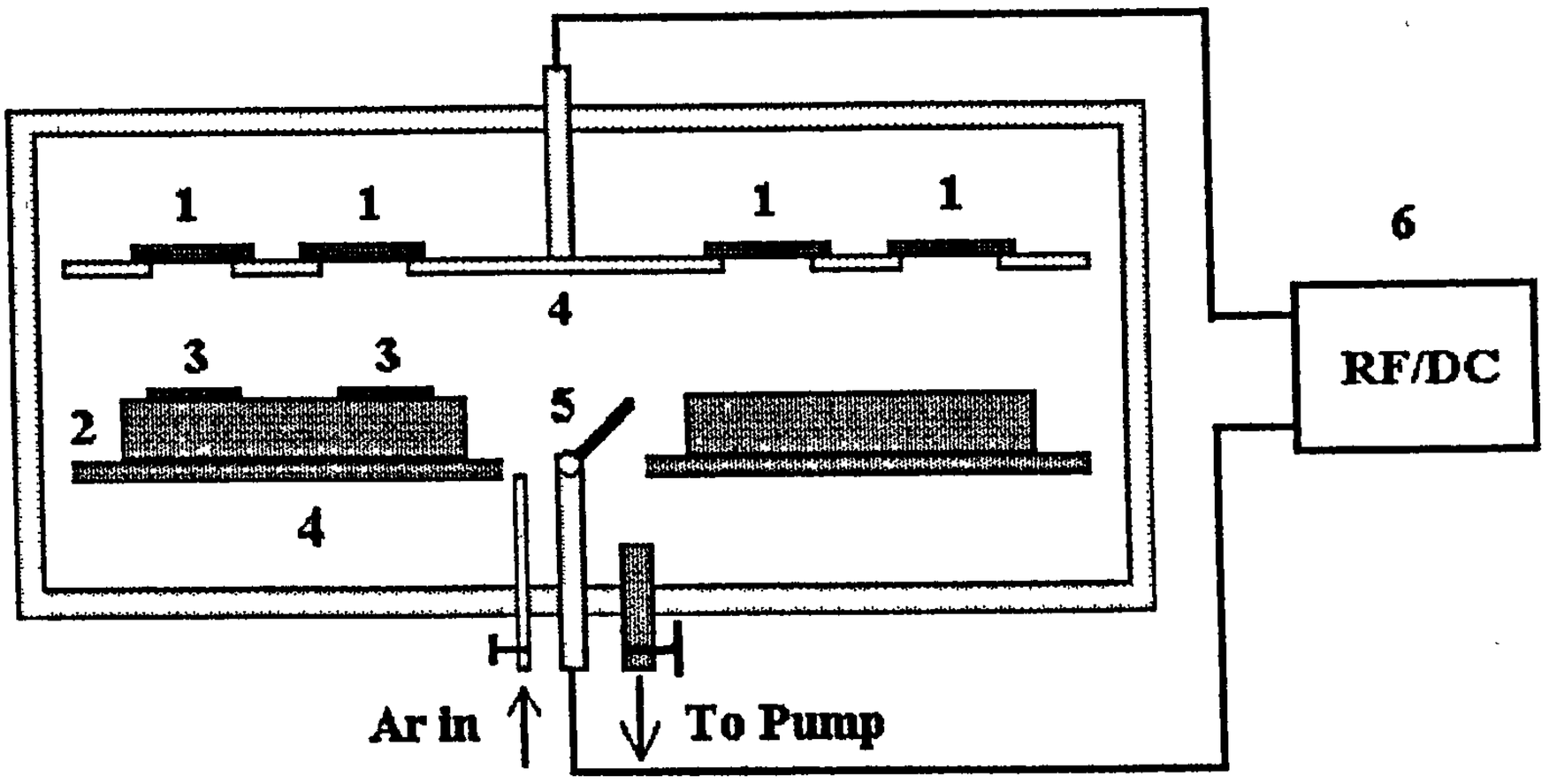

Figure 2.3 Nanoclusters deposited by rf-sputtering.

1) substrate for the films. 2) SiO_2 target. 3) Si or C targets. 4) probe. 5) switch for different targets. 6) power supply for RF/DC.

2.3 Photoluminescence (PL) and Excitation Dependence of PL (PLE)

Photoluminescence (PL) is one of the most useful optical characterisation methods for semiconductor research, with its powerful and sensitive ability to find impurities and defects in silicon and group III-V element semiconductors which affect material quality and device performance. Thus given impurity produces a set of characteristic spectral features. This fingerprint identifies the impurity type, and often several different impurities can be seen in a

single PL spectrum. In some cases PL goes beyond bare identification, to measure impurity concentrations. In another use, the halfwidths of PL peaks are an indication of sample quality and crystallinity, although such analysis has not yet become highly quantitative. Finally, PL is sensitive to stress, and can measure its magnitude and direction.

PL can also be used to infer semiconductor band gaps. This is important for systems such as $Al_xGa_{1-x}As$ and other ternary alloys since the gap varies with the compositional parameter x, yet must be accurately known for applications. When the relation between gap energy and x is known, the PL determination of the gap can be inverted to determine x. If PL is measured from scanning across the face of a sample, this becomes a useful tool to determine inhomogeneity. Among the optical characterisation methods, PL is probably the best developed to carry out such spatial scanning, with commercial equipment available.

The usefulness of PL to measure band gaps is illustrated in the work of Wagner (Wagner, 1984 and 1985). He made a complete PL and photoluminescence excitation (PLE) analysis of n- and p-silicon with phosphorus, boron, or arsenic doping levels from 10^{17} to $4\times10^{20}cm^{-3}$. The optical measurement of band gap involves complications. An absorption measurement determines the gap between the top of the valence band and the Fermi Level. When the doping is heavy, the Fermi energy is significant and the absorption band gap - called the "optical gap" - is greater than the conduction band gap measured from the valence band to the bottom of the conduction band. In conventional PL, the emitted photon must arise from the states between the bottom of the conduction band and the Fermi level, hence PL spectra represent a range between optical band gap and the 'real' conduction band gap.

Because of the direct relation between band gaps and PL(E) measurements, most of the time researchers in experimental nano-physics show the PL spectra from their nanostructures as means of comparing size distribution with blue shift and absorption. For this reason, many of PL measurements have been obtained in this study and will be given.

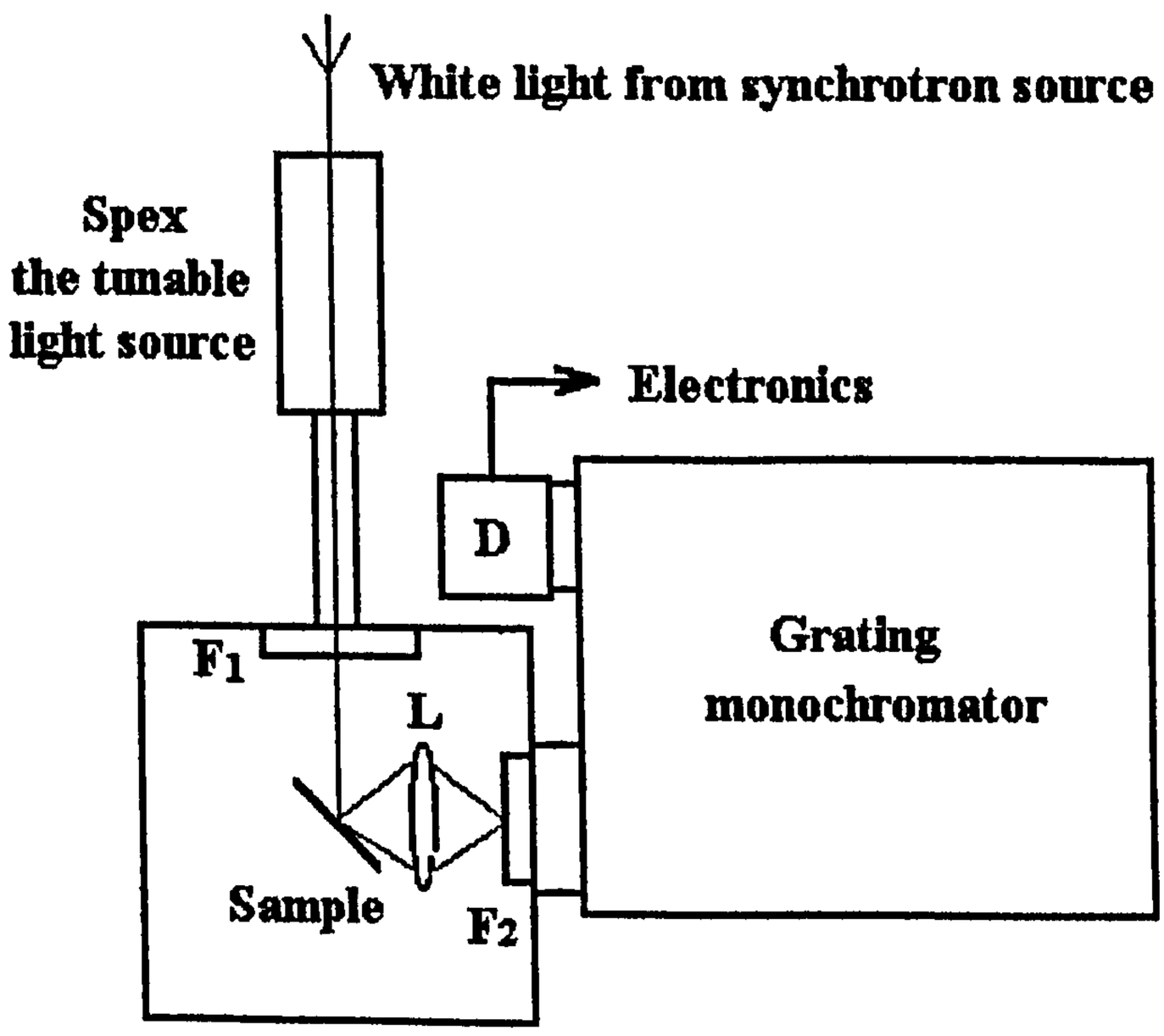

Figure 2.4. Photoluminescence arrangement. L - lens; F1 - band-pass-filter; F2 - cut-on-filter; D - detector (Photomultiplier in photon counting mode).

The PL measurements were carried out at DRAL Daresbury Laboratory Synchrotron Radiation Source, beam line 12.1, at room temperature. The bandwidth of the tuneable light source was less than 10 nm. The excitation wavelengths (energies) were from 260 nm (4.768 eV) to 600 nm (2.254 eV). In order to compare the PLE data, all the PL spectra have been normalised by excitation light power, i.e. as if all of the PL data were taken under the same excitation power across the 260 nm to 600 nm range. This normalisation process was used as it had been found that the emission intensity linearly increases with excitation power under low-light-source powers (Fuchs, et al., 1992 and Murayama, et al., 1992), and the power of this tuneable light source is lower than 10 μW. The spectra were also calibrated by the response efficiencies of the analyzing Minimate monochromator and detector system. The measurement arrangement is shown above in Figure 2.4.

2.4 K - Edge X-ray Absorption Spectroscopy (XAFS)

The introduction of synchrotron radiation has made possible the measurement of high-resolution low-noise x-ray absorption spectra. Extraction of the oscillatory structure (EXAFS and XANES) from these spectra provides information on the local atomic environment in molecules and condensed material by use of the theory of the electron scattering which gives rise to the structure.

The theory of photoelectron scattering has reached a high level of development over the past 20 years. It now provides an essentially complete description of the processes leading to EXAFS and XANES. It shows how structural information is contained in the spectrum as well as the effects of inelastic processes.

The availability of the intense beam of continuous x-radiation from synchrotron sources such as electron storage rings has stimulated the development of a technique of structure determination which is particularly suited to studies of short range inter atomic correlations. It has long been observed that in condensed matter, the x-ray absorption cross-section for the photoexcitation of an electron from a deep core state exhibits oscillations as a function of photon energy. The oscillation structure can extend for many hundreds of volts above the edge (Kronig, 1931 and 1932). This structure is known as the extended x-ray absorption fine structure (EXAFS). The oscillations are a final state electron effect, arising from the interference between the wavefunction of the outgoing photoelectron and that small part of itself which is scattered back from neighboring atoms.

The primary objective of EXAFS studies is to determine the local atomic environment of the excited atom by analyzing the measured oscillatory structure. The interference which gives rise to the EXAFS reflects directly the total phase of the backscattered wave, which is largely made up of the product of the photoelectron wavevector and the distance traveled but which also includes contributions from the scattering process and from the passage of the photoelectron out and back through the potential of the excited atom. The major contribution to the absorption matrix element comes from regions of space very close to the

nucleus of the excited atom since the core state is highly localised. The amplitude of the oscillations depends on the number and electron scattering strength of the scattering atoms. The EXAFS and following analysis depend only on the local atomic environment by reason of the fact that only elasticity scattered electrons can contribute to the interference and the elastic mean free path of the electrons is short.

Consequently, analysis of the EXAFS gives information not only on the distance but also on the number and chemical type of the near neighbours of the excited, or central, atom. Since the EXAFS spectrum is measured on a known absorption edge, due to an atom of known chemical type, the technique is chemically specific, giving the co-ordination of a known type of atom. In other words, EXAFS analysis could yield local structural information including bond angle, length, co-ordination numbers of different shells and ordering. From the local structural details, very detailed and interesting micro-information can be deduced.

2.4.1 Experimental layout

The experimental layout of station 3.4, at DRAL Daresbury Laboratory, is described below and illustrated in Figure 2.5. The XAFS station HE-PGM2 of BESSY Laboratory employed in this study has a similar set up.

X-ray absorption spectroscopy experiments require a combination of high intensity and excellent energy resolution. Accordingly, a two crystal vertically dispersing wide aperture

monochromator is used . It will generally operate behind a Be window unless soft x-rays are required. After this the incident beam intensity is registered by a semi-transparent reference grid. This is necessary so that absorption spectra can be corrected for the decaying storage ring beam current and the instrument response of the monochromator/mirror combination.

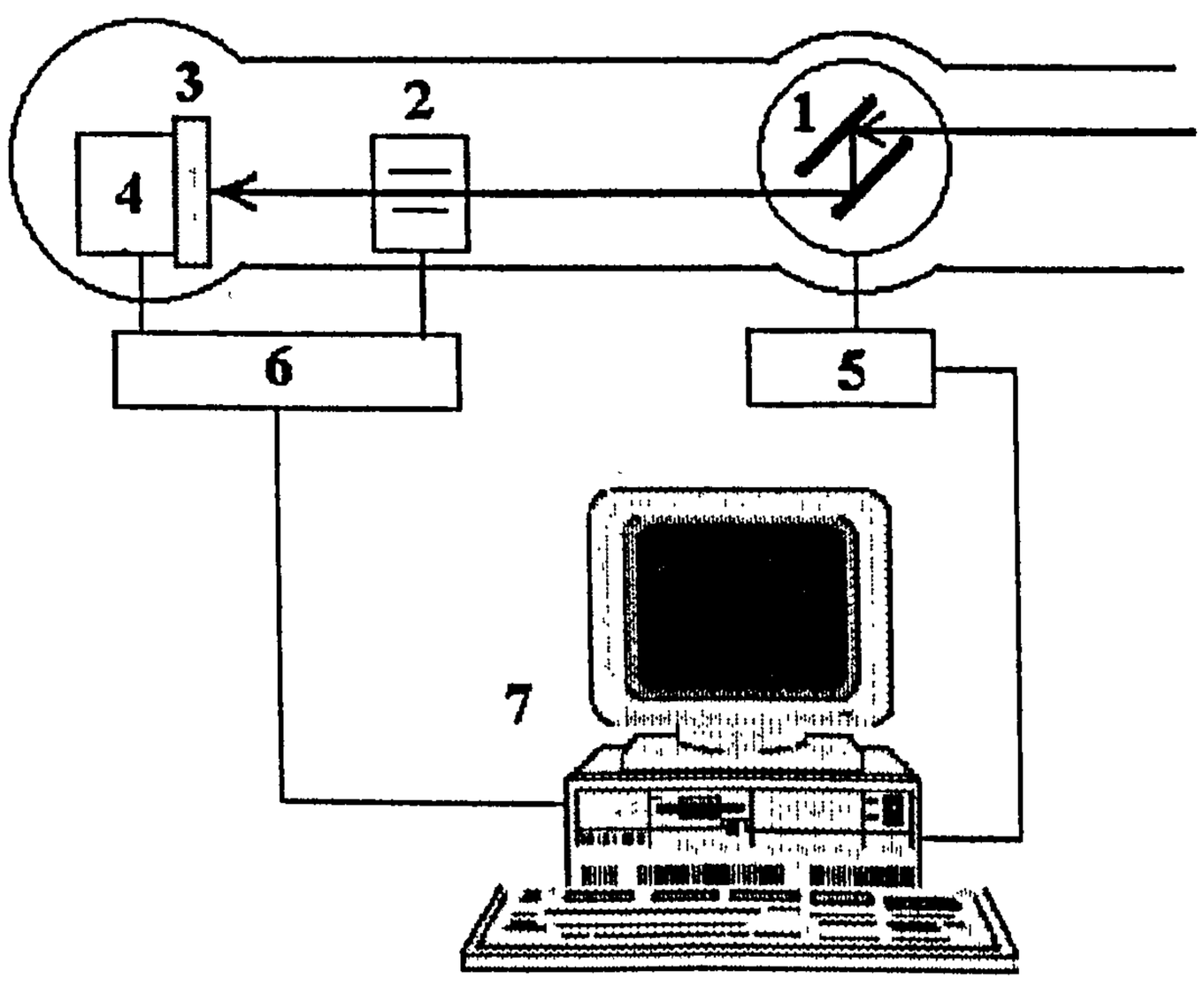

Figure 2.5 Layout for x-ray absorption spectroscopy experiment in the total-yield mode. Samples were placed in vacuum chamber. 1. Double crystal monochromator. 2. Reference grid, I_o. 3. Sample. 4. Electron detector. 5. Monochromator drive. 6. Analogue device. 7. Computer.

After scattering, the excited K-shell electrons of the atoms of the sample are collected by the current/electron detector for analysis.

In the work described in this thesis, the Si K-edge XANES and EXAFS were carried out at CCLRC Daresbury Laboratory Synchrotron Radiation Source, beam line 3.4. The EXAFS was determined by the total-yield technique, and taken around the Si K-edge at about 1840 eV. For EXAFS the x-rays were incident on the samples normally, and the absorption was measured as the current required to neutralise the samples as a result of photoelectron emission. (e.g., Bayliss, 1994). Scans were made from 1800 to 2500 eV (k range up to 15 $Å^{-1}$), with 742 independent points. The k range used in the Fourier transform fitting procedures described was 3 - 12.5 $Å^{-1}$, with ~600 independent points. For comparison EXAFS data were also taken from a c-Si wafer, a-Si and a-SiO_2 films, which were also used to calibrate the system. The structural measurements were carried out at room temperature. All of the raw experimental data have been shifted by -0.5 eV, based on reference data from a bulk c-Si wafer, due to the error in monochromator calibration.

C and O K-edge XANES and EXAFS were obtained in fluorescence mode on the HE - PGM2 station at the BESSY Laboratory around their K - edges at about 283 eV for carbon and 531 eV for oxgyen. The experimental layout was similar as that for Si K-edge XAFS. The main difference was the electron detector was replaced by fluorescent photon detector.

The computing program for theoretical fitting of EXAFS used in this study was EXCURV92.

2.4.2 Basic principles of EXAFS

The attenuation of x-ray passing through a medium occurs via three principal processes: scattering, pair production and photoelectric absorption. In the energy range of interest for EXAFS studies (1-40 keV) photoelectric absorption dominates the attenuation process. In photoelectric absorption a single x-ray photon is absorbed by an atom, and gives up its energy to a single electron which is thereby excited into a higher energy level. The energy balance is expressed by

$$E_f = \hbar\omega - E_b \tag{2.1}$$

where $\hbar\omega$ is the energy of the x-ray photon, E_b the (positive)binding energy of the electron in its initial state and E_f its energy after emission from the atom. It is assumed that the final state electron is unbound, i.e. that it has a continuous distribution of allowed energies.

For K-absorption edges, the most often used in EXAFS spectroscopy, which correspond to excitation of an electron from the 1s level, the probability of x-ray absorption with the dipole approximation is given by (Bransden, 1983)

$$P = \frac{2\pi^2 e^2}{mc^2\omega}\left|\langle f|\vec{\varepsilon}\bullet\vec{r}|i\rangle\right|^2 \rho(E_f) \tag{2.2}$$

where $|i\rangle$ is the wavefunction of the initial 1s state, $|f\rangle$ that of the final state and $\rho(E_f)$ is the density of allowed states at the final state energy E_f . ε is the electric field polarisation vector of the x-ray beam. The selection rules in the dipole approximation force $|f\rangle$ to be a p state if the initial state is s-like. For x-ray energies well above the absorption edge, the density of states $\rho(E_f)$ is a smooth function and may be approximated by that of a free electron of momentum k and energy $\hbar^2k^2/2m$ where

$$\frac{\hbar^2k^2}{2m} = E_f + \overline{E} = \hbar\omega - E_{edge} + E_0 \qquad (2.3)$$

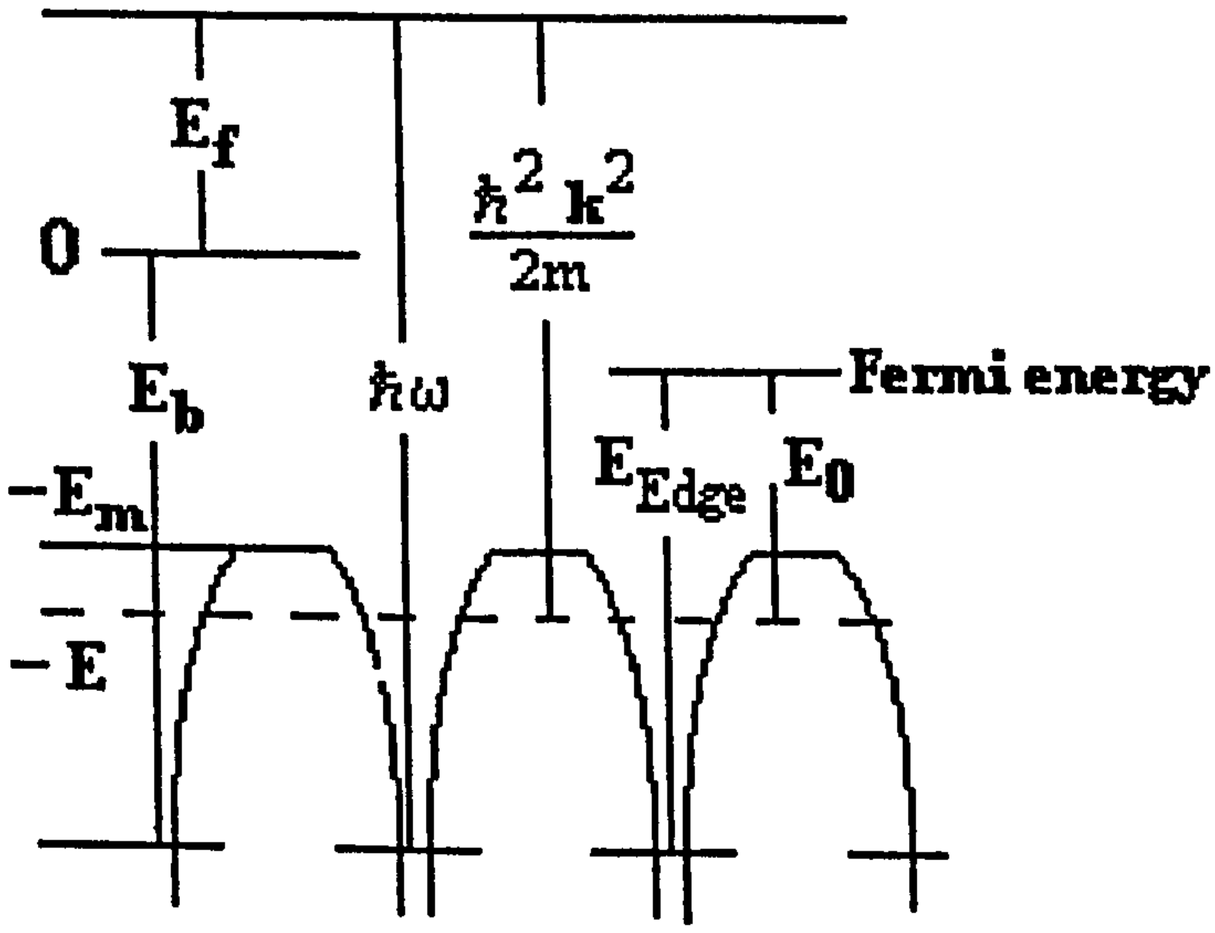

Figure 2.6 energies in the x-ray absorption process.

in which k is the photoelectron momentum and $\overline{E}$ is the energy of a free electron of zero momentum and corresponds to the effective mean potential experienced by an excited electron in the medium. The various energies are shown diagrammatically in Figure 2.6. It should be noted that we measure the photoelectron energy and momentum not from the position of the edge, but from a lower energy. The absorption edge occurs at the Fermi energy (or at least at the energy of lowest unoccupied state) and corresponds to a photon energy E_{edge}. The offset E_0 is usually called the threshold energy: it is of order of 10 eV. With the free electron assumption for $\rho(E_f)$ the only factor that can give rise to the EXAFS signal is the matrix element. Now the initial state wavefunction is fixed and does not vary with ω. The final state wavefunction $|f\rangle$ does vary with ω and it is this variation which gives rise to the fine structure.

The wavefunction $|f\rangle$ may be considered as a sum of two contributions. The first type - for a monoatomic gas such as argon with no fine structure and the x-ray absorption coefficient varies monotonically with ω - is isolated atom related. We are interested in the second type - the central atom is surrounded by other atoms, as in any condensed phase - where the outgoing electron will be scattered by the surrounding atoms, give rise to incoming waves. These incoming, or backscattered, waves can interfere constructively or destructively with the outgoing wave. This interference gives rise to an oscillatory variation in the matrix element as a function of ω, since the wavelength of the photoelectron is a function of ω according to equation 2.3. The significant region of space for the interference is the region where $|i\rangle$ exists, that is close to the nucleus. Constructive interference there increases the

matrix element, and hence the absorption coefficient, whilst destructive interference lowers the matrix element below the free atom value.

The absorption coefficient for a condensed sample can therefore by written as

$$\mu(k) = \mu_0(k)[1+x(k)] \tag{2.4}$$

where k, the photoelectron momentum, may be expressed in terms of the photoelectron energy, and hence the photon energy, by use of equation 2.3. $\mu_0(k)$ is the smoothly varying background which physically corresponds to the absorption coefficient of an isolated atom. The fine structure, or EXAFS function, arising as a consequence of the interference between outgoing and backscattered electron waves is therefore defined by

$$\chi(k) = [\mu(k) - \mu_0(k)] / \mu_0(k) \tag{2.5}$$

We note that $\mu_0(k)$ is that part of the atomic absorption coefficient which is only due to transitions from the initial state of interest, i.e. the contribution of one particular edge. The first step in data reduction is to remove the contributions of the other edges from the measured absorption coefficient, which may be done by fitting a smooth function to the absorption below the edge of interest and extrapolating to higher energies. Similarly we obtain $\mu_0(k)$ by fitting such an expression to the edge contribution and so obtain the EXAFS function $\chi(k)$.

The expression for the EXAFS function $\chi(k)$ which describes the oscillatory part of the K absorption coefficient is give by Stern (Stern, 1974)

$$\chi(k) = -A(k)\sum_j (N_j / kR_j^2)\left|f_j(k,\pi)\right|\exp(-2\sigma_j{}^2k^2).\exp(-2R_j/\lambda)\sin(2kR_j + 2\delta_1 + \varphi_j) \qquad (2.6)$$

in which the EXAFS is defined in terms of sets of identical scattering atoms, usually referred to as shells: a typical shell contains N_j identical scattering atoms at a mean distance R_j from the excited atom, each with an electron-scattering factor f_j. The phase of the backscattered wave is largely due to the product of the photoelectron wavevector k and the total distance traveled, $2R_j$. This is the distance out to the scattering atom and back since the major contribution to the absorption matrix element comes from regions of space very close to the nucleus of the excited atom, where the highly localised initial core state exists. The phase also contains contributions from the scattering process, the phase φ_j of the electron-scattering factor, and from the passage of the photoelectron out and back through the potential of the excited atom, $2\delta_1$ (for a K-edge, the photoelectron must have angular momentum l=1). The amplitude of the backscattered wave depends on the number of scattering atoms, N_j, and their scattering strength $\left|f_j(k,\pi)\right|$. There is also a Debye-Waller factor which depends on $\sigma_j{}^2$, the mean-square variation in R_j. In addition there are two factors which reflect the many-body nature of the x-ray absorption process: an elastic mean free path parameter (only elastically scattered electrons can take part in the interference

process) and an amplitude factor A(k), which measures the proportion of absorption events that result in the excitation of just a single photoelectron.

In the case of (2.6), the area under each peak corresponds to a partial coordination number N and our analysis is then described in terms of 'shells of atoms'. A typical shell contains N_j atoms, all the same chemical type, lying at an average distance R_j from the central atom. The peak shape we have used gives rise to the usual Debye-Waller factor. In a crystal, the mean square variation in interatomic distance is due to thermal motion, but we note that amplitudes of the two atoms, because of these thermal motions, are to some extent correlated: this is due to the contribution from long wavelength phonons which have little effect on short interatomic distances. In an amorphous system there will also be an additional contribution to σ_j^2 from the static variability in the distances due to structural disorder. The two contributions may be separated by making temperature-dependent measurements.

Thus, it has shown that analysis of the EXAFS can yield information not only on the distance but also on the number and chemical type (through $|f_j(k,\pi)|$) of the near neighbours of the excited atom. Only near neighbours contribute because of the presence of the mean free path factor exp(-2R/λ): EXAFS spectra typically contain information on atoms less that 5 Å from the excited atom. Also, since the EXAFS is measured on a known absorption edge, for an atom of known atomic number, the technique is chemically specific, giving the environment of a known type of atom.

2.4.3 Near edge x-ray absorption fine structure (NEXAFS)

NEXAFS is also called XANES (x-ray absorption near edge structure). It is the structure which lies close to the absorption edge: the upper energy limit is usually set arbitrarily some 50 eV above the edge. In this region of low photoelectron energy the elastic mean free path is long and the electron scattering factor $f(k,\pi)$ is generally large. Multiple scattering can thus be highly important. As the scattering series of the multiple scattering cause a quite complicated final-state wavefunction, specially methods, such as, band-structure and cluster methods, have been developed to calculate the XANES spectra of crystalline materials (Tyson, et al., 1992).

The result of a XANES calculation is the x-ray absorption coefficient $\mu(\omega)$, which may be compared with experiment. In all cases the calculation is so time-consuming computationally and involves so many atomic co-ordinates that it is not practicable to try to fit the calculated spectrum to experiment.

However, the experimental spectra of XANES can directly suggest the bonding states and even, the band shift for the known atoms of given material. XANES has been a useful tool for obtaining information on PS as demonstrated by Sham, et al, (Sham, et al, 1993) where the edge shift towards higher energy of about 1 eV from porous Si compared with bulk Si, has been identified as a quantum confinement shift.

2.4.4 Extended x-ray absorption fine structure (EXAFS)

The EXAFS region is conventionally taken to start some 50 eV above the edge, although single-scattering calculations may often be taken down to within 10-15 eV of the edge. Observable structure often exists over 1000 eV above the edge. The high-energy photoelectron has a short mean free path and electron scattering is comparatively weak. In this region the scattering series rapidly converges and in many cases only single-scattering processes need be considered. Thus, EXAFS calculations are reasonably simple and computationally rapid. These attributes lead to the possibility of fitting calculated EXAFS spectra to experiment and so obtaining detailed structural information.

In order to calculate the EXAFS function $\chi(k)$ we need to calculate the wavefunction of the photoelectron. Since the initial state has a well defined angular momentum it is most convenient to expand the photoelectron wavefunction in terms of eigenfunctions of the angular momentum operator. Then we can have

$$|f\rangle = \sum_{lm,l'm'} (\vec{I} + \vec{Z})_{l'm',lm} |lm\rangle \tag{2.7}$$

where the unit matrix $\vec{I}$ gives the outgoing part of the wave and the matrix $\vec{Z}$ gives the scattered part. The components of $|f\rangle$ which contribute to the absorption will be strongly limited by the selection rules.

With this form for the final-state wavefunction the EXAFS function defined by (2.4) is a linear function of matrix $\vec{Z}$:

$$\chi(k) = (1/\mu_0)\sum_{m_0}\sum_{lm,l'm'}\langle\, l_0 m_0|\vec{\varepsilon}\bullet\vec{r}|lm\,\rangle 2\,\mathrm{Re}\left\{\vec{Z}_{lm,l'm'}\exp\left[i(\delta_l+\delta_{l'}\right]\right\}\langle l'm'|\vec{\varepsilon}\bullet\vec{r}|l_0 m_o\rangle \qquad (2.8)$$

where l_0 and m_0 are the angular momentum quantum numbers of the initial state, the m_0 sum being over the degenerate sub-levels of total angular momentum l_0 which is fixed by the edge. For a K edge, with excitation from a *1s* state, we have l_0=0 so that m_0=0 only. In (2.8) the matrix elements contain wavefunctions for isolated atoms only and, with the excited atom phase shift factored out as shown, are real (Gurman, 1983). All of the effects of scattering are contained in the matrix $\vec{Z}$.

Equation (2.8) is often described as a first-order approximation, implying a neglect of the $\vec{Z}^2$ term and a consequent inaccuracy. However, the optical theorem shows that it is, in fact, exact.

In the case of a polycrystalline or amorphous sample the angle between $\vec{\varepsilon}$ and $\vec{r}$ is randomly distributed, so that we never need to calculated the atomic matrix elements. From (2.8), we have

$$\chi(k) = (2/2l+1)\sum_{m}\mathrm{Re}\left[\vec{Z}_{lm,lm}(2i\delta_l)\right]$$

$$l = l_0 + 1 \tag{2.9}$$

The remaining question is to work out the matrix $\vec{Z}$ which describes the scattering of the outgoing photoelectron. Because (i) only elastic scattering events need be considered; (ii) the final-state wavefunction is very close to the nucleus of the excited atom; (iii) the elastic mean free path is short, thus, in the expanding of $\vec{Z}$ in a series over different paths and orders of scattering, only low orders contributed and in many cases only single (back) scattering events contribute significantly. (2.10) is one of the approximations of expanding, using the Fast Curved Wave (FCW) theory (Gurman, 1984)

$$\sum_m \left[\vec{Z}_{lm,lm}(2i\delta_l)\right] = \sum_{L_1 L_2} \exp(2i\delta_l)\left[h_{L_1}{}^{(1)}(kR)\right]^2 T_{L_2}(2l+1)(2L_1+1)(2L_2+1)[C(lL_1L_2;000)]^2 \tag{2.10}$$

So, we have

$$\chi(k) = (2/2l+1)\,\mathrm{Re}\sum_{L_1 L_2} \exp(2i\delta_l)\left[h_{L_1}{}^{(1)}(kR)\right]^2 T_{L_2}(2l+1)(2L_1+1)(2L_2+1)[C(lL_1L_2;000)]^2 \tag{2.11}$$

where, $h_{L_1}{}^{(1)}(kR)$ is called Hankel function.

In the case of single-crystal samples we do not average over the directions of $\vec{r}$. In this situation extensively used in surface studies, beam polarisation and direction effects become important and information on bond directions can be obtained.

At high photoelectron energies the Hankel functions which appear in (2.11) may be approximated by their asymptotic forms, which are exponentials. The angular momentum sums may then be performed analytically and we find that the expression for the EXAFS function reduces to

$$\chi_{PW}^{(1)}(k) = (-1)^l (1/kR^2)|f(k,\pi)|\sin(2kR + 2\delta + \varphi) \qquad (2.12)$$

in which $f(k,\pi)$ is the usual electron-backscattering factor. This equation refers to a single scattering atom. To get the total EXAFS signal it is necessary to sum over all scattering atoms, this process introduces the pair distribution function $g_{\alpha\beta}(r)$. Usually, $g_{\alpha\beta}(r)$ is assumed to be written as a sum of Gaussian peaks, centered at R_j with mean-square deviation σ_j^2 and containing N_j atoms. We then find, assuming the form of (2.12) for integration purposes, that the EXAFS function due to a single peak is given by (Sayers et al., 1971),

$$\chi_\alpha^{(1)}(k) = \sum_{j\beta} N_j \exp(-2\sigma_j^2 k^2) \chi_{\alpha\beta}^{(1)}(k, R_j) \qquad (2.13)$$

The assumption of a Gaussian peak shape may be relaxed by use of the cumulant expansion (Bunker, 1983). Furthermore, there is now the possibility of using exact forms, such as the FCW theory, for the single-atom EXAFS function $\chi_\beta(k,R_j)$.

2.4.5 Fourier transform of EXAFS

XAS is mostly used to determine the local structure around the excited atom in amorphous solids, liquids, complex crystals and biological molecules, i.e. it is the EXAFS which is generally of most interest. The chief problem of data analysis is how best to obtain this structural information, or the atomic coordinations, from an experimental spectrum. The methods of data analysis in use at the present time may be grouped into two classes: real space analysis, where we work on the Fourier transform of the EXAFS spectrum $\chi(k)$, and k-space analysis where we work with the spectrum itself.

In order to treat this problem and the methods employed to solve it, we shall use the form of the EXAFS given as (2.6). In practice, wave curvature effects are always important, so we need to use (2.11). Multiple-scattering contributions may also be significant. Although these effects greatly complicate the programs used in practice, they do not alter the principles of data analysis.

The first stage in data analysis is to extract the EXAFS function $\chi(k)$ from the measured absorption (or fluorescence or total yield) data. The first step is to remove the contributions of lower energy edges from that due to the edge of interest. This is performed by fitting a smooth function, to the absorption coefficient below the edge and extrapolating this to higher energies. Subtracting this from the data gives the $\mu(k)$ used in (2.4). Similarly we obtain $\mu_0(k)$ by fitting such a smooth form to the edge contribution to obtain the EXAFS function defined by (2.4). This process is usually fairly straightforward although the small

size of the EXAFS function compared to unity means that the fitting procedure used to obtain $\mu_0(k)$ must be rather accurate.

The simplest form of analysis, and the one which was almost exclusively used in the early days (1970-1980) of EXAFS studies, is to Fourier transform $k_\chi(k)$ with respect to *sin(2kr)* or *exp(-2ikr)*. The latter is to be preferred since taking the modulus of a complex transform removes some of the problems associated with a finite data range: we do not have data down to $k=0$ owing to the presence of the threshold energy E_0 (equation 2.3): the lower limit k_{min} usually being 2-3 $Å^{-1}$.

The result of a Fourier transform is a series of peaks in real space, one corresponding to each shell of atoms contributing to the EXAFS, which may overlap. There are also peaks due to noise in the spectrum and to the effects of the finite data range: these last may be minimised by use of a window function at the cost of some peak broadening. There may also be a strong contribution at an unphysically short distance: this is usually a sign of poor background subtraction. The peaks due to real shells are shifted from the true interatomic distances by the effects of the extra phase factor $2\delta+\varphi$ and their widths are dominated by the effects of the finite data range, not in the majority of case by the Debye-Waller factor.

To improve this simple analysis we may weight the spectrum by a higher power of k. k^3 is most commonly used to counteract the decrease in amplitude with increasing k arising from the Debye-Waller factor and the fall off in $|f(k,\pi)|$: a function with constant amplitude gives a sharper Fourier transform. We might also take the transform with respect to $\exp[-i(2kR+2\delta+\varphi)$ using calculated phases for the strongest contribution. This moves all

peaks close to their true interatomic distances since the phase is dominated by the excited-atom contribution.

A simple Fourier transform gives a good idea of the amount of information in the experimental EXAFS spectrum and of the principal interatomic distances in the sample. To obtain more information we must fit to $\chi(k)$. This is always best done by fitting the raw data.

Fitting the experimental spectrum in k space involves calculating a spectrum using an assumed set of structural parameters and scattering data and varying the structural parameters until a best least-squares fit is obtained. The accuracy of fit, and of the resulting structural parameters, clearly depends on the quality of the scattering data used and much work has gone into evaluating methods of calculating electron-scattering phase shifts. At present, the best results are obtained using complex energy dependent potentials based on the LDA (Lee and Beni, 1977, Mustre et al., 1991). k -space fitting can be rather time-consuming computationally but it does extract the maximum amount of structural information. It is also amenable to statistical analysis: this enables reliable estimates of the uncertainties of the (often correlated) structural parameters to be obtained. It also helps to avoid obtaining more information that is actually present.

The preset parameters in the curve-fitting analysis of an EXAFS spectrum are the atomic scattering data, including inelastic effects and the core-hole lifetime, and the amplitude factor A(k), obtained from standard values or by fitting the spectrum from a sample of known

structure. This process also acts as a check on the accuracy of the scattering data used. In a free analysis run the user sets the number of shells to be included and the type of atom making up each shell. The parameters varied during the least-squares fitting process are the correlated pairs of parameters (E_0, R_j) and (N_j, σ_j^2) which control the phase and amplitude, respectively, of the EXAFS signal. Correlation between parameters is a major problem in EXAFS analysis, more so than in diffraction analysis because of the lack of data going down to $k = 0$, and this greatly increases the uncertainties on the fitted parameters. The presence of correlation means that a proper statistical analysis of the quality of the fit is essential. A good data-analysis program will search for a best fit automatically, varying those parameters selected by the user. Fitting tends to proceed interactively and iteratively, fixing the phase by varying E_0 and R_j, then the amplitude using N_j and σ_j^2, then the phase and so on until a good fit, defined by good reliability factor, is obtained. At this final stage a statistical package will give the uncertainties on the fitted parameters.

With good experimental data, over as long a k range as is possible, and well separated shells, we may expect to obtain interatomic distances with an accuracy of ± 0.02 Å or a little better. N and σ^2, which are strongly correlated by the lack of low-k data, can be fitted to about ±10%. The variation in $f(k,\pi)$ is such that we can reliably identify atoms whose atomic numbers differ by about ten or more: such identification can, of course, often be made more exact by using other chemical information or the bond lengths.

In the curve-fitting method of EXAFS analysis described above, the EXAFS data are the only information used. In complex systems, containing many different shells of scattering

atoms, the large number of parameters required cannot be justified by the information content of the EXAFS spectrum. The refinement is then underdetermined and a large number of solutions become possible, with no clearly defined minimum in the fit index. This is a problem which occurs particularly in biological studies. The only solution is to increase the amount of information available by including other data. The techniques of restrained and constrained refinement have been developed for this purpose (Binsted, et al., 1992).

It is possible to separate out the contributions to the EXAFS function from different shells of atoms, i.e. from different peaks in the partial radial distribution functions (RDFs), if these are well-defined, and this forms the basis of the simplest method of *k*-space analysis. To perform this separation, the experimental EXAFS spectrum is first Fourier transformed with respect to *exp(-2ikR)*. A small part of the resulting real-space spectrum, containing only one peak, is then backtransformed to k-space, the result being the contribution to the EXAFS from atoms lying in a single shell; such atoms are assumed to be all of the same chemical type. This is referred to as a filtered spectrum. This measure has occasionally been used in the work of this thesis for further accuracy of fitting.

Data-analysis programs based on the theory have also reached a high level. Several curve-fitting programs now exist which can rapidly and accurately extract the maximum amount of information from an experimental data set and, perhaps as important, the uncertainties on these parameters. The EXAFS fitting program used in the work of this thesis is the popular program called EXCURV92.

2.5 TEM

TEM is a powerful method for looking at real-space images. High-resolution TEM can provides material details at the atomic level. TEM with a resolution close to the atomic level is essential for this work, as the sizes and size distributions of nanomaterials are the first message we want to know. This information can lead to an understanding of mechanisms of visible emission from the nanosized materials, for example if the sizes/mean sizes and size distributions fall in the ranges indicated by quantum confinement theories, and correlation with the relevant peak wavelength of the PL spectra. Otherwise, the visible emission could come from either chemical specious or defect levels lying in the band-gap of large band-gap materials.

Cluster size distributions in the work of the thesis were obtained from TEM real-space images using a Jeol JEM 100CX in the Institute of Polymer Technology and Materials Engineering, Loughborough University of Technology. The resolution of this instrument is ~0.5 nm. Figure 2.7 is a cluster image obtained by the TEM.

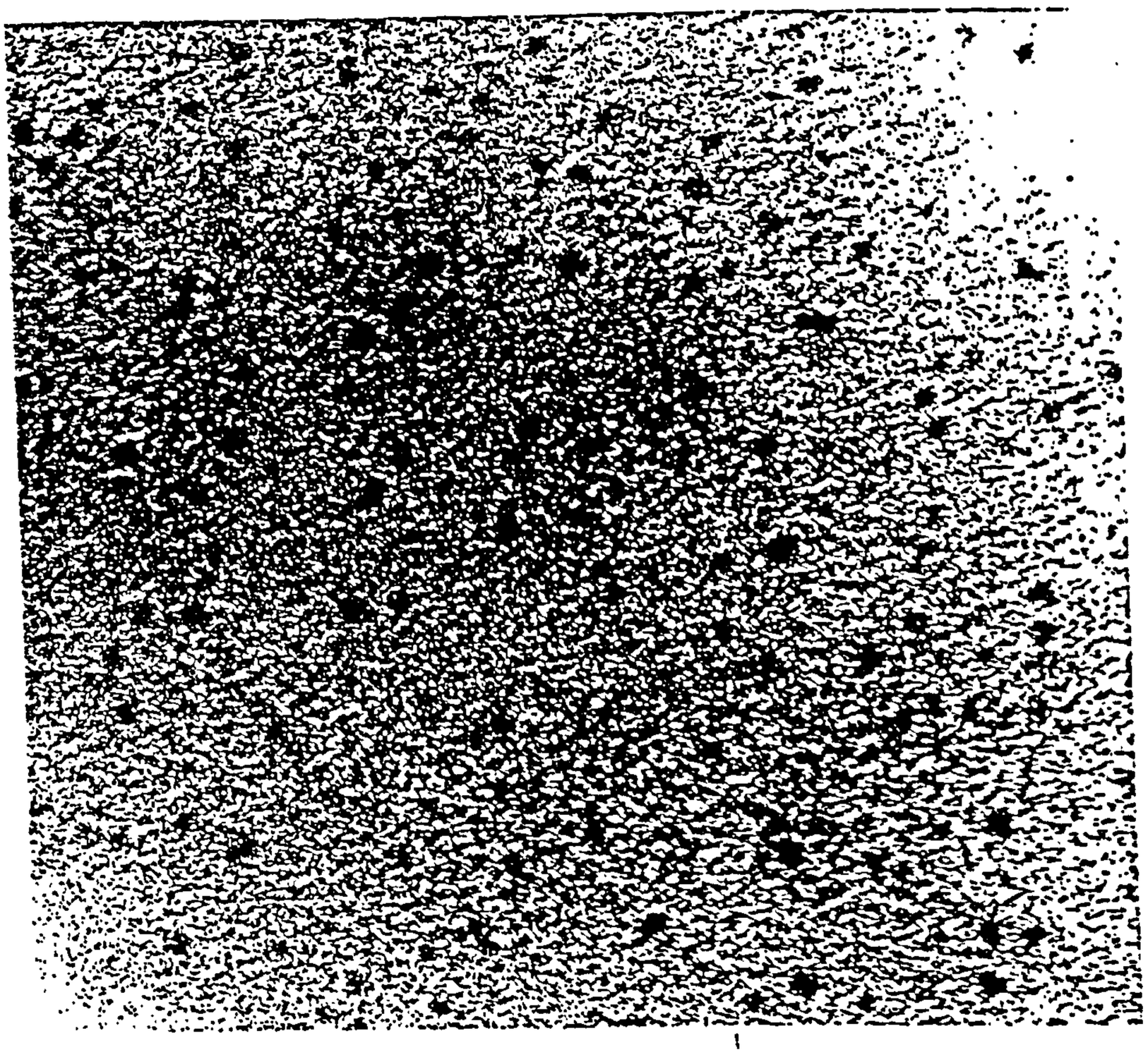

Figure 2.7 Si clusters observed using TEM from one of the clustered films.

CHAPTER 3 STUDY ON POROUS SI (PS)

In this Chapter, the experimental characterisations of both freshly produced porous Si and some 'non-fresh' porous Si are given, please also see Appendices. B, D and G.

3.1 Photoluminescence From Different Emitting PS

Following the preparation condition of porous Si described in 2.3, different emitting PS has been made and the recorded photoluminescence is shown below.

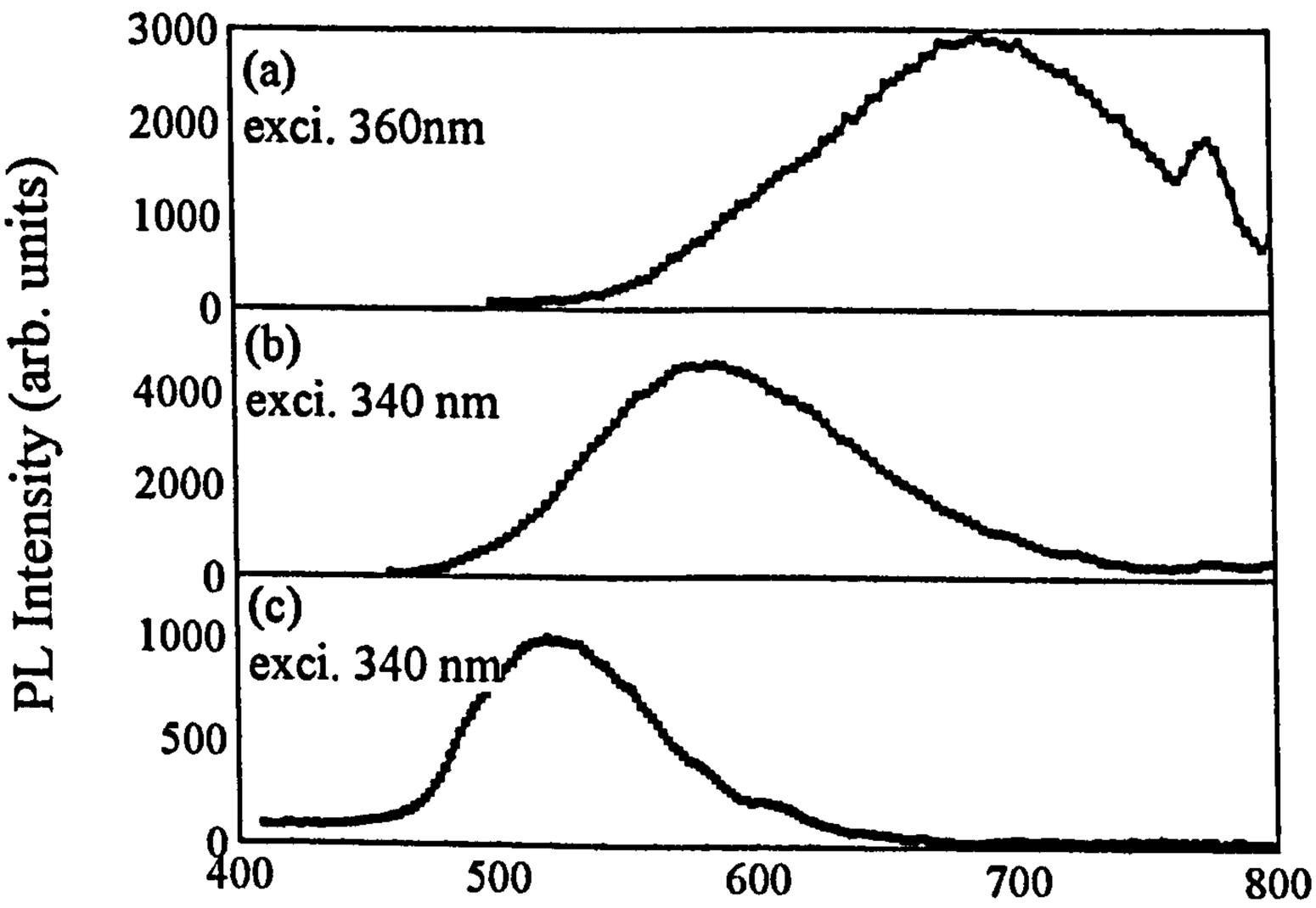

Figure 3.1 Photoluminescence from freshly produced porous Si

emitting with PL peaks in the (a) red, (b) yellow and (c) green. The measurements were recorded at room temperature.

This Figure shows the PL of a group of freshly produced red, yellow and green PS, with peaks located at 690, 580 and 520 nm (1.8, 2.14 and 2.38 eV) respectively, under the excitations given in the Figure. These spectra are typical of PS, the energy-width of the main feature (~0.8 eV) frequently believed to be caused by the broad size-distribution of the nanostructures, and different transitions between bands and within the band-gap (Koch, et al., 1993).

Figure 3.2 shows the photoluminescence from 'non-fresh' porous Si. The samples were exposed in air for hours or days before measurement at room temperature, except the PL of green PS which was recorded under lower temperature, -180 °C and 3 hours after the sample exposed in air. The PL spectra peaks are 520 nm, 605 nm, 635 nm and 680 nm, the relevant energies are about 1.82 eV, 1.95 eV, 2.05 eV and 2.38 eV, respectively. Due to the strong luminescence degradation from exposing in air, the green PL was weak even when at low temperature. However, the green peak has been shifted from about 540 nm at room temperature to 520 nm, because of the band gap widening at low temperature (Nag, 1972).

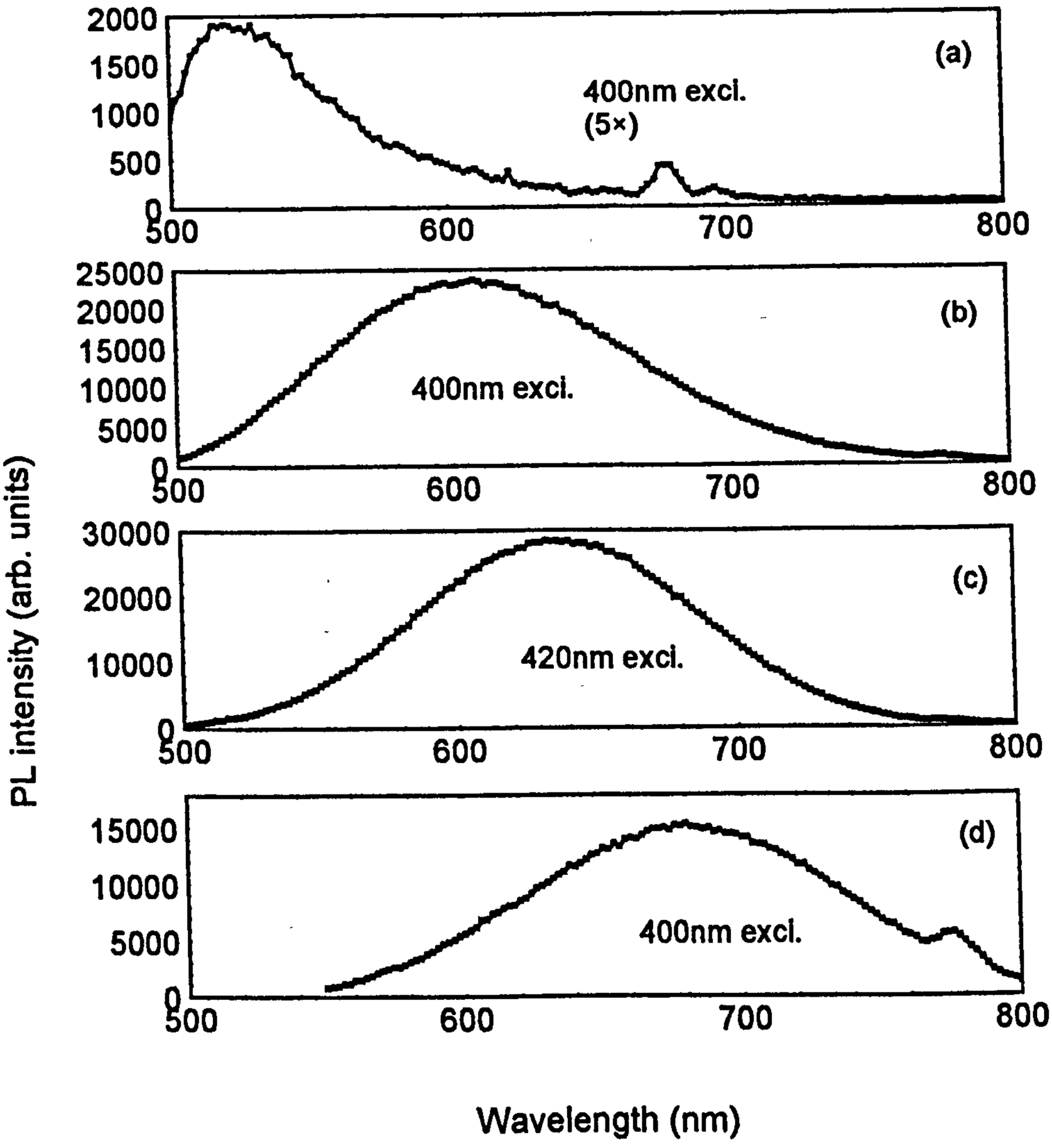

Figure 3.2 Photoluminescence from the other group of porous Si (a) green, (b) yellow, (c) orange and (d) red. The excitation wavelengths are given.

3.2 The Emission Peaks With Excitations

How would the luminescence peaks or emitting energies vary with excitations wavelength? A series of measurements have been carried out to determine this. Figure 3.3 shows the PL emission peak shifts under different excitation wavelengths.

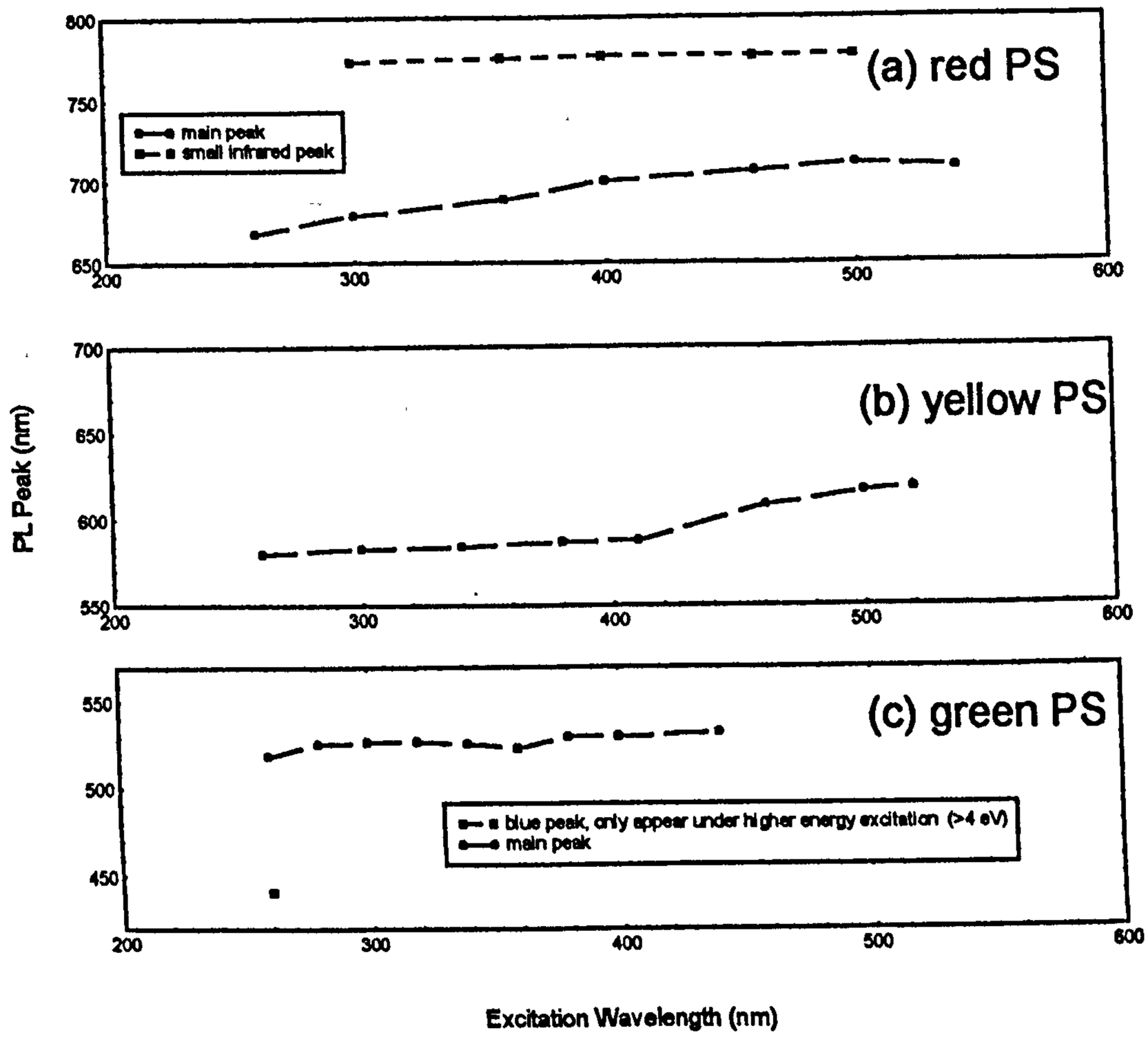

Figure 3.3 The PL peak positions as a fuction of excitation wavelengths for freshly produced porous Si, (a) red, (b) yellow and (c) green PS.

As shown in Figure 3.1, there are two peaks in the PL spectrum of red emitting PS. These two peaks have a quite different response to the excitation wavelength, as shown in Figure 3.3 (a). That the main peak shifted about 40 nm towards the blue from 707 nm to 667 nm, with increasing excitation energy (from 2.3 eV to 4.77 eV), implies that the emission is still related to a transition occurring within the fundamental

band gap, as deeper band states would be involved in the transition and result in a higher energy radiative transition when such states had been excited. Further, following this lead, this strong excitation related blue shift can only suggest that a band gap exists in porous Si and has been enlarged to the visible range. If it is due to quantum confinement, we still need information on the size and dimensionality of porous Si. This will be discussed later.

On the other hand, the small peak at about 780 nm shown in Figure 3.3 (a), did not shift very much, only about 1 nm, when excited by 300 nm and 500 nm light. The small peak disappeared when the excitation wavelength was shorter than 300 nm. This behaviour suggests that the small peak could be related to a chemical agency, such as silioxene ($Si_6O_3H_6$).

Similar to red PS, the PL peaks of yellow PS, Figure 3.3 (b), also shifted towards the blue for 35 nm from 616 nm to 581 nm in the excitation energy range. There is however some difference in the shifting behaviours.

There is about a 13 nm blue shift recorded from the green PS when excited by light with wavelengths from 440 nm to 260 nm, Figure 3.3 (c). This shift is not as strong as those of both the red and yellow PS. It can be understood that green PS has a quite large band gap, so that to excite the deep level states a higher excitation energy is required to keep the same rate of shift as for red and yellow PS with smaller band gaps. The single point shown on the left of Figure 3.3 (c) was due to the presence of a

blue emission peak. This real blue emission, with a peak at about 440 nm, only appeared when the sample was excited by the light with a energy higher than 4.43 eV (or 280 nm in wavelength). There are several possibilities that could lead to blue emission, such as carbon related emission, size effect, Si-O bonding, etc., however, reasons for the existence were not investigated in this project.

3.3 Structural Information of The Freshly Produced Red, Yellow and Green Emitting PS

3.3.1 From NEXAFS

As the penetration depth of photo-exciting radiation is on a scale of hundreds of nanometers, measurement of XAFS is quite suitable to detect details of the structure within this effective radiative layer of PS. Figure 3.4 shows the normalised photon absorption of Si-K-edge NEXAFS from PS, c-Si, a-Si and a-SiO_2. The absorption peaks of the features of Si-Si and Si-O bonds are indicated at 1840 and 1847 eV. A further feature at ~1844 eV has previously been assigned to the presence of SiOH-related bonding.

It can be seen that firstly the absorption behaviour of c-Si includes the 1847 eV feature, probably due to the presence of a surface native oxide. Secondly, the PS Si-Si bond absorption gradually decreases and Si-O bond absorption increases with PL blue-

shift : less Si-O absorption in NEXAFS implies the samples are 'fresh', similar to some of the work in Ref. 10, but unlike the data of Ref. 9 and some of our previous studies on other types of PS, where NEXAFS shows stronger Si-O absorption. One explanation for the trends is that the average surface:volume ratio of Si cores increases with blue-shift. Moreover, this increasing ratio suggests the average volume of the nanocores decreases.

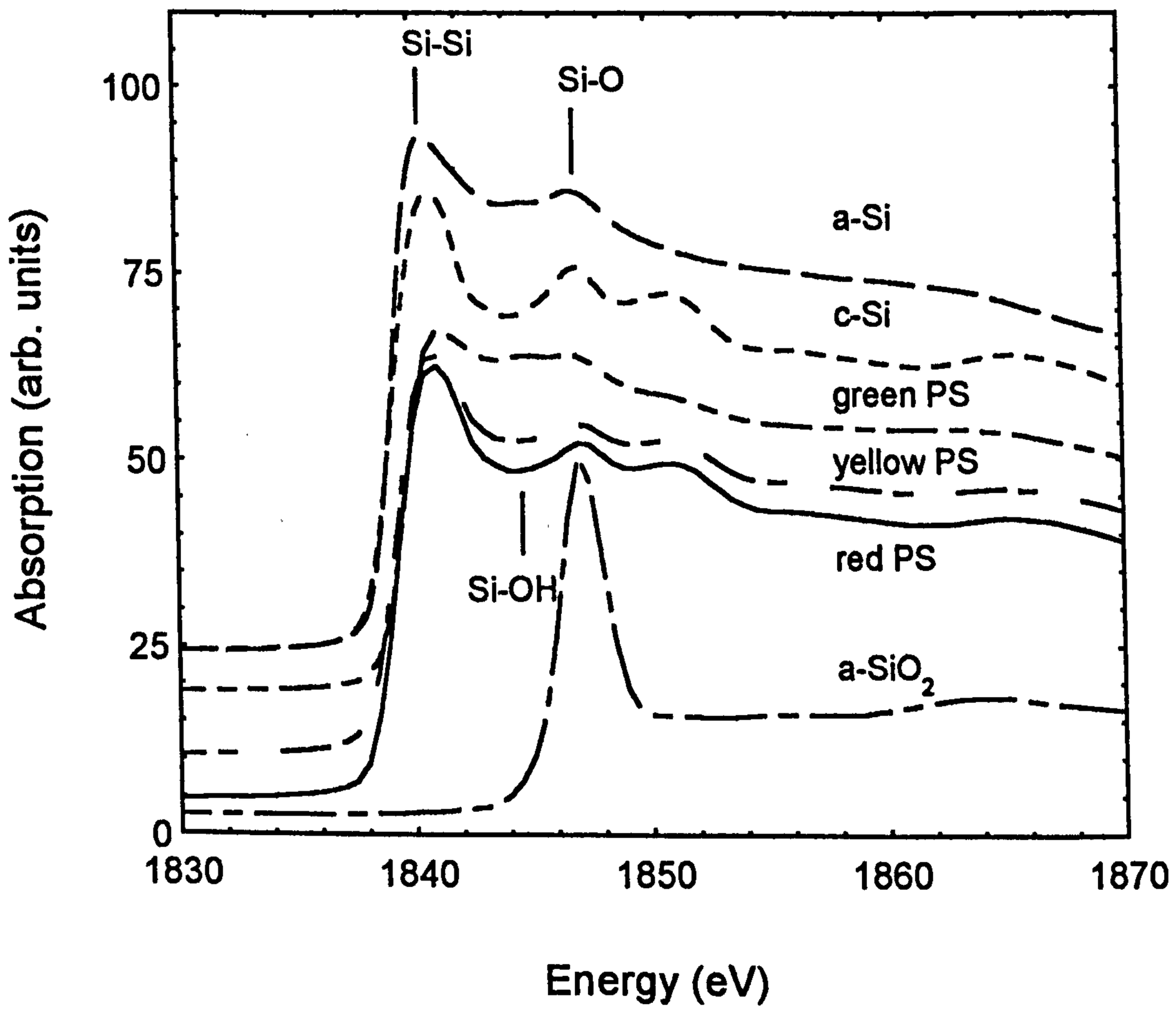

Figure 3.4 NEXAFS of porous Si, c-Si, a-Si and a-SiO_2. The

features related with Si-Si, Si-O and Si-OH bonding are indicated. The curves have been labelled.

3.3.2 From EXAFS

The normalised EXAFS of the porous Si, c-Si and a-Si is shown in Figure 3.5, where the scans were made from 1800 to 2500 eV (k range up to 15 $Å^{-1}$), with 742 independent points.

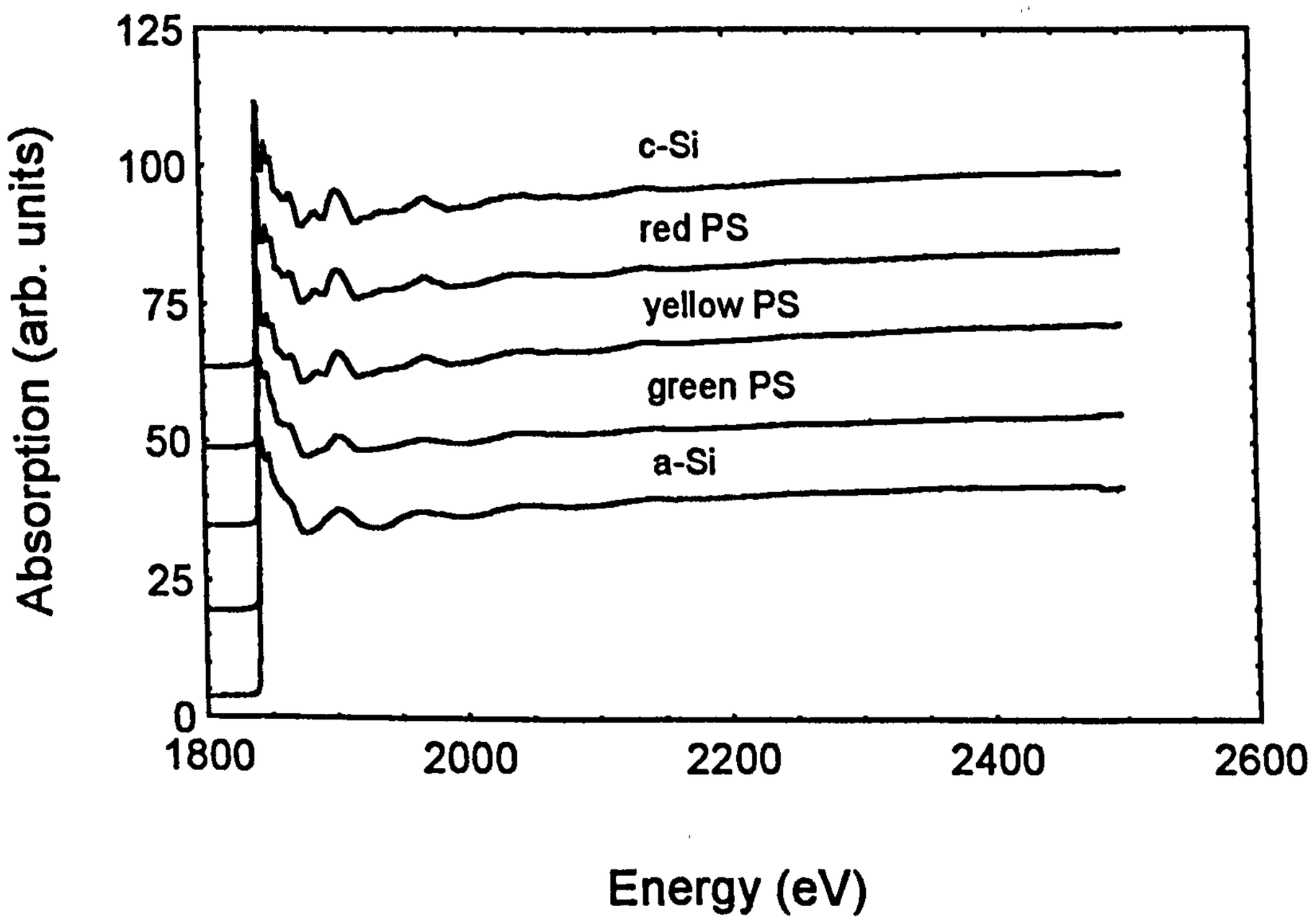

Figure 3.5 EXAFS of porous Si, c-Si, and a-Si. The curves have been labelled.

3.4 Theoretical Fitting and Fourier Transform of EXAFS

More information on the nanostructure has been obtained from the analysis of the EXAFS data using EXCURV92 (Binsted, et al., 1992). During the analysis with EXCURV92, the relaxed approximation was selected for the excited K-shell. Three shells were set as Si (centre) - Si, Si - Si (centre) and O - Si, for which the amplitudes and backscattering phase shifts were calculated within EXCURV92. Further, all spectra were phase-shift corrected within EXCURV92 so that the peaks appear at their true positions.

The fitting quality was good as shown in Figure 3.6, in which the theoretical fitting is quite close to that of experimental data. The fitting errors will be discussed and given later. It is can be seen that the oscillation features from the red PS are very close to those from c-Si. This indicates that at least the red PS has a c-Si-like structure. The oscillation feature from yellow PS clearly indicates that the structure is still crystalline. For the k^3-weighted EXAFS, $k^3\chi$, of green PS, although certain features characteristics of crystalline Si can be seen, it seems close to that of a-Si. Is this feature due to the absorption of amorphous phase or nanostructure? Figure 3.6 did not give much information. This information is related to one fitting parameter, the Debye-Waller Order Factor. Details about the factors relevant to PS will be given and discussed later, in Chapter 6.

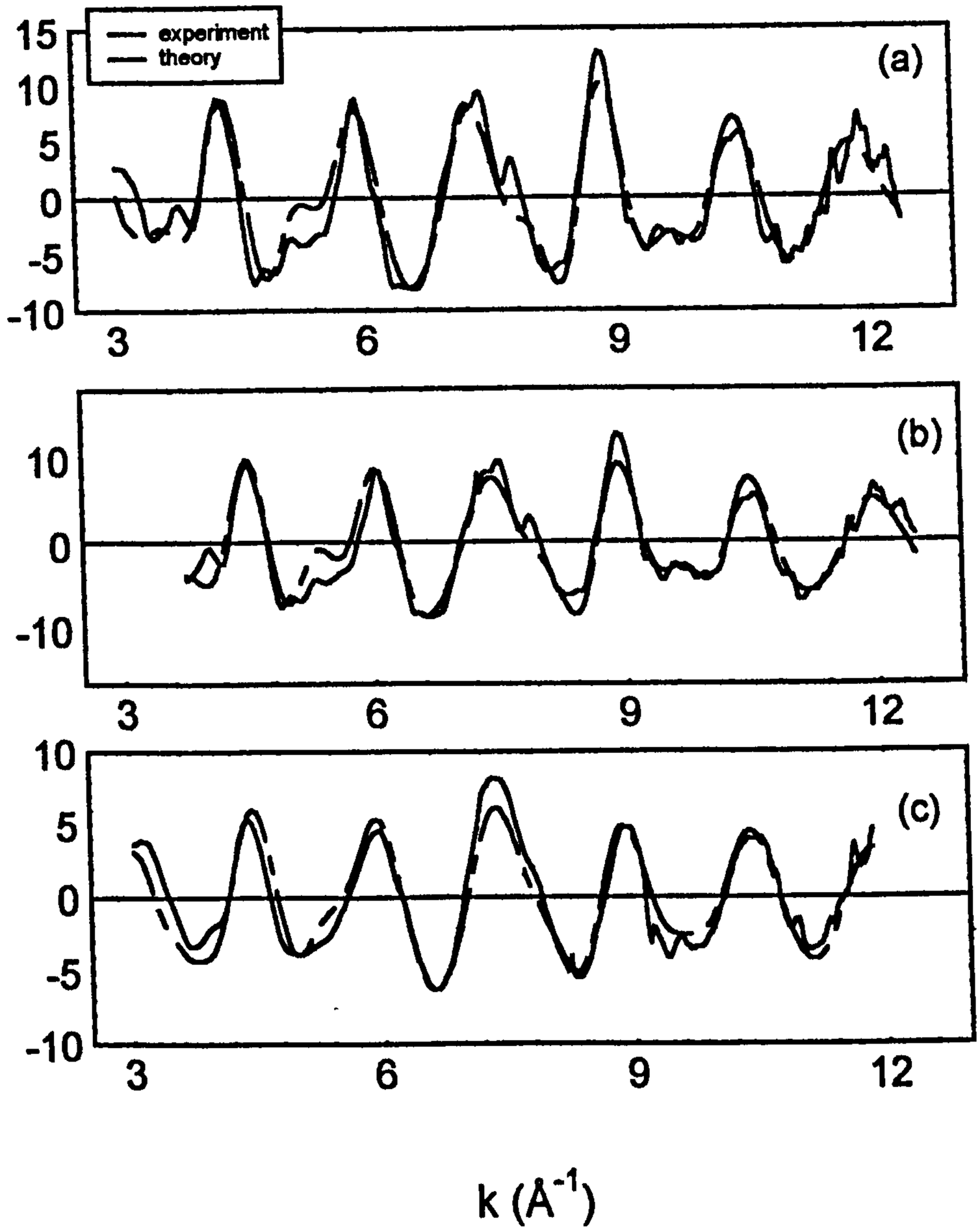

Figure 3.6 k^3 weighted EXAFS function $k^3\chi(k)$ of (a) red PS, (b) (b) yellow PS, and (c) green PS.

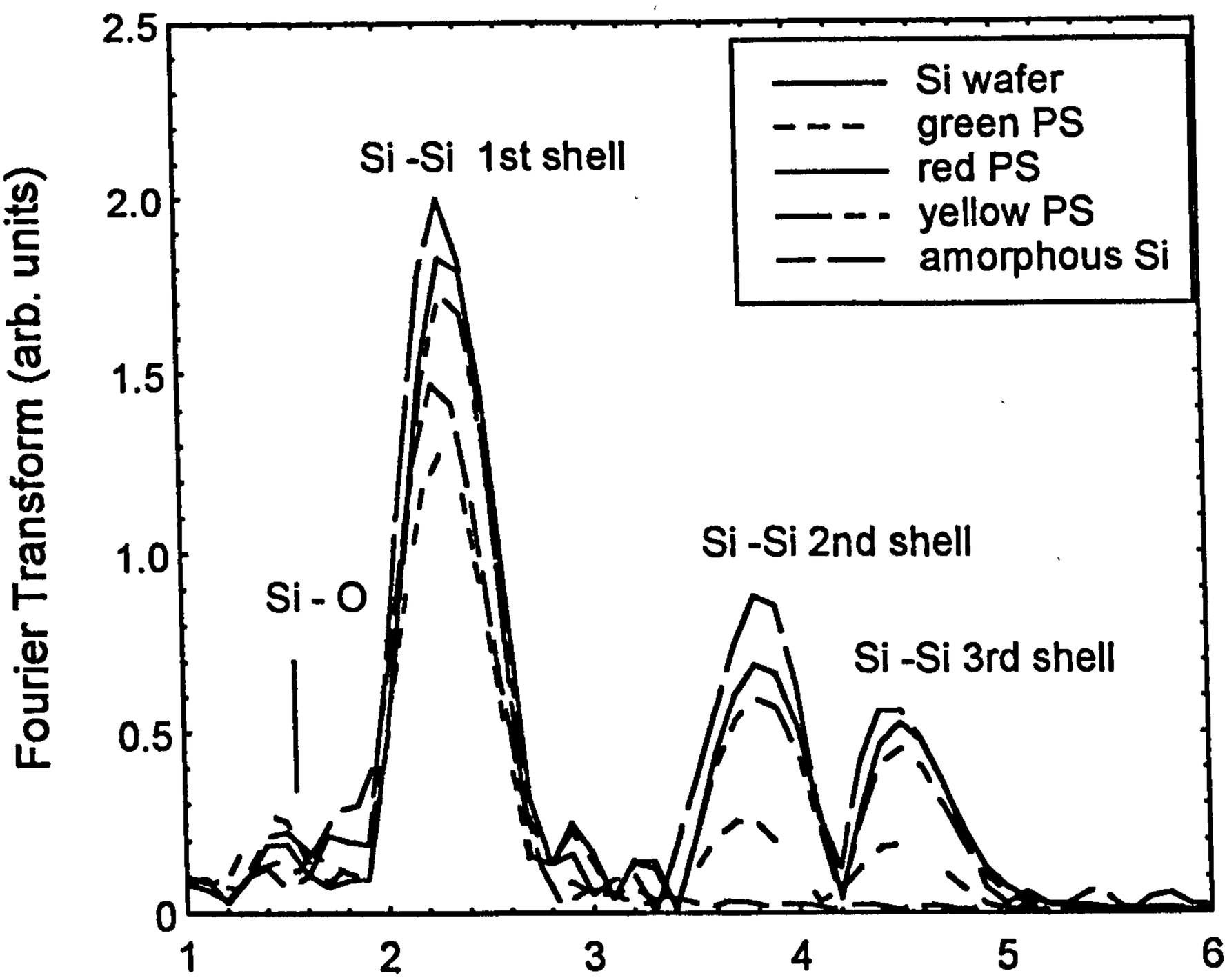

Figure 3.7 Fourier transformed EXAFS of the PS, c-Si and a-Si. Only theoretical fittings are shown.

The k^3 weighted EXAFS, together with their theoretical fittings, can be Fourier transformed in to real space, instead of k space. Figure 3.7 shows the Fourier transforms (FT) of the k^3-weighted EXAFS function $k^3\chi(k)$. For clarity, only theoretical FTs are given here. That the fits were good could be seen from error maps, the fit indexes (~0.00014), and residuals (~13) (Joyer, et al., 1987). Such fits almost completely overlap the experimental curves for the first, second and third Si-Si shells; as an example both experimental and nonfiltered fitted data for the yellow PS are

shown in Figure 3.8. For this material the Si-Si shells occur at 2.34, 3.81 and 4.50Å, respectively. All distances are ±0.02Å. Including multiple scattering was found not to increase the quality of the fit in any of the shells.

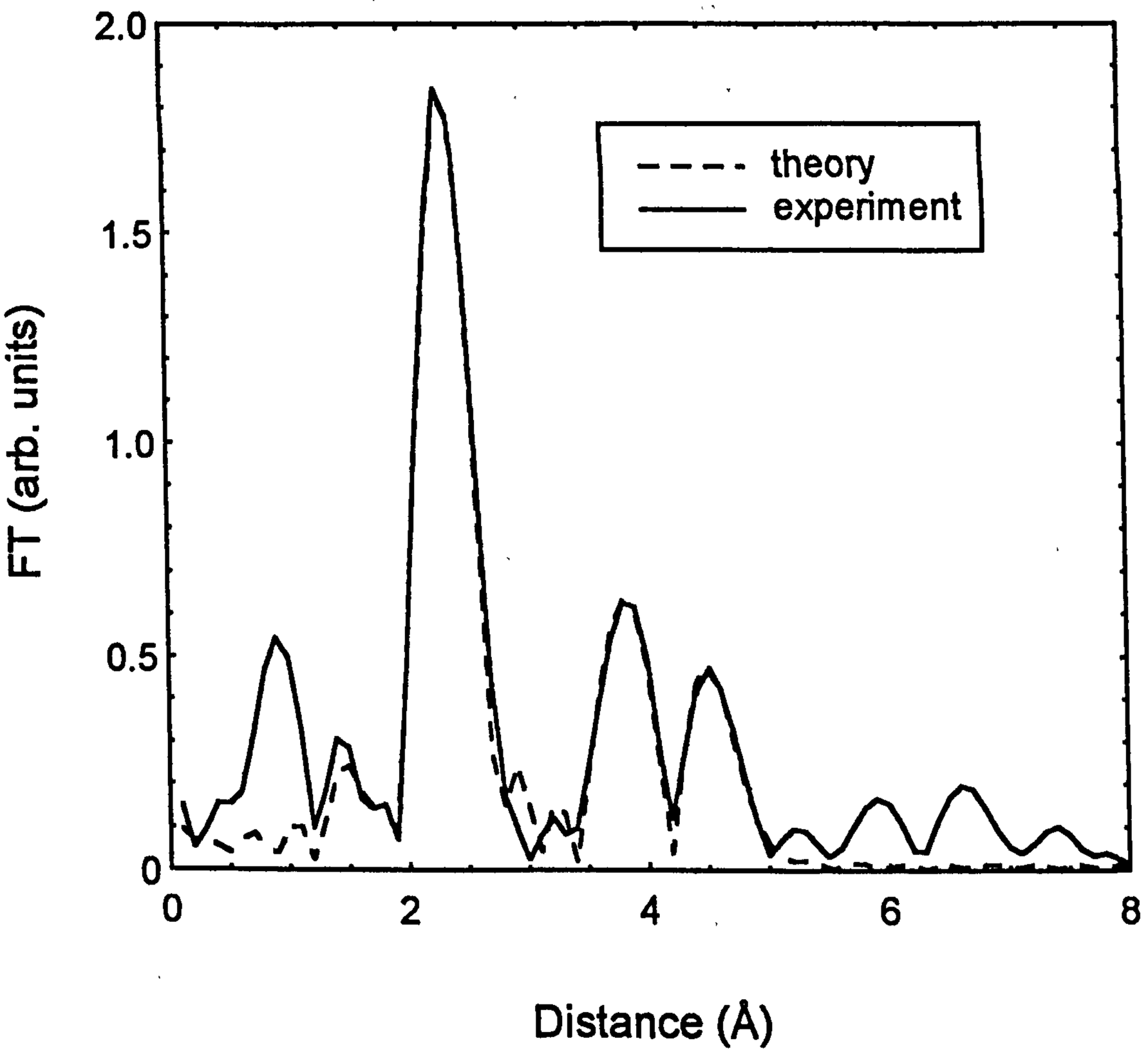

Figure 3.8 The Fourier transform of the both experimental and fitted EXAFS from the yellow PS.

The fitted Si-Si nearest-neighbour partial coordination numbers $N_{Si\text{-}Si}$ for the PS, c-Si and a-Si are given in Table I, in which all the relevant errors are given. While the first shell $N_{Si\text{-}Si}$ of red and yellow PS, 3.8±0.15 and 3.65±0.13, are close to 4 (that of bulk

c-Si) those for the 2nd and 3rd shells dramatically drop to 7.4 and 8.2 respectively for red PS, and 5.7 and 6.5 respectively for yellow PS (compared with 12 in both shells for bulk Si). The rapid fall off for the 2nd and 3rd shells means that a significant part of the medium-range order has been lost. For the green PS, N_{Si-Si} of all of the three shells drops significantly, to 3.0±0.2, 3 and 4, implying the size decreases further. This agrees with sample preparation processes, respectively. In addition, the first shell N_{Si-O} increases with PL blue-shift, agreeing with the implication from NEXAFS of the increasing surface:volume ratio.

Table I. The coordination numbers of Si-Si shells from EXAFS

	1st N_{Si-Si}	2nd N_{Si-Si}	3rd N_{Si-Si}
red PS	3.8±0.15	7.4±0.44	8.2±0.75
yellow PS	3.65±0.13	5.7±0.38	6.5±0.67
green PS	3.0±0.2	3±0.49	4±0.73
c-Si	4±0.1	12±0.35	12±0.58
a-Si	4±0.1	0	0

However, this shell is not well-fitted by theory, as shown in Figure 3.8, possibly because of the involvement of O, OH and H, the possible passive species of P_b centres (Meyer, et al, 1993). As a technique EXAFS is relatively insensitive to the presence of

H, since H atoms are such weak scatterers. Anyway, the modelling described in Chapter 5 and 6 only takes into account the average number of Si-Si bonds.

Table II gives the fitted 1st, 2nd and 3rd shell distances from the PS samples. All distances are ± 0.02Å.

Table II. The distances of Si-Si shells of PS and c-Si from EXAFS

	1st R (Å)	2nd R (Å)	3rd R (Å)
c-Si	2.31	3.82	4.46
red PS	2.34	3.81	4.49
yellow PS	2.34	3.81	4.50
green PS	2.34	3.79	4.55

Thus, many properties of porous Si have been characterised by EXAFS from theoretical fitting and NEXAFS, and also PL and the PL peak shift with excitation have been shown in details. These characterisations will be discussed in Chapter 5 and 6.

3.5 Summary

This Chapter presents the study of freshly produced red, yellow and green porous silicon, and some aged porous silicon (exposed in air for days or hours), by means of PL, PLE, EXAFS and NEXAFS.

Differently emitting porous Si samples were made by varying anodisation conditions. PL shows that the emitting wavelength covers most of the visible range from 520 nm to 690 nm. The main PL peak shifted towards higher energy when excited by higher energy. Even blue emission appeared when the green porous Si was excited by 280 nm or shorter wavelength light. However, an infrared peak at about 750 nm from the red porous Si did not shift under different excitation energies. This indicates that the mechanisms of the two kinds of emission are different.

The near-edge x-ray absorption structures (NEXAFS) of red porous Si showed features characteristics of bulk Si and green porous Si was close to amorphous Si, while yellow porous Si lies in between. Is that correct? Both EXAFS and Fourier transformed EXAFS fitting clearly indicate a loss of medium range order. Locally, the porous Si is still crystalline: there are still Si-Si second and third shells existing, while amorphous Si gives absolutely no contribution from these shells. In other words, the information suggests that porous Si consists of very small structures, maybe only on a scale of nanometers (only nanometer scale structures can affect the second and the third shell obviously). A very important point can be drawn from in Figure 3.7, i.e. the

three shell amplitudes were decreasing gradually with the relevant PL peak blue shift. It implies the whole character of porous Si. Furthermore, using the co-ordination numbers, some understanding about the mechanism of visible photoluminescence could be attempted. The modelling carried out and resulting interpretation will be given in Chapters 5 and 6.

CHAPTER 4 STUDY ON SILICON AND CARBON CLUSTERED FILMS

In this Chapter, the experimental characterisation of blue emitting nanoclustered Si and C films are given, also please see Appendices. A, C, E and F. Except where mentioned otherwise, the experimental properties of size distribution, PL and EXAFS have all been obtained from both samples 1 and 2 of Si clustered films, and sample 1 of C clustered film. Because all of the relevant data has come from the same sample, we can clearly identify these materials in some detail.

4.1 Size Distributions

Size distribution is the most important property of quantum nanodots. As mentioned in Chapter 1, this property has been given for all kinds of three dimensionally confined dots in many articles published by different researchers. This is because the distribution provides a measure of knowing if quantum confinement is actually having a effect and leading to a huge band-gap blue shift to visible range or higher energy, the bandgap energies of bulk element group IV semiconductors, such as Si, Ge and graphitic C being in the infrared or far infrared. From TEM real space images we can count the numbers of dots with different sizes and determine the size distribution, often averaged over many areas of the samples.

If using high resolution TEM, more structure details can be seen, such as their ordering or latticed structures, surface structures and even the structure variation of the

transition layer from nanocores to their surface. Unfortunately, the resolution of the TEM employed in this study was not high enough to search for such lattice related details. However, the size distributions of nanodots still can be clearly obtained and are shown bellow, while the relevant photoluminescence properties will be shown in the next section

4.1.1 Si Clusters embedded in SiO_2 matrices

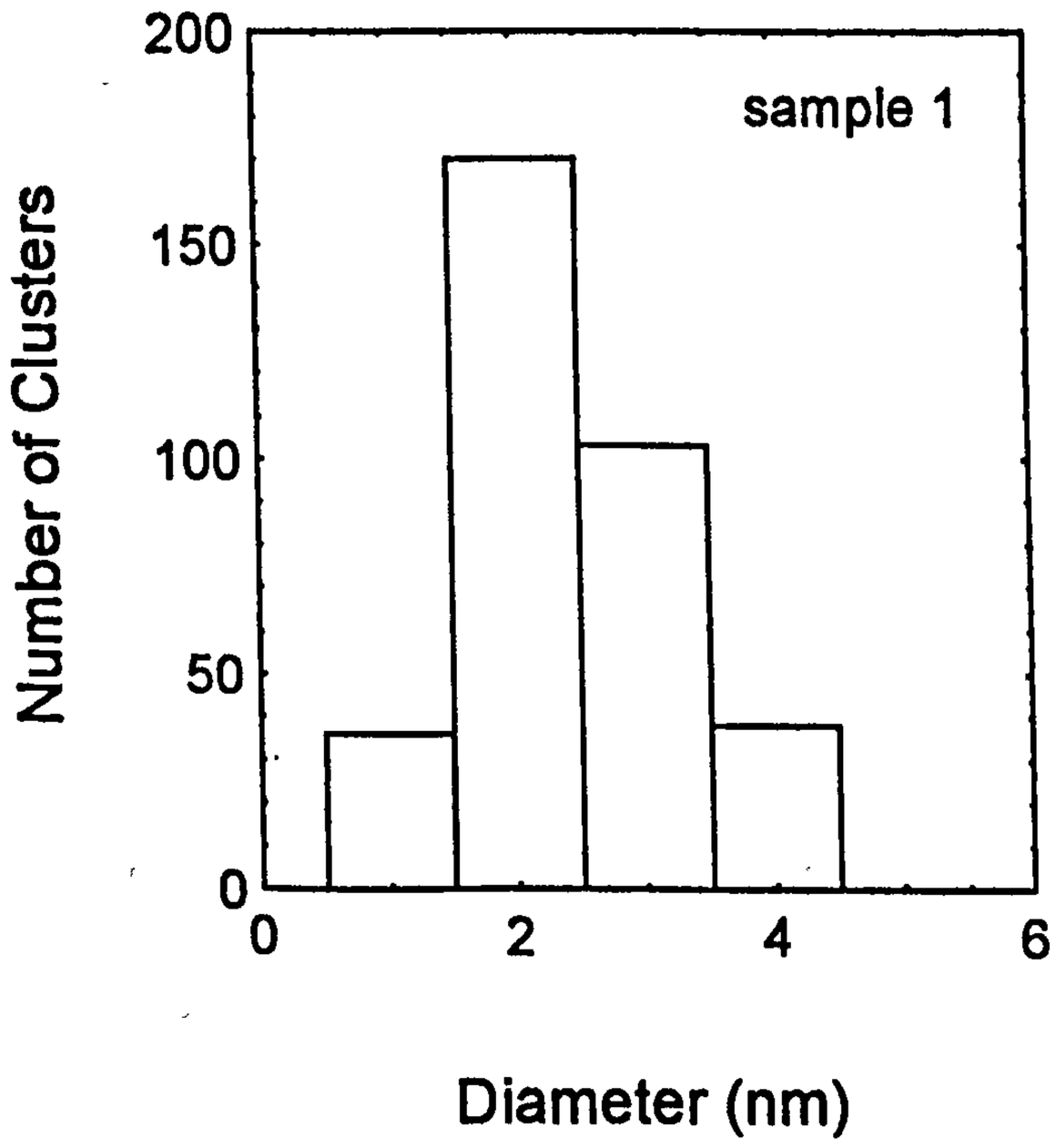

Figure 4.1 Size distribution of the nanodots in Si clustered film 1. The film was prepared using 12 pieces of small Si wafers, 3×10^{-3} mbar Ar, 400W rf power,

20min deposition time, then annealed for 20 min at 800°C in N_2.

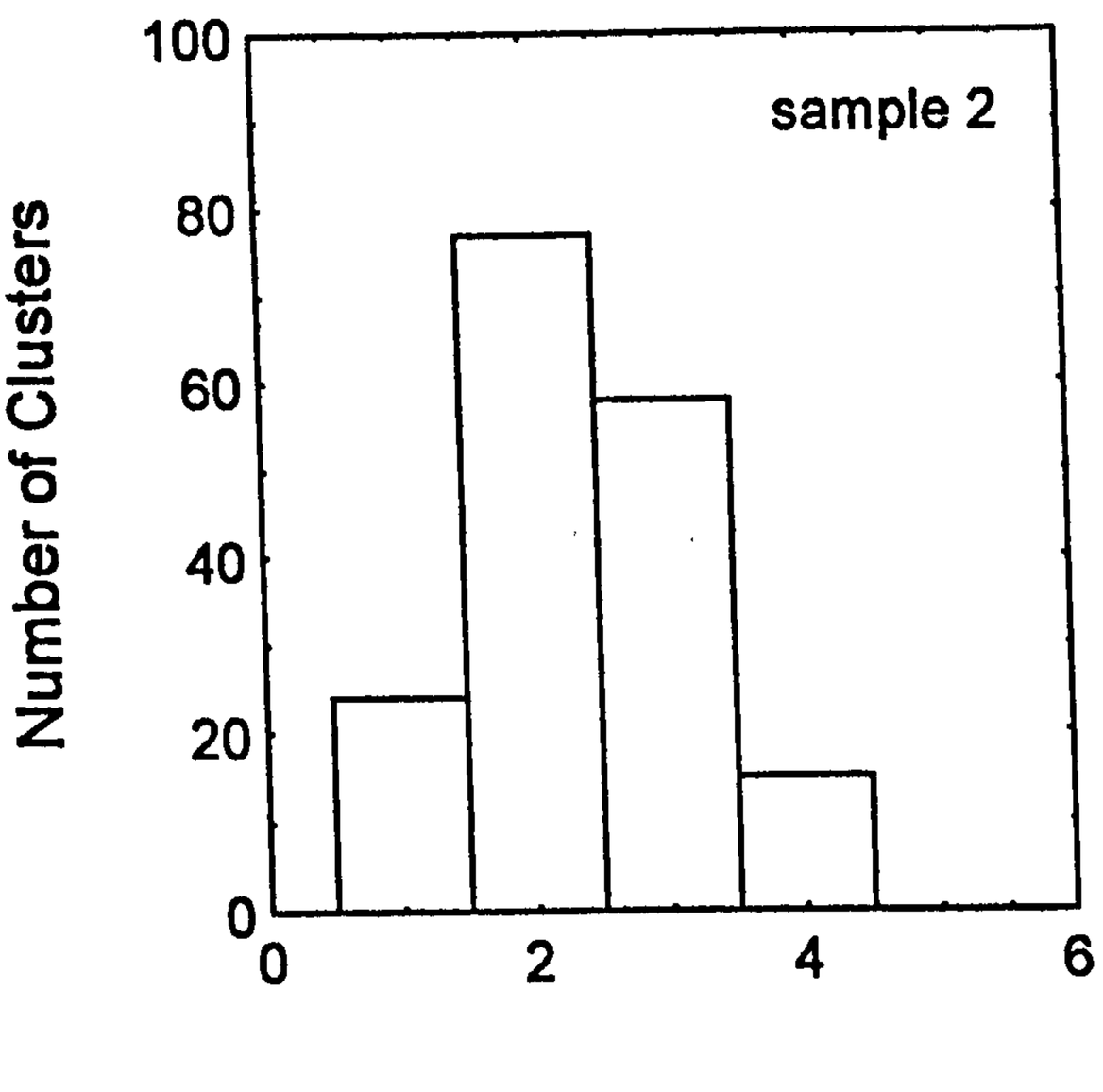

Figure 4.2 Size distribution of the nanodots in Si clustered film 2. It was prepared using 8 pieces of small Si wafers, 3×10^{-4} mbar Ar, 400 W rf power and 35 min deposition time, then annealed for 20 min at 800°C in N_2.

Figures 4.1 and 4.2 show the size distributions of the nanodots of 2 Si clustered films. The sizes of the nanodots of the two Si cluster samples vary from 1 to 4.5 nm. There is no cluster size bigger than 4.5 nm. Due to the TEM resolution, there is no image

showing any clusters with a size smaller than 1 nm. Although there are differences in detail in the two distributions, as we can see in Figures 4.1 and 4.2, the peaks of the distributions are at similar sizes at around 2 nm. In terms of mean size, we have about 2.3 nm and 2.4 nm for samples 1 and 2, respectively. Hence, if we believe in the quantum confinement effect, we should expect that the energies of the PL will be similar.

4.1.2 C Clusters embedded in SiO_2 Matrices

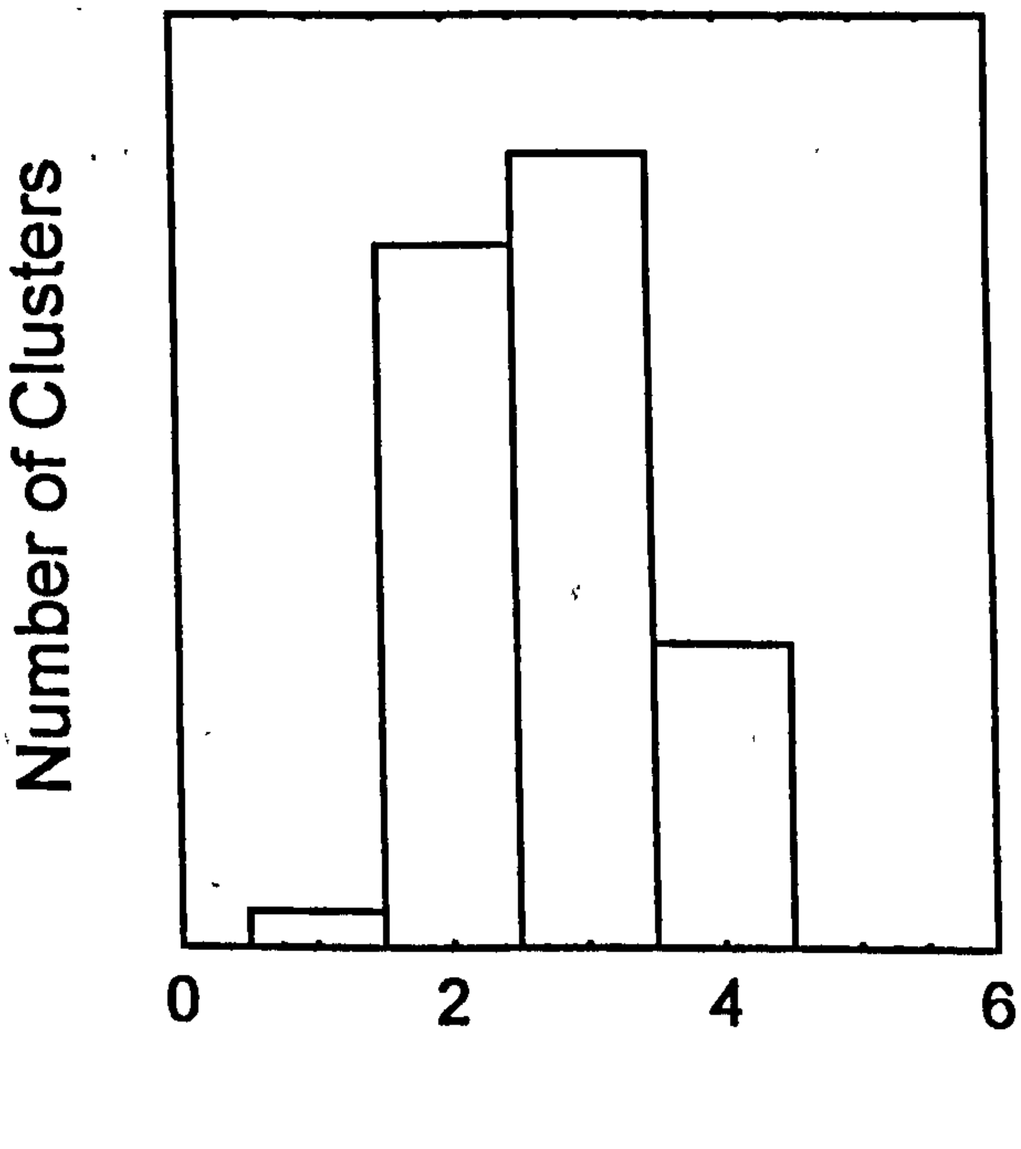

Figure 4.3 Size distribution of the nanodots of C clustered film sample 1.

The sizes of carbon clusters vary from 1 to 4.5 nm, similar to those of the silicon clusters, while peak in the size distribution is around 3 nm, as given in Figure 4.3. As the count for the range 2.0±0.5 nm is very close to that of the maximum size range, we can conclude that the mean size will be in the range from 2.6 - 2.7 nm.

4.2 Blue Light Emission from The Clustered Films

4.2.1 From Si nanoclusters

In Figure 4.4, the PL of the two Si-cluster samples *1* and *2* are shown for 3 different excitation wavelengths. Peaks are located from ~420 to 495 nm, and from ~450 to 490 nm, depending on the sample preparation conditions. On the contrary no emission was detected for as-deposited samples. Although many samples have been made in very different conditions, data from only two samples, those with highest PL intensities, are shown in this report. For all the samples made there is a dependence of the PL intensity on the number of small Si wafers on the SiO_2 target : the intensity increases as the number changes from 3 to 12 and rapidly decreases as the number changes from 14 to 20. This implies that the emission is cluster-related, rather than SiO_2-related.

Compared with the reported longer-wavelength photoluminescence mentioned in Chapter 1, from clusters of Si, C and Ge which show broad single peaks (Dimaria, et al., 1994, Ito, et al., 1992, Maeda, 1991, Maeda, et al., 1995, Kanemitsu, et al, 1992), our films show PL spectra consisting mainly of two or three strong peaks, and also some smaller peaks. The multiple-peak PL spectra could be caused by a non-uniform and highly asymmetric size distribution, as Kanemitsu et al., (1993) suggested for situations when the average cluster size is very small. Alternatively it could be due to a 'size step' effect (one single atomic layer step), used to explain the multiple peaks of porous silicon PL. In this case low energy (perfect) surfaces are made more stable against further etching during anodization (T. Tahagahara, et al., 1992).

The PL intensity shown in Figure 4.4 increases rapidly with excitation photon energy and this suggests that there is a continuous increase in the density of states in the conduction band above the band minimum. Additionally, since there is some PL intensity, although very weak, for excitation photon energies very close to the PL emission energy, there could be a band tail attached to the conduction band. This band tail could be the result of the presence of an amorphous phase, since the structure of such small nanometer-sized dots can be easily distorted by stress from the surrounding material, SiO_2.

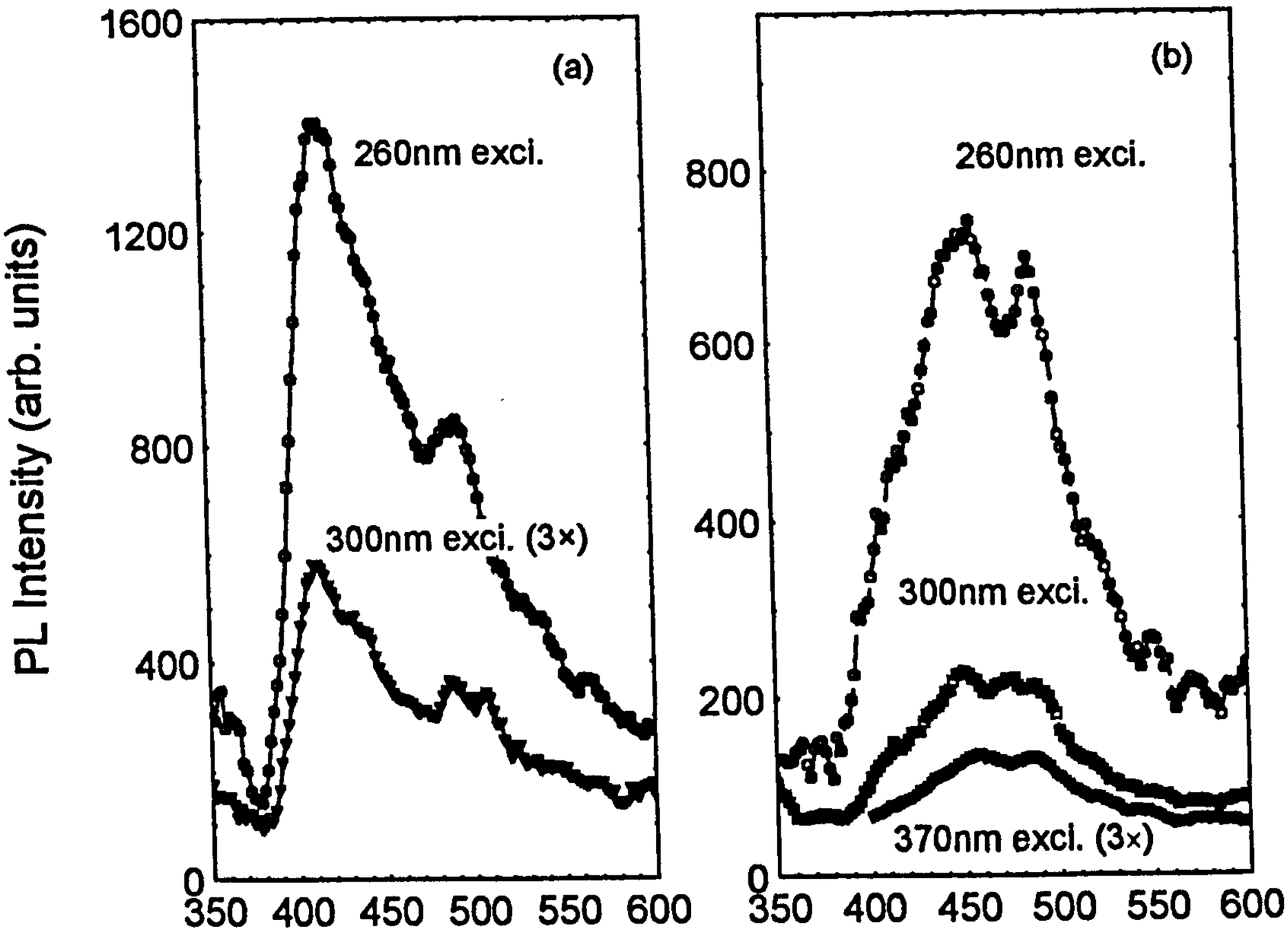

Figure 4.4 Photoluminescence from Si clustered films.

(a) sample 1 and (b) sample 2.

4.2.2 From C nanoclusters

Typical PL from C clusters embedded in SiO_2 is shown in Figures 4.5(a) and (b) for blue emitting samples, and in (c) for samples emitting in both the blue and UV. Figure

4.5(a) is due to sample 1, for which the size distribution given in Figure 4.2. The respective excitation wavelengths are given.

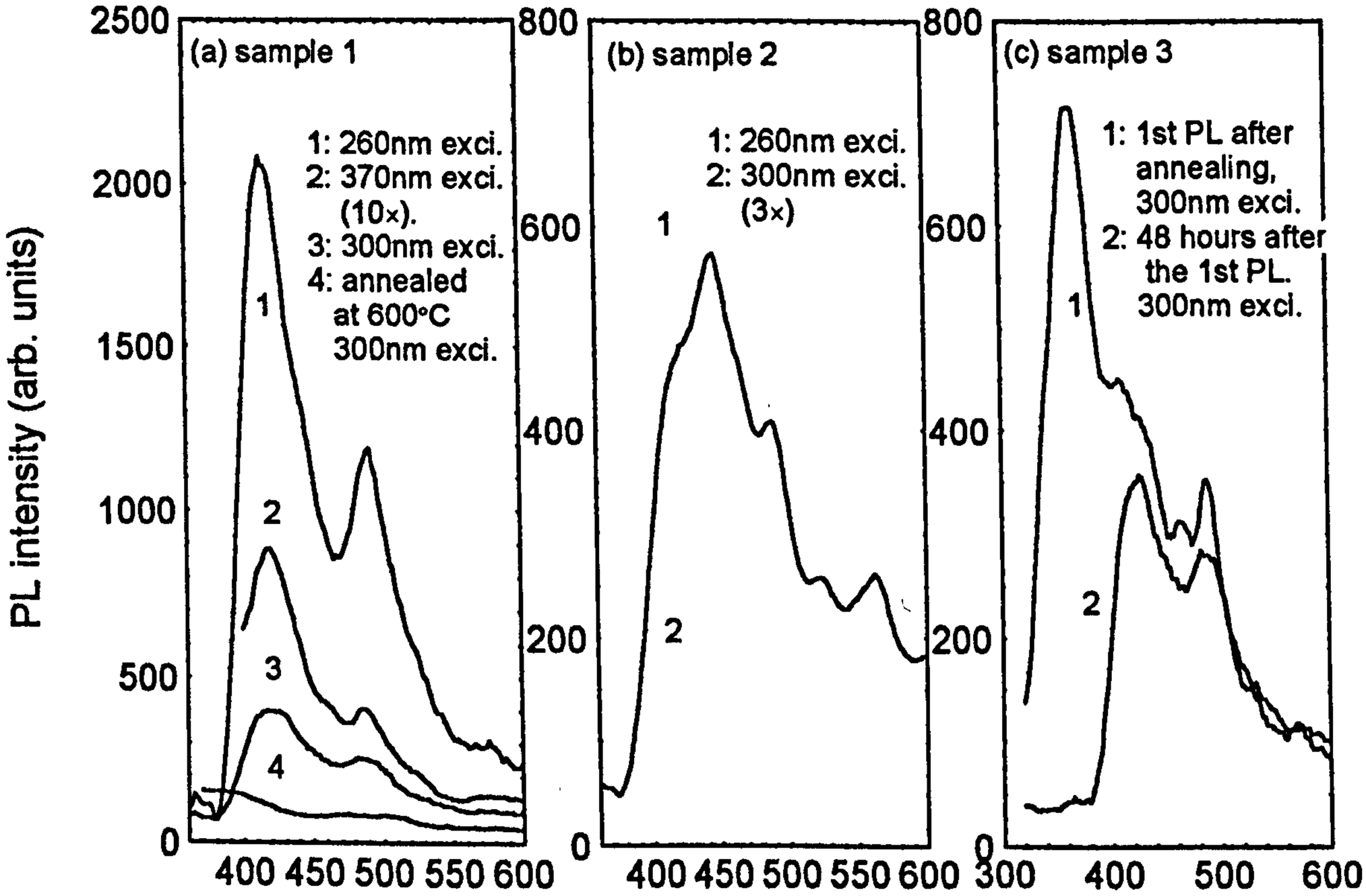

Figure 4.5 Photoluminescence from C clustered films (a) sample 1, (b) sample 2 and (c) sample 3.

The most efficient PL is always from films annealed at 800°C, the PL being visible to the naked eye when excited by the lower power densities used in this work. Much weaker PL was detected from films annealed at 600°C. There was no emission

detected in the range from 340 - 800 nm for as-deposited samples. Weak but detectable PL has been recorded by Maeda, et. al. (1995) from as-deposited Ge/SiO_2 systems, using laser excitation powers in the $mWcm^{-2}$ range. Thus it is believed that the undetectable PL of as-sputtered samples was due partly to the very low power of the tunable light source (in the range of 3-38 μWcm^{-2} on the samples) and partly to the existence of only a few clusters which have the correct size and form suitable radiative transition centers in the films before being annealed. As shown in (c), both UV and blue PL could be recorded from the same sample when it was measured a few hours after annealing. However two days after the first measurement the UV emission had disappeared and only blue emission remained. About half of the carbon clustered films made exhibit this characteristic of unstable UV PL, although the UV PL intensities varied greatly compared with those of the blue peaks. The blue emission remained almost constant over a period of many months. In general the blue PL spectra of all our samples consisted of one or two strong peaks which varied in intensity and peak wavelength with deposition conditions.

4.3 Structural and Bonding Information

The optical property, PL, and dimensional property, mean size and size distribution of nanoclusters have been given above. To make any conclusions of what is the optically active material involved and why has it this behavior, we need further identification of the following points: (1) what kind of material or elements made up the nanostructures

(2) are the clusters crystalline or amorphous? Si, C and O K-edge XAFS have been made to obtain possible answers.

4.3.1 Si K-edge XAFS from Si clustered films

In Figure 4.6 the Si K-edge NEXAFS (near edge XAFS) are given for Si/SiO_2 films as-deposited on Si substrates and after annealing at 800°C (sample 1of C clustered films). Data from a Si wafer and SiO_2 are also shown for comparison. Note that the data from the SiO_2 film does not show a contribution from the Si substrate : as both the Si/SiO_2 sample *1* and the SiO_2 films were deposited under the same conditions and have similar thicknesses, the Si substrate does not therefore contribute to the EXAFS from the Si/SiO_2 films. The data thus represent the properties of the film alone. The absorption spectrum from as-deposited Si/SiO_2 in Figure 4.6 shows only one absorption peak at ~1847 eV which is the signature of Si bonded to O atoms. After annealing at 800°C, however, this peak decreases and characteristic absorption by Si atoms in a Si environment can be seen at ~1841 eV. This implies that Si 'clusters' have formed from the amorphous as-deposited SiO_x ($x<2$) sample during the annealing process.

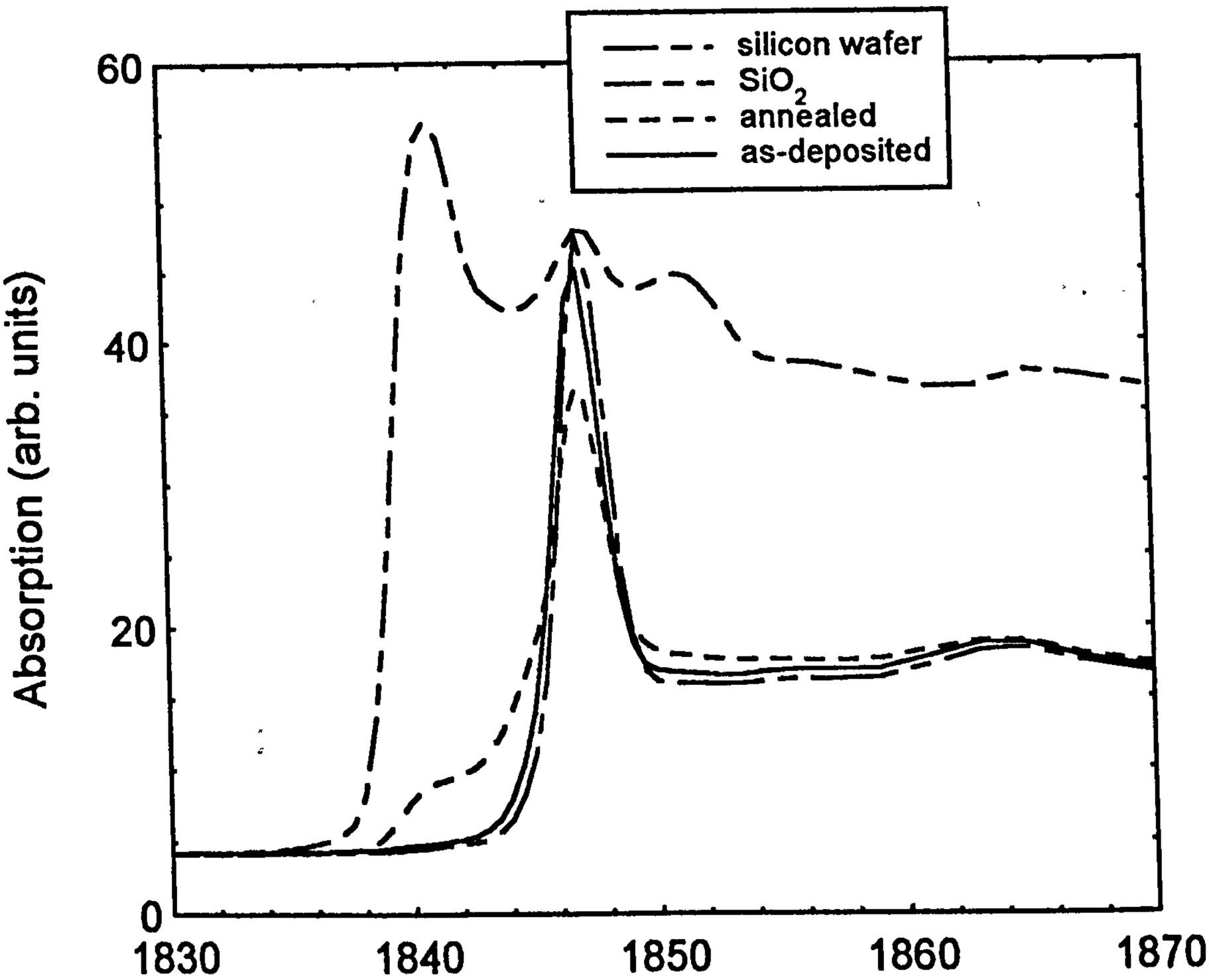

Figure 4.6 Si near edge x-ray absorption fine structure from as deposited Si clustered film and its annealed film (sample 1), SiO_2 and bulk Si.

The Fourier transforms of the EXAFS show details of the local structure of the nanosize clusters. In Figure 4.7, both experimental and theoretically-fitted Fourier transforms of as-deposited and annealed Si clustered films (from the sample 1-type group) are shown. In the unannealed material the Fourier transforms are very similar to those of SiO_2 (Bayliss and Gurman, 1991), with a Si-O bond-length at 1.58Å, and a

second shell corresponding to Si-O-Si at ~3.2Å. After annealing, the nearest neighbour partial coordination number of Si-Si bonds increases from zero, for the as-deposited material, to 0.6 for the material with the highest contribution from Si-Si bonds. On the contrary, the Si-O bond peak of the Fourier transform decreases significantly. The second shell corresponding to Si-O-Si is still present.

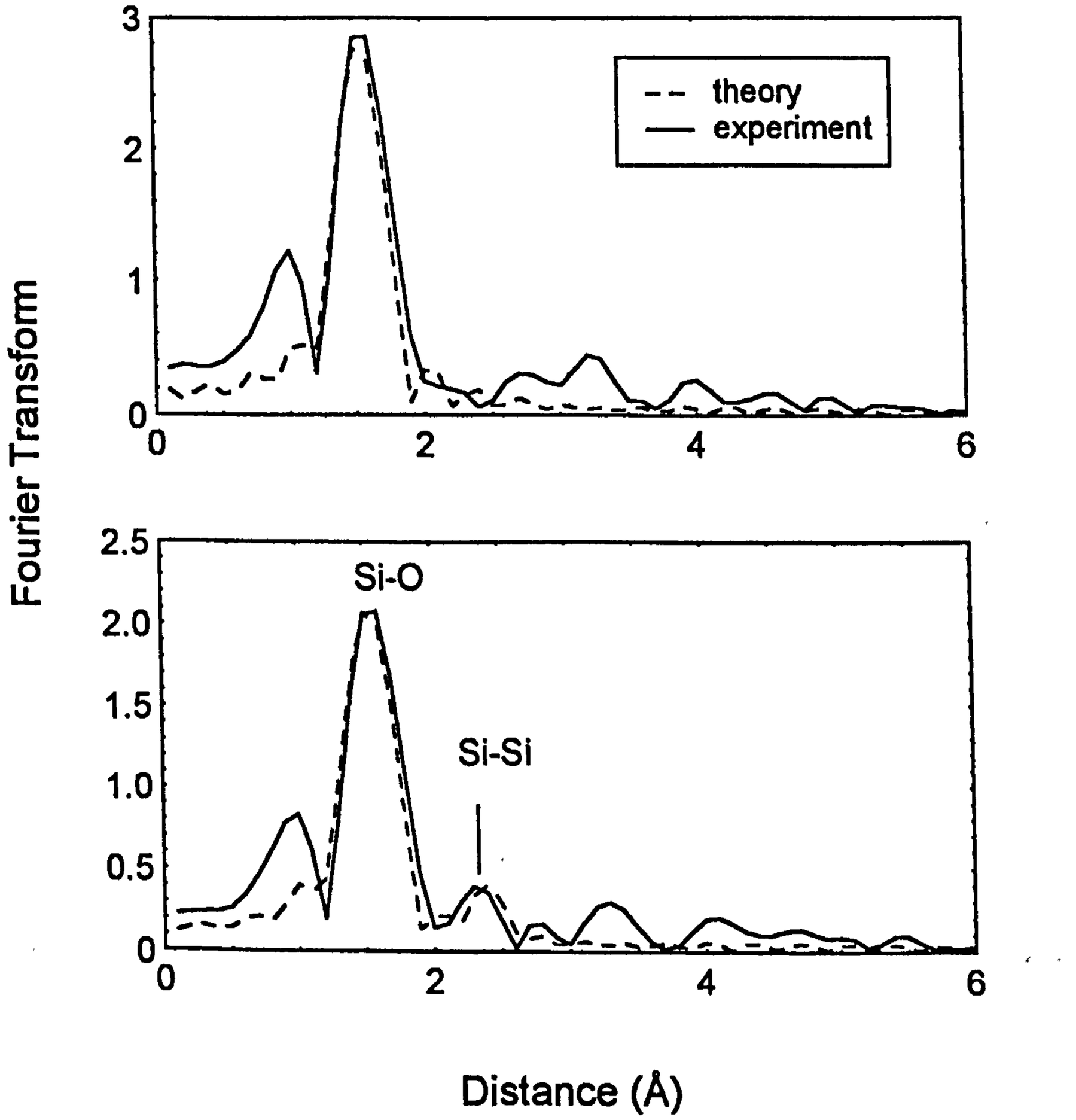

Figure 4.7 Fourier transformed EXAFS of Si clustered films of sample 1-type (a) as-deposited and (b) annealed.

As with most EXAFS data fits, however, the 4σ error in the partial coordination numbers obtained by statistical analysis of the fit is rather high : ± 0.5, but still clearly shows the existence of Si-Si bonds. Since the total coordination number is 4, and silicon oxide is chemically ordered both throughout understoichiometry and at stoichiometry, more than one eighth of the Si atoms are potentially bonded in elemental Si regions. The Si-Si bond length in the annealed sample is 2.35 ± 0.02Å, as expected, whereas the Si-O distance is 1.58 ± 0.02Å within error of the expected 1.62Å.

Although crystalline lattice regions have been observed by others in high resolution TEM images (Maeda, et al, 1995 and 1991, Morisaki, et al., 1993, Kanemitsu, et al., 1993) in similarly-prepared materials, our EXAFS data do not show direct evidence for crystallinity : the fitted Debye-Waller factors of the first shell Si-Si bonds at about 0.006±0.003 $Å^2$ suggest a structure which could involve amorphous and crystalline phases for which the factors are 0.004 and 0.007 $Å^2$ respectively. Alternatively, the EXAFS suggests that the structure is composed of clusters which have crystalline cores surrounded by disordered bonds. Either way the absence of any features corresponding to second shell Si-Si-Si is not surprising considering the small first shell Si-Si contribution and the rapid fall off of EXAFS with distance.

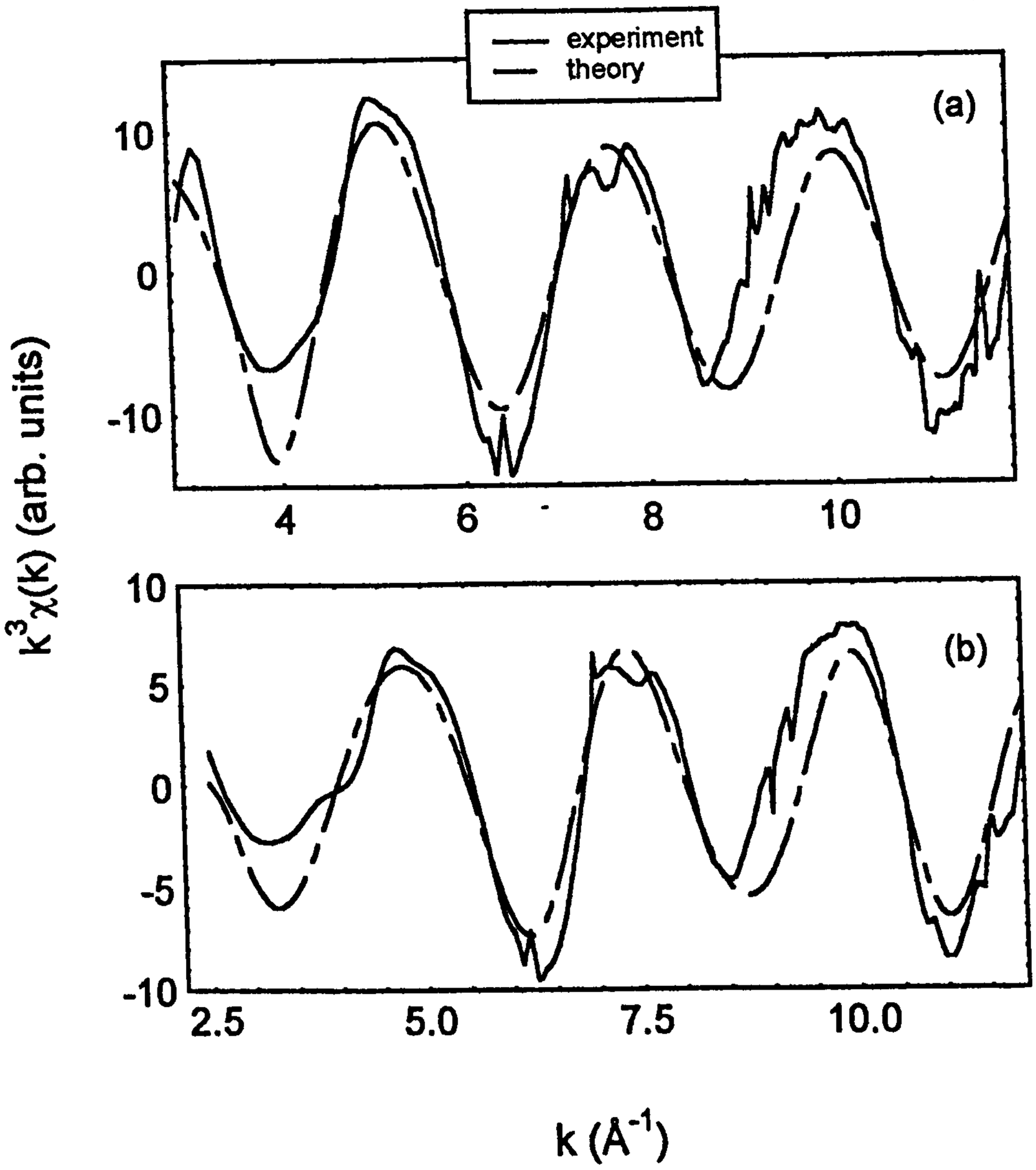

Figure 4.8 k^3 weighted EXAFS $k3\chi(k)$ typical of sample 1 group (a) as-deposited and (b) annealed.

The fine structure of Si k-edge absorption typical of sample 1 group is given in Figure 4.8. Firstly, it is can be seen that the theoretical fitting was good for both before and after annealing samples. Secondly, the more important information is that certain crystalline-related fine structure has clearly shown up after the sample was annealed.

This also confirms the information from Fourier transformed EXAFS given in Figure 4.7.

4.3.2 Si K-edge XAFS from C clustered films

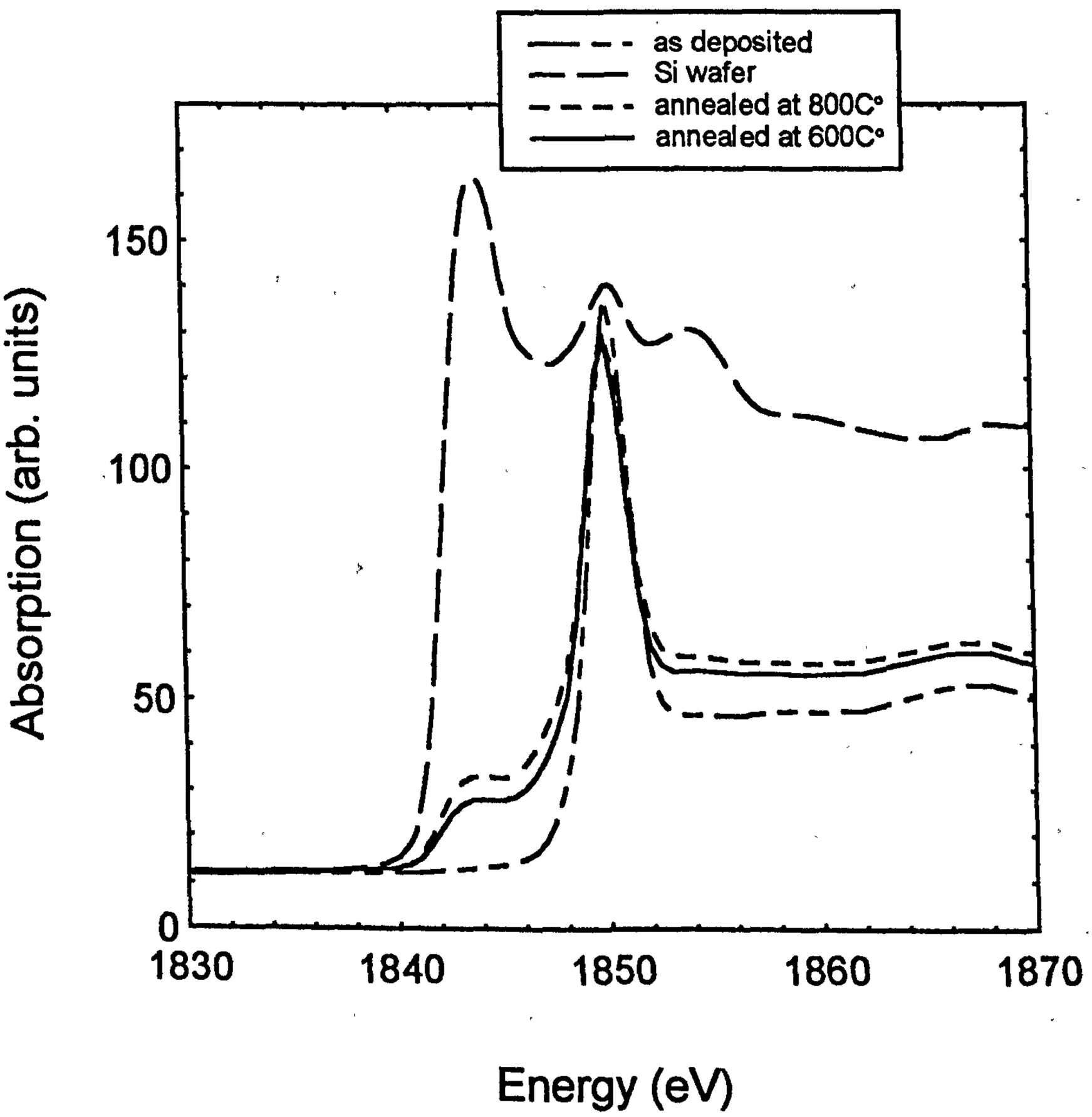

Figure 4.9 NEXAFS of Si K-edge from bulk Si and C clustered

films (typical of the sample 1 group in the Figure 4.5 of C-cluster PL).

As there are many Si (from SiO_2) and C atoms in the films, it is necessary to identify what kind of chemical environment gives rise to the observed PL. Without evidence, we cannot rule out the possible contribution of emission from silicon related nanostructures. This is because once SiO_2 has been doped by C, the SiO_2 matrices would be modified to SiO_x, leaving a possibility that the excess Si in SiO_2 would form a kind of cluster-like group. So, if we want to know what is inside the nanodots, the first step is to check out Si related information. Si K-edge XAFS, as shown in Figure 4.9, is suitable for this along with information about PL intensities.

The near edge XAFS are shown spectra from two different annealed samples which cut from the same as-deposited film (sample 1 group as characterised by PL spectra). Comparing with the data of Figure 4.5 of PL from carbon clustered films, a clear decrease of Si-Si bond absorption for 800°C annealed films has been observed from Si NEXAFS, when compared with that from 600°C annealed films. The PL intensity however increases for such samples, as discussed above. Thus we can rule out the possibility that Si-Si bonding is required for the observed blue emission.

4.3.3 C K-edge XAFS from C clustered films

As described above Si-Si bonding is not responsible for the observed blue emission, or at least, confined Si-Si bonds are not the principal feature atoms which construct the nanosized dots. On the other hand, C K-edge absorption has given a direct relationship between increase in intensity of PL and increase in density of C-C bonds, as shown in Figure 4.10 when compared with the PL of Figure 4.5.

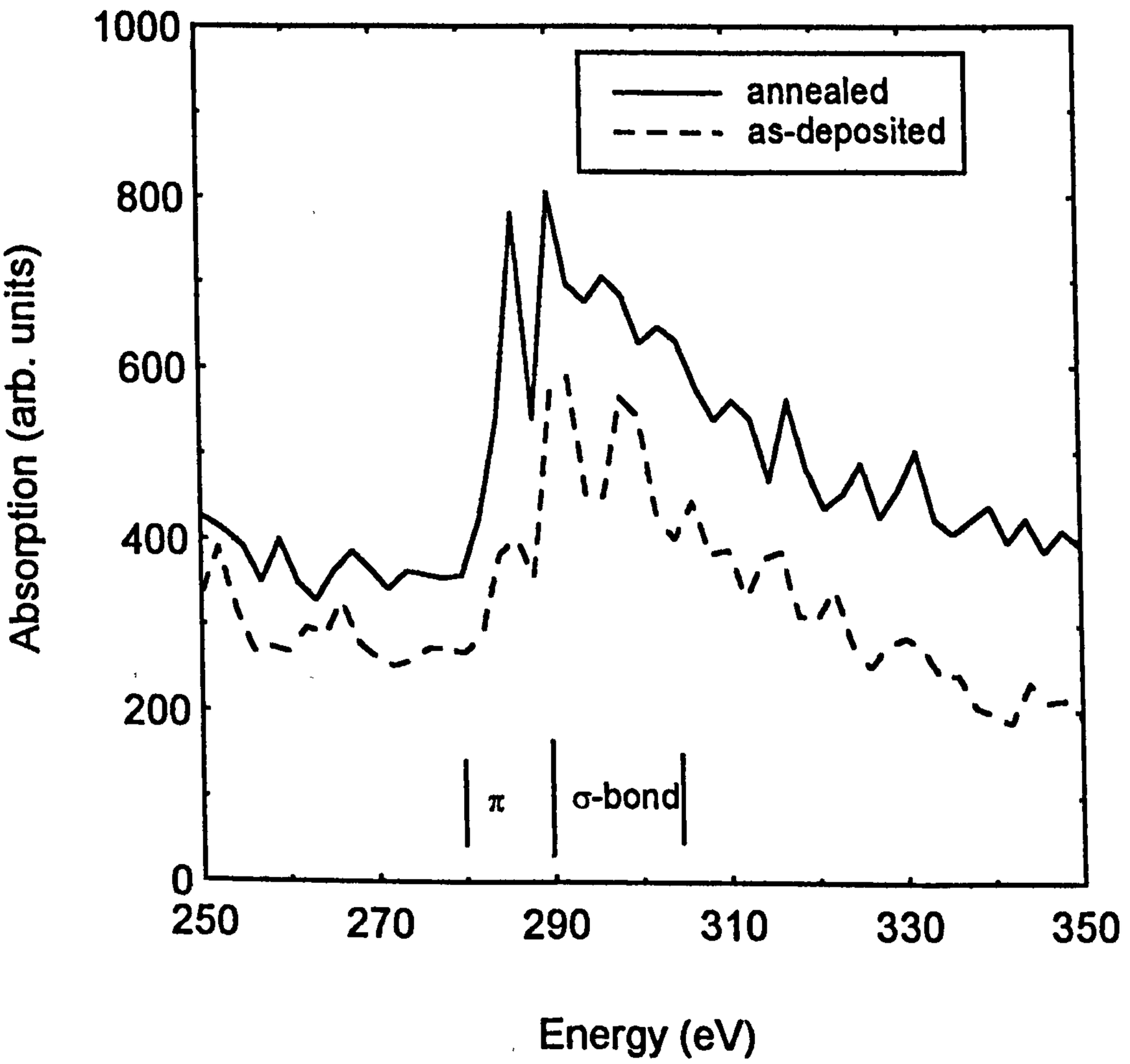

Figure 4.10 C K-edge NEXAFS of the carbon clustered films,

sample 1 group.

Because of the smaller quantities of carbon atoms/clusters compared to those of Si and O atoms in the films, and a lower intensity of synchrotron radiation transmitted through the monochromator, as well as the larger energy step chosen for the scans, the NEXAFS of the C K-edge is fairly noisy. However, the near edge absorption still presents certain important information about carbon bonding states in the clustered films. The clear increase of the absorption peak below 290 eV in the annealed films, indicative of the presence of π bonds, compared with that in the as-deposited films indicates that graphitic carbon clusters have formed from oxygen rich-carbon clusters : the strong σ bond absorption observed above 290 eV could be a result of C-O bonding (Schedel-Niedrig, et al., 1993), and furthermore only the annealed clustered films give off strong luminescence.

4.3.4 O K-edge XAFS from C clustered films

Besides the structural information from C NEXAFS, studying the x-ray absorption by oxygen atoms in the film and the oxygen related bond states would provide useful indirect information. In Figures 4.11 and 4.12, both Fourier transformed O K-edge EXAFS and the relevant k^3 weighted EXAFS spectra are given, in which both as-deposited and annealed films were measured.

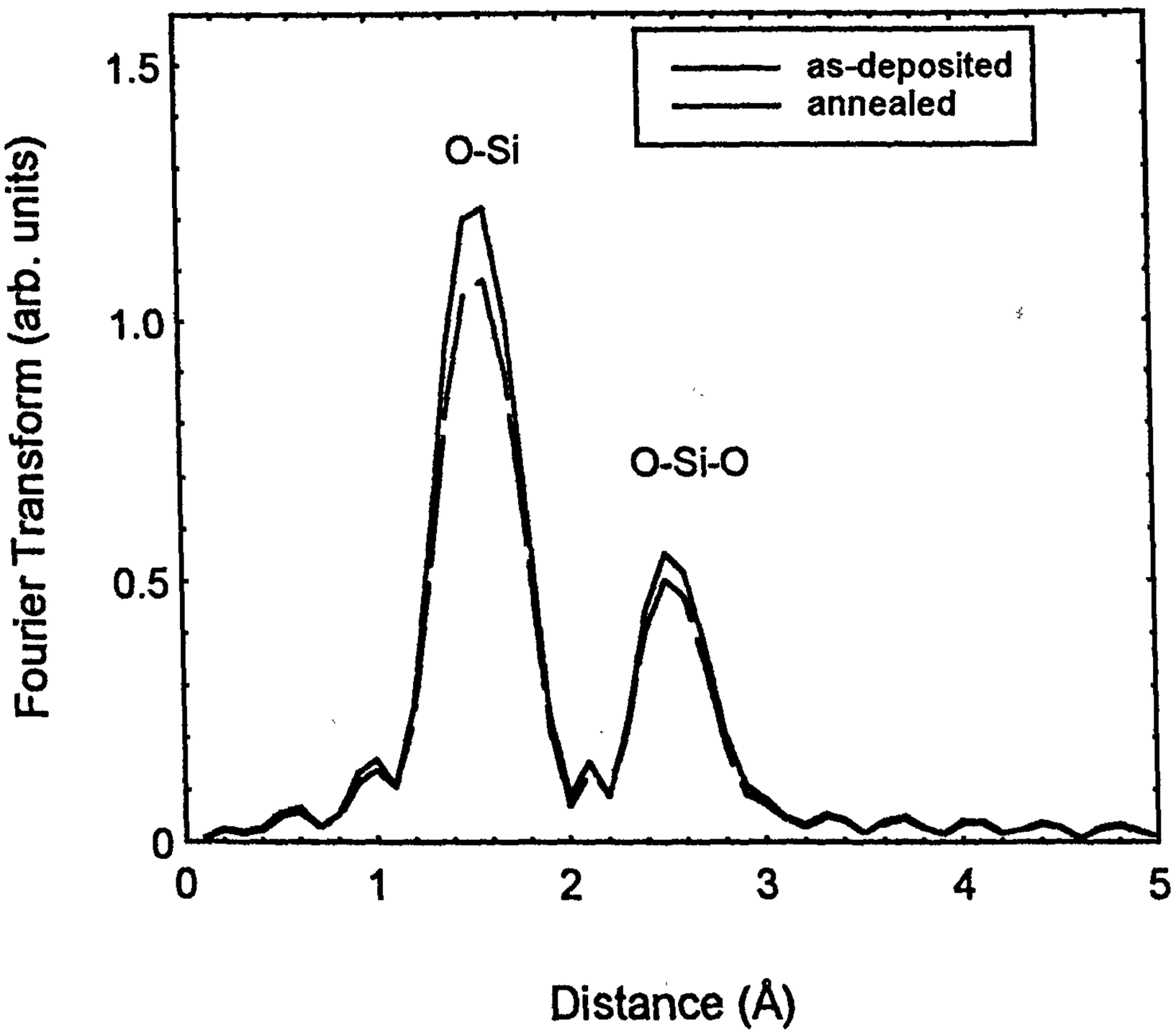

Figure 4.11 Fourier transformed O K-edge EXAFS of the C clustered films, sample 1 group. For clarity, only theoretical fitting is shown here.

We can see that both the shells of Si-O and O-Si-O from annealed samples are stronger than those from as-deposited samples. Because the possibility of Si-Si - bonded clusters has been ruled out, the other explanation is that a considerable number of oxygen atoms re-bond with Si after annealing from various O-C bonding states in the as-deposited materials, leaving the carbon atoms having the chance forming clusters or dots.

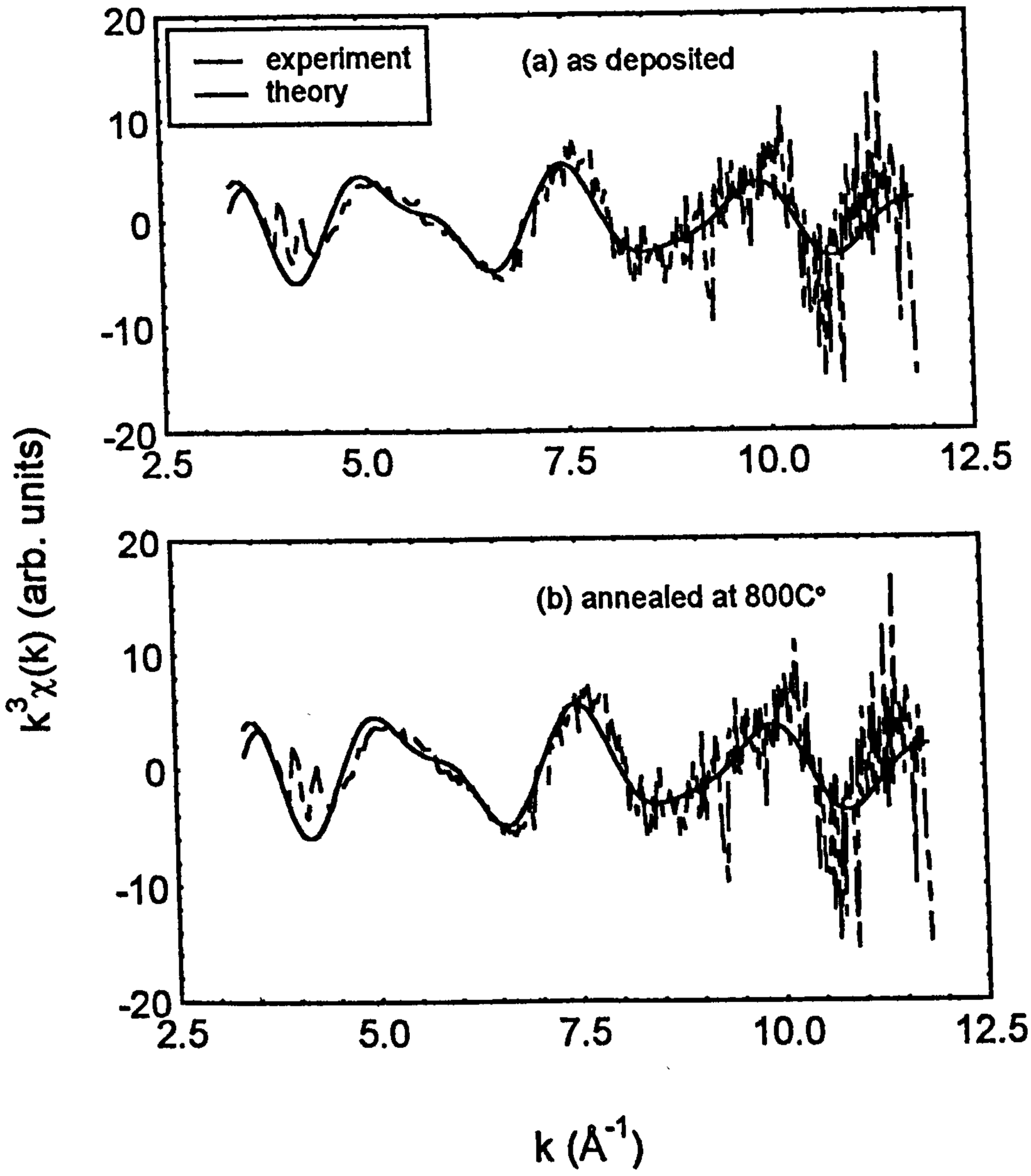

Figure 4.12 k^3 weighted oxygen k-edge EXAFS $k3\chi(k)$ of the carbon clustered films, sample 1 group.

4.4 Summary

In this Chapter nanoclustered films containing either silicon or carbon elements have been studied in terms of photoluminescence, nanosize distributions, mean sizes, x-ray absorption, and Si-Si, Si-O and O-Si-O shell coordinations, ordering factors this was effected by means of PL spectroscopy, real space images from TEM and the large energy range of NEXAFS and EXAFS from C K-edges, O K-edges to Si K-edges. Since the series of experimental measurements were based on grouped samples -- cut from same original as-deposited films and then annealed at different temperatures and different intervals, the different data are logically related to each other, and can reinforce the inferences made. Using these data for further discussion, it should be possible to determine a comprehensive understanding of the appropriate structures.

For the samples of Si clustered films, it is known that the element, Si makes up the nanodots, as there is no other choice. Further, the optical and structural data suggest only that the crystallized clusters (annealed at higher temperature) are responsible for the strong optical emission, and the emitting energy is directly related to the size of the dots.

For C clustered films, things are more complicated, because two types of element, Si and C, could be involved in making up the nanoclusters which could then be responsible for the visible luminescence. First of all, Si K-edge NEXAFS does not suggest that Si-Si bonding was the source of the emission when compared with

relevant PL data. Also, C K-edge NEXAFS implies an increasing C-C π bond density which correlates with increasing PL intensity, while O K-edge data give indirect evidence of clusters formed after annealing. Finally, clusters made up of C atoms are identified as the responsible species of the visible emission.

The mechanism of the blue emission will be discussed in Chapter 6.

CHAPTER 5 THEORETICAL CALCULATIONS AND MODELING IN ORDER TO UNDERSTAND FOURIER TRANSFORMED EXAFS

Up to now, series of experimental data have been obtained and grouped in terms of NEXAFS, Fourier transformed EXAFS and TEM. Although ChapterS 3 and 4 have determined the elements making up the nanostructures and the materials which are responsible for the visible emission, we still need to know the emission mechanism, i.e. how the emitting energies are shifted in the visible range. In this Chapter, relevant theoretical calculations are given, and modeling of Fourier transformed EXAFS of porous Si, as well as mean sizes of nanoclusters, will be compared with the calculations.

5.1 Theoretical Calculations of Band-gap Variation with Quantum Confinement

Many mechanisms have been proposed to explain the visible emission as mentioned in Chapter 1. The experimental data presented here of a gradually reduced 1st, 2nd and 3rd shell partial coordination numbers $N_{Si\text{-}Si}$ of porous Si as the emitting energies increase and the size distributions of the nanoclusters, however, would only suggest the quantum confinement model as the most appropriate. Thus this section will only concentrate on calculations based on quantum confined models.

Although the very basic quantum confinement model has been shown in Chapter 1, the actual theoretical approach is more complex when taking into account the confined dimension, size and nanocrystalline shape. Calculations have been tried in many theoretical ways, such as by First-principles analysis (Hybertsen and Needels, 1994), mean-field approach (John and Singh, 1994), tight-binding model (Sanders and Chang, 1992), effective-mass approximation (Takagahara and Takeda, 1992 and Fishman, et al., 1993), and linear combination of atomic orbitals (LCAO) (Delerue, et al., 1993).

Only the calculations from LCAO (Proot, Delerue, 1992, and Delerue, et al., 1993) and effective-mass approximation (Takagahara and Takeda, 1992) will been mentioned below, because these calculations cover a broader energy range than the others and consider both nanowires and nanodots of different shapes and crystalline orientations. These properties are of most interest for the work presented in this thesis.

5.1.1 Linear combination of atomic orbitals (LCAO)

In this work, they calculated the electronic structure of crystallites (dots) and wires with a diameter up to 4.3 nm (2049 atoms in the crystallite). For simplicity, they have taken crystallites and wires with respectively spherical and cylindrical shapes. They also keep the same crystallographic structure as for bulk silicon. The dangling bonds

at the surface are supposed to be saturated by hydrogen atoms to avoid localized states in the bandgap.

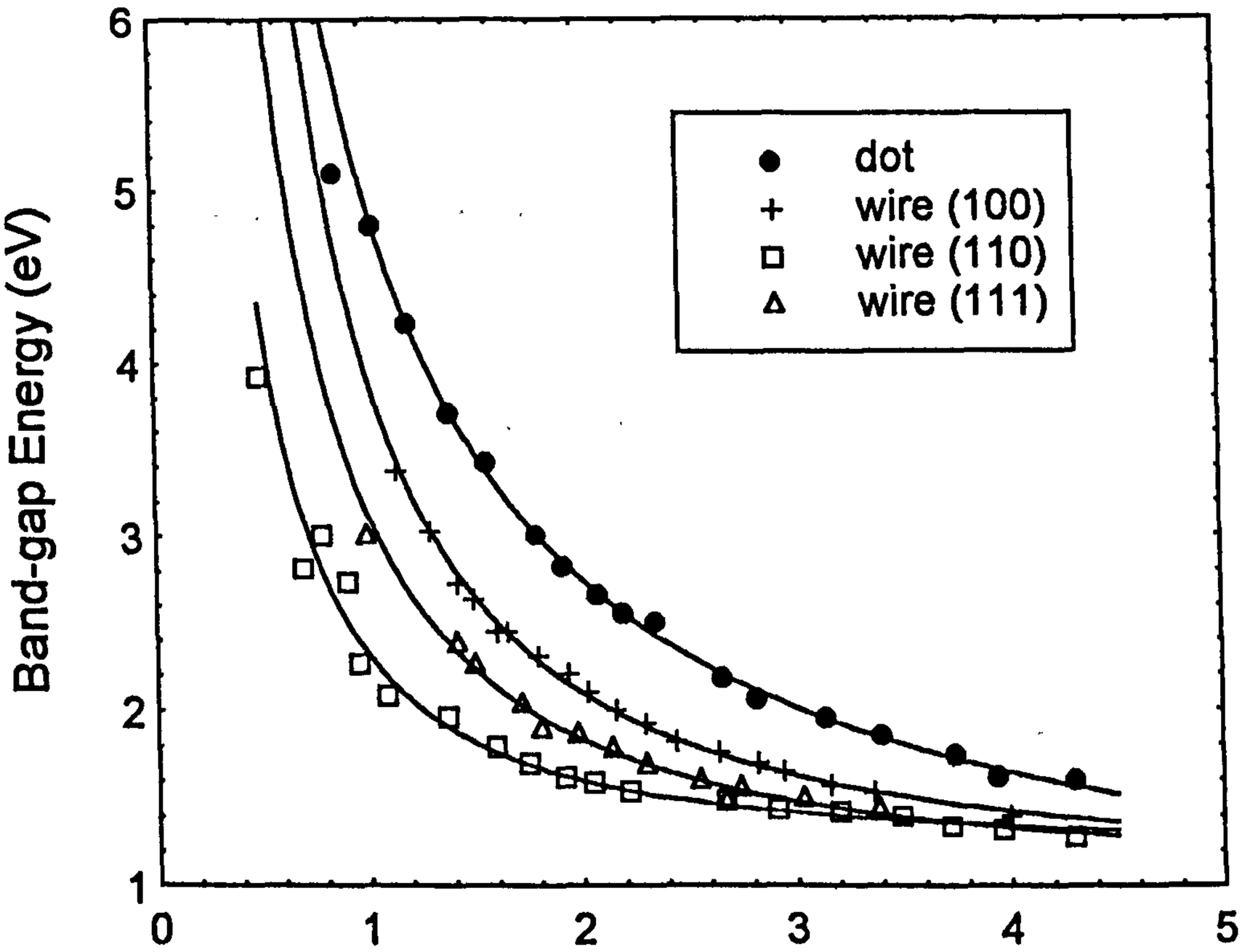

Figure 5.1 Calculated optical band gap energies for various silicon crystallites or wires with respect to their diameter *d*. The continuous lines are an interpolation and an extrapolation of these results by a d^n law. (after Delerue, et al., 1993)

Results for the bandgap energies of the nanostructures with respect to their diameter are plotted in Figure 5.1. They are given for crystallites (dots) and for wires in the

100, 110 and 111 directions. As we can see, the confinement is obviously more strong or important in crystallites but a strong anisotropy exists between that for the different directions of the wires.

5.1.2 Effective-mass approximation

Figure 5.2 shows a calculation from effective-mass approximation in which only nanocrystalline silicon spheres upto 14 nm in diameter were considered.

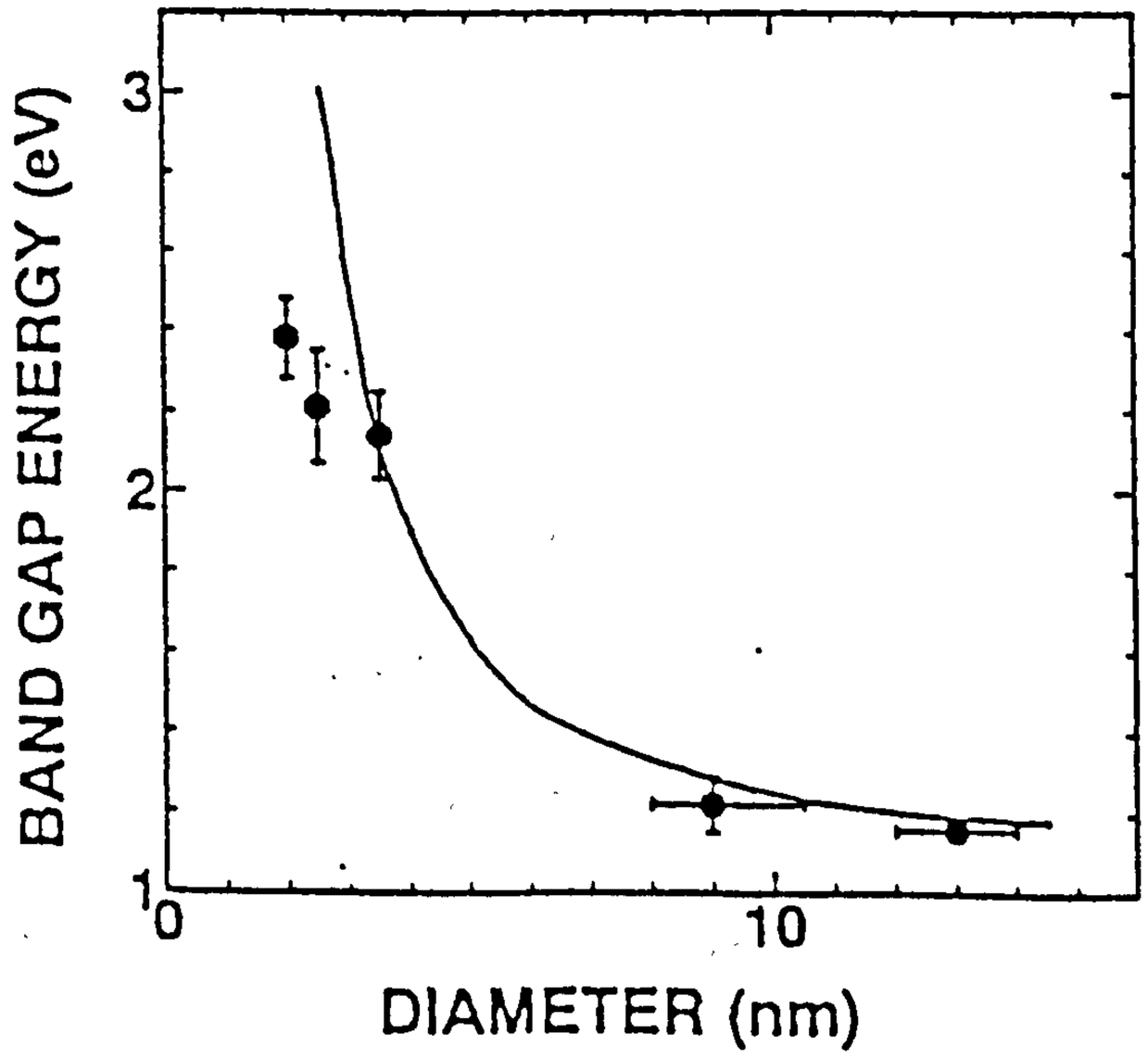

Figure 5.2 Band-gap energy as a function of the diameter of crystalline silicon spheres. The solid line is a theoretical calculation by an effective-mass

approximation, The dots are experimental data of Si nanospheres (after Takagahara and Takeda, 1992)

5.2 Modeling to Understand The Fourier Transformed EXAFS

Full local structural information has been obtained and was given in Chapters 3 and 4. The interpretation of the data will lead us to an understanding of whether porous silicon is made up of nanostructures and if they are nanowires or dots. This can be achieved by comparing the analysed data with the theoretical calculations above.

5.2.1 Nanowire and nanowire network model for porous Si

The Si-Si first shell fitting data from the red, yellow and green emitting porous Si (given in Chapter 3) are used in the modeling work, for the reasons (i) the fitting is of high quality (i.e., there are reasonably lower fitting errors) and (ii) they are straightforward to compare with data from a structural model.

The dependence of the average size with partial coordination numbers of two types of nanowire for both (100) and (111) orientations have been calculated to match the experimental 1st shell $N_{Si\text{-}Si}$. The results are shown in Figure 5.3 : (i) one-dimensional wires of cylinder-like (100) (curve 3), and hexagonal-column-like (111) orientation

(curves 4 and 5, for details see Figure 7); (ii) 'wire network' (curves 1 (111) and 2 (100)) with one-plus-a-fraction structural dimensionality, in which the number of surface Si atoms is only half that of bare wires of diameter d, based on the concept that the carriers within a wire network could also be confined in two dimensions (Canham, 1990, and Lehmann, 1991).

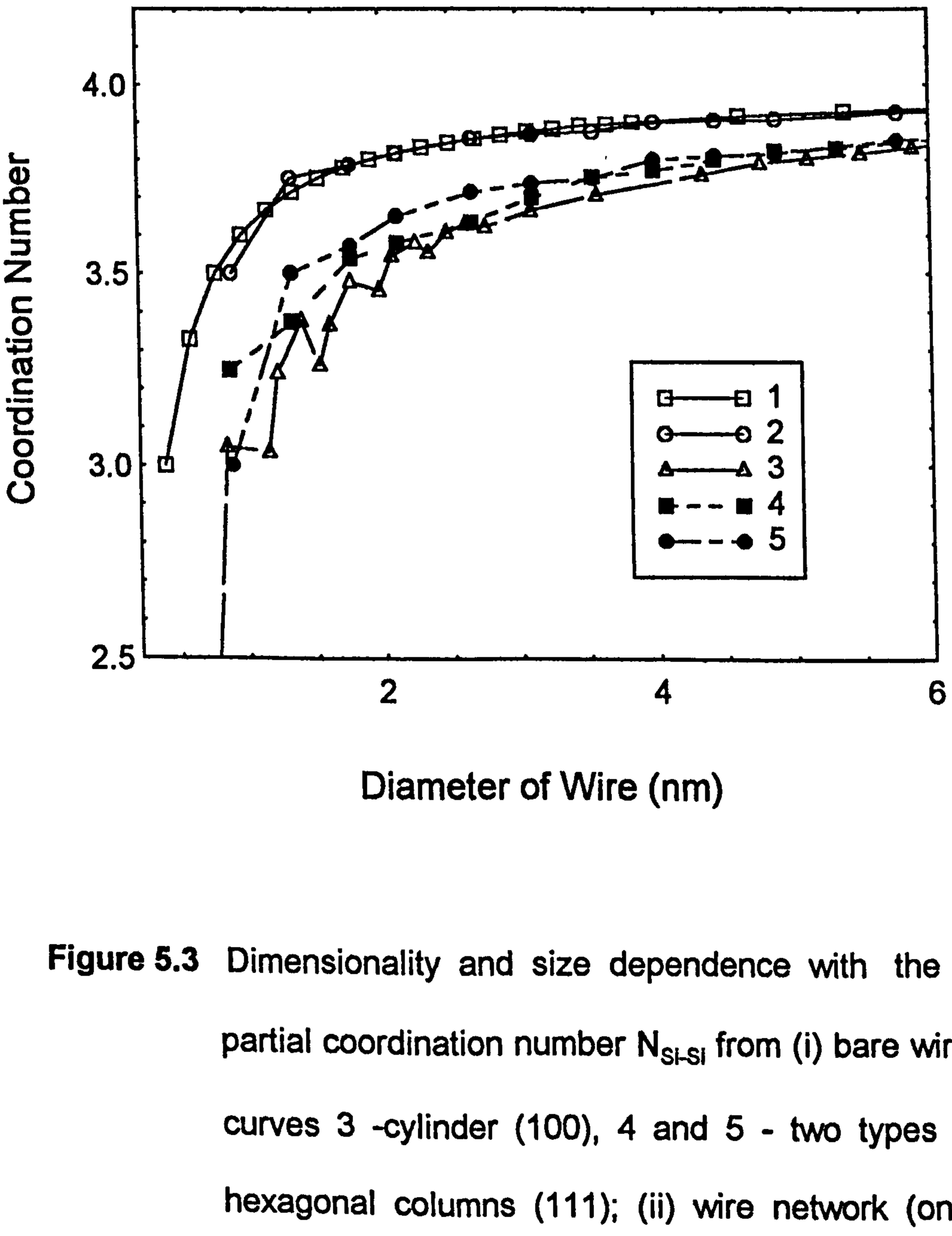

Figure 5.3 Dimensionality and size dependence with the partial coordination number N_{Si-Si} from (i) bare wire: curves 3 -cylinder (100), 4 and 5 - two types of hexagonal columns (111); (ii) wire network (one-

plus-a-fraction dimension) : curves 1 - (111) and 2 - (100), details see Figure 5.4.

In the model, it is supposed that the wires are ideally one dimensional, and the wire networks are ideal one dimension plus a fractional dimension. Consequently, as før as the surface atoms are concerned only the non-bonded Si atoms around the cylinder or column surface were taken into account, such as those bonded with O, H and OH, but Si. In other words, the Si dangling-bond atoms on the tops of the two sides were ignored.

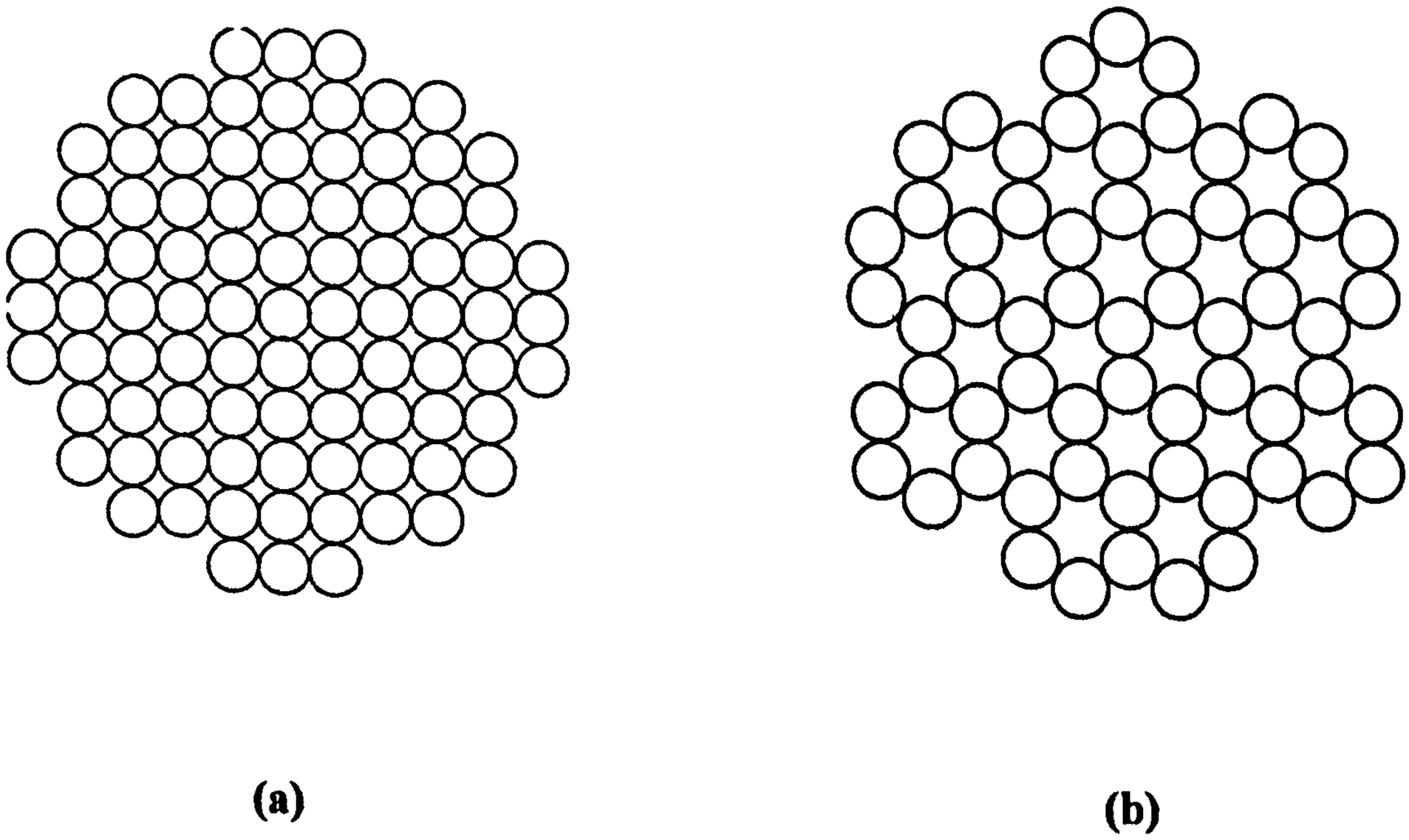

(a) (b)

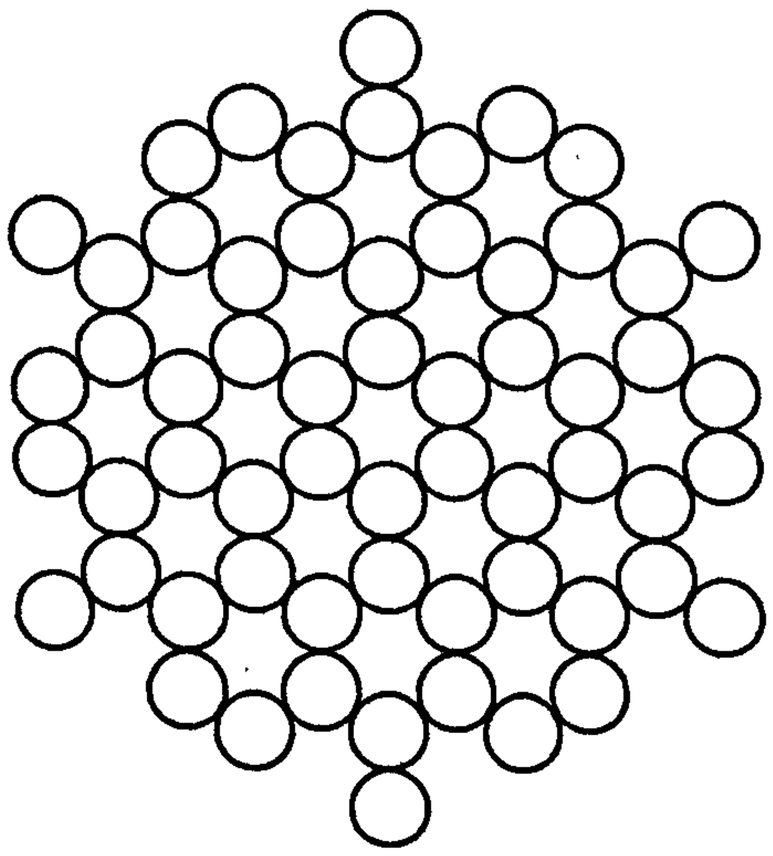

(c)

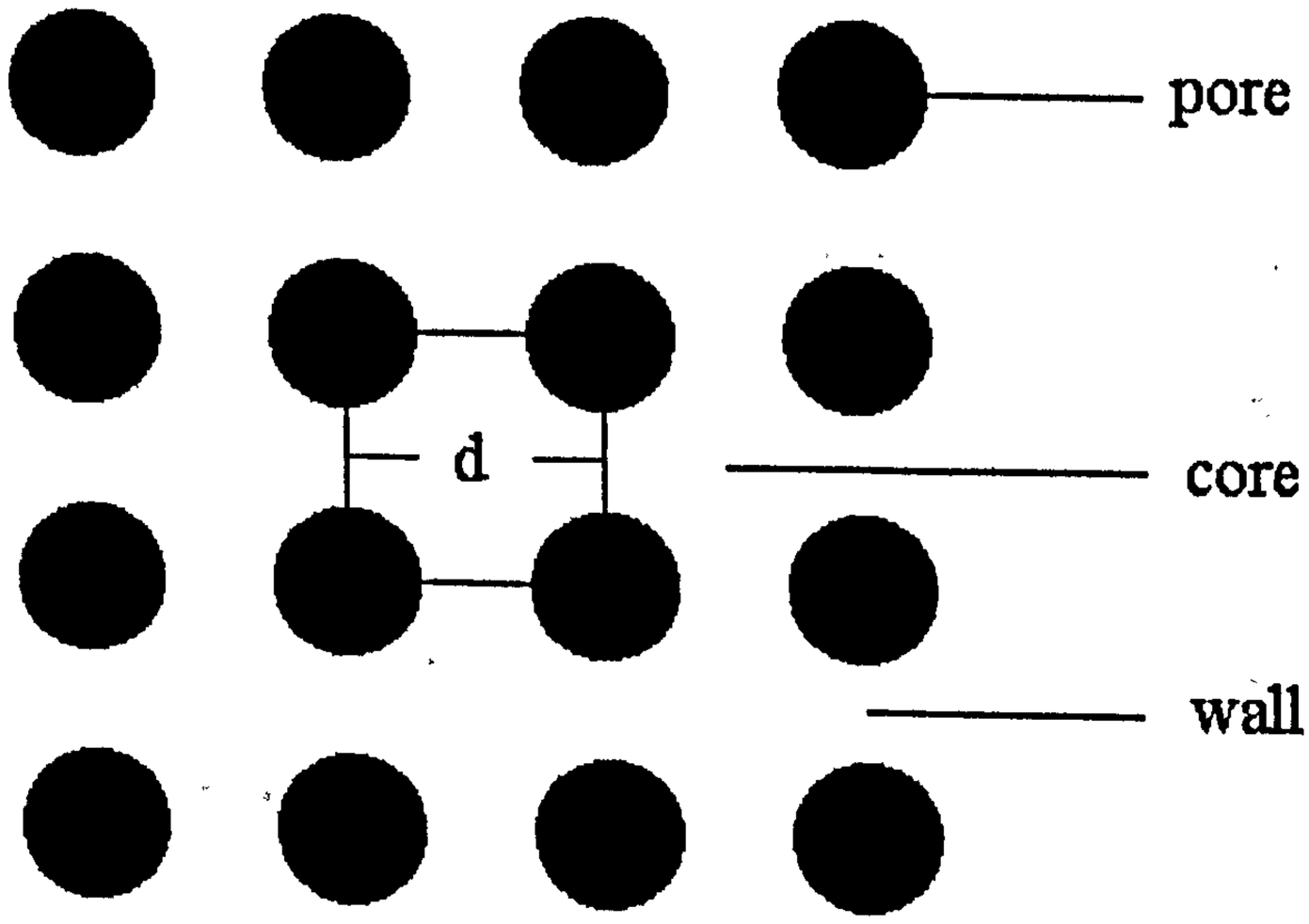

(d)

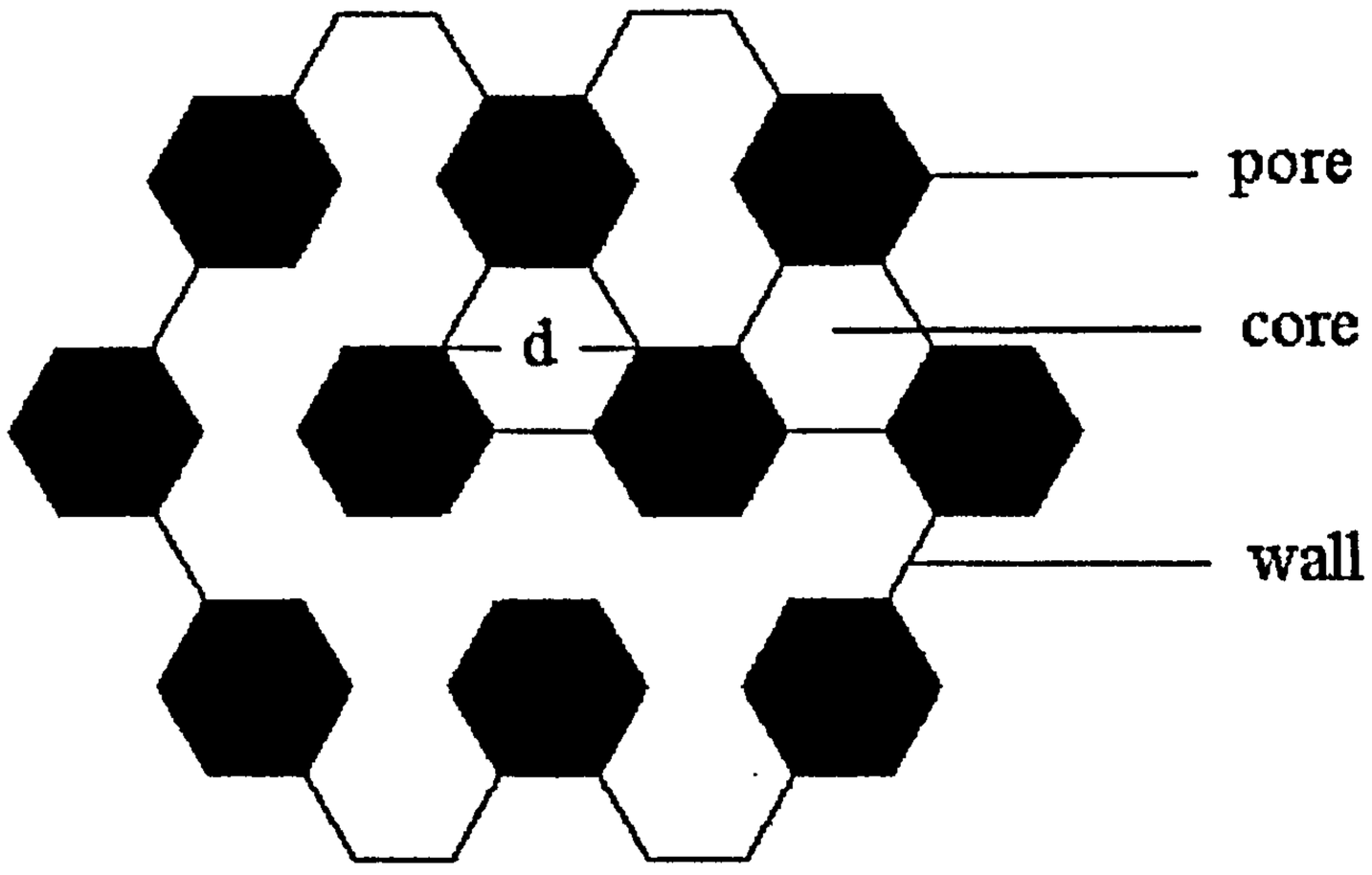

(e)

Figure 5.4. The idealized atomic plan views of the bare wires and plan views of the wire networks. (a) bare wire (100), (b) bare wire (111) (type 1) and (c) bare wire (111) (type 2), appropriate for curves 3, 4 and 5 in Figure 5.3, respectively. Also shown are (d) cylinder-like structure in (100) and (e) hexagonal column-like structure in (111), appropriate for curves 2 and 1 in Figure 5.3 respectively, in which the number of surface Si atoms is only half that of bare wires of diameter d.

For the cylinder-like wire (100), there is a Si atom at the center of the cylinder of radius r=d/2. If the center points of the surface Si atoms are at or within the circle of radius r, the bonds to these atoms were counted based on the bonding conditions. For the (111) orientation, two types of hexagonal columns have been used, one is with an atom at the center (curve 4 in Figure 5.3), the other has no atom at the center (curve 5 in the Figure). The diameter, d, was the mean of the maximum and minimum distances (center point to center point of the surface atoms) across the hexagon, with step-increases of a full atomic layer all round.

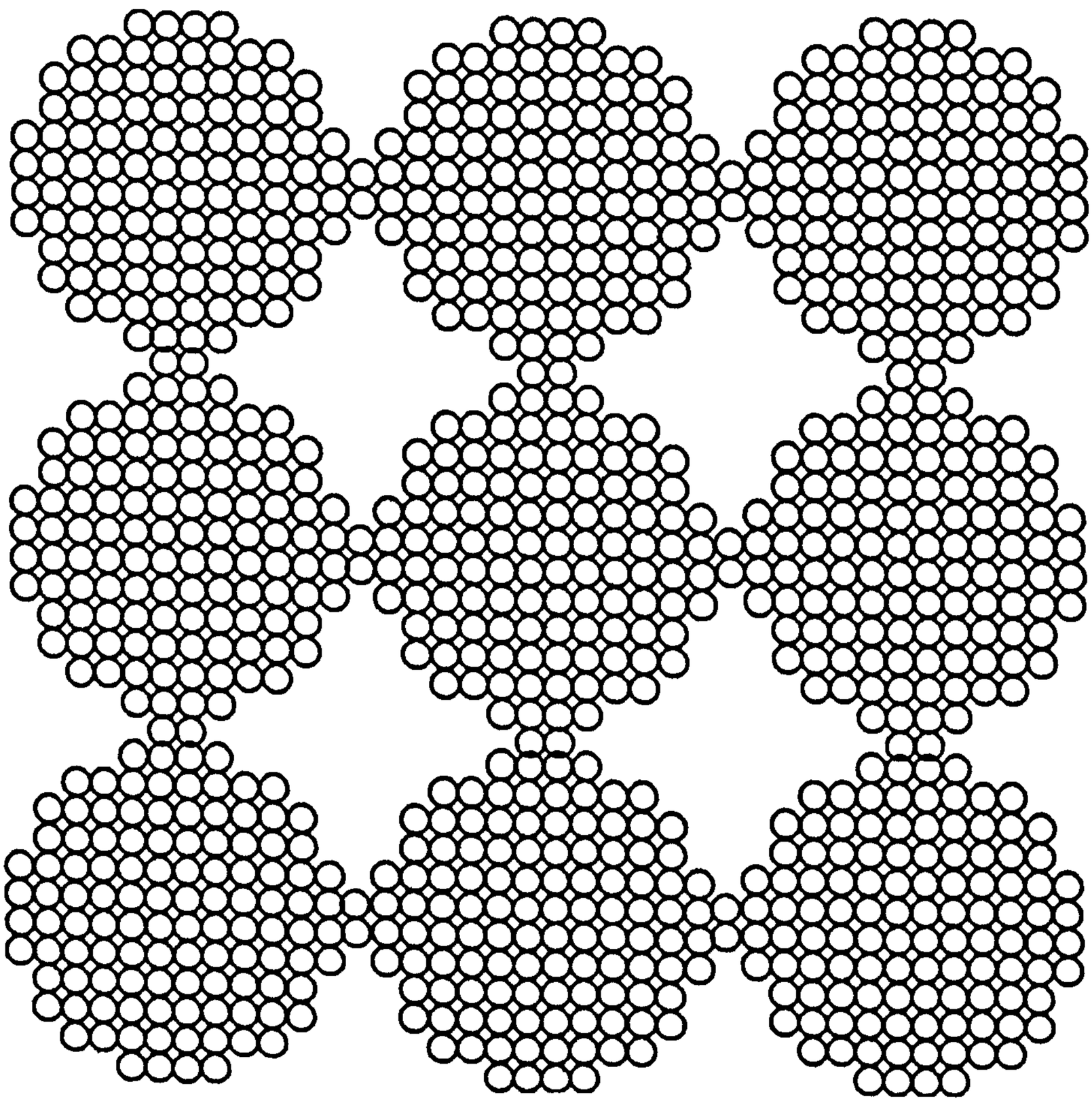

Figure 5.5 A detailed network model plan view of cylinder-like (100).

The details of the model are shown in Figures 5.4 (a), (b) and (c) for the bare wires, with idealized atomic plan views appropriate for curves 3, 4 and 5 in Figure 5.3, respectively. The idealized plan views of the wire network are also shown in Figures 5.4 (d) and (e) superimposed on the cylinder-like (100) (curve 2 in Figure 5.3) orientation with 25% porosity and on the hexagonal column-like (111) (curve 1 in Figure 5.3) orientation with 33% porosity, respectively. This is based on the constraint that the number of surface Si atoms is only half that of bare wires of diameter d, the other half forming bonds with the neighbouring wires. One should note that the porosity of the idealised plan should be smaller than that obtained experimentally for the same nanosize, as there are a large number of bigger pores with diameters in the tens or hundreds of nm which have not been considered in the idealised calculation. The larger pores have been observed by many researchers with TEM, however, they do not make a direct contribution to the nanostructure. A more detailed network plan view is shown in Figure 5.5.

5.2.2 Nanodot for clusters

The mean sizes of the blue emitting silicon and carbon clusters are from 2.3 to 2.4 nm as given by TEM in Chapter 4. When compared with Figures 5.1 and 5.2, the theoretical calculations of confined emission energies for nanodots, we can see that the blue emitting energies correlate with their sizes. Then, there is no modeling work needed to complicate the simple figure.

5.3 Summary

Although there are many theoretical calculations for quantum confinement of wires and dots, results of the relationship between sizes and bandgap energies are more or less same. In this thesis, only the calculations from LCAO and effective-mass approximation are cited for further discussion of our data and modeling because their work covers a broad energy range as well as structural varieties including different shapes, orientations and dimensionalities (wires and dots).

Models have been proposed to interpret the theoretical fitting of Fourier transformed EXAFS from the freshly produced red, yellow and green porous Si. They include wires and wire networks with (100) and (111) orientations, and two kinds of cross section shapes. The models cover wire diameters from 0.5 nm to 6 nm, correlating with a coordination number from 2.5 to close to 4 (the number for bulk tetrahedron structure).

CHAPTER 6 THE MEAN SIZE AND DIMENSIONALITY OF POROUS SI AND NANOCLUSTERS

Enough information has been obtained now to identify some details of the emission mechanism taking place in two kinds of nanomaterials: porous Si and clustered films. They include (i) structural properties from TEM, EXAFS, NEXAFS and their theoretical fitting, (ii) optical properties from PL and PLE, (iii) theoretical quantum confinement calculations and (iv) modeling work which not only provides an understanding of the theoretical fitting but also will allow the inter-connection between these different types of information. In this Chapter, all of the relevant knowledge obtained will be used to produce a description of the kinds of material they are, as well as lead to a suggestion for the visible emission mechanism.

6.1 The Nanowire and Wire Network Structures of Freshly Produced Red, Yellow and Green Porous Si

6.1.1 The mean sizes and dimensionalities

Obtaining accurate coordination numbers, $N_{Si\text{-}Si}$(3.8 ± 0.15, 3.65 ± 0.13, 3.0 ± 0.2) and ordering factors from theoretical fitting of EXAFS for the red, yellow and green PS, allows us to estimate the possible average sizes present, as well as the relevant

structural dimensionality, and to determine if quantum confinement is responsible for the properties of the PL. To achieve this aim, several other values are required : (i) PS band-gaps; (ii) theoretical calculation of variation of band-gap with size of nanowire and nanodot; and (iii) the correlation between coordination number and average nanosize with different dimensionality. As mentioned in previous Chapters, these required values have been obtained. They are summarised in the following and shown in Figure 6.1 (a), (b), (c) and (d).

(i) In most published works the nanosizes determined by TEM have been compared only with the PL peak energy, i.e. the peak energy is used as an estimate for the bandgap energy in order to estimate the size distribution, assuming a band-to-band transition model. Following this, from the work of this project the peak energies E_{g2} are 1.8, 2.14 and 2.38 eV, respectively for red, yellow and green PS, as shown in Figure 6.1(a). The bandgaps E_{g1} obtained assuming a recombination centre model from PLE measurements at room temperature are also given in Figure 6.1(a).

(ii) The theoretical calculation of confined bandgap with nanosize of PS by the linear combination of atomic orbitals (LCAO) technique is cited in Figure 6.1(b) (after Delerue, et al., 1993) where both nanodot and wire bandgaps were given.

(iii) The coordination numbers of the first Si-Si shell of the porous silicon from careful theoretical Fourier transform fitting are 3.8±0.15, 3.65±0.13, 3.0±0.2. These values are shown in Figure 6.1 (c) with errors of fitted parameters.

(iv) The average size dependence with partial coordination numbers of two types of nanowire (naked wire and wire network) for both (100) and (111) orientations have been calculated to enable comparison with the experimental 1st shell $N_{Si\text{-}Si}$, and are shown in Figure 6.1 (d).

Comparing Fig. 6 (a), (b), (c) and (d), and knowing both bandgap energies E_{g1} and E_{g2}, we can estimate the mean dimensionality and the sizes of porous Si in the radiative wavelength range from 690 nm to 520 nm within a sampling depth of hundreds of nm. As indicated by lines in Figure 6.1, it is can be seen that the nanostructure of red and yellow porous Si is predicted to consist of a one-plus-a-fraction dimensionality wire network, and that of green porous Si to consist of nanowire.

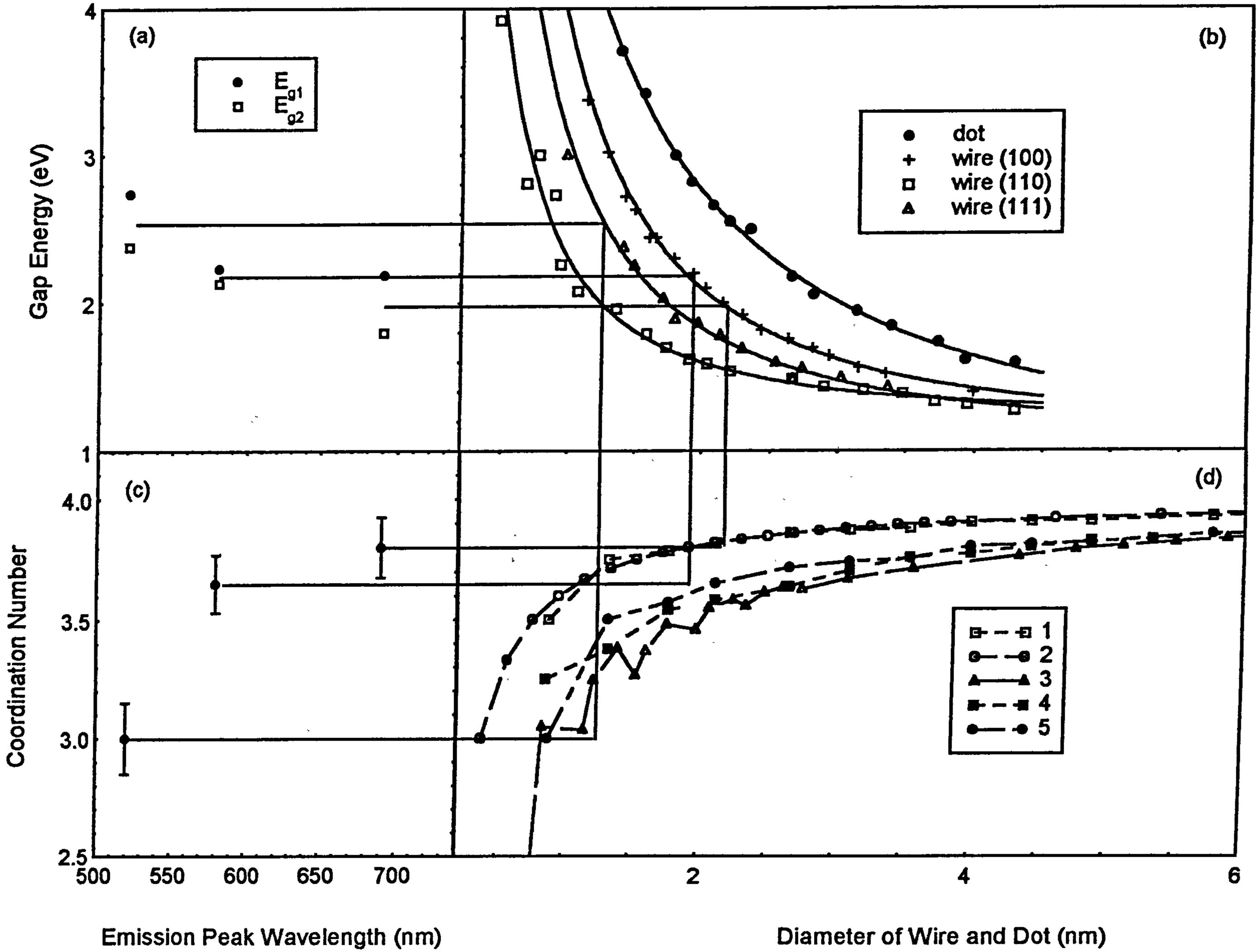
(a)
E_{g1}
E_{g2}
(b)
dot
wire (100)
wire (110)
wire (111)
Gap Energy (eV)
4
3
2
1
(c)
(d)
Coordination Number
4.0
3.5
3.0
2.5
1
2
3
4
5
500
550
600
650
700
2
4
6
Emission Peak Wavelength (nm)
Diameter of Wire and Dot (nm)

Figure 6.1 Dependence of dimensionality and size with porous Si emission "colour". (a) Bandgaps of the three types of emitting porous Si: E_{g1} from PLE and E_{g2} from PL peaks. (b) Theoretical calculation of confined bandgap energy of PS of wires and dot by LCAO (after Delerue, et al 1993). (c) 1st shell N_{Si-Si} of red, yellow and green porous Si from EXAFS fits. (d) Dimensionality and size dependence with the N_{Si-Si} from (i) bare wire: curves 3 -cylinder (100), 4 and 5 - two types of hexagonal columns (111); (ii) wire network (one-plus-a-fraction dimension): curves 1 - (111) and 2 - (100), details see Figure 5.4. As shown by the guiding lines, the PS in this study favour the nanowire network and wire structures, with average diameters of 2.2, 1.9 and 1.3 nm, respectively for red, yellow and green porous Si.

The mean core diameter of red porous Si is about 2.2 nm with a larger fractional dimensionality and, that for yellow porous Si is about 1.9 nm with a smaller fraction. Furthermore, the mean size of green porous Si is much smaller, only about 1.3 nm with a dimensionality of one or less than one. On the other hand it is not suitable to predict a nanodot model which is consistent with the data of both band-gap energy and partial coordination number as it would lie outside the experimental data plus error. The characteristic structure and mean size of green porous Si is different from that of red and yellow because of both $N_{si\text{-}si}$ and E_{gl}. The $N_{si\text{-}si}$ has the characteristic that the difference between red and yellow PS is smaller than that between yellow and green PS. The E_{gl} varies similarly, although $N_{si\text{-}si}$ and E_{gl} are obtained by very different means - EXAFS and PLE respectively (see Fig. 6.1). This implies that the transition behaviour varies with peak energy, however the details are not given here because it is not the topic of the thesis.

This type of nanowire with a dimensionality greater than one was proposed in very early work for PS porosity up to ~50%-80% (Canham, 1990, Lehmann and Gösele, 1991). Because the necks between the pores are thinner than the cores (or the quasi-rods), a stronger confinement effect results in potential barriers keeping the carriers in lower energy cores. This kind of nano-quantum-wire, the carrier being mainly confined to two dimensions but with structural dimensionality greater than one, could be called a 'wire network'.

In short, the experimental and theoretical work provide us with an understanding of freshly produced porous Si (anodized from the Si wafer with a resistance from 1 to 5 Ω cm at least). The red, orange and yellow emitting porous Si consist of nanowire networks with the mean diameter varying from 2.2 to 1.9 nm, while the mean fractional dimensionalities concerning the network connections are from 0 to 0.5. The green emitting porous Si consist of bare nanowires with the mean size about 1.3 nm, while the mean whole dimension is 1 or little less than 1.

6.1.2 Ordering

Is there any amorphous phase in porous Si? It can be imagined that a material consisting of nanosized wires should have a huge surface:volume ratio. The cores in a diameter range from 1.3 to 2.2 nm might be expected to be too vulnerable to keep the original crystalline phase, due to reconstruction of the surface of the cores, and the cores phase could be distorted to a certain level due to the stress at the interface of crystalline-core/SiO_2 for aged PS.

The other crucial fact is that the presence of an amorphous phase could also reduce the second and third shell partial coordination numbers, $N_{Si\text{-}Si}$, and could this be the reason for the rapidly reduced second and third shells shown in Figure 3.7 (Chapter 3). The nanostructure modeling work above would not be necessary if it was obvious that amorphous phase was present in the freshly anodized porous Si. Do these facts apply

to freshly anodized porous Si? We need to find out. Fortunately, the theoretical fitting of the Fourier transformed EXAFS also provides the ordering factor, the Debye-Waller order factors, which can be used to identify the order or disorder of the materials of interest.

Table III. The Debye-Waller order factors of Si-Si shells

	$A_1(k)$ / Å^2	$A_2(k)$ / Å^2	$A_3(k)$ / Å^2
red PS	0.0042±0.0008	0.011	0.01
yellow PS	0.0038±0.0008	0.011	0.012
green PS	0.0048±0.001	0.013	0.013
c-Si	0.004±0.0007	0.01	0.011
a-Si	0.007±0.0006		

Table III gives the Debye-Waller order factors, A(k), of the first, second and third Si-Si shells (with fitting errors for the first shell which is most of interest) for the PS, c-Si, a-Si and a-SiO_2. The A(k) of the 1st, 2nd and 3rd are quite close to that of crystal Si, but far from a-Si, especially for the first shell for which the errors are given. Such values for A(k) suggest as expected that the core of the fresh PS is nanosized crystalline silicon, in agreement with the results reported by Naudon, et al., (1994), and Y. Uchida, et al., (1993). The other reported study on fresh near infrared red and red

emitted porous Si also using NEXAFS and EXAFS by Schuppler et al., (1994) did not give these factors. The small difference between the A(k) of green PS and c-Si can be explained since the high surface:volume ratio of this nanostructure effects a detectable x-ray absorption due to the surface passivated layer.

When we look back at Figure 3.6, a crystalline related nanostructure also can be inferred as indicated by the Debye-Waller order factor. Figure 3.6 (a), (b) and (c) show both experimental and back transformed, nonfiltered EXAFS data with k^3-weighting from the red, yellow and green porous Si. It can clearly be seen that both the curves from every PS have the characteristics of crystalline Si even with quite reduced coordination numbers.

Thus, these fitted ordering factors suggest an important characteristic of porous Si before degradation and both further and native oxidisation, i.e. anodisation only produces a nanostructure: consequently, the quantum size effect would be the first choice for the reason for bandgap-widening resulting in the far infrared bandgap of bulk Si shifting to visible range from red to green.

6.2 Zero Dimensional Quantum Dots - The Clusters

The mean nano-sizes and size distributions have been obtained and summarised in the relevant sections of previous Chapters. Indeed, the clusters sizes are in a scale of

nanometers, so, quantum confinement would be a first thought for the mechanism of visible emission. However, it is still necessary to know the relevant relationships and some other structural information.

6.2.1 Blue shift with the mean sizes

The mean sizes of the Si nanodots in the two clustered films are about 2.3 - 2.4 nm and the photoluminescence peaks varied from 420 nm (2.95 eV) to 495 nm (2.5 eV), as presented in Chapter 4. The C related nanodots however have a mean size of 2.5 nm. The relevant emission peak energies (two peaks) for these films are from 2.95 eV (420 nm) and 2.53 eV (490 nm).

According to the theoretical calculation of the electronic structure of silicon nanocrystallites by an effective-mass approximation (Takagahara and Takeda, 1992) and by LCAO (Delerue, et al., 1993), nanoclusters ~2.4 nm in diameter are expected to have a bandgap of 2.3-3.2 eV, as shown in Figure 5.1 and 5.2. The PL peak energies of clustered films in this work fall in this region.

As there is no series of quantum confinement calculations related to carbon materials reported, we cannot compare the known mean size with theoretical calculation. However, the calculations for silicon nanomaterials still can be used for comparison, since once the electron is confined in three dimensions, the size effect will be much

stronger than the effects which come from either electron-effective-mass in a particular material or the original band gap of the bulk material. Therefore, when comparing the mean size and emission peak energies of the carbon clustered film with the theoretical calculations for silicon, the PL peak energies of carbon nanodots also fall in the predicted range.

From EXAFS it appears that the formation of more Si-Si bonds in the Si-clustered samples increases PL efficiency. Furthermore, higher PL efficiency comes from the samples which have many more clusters as observed by TEM. Thus we have an indication that the existence of small elemental Si clusters provides one correct environment for greater PL efficiency in the blue.

It has been proposed that the blue emission could come from defect levels within the bandgap of SiO_2 (Kontkiewicz, et al., 1994). The work in this thesis does not support this, as no photoluminescence has been found from as-sputtered films even though sputtered SiO_2 would be expected to have many defect states within the bandgap. In other words, the PL from the defects within the SiO_2 bandgap in unannealed material is not detectable with the system used when excited by power densities of μWcm^{-2}. We find that strong PL is only observed when clusters are found by TEM, that is after annealing. Is is also found that there is a direct dependence of PL intensities on the number density of Si clusters in annealed films. The PL expected from the defects in the SiO_2 band-gap did not give an obvious contribution. Furthermore, the SiO_2 network is not expected to change much on annealing. It is known that after annealing

programs at 1100°C the oxide still exists as a random network. Therefore, the effect of disorder-quenching of PL, due to defect sites in the as-sputtered specimens, will not change much on annealing.

6.2.2 Order in the clusters

Crystalline lattice regions have been observed by others in high resolution TEM images (Morisaki, et al., 1993, Kanemitsu, et al., 1993, (1993), and Maeda, et al., 1991 and 1995), in similarly-prepared materials but with larger sized nanodots. Evidence for the presence of clusters has been obtained from TEM - crystalline regions have been observed in the diffraction patterns from the samples composed of large clusters (about 15-20 nm diameter) which show emission at much longer wavelengths. In addition, TEM shows that clusters, presumed to be a-SiO_x ($x<2$), are present in as-deposited films (i.e. before annealing) with an average size ~1.5 times larger than that after annealing. It is likely that these regions provide the basis for crystallization of Si clusters on annealing.

The blue-emitting material however contained very small clusters, and we could not obtain evidence for crystallinity in these samples, possibly because of the resolution of the instrument, or because of the volume of material studied. One should notice that the nanodots studied here are the smallest constructed nanoclusters in any reported research result ever. Because of the small sizes we constructed, the highest emission

energies (in true blue) have been recorded and reported (please see the Appendices A and C).

EXAFS fitting data of Si nanoclusters do not show direct evidence for crystallinity : the fitted Debye-Waller factors of the first shell Si-Si bonds at about 0.006±0.003 $Å^2$ suggest a structure which could include amorphous and crystalline phases for which the factors are 0.004 and 0.007 $Å^2$ respectively. Alternatively, and the explanation which is consistent with the PL and TEM data, the EXAFS suggests that the structure is composed of clusters which have crystalline cores surrounded by disordered bonds.

The PLE of Si clustered films suggests the same result. PL intensity shown in Figures 4.4 and 4.5 increases rapidly with excitation photon energy and this suggests that there is a continuous increase in the density of states in the conduction band above the band minimum. Additionally, since there is some PL intensity, although very weak, for excitation photon energies very close to the PL emission energy, there could be a band tail attached to the conduction band. This tail could be due to the disorder of the clusters found by EXAFS.

When we look at the structural information about carbon clusters, the same conclusions are drawn, i.e., the clusters would have crystalline graphite-like structure, as suggested by the bonding states assigned to the C XAFS of the annealed films. These data give no indication of the role of large band-gap diamond-like carbon materials which remain the other possibility for the size effect. The electronic

structure, including the Fermi level, of nano-sized graphite would be shifted from that of the bulk under quantum confinement, resulting in the appearance of a large band-gap, while attached by band tails caused by a disordered phase surrounding the cores.

6.3 Summary

Putting together (i) PS band-gap energies from PL peaks and PLE, (ii) theoretical calculation of variation of band-gap with size of nanowire and nanodot, (iii) experimental coordination numbers of PS Si-Si first shell and (iv) the correlation between coordination number and average nanosize with different dimensionality from the model proposed in the work, the quantitative nanostructure of freshly produced porous Si (anodized from the Si wafer with a resistance of 1-5 Ωcm) has been determined. The red, orange and yellow emitting porous Si consists of nanowire networks with the mean diameter varying from 2.2 to 1.9 nm, while the mean fraction dimensionalities comprising the network connections are from 0 to 0.5. The green emitting porous Si consists of bare nanowires with mean size about 1.3 nm, while the mean dimensionalities is 1 or a little less than 1. Furthermore, the theoretical fitting suggests that the nanocores of the wires of 'fresh' porous Si are crystalline, without any sign of disorder.

On the contrary, the nanodots/nanoclusters seem to have crystalline cores surrounded by disordered bonds. The size distribution and mean size are, however, also in line

with the prediction of quantum confinement for the emission energy in the blue visible range.

CHAPTER 7 CONCLUSION

Two types of novel materials, nanostructure, have been fabricated in this study. They include porous silicon and nanoclusters embedded in SiO_2. Using the anodisation technique, visibly emitting porous silicon with emitting peaks from red (690 nm), orange (630 nm), yellow (600 nm) to green (530 nm), were fabricated. This range of emission covers all of the energy range achieved by different research groups by the technique of anodisation only. The full set of porous silicon samples gave the possibility of quantitatively knowing the reason why the emitting energy in Si can vary from far-infrared to that of red and even green, i.e. the mechanism of visible emission or strong blue shift and how the visible emission response depends on nanoshape, dimensionality and nanosize. This necessitated the carrying out of a series of carefully designed and operated experments. As mentioned in Chapter 1, there are many mechanisms that have been proposed to understand the strong blue shift. Porous silicon is such a large scale microsystem: the aim was that this study would make clear the mechanism of visible emission from porous silicon, especially for freshly produced porous silicon.

The nanoclustered films (also called semiconductor doped SiO_2) were fabricated by rf-sputtering. In the fabrication process, different sputtering conditions have been tried to produce the best emission including the highest energy in the blue and the highest luminescence intensity. The conditions include s variety of sputtering pressures, rf-powers, and most importantly mixed targets. As the mixed target was a combination of

both SiO_2 base target and small pieces of semiconductor (silicon, germanium, or carbon) which were laid on the base target, the pieces of semiconductor were the key to the higher energy emission. Consequently, experiments were carried out by sputtering films using different pieces of semiconductor targets. Further treatment to the as-deposited films was needed to transform the phase of existing dots. The films were annealed in nitrogen for 20 or 30 min at 600 or 800°C.

In characterization of the two kinds of materials, a number of experiments have been carried out: photoluminescence (PL), photoluminescence excitation dependence (PLE), transmission electron microscopy (TEM), extended x-ray absorption fine structure (EXAFS) and near edge x-ray absorption fine structure (NEXAFS) of silicon, carbon and oxygen K-edges.

From these characterisations, many properties about the two types of nanostructures have been discovered. They include the properties of optical emission, optical band gap, local ordering of the nanostructures, coordination numbers of the nanomaterials, and mean size and size distribution.

7.1. Porous Silicon

In characterizing porous Si, EXAFS experiments played an important part. The careful fitting of the Fourier transformed EXAFS data for the PL samples provided coordination numbers with very small theoretical fitting error. However, the EXAFS theoretical fitting only gives the local structure information in terms of coordination numbers of bonding states for the study here. Therefore, theoretical modeling work was needed and has been proposed to compare the coordination numbers with possible nanostructure types. Together with cited LCAO theoretical calculation, experimental coordination numbers, and both emitted peak energies and possible optical band-gaps, this model gives us a complete picture of image about the red, yellow and green porous Si, as described in the following:

Although more than one mechanism is likely to be involved in the luminescence of PS, EXAFS and theoretical fits show a relatively simple picture for freshly produced PS with PL peaks from 690 nm to 520 nm, which is nearly the full range we can obtain using only anodization processes. (1) The nanocores of the PS are crystalline and quantum confinement is the only mechanism widening the bandgap at this stage. Obviously disorder from degraded PS by x-ray and long time native oxidisation has been observed in our other studies. (2) A nanowire network (one-plus a fraction dimensionality) for red and yellow PS, and nanowire (one dimensional or less) for green PS, are suggested. The mean core sizes are 2.2, 1.9 and 1.3 nm respectively for red, yellow and green PS. This

nanostructure shape of quantum wire is much more positive for PS applications in EL than are quantum dots. (3) The fractional dimension could be one of the causes of the slow band and lifetime variety in this band, as the fraction dimension can let carriers act more indirectly.

7.2 More Information from The Nanowire Model for Porous Si

A range of Si wafer resistance from 1 to 30 Ωcm have been used to try and make green and yellow emitting PS by the same process described in this work. The general result is that it is very difficult to produce green PS from higher resistance wafer. It leads to the conclusion that the starting distance between nanopores plays an important part in producing differently emitting PS. The resistance would be one of the key factors controlling the distance : it is suggested that the distance between pores are much longer in higher resistance material when the same processes are used as described in this work and the resulting PS has thicker wires (and bigger dots as reported by Schuppler, et al., (1994), when the wires were etched until they formed separate 'dots') and only emits red and orange PL. Since the same radiative colour is obtained both from a nanowire network (suggested in this work for red PS) and nanodots in the report by Schuppler, et al. (1994) which give rise to similar PL, the different nanostructures may well depend on wafer resistance or starting distance between pores. However, the wire shape is more common than the dot shape, as about 60% of published data on the resistance of Si wafers used for

PS fall in the 1 to 10 Ω cm range, instead of a few % ≥ 50 Ω cm. Also the average wire shape is more suitable for EL applications, demanding lower voltage and higher current, and delivering higher EL efficiency.

The wall between the cores of the nanowire network could allow more indirect carrier-transition behaviour with longer lifetimes as in bulk Si, and more direct behaviour with shorter or even much shorter lifetime within bare wire or dots respectively. For PS with red, orange or yellow emitting peaks, a size distribution (related to the broad PL spectrum) implies a distribution of dimensionality or a fraction dimension. This fraction therefore would lead to a lifetime increasing with increasing PL wavelength, that is the wavelength is fraction-dimension-related. This behaviour has been found present in the so-called slow PL band which is related to an emitting energy about ≤ 2 eV, and where the lifetime continuously increases from 60 to 220μs with increase in PL wavelength from 620 nm to 800 nm (Tessler, et al., 1993, Takazawa, et al., 1994, Kovalev, et al., 1994 and Pavesi, et al., 1993). After the as-anodised PS is oxidised by dry-oxidisation at 800°C, this lifetime dependence on wavelength decreases to about 60 - 80μs in the same energy range (Takazawa, et al., 1993). This can not be explained by the tunneling model alone (Takazawa, et al., 1993), but can be explained by the fraction dimension : most of the fraction dimension in the distribution has been consumed by further oxidisation, so the indirect behaviour is reduced to that of bare nanowire because the carriers only have one-dimensional mobility.

7.3 Nanoclusters

7.3.1 Blue shift and cluster-related materials

On the other hand, the understanding about the blue emission from clustered films is more simple, once the mean size and their size distribution have been obtained. Comparing the mean size or size distribution with the peaks of the photoluminescence, it can clearly be concluded that the strong blue shift was due to quantum confinement. In this study, the mean size were 2.4 or 2.5 nm for silicon clusters or carbon clusters, while the emission peaks were at from 420 nm to 495 nm in the blue range of visible.

Thus this work has concentrated on the identifying of the materials which make up of the nanodots. Firstly, the identification of silicon clusters was more simple, as there was only one possible element - Si - which could make up the clusters in the sputtered films - Si. The relevant Si K-edge XAFS (both EXAFS and NEXAFS) of as-deposited and annealed samples suggested the nanocluster formation and transformation to crystalline core from amorphous phase. The TEM suggested the similar results. Secondly, the identification of the carbon clusters was more complicated, as there were two elements which could be involved in the composition of the clusters. So, a broad energy range of the silicon, carbon and oxygen K-edge XAFS was needed to work out which constituents. (i) Si K-edge XAFS for the samples different annealing treatments ruled out the possibility of Si related nanoclusters, when compared with the photoluminescence intensities and emission

peaks; (ii) oxygen K-edge XAFS showed that the strong PL was related with the higher O absorption, or shown suggested that the oxygen atoms were drawn out of the nanoclusters; (iii) the presence of π bonds compared with that in the as-deposited films indicates that graphite-like carbon clusters have formed from oxygen rich-carbon clusters : the strong σ bond absorption observed above 290 eV could be a result of C-O bonding, and furthermore only the annealed clustered films give off strong luminescence.

It can be concluded that both the Si and C clusters are likely to have a crystalline core, either tetrahedral Si or graphitic C, however there is evidence for some disorder and the size and role of the interface regions are not known. Our data agree with the widely-held quantum confinement mechanism for nanosized-semiconductor emission.

The most important property about the clustered films is the higher emitting energy - in the bluev range. In Chapter 1, the reported studies on Si, Ge and C clustered films have been given a full review. Nanoclusters embedded in SiO_2 fabricated by rf-sputtering by others have only given rise to efficient PL color from red to green (from 800 nm to 510 nm) while the mean sizes were from 10 to 3 nm. The clusters work presented here fulfilled the full visible range of emission at higher energies.

7.3.2 Answers for other mechanisms

It has been proposed that the blue emission could come from defect levels within the bandgap of SiO_2 (Kontkiewicz, et.al., 1994). Our work does not support this, as no PL has been found from as-sputtered films even though sputtered SiO_2 would be expected to have many defect states within the bandgap. In other words, the PL from the defects within the SiO_2 bandgap in unannealed material is not detectable with the system used when excited by power densities of μWcm^{-2}. We find that strong PL is only observed when clusters are found by TEM, that is after annealing. It was confirmed that there was a direct dependence of PL intensities on the densities of Si clusters in annealed films. The PL expected from the defects in the SiO_2 bandgap did not give an obvious contribution.

As we know diamond-like carbon also has a large band-gap without any size effect, one would ask that if there is a possibility that the blue emission comes from diamond-like carbon? The near edge absorption fine structure of C XAFS from the annealed sample, which is graphite-like rather than diamond-like, has answered this question.

The origin of the unstable UV emission is not clear at this stage. The micrographs from TEM show that there are dark regions with sizes around 1 nm in diameter. It is suggested that Si-related clusters existing in the films with a size around 1 nm could be a possible species responsible for this PL. Their existence could be a result of some oxygen atoms

reacting with C atoms leaving the matrices Si rich. This is in agreement with the Si-Si bond absorptions observed in Si K-edge EXAFS. Due to the strong stress between Si-Si and SiO_2, the crystalline Si-Si bonds could relax or distort to an amorphous phase or more Si-O bonds could be involved in the ultra-small clusters, which finally would lose their radiative transition function. However, the resolution of the TEM employed in this work is not high enough to estimate the density and size distribution for cluster sizes around and smaller than 1 nm. Further studies on these systems are planned which will include high resolution TEM to help clarify this.

REFERENCES

Alivisatos, A.P., MRS Bulleting, August, 23(1995).

Bayliss, S.C., and S. J. Gurman, S.J., J. Non-Cryst. Sol. **127,** 174(1991).

Bayliss, S.C., Hutt, D.A., Anstee, P., Zhang, Q. , Danson, N., Bates, J., and Waddilove, A., J. Appl. Phys. 76, 9 (1994).

Bayliss, S.C., Hutt, D.A., Zhang, Q., Danson, N., and Smith, A., Sol. Stat. Commu. 91, 371 (1994).

Beale, M.I., Benjamin, J.D., Uren, M.J., Chew, N.G., and Cullis, J. Cryst. Growth. 73, 622(1985).

Behrensmeier, R., Namavar. F., Amisola, G.B., Otter, F.A., and Galigan, J.M., Appl. Phys. Lett. **62,** 2408 (1993).

Berbezier, I., and A. Halimaoui, A., J. Appl. Phys. **74,** 5421 (1993).

Binsted, et al., Biochemistry 31, 12117(1992).

Binsted, N., S.J. Gurman, S.J., and J.W. Campbell, J.W., SERC Daresbury Lab. EXCUV92 (1992).

Bomchil, G.,, Halimaoui, A., and Herino, R., Microelectron. Eng. 8, 293(1988).

Brandt, M.S., Fuchs, H.D., Stutzman, M., Weger, J., and Cardona, M., Solid State Comm. 81, 307(1992).

Brandt, M.S., H.D. Fuchs, A. Hopner, M.Rosenbauer, M. Stutzmann, J. Weber, M. Bransden, B.H., and Joachain, C.J., Physics of Atoms and Molecules, Longman, London (1983).

Bunker, G., Nucl. Instrum. Methods. 207, 437(1983).

Buuren, T.V., Gao, Tiedje, T., Dahn, J.R., and Way, B.M., Appl. Phys. Lett. **60**, 3013 (1992).

Canham, L.T., Appl. Phys. Lett. **57**, 1046 (1990).

Canham, L., New Scientist, 10 April 1993, p.23.

Cardona and H.J. Queisser, MRS Symposia Proceedings No. 262 (Materials Research Society, Pittsburgh, 1993), p. 179.

Catlow, C.R.A., and Greaves, G.N., Applecations of Synchrotron Radiation, Chapman and Hall, New York (1990).

Collins, R.T., and Tishcler, M.A., IEEE, Circuits & Devices, Sep. 22 (1993).

Costa, J., Roura, P., Sardin, G., Morante, J.R., and Bertran, E., Appl. Phys. Lett. 64, 463(1994).

Dean, P. J., Haynes, J.R., and Flood, W.F., Phys. Rev. 161, 711(1967).

Delerue, C., and Allan, Appl. Phys. Lett. 61, 1948(1992).

Delerue, C., Lannoo, M., and Allan, G., J. Luminescence 57, 249(1993).

Delerue, C., Allan, G., and Lannoo, M., Phys. Rev. B (1994).

Dimaria, D.J., Kirtley, J.R., Parkulis, E.J., Dong, D.W., Kuan, T.S., Pesavento, F.L., Theis, T.N., and Cutro, J.A., J. Appl. Phys. **56**, 401(1984).

Dubbelday, W.B., et al., Appl. Phys. Lett. 64, 1694(1993).

Earwaker, L.G., Far, J.P.G., Grzesczyk, P.E., Sturland, I., and Keen, J.M., Nucl. Instrum. Metods Phys. Res. B 9,317(1985).

Eroil, A., Cargill, G.S., RFrahm, R., and Boehme, R.F., Phys. Rev. B **37**, 2450 (1988).

Fishman, G., Mihalcescu. I., and Romestain, R., Phys. Rev. B 48, 1464(1993).

Fuchs, H.D., Stutzmann, M., Brandt, M.S., Rosenbauer, M., Weber, J., and Cardona, M., Physica Scripta. **T45**, 309(1992).

Fuchs, H.D., et al., Phys. Rev. B 48, 8172(1993).

Furukawa, S., and Miyasato, T., Phys. Rev. B 38, 5726(1988).

Gregg,S.J., and Sing, K.S.W., Adoorption, Surface Area and Porosity (Academic, New York, 1982).

Grosman, A., Otrtega, C., Siejka, J., and Chamarro, M., J. Appl. Phys. 74, 1992(1993).

Gurman, S.J., J. Phys. C 16, 2987(1983).

Gurman, S.J., J. Synchrotron Rad. 2, 56(1995).

Gurman, S.J., Binsted, N., and Ross, I., J. Phys. C 19,1845(1984).

Hanamura, E., Phys. Rev. B 38, 1288(1988).

Haug, H, Opticla Nonlinearrties and Instabilities in Semiconductors, Acdemic Press, Inc., 1988, P.237.

Hayashi, S., Kataoka, S.M. and Yamamoto, K., Jpn. J. Appl. Phys. **32**, l274(1993).

Hou, X.Y., Shi, G., Wang, W., Zhang, F.L., Hao, P.H., Huang, D.M., and Wang, X., Appl. Phys. Lett. **62**, 1097(1993).

Hybertsen, M.S., Needels, M., Phys. Rev. B, 48, 4608(1993).

Ito, T., Ohta, T., and Hiraki, A., Jpn. J. Appl. Phys. **31**, L1(1992).

John, G.C., and Singh, V.A., Phys. Rev. B 50, 5329(1994).

Joyer, R.W., Martin, K.J., and P. Meehan, P., J. Phys. **C20**, 4005 (1987).

Kanemitsu, Y., Uto, H., Masumoto, Y., Matsumoto, T., Futagi, T., and Mimura, H., Kawaguchi, T., and Miyazima, S., Jpn. J. Appl. Phys. 32, L215(1992).

Kanemitsu, Y., Uto, H., Masumoto, Y. and Maeda, Y., Appl. Phys. Lett. **61**, 2187(1992).

Kanemitsu, Y, Ogawa, T., Shiraishi, K., Takeda, K., Phys. Rev. B, 4883(1993).

Kayanuma, Y., Phys. Rev. 38, 9772(1988).

Koch, V.P., Fischer, T., Shcheglov, K., Brandt, M.S., and Koch. F., Proceeding Volume of 1st International Symposium of Advanced Luminescent Materials, 188th Meeting of The USA Electrochemical Society, Inc. Chicago, USA, October 8-13, 1995.

Koch, V.P., Fischer, T., Shcheglov, K., Brandt, M.S., and Koch. F., Phys. Rev. **B 48**, 2827 (1993).

Koch, F., Koch, V.P., and Muschik, T., J. Luminescence **57**, 271 (1993).

Kontkiewicz, A. j., et.al., Appl. Phys. Lett. **65**, 1436(1994).

Kovalev, D. I., Yaroshetzkii, I. D., Muschik, T., Petrova-Koch, V., and Koch, F., Appl. Phys. Lett. **64**, 214 (1994).

Kronig, R. de L., Z. Phys. 70, 317 (1931).

Kronig, R. de L., Z. Phys. 75, 190(1932).

Lavine, J.M., Sawan, S.P., Shieh, Y.T., and Bellezza, A.J., Appl. Phys. Lett. **62,** 1099 (1993).

Lee, H.J., et al., J. Appl. Phys. 75, 8086(1994).

Lee, P.A., and ~~Bein~~ Beni, G., Phys. Rev. B 15, 2862(1977).

Lehmann, V., and Gösele, U., Appl. Phys. Lett. **58**, 856 (1991).

Loni, A., Simons, A.J., Calcott, P.D., and Canham, L.T., J. Appl. Phys. 77, 3557(1995).

Lyer, S.S., and Xie, Y.H., Science 260, 2 April, 40 (1993).

Maeda, Y., Tsukamot, T., Yazawa, Y., Kanemitsu, Y., and Masumoto, Y., Appl. Phys. Lett. **59**, 3168(1991).

Maeda, Y., Phys. Rev. B **51**, 1658(1995).

Meyer, B.K., Petrova-Koch, V., Muschik, T., Linke, H., Omling, P., and Lehmann, V., Appl. Phys. Lett. **63**, 1930 (1993).

Mimura, H., Futagi, T., Matsumoto, T., Nakamura, T., and Kanemitsu, Y., Jpn. J. Appl. Phys. **33**, 586 (1994).

Morisaki, H., Hashimoto, H., Ping, F.W., Nozawa, H., and Ono, H., J. Appl. Phys. **74**, 2977(1993).

Münder,H., et al., J of Luminescence 57, 5(1993).

Murayama, K., Miyazaki, S., and Hirose, M., Jpn. J. Appl. Phys. **31,** L1358(1992).

Mustre, D.L., et al., Phys. Rev. B 44, 4146(1991).

Nag, B.R., Theory of Electrical Transport in Semiconductors, Pergamon Press, 1972, Chapter 2.

Naudon, A., Goudeau, P., Halimaoui, A., Lambert, B., and Bomchil, G., Appl. Phys. Lett. **75**, 780 (1994).

Nassiopoulos, A.G., Grigoropoulos, S., Papadimitriou, D., and Gogolodes, E., Phys. Stat. Sol. (b) 190, 91(1995).

Nishida, A., et al., Jpn. J. Appl. Phys. 31, L1219(1992).

Pavesi, L., Ceschini, M., and Rossi, F., J. Luminescence **57**, 131 (1993).

Pickering, C., et al., J. Phys. C. 17, 6535(1984).

Prokes, S.M., Searson, P.C., and Macaulay, J.M., J. Electrochem. Soc.. 139, 3373(1992).

Proot, J. P., Delerue, C., and Allan, G., Appl. Phys. Lett., 61, 1948 (1992).

Rüter, D., Kunze, T., and Bauhofer, W., Appl. Phys. Lett. 64, 3006(1994).

Sanders, G.D., and Chang, Y.C., Phys. Rev. B 45, 9202(1992).

Sayers, D.E., Stern, E.A., and Lytle, F.W., Phys. Rev. Lett. 27, 1204(1971).

Schedel-Niedrig, T., et.al., BESSY- Jahresberidht, 196(1993).

Schuppler, S., Friedman, S.L., Marcus, M.A., Adler, D.L., Xie, Y.H., Ross, F.M., Harris, T.D., Brown, W.L., Chabal, Y.J., Brus, L.E., and Citrin, P.H., Phys. Rev. Lett. **72**, 2648 (1994).

Snow, E.S., and Campbell. P.M., Appl. Phys. Lett. 64, 1932(1994).

Sham, T.K., et al., Nature 363, 331(1993).

Steckl, A.J., Xu, J., and Mogul, H.C., J. Electrochem Soc. 141, 674(1994).

Steigerwald, M.L., Alivisatos, A.P., et al., Am. Chem. Soc. 110, 3046(1988).

Stern, E.A., Phys. Rev. B 10, 3027(1974).

Tahagahara, T., and K. Takeda, K., Phys. Rev. B **46**, 15578(1992).

Takazawa. A., T. Tamura, T., and M. Yamada, M., J. Appl. Phys. **75**, 2489 (1994).

Takazawa, A., Tamura, T., and Yamada, M., Appl. Phys. Lett. **63**, 940 (1993).

Tessler, L.R., Alvarez, F. and Teschke, O., Appl. Phys. Lett. **62**, 2381 (1993).

Teschke, O., et al., Appl. Phys. Lett. 63, 1927(1993).

Tsutomu, S. L., Nakao, S., and Saitoh, K., Appl. Phys. Lett. 65, 1814(1994).

Tsybeskov, L., Vandyshev, J.V., and Fauchet, P.M., Phys. Rev. B 49, 7821(1994).

Tyson, T.A., et al., Phys. Rev. B 46, 5997(1992).

Uchida, Y., Koshida, N., Koyada, H., and Yamamoto, Y., Appl. Phys. Lett. **63**, 961 (1993).

Uhlir, A., Bell System Tech. J. 35, 333(1956).

Vial, J.C., Bsiesy, A., Gaspard, F., Herino, R., Legeon, M., Muller, F., Romestain, R., and Macfarlane, R.M., Phys. Rev. **B 45**, 14171 (1992).

Wagner, J., Phys. Rev. B 29, 2002(1984).

Wagner, J., Phys. Rev. B 32, 1323(1985).

Wolford, D.J., Reimer, J.A., and Scott, B.A., Appl. Phys. Lett. 42, 369(1993).

Xia, J.B., and Chang, Y.C., Phys. Rev. B 48, 5179(1993).

Zhang, D., Kolbas, R.M., et al. Appl. Phys.Lett. 65, 2684(1994).

Zhao, X. W., Schenfeld, O., Kusano, J., Aoyagi, Y., and Sugano, T., Phys. Rev. B 50, 18654(1994), Appl. Phys. Lett. 65, 1290(1994).

APPENDIX A To be published in Solid State Comm. 1996

THE STABLE BLUE AND UNSTABLE UV PHOTOLUMINESCENCE FROM CARBON NANOCLUSTERS EMBEDDED IN SIO_2 MATRICES

Qi Zhang, S. C. Bayliss and W. Frentrup*

Department of Applied Physics, School of Applied Sciences, De Montfort University, Leicester. LE1 9BH. UK.

*Humboldt-Universität Zu Berlin, Institut Für Physik, Invalidenstr, 110, 10115 Berlin, Germany.

(Received)

Strong and stable blue photoluminescence (PL) from annealed C clusters embedded in SiO_2 (deposited by rf-sputtering) was recorded, under excitation power on a scale of μWcm^{-2}. UV PL was also recorded from about half of the annealed samples, but this was not stable - the intensity decayed with time. Carbon and oxygen K-edge XAFS (x-ray absorption fine structure) suggest that 1) the nanoclusters present are C-based materials, 2) the luminescent materials probably involves π bonded carbon. The size distributions of the nanoclusters obtained by TEM suggest that a quantum-confined size effect can also apply to the blue PL.

Keywords: A. nanostructures, C. EXAFS, NEXAFS, C. TEM, E. luminescence

Introduction

In previous reports[1-6], intense visible photoluminescence (PL) from red to green has been observed from annealed Si, Ge or C nanoclusters or nanocrystallites (three-dimensionally-confined quantum dots) embedded in SiO_2 matrices. Weak UV and blue PL was detected from as-deposited samples[6]. The strong blue-shift in the PL has been explained in terms of a quantum size effect causing an expanded bandgap. Our previous work showed strong PL in the visible blue/blue green range (peaks from 420 nm to 490 nm) from both Si and C annealed clusters embedded in SiO_2[7-9]. Si K edge XAFS (x-ray absorption fine structure) and TEM measurements of the Si/SiO_2 films have suggested that the species related to visible emission from Si clustered films are Si nanoclusters, of sizes from 1.5 to 4.5 nm. In this report, we present a study of both stable blue and unstable UV emission from annealed C clusters embedded in SiO_2. Carbon K- edge XAFS and Fourier transformed oxygen K-edge EXAFS were analysed to understand more about the emission-related species and the local structure. Again, the origin of the blue shift is discussed in terms of the mean cluster size and its distribution.

Experimental

The C/SiO_2 films (thickness >1 μm) were deposited on Si wafers by rf co-sputtering in Ar. On the pure SiO_2

20 cm target, between 5 and 16 pieces of pure graphite rod of 6 mm diameter were placed in an area of ~10 cm in diameter to make the mixed targets. The deposition conditions were: 6×10^{-4} - 1×10^{-2} mbar Ar, 500 - 1250W rf power. The samples were subsequently annealed at 600°C and 800°C for 20 min in a N_2 atmosphere flowing at a rate of 3 *l* min^{-1}. The PL measurements and Si K-edge XAFS (in total yield mode) were performed at DRAL Daresbury Laboratory using stations 12.1 and 3.4, respectively. C and O K-edge XAFS were obtained in fluorescence mode on the HE - PGM2 station at the BESSY Laboratory. The XAFS data from the clustered films do not contain any contribution from the Si substrate as the film thickness is much greater than the XAFS sampling depth. For PL the tuneable UV source provided excitation at 260 nm, 300 nm and 370 nm, using a bandwidth of 10 nm and a power of 3 - 38 μWcm^{-2} on the samples. For all of the samples, PL was only observed from annealed films. The PL data has been normalised to take into account the spectral sensitivity of the system and variations due to beam decay. Cluster size distributions were obtained from TEM real-space images from the edges of tilted samples using a Jeol JEM 100CX.

Results and discussion

Although many samples have been made in very different conditions, data from three samples are shown here. Typical PL from C/SiO_2 is shown in Figures 1(a)

and (b) for blue emitting samples, and in (c) for samples emitting in both the blue and UV. The depositing conditions are (a) 8×10^{-3} mbar, 1200 W rf power, 30 min; (b) 6×10^{-3} mbar, 800 W rf power, 40 min; (c) 6×10^{-3} mbar, 1200 W rf power, 30 min, for sample 1, 2 and 3 in Figure 1, respectively. The respective excitation wavelengths are given. The most efficient PL is always from films annealed at 800°C, the PL being visible to the naked eye when excited by the lower power densities used in this work. Much weaker PL was detected from films annealed at 600°C. There was no emission detected in the range from 340 - 800 nm for as-deposited samples. Weak but detectable PL has been recorded by Maeda[6], et. al. from as-deposited Ge/SiO_2 systems, using laser excitation powers in the $mWcm^{-2}$ range. Thus we believe that the undetectable PL of as-sputtered samples was due partly to the very low power of the tuneable light source (in the range of 3-38 μWcm^{-2} on the samples) and partly to the existence of only a few clusters which have the correct size and form suitable radiative transition centres in the films before being annealed. As shown in (c), both UV and blue PL could be recorded from the same sample when it was measured a few hours after annealing. However two days after the first measurement the UV emission had disappeared and only blue emission remained. About half of the carbon clustered films made exhibit this characteristic of unstable UV PL, although the UV PL intensities varied greatly compared with those of

the blue peaks. The blue emission remained almost constant over a period of 6 months. In general the blue PL spectra of all our samples consisted of one or two strong peaks which varied in intensity and peak wavelength with deposition conditions.

As there are many Si (from SiO_2) and C atoms in the films, it is necessary to identify what kind of chemical environment gives rise to the observed PL. C, O and Si K-edge XAFS have been employed to determine more information about the materials showing visible emission. A clear decrease of Si-Si bond absorption for 800°C annealed films has been observed from Si NEXAFS[10], when compared with that from 600°C annealed films. The PL intensity however increases for such samples, as discussed above. Thus we can rule out the possibility that Si-Si bonding is required for the observed blue emission. On the other hand, C K edge absorption has given a direct relationship between increase in intensity of PL and increase in density of C-C bonds, as shown in Figure 2.

Because of the smaller quantities of carbon atoms/clusters compared to those of Si and O atoms in the films, and a lower intensity of synchrotron radiation transmitted through the monochromator, as well as the larger energy step chosen for the scans, the NEXAFS of the C K-edge is fairly noisy. However, the near edge absorption still presents certain important information about carbon bonding states in the clustered films. The

clear increase of the absorption peak below 290 eV in the annealed films, indicative of the presence of π bonds, compared with that in the as-deposited films indicates that graphitic carbon clusters have formed from oxygen rich-carbon clusters : the strong σ bond absorption observed above 290 eV could be a result of C-O bonding[11], and furthermore only the annealed clustered films give off strong luminescence. This discussion agrees with the implications from the Fourier transformed O K-edge EXAFS of the carbon clustered films, Figure 3. Both the first shells of Si-O and O-Si-O from annealed samples are stronger than those from as-deposited samples. One possible explanation is that a considerable number of oxygen atoms re-bond with Si after annealing from various O-C bonding states in the as-deposited materials.

Having determined the material species involved in the clusters, we can discuss the origin of the stable blue emission. It has been proposed that the blue emission could come from defect levels within the bandgap of SiO_2[12]. Our work does not support this, as no PL has been found from as-sputtered films even though sputtered SiO_2 would be expected to have many defect states within the bandgap. In other words, the PL from the defects within the SiO_2 bandgap in unannealed material is not detectable with the system used when excited by power densities of μWcm^{-2}. We find that strong PL is only observed when clusters are found by TEM, that is after annealing, as reported in our previous work[7]. In that

work it was confirmed that there was a direct dependence of PL intensities on the densities of Si clusters in annealed films._The PL expected from the defects in the SiO_2 bandgap did not give an obvious contribution. Furthermore, the SiO_2 network is not expected to change much on annealing. It is known that after annealing programmes at 1100°C the oxide still exists as a random network. Therefore, the effect of disorder-quenching of PL, due to defect sites in the as-sputtered specimens, will not change much on annealing. The size distributions of the blue-emitting C clusters observed by TEM are shown in Figure 4. As expected, based on a quantum confinement model for blue emission, the cluster size is very small and there are no clusters of size >4.5 nm. The clusters would have crystalline graphite-like structure, as suggested by the bonding states assigned to the C XAFS of the annealed films. These data give on indication of the role of large band-gap diamond-like carbon materials which remain the other possibility for the size effect. The electronic structure, including the Fermi level, of nano-sized graphite would be shifted from that of the bulk under quantum confinement, resulting in the appearance of a large band-gap. According to the theoretical calculation of the electronic structure of silicon nanocrystallites by an effective-mass approximation[13] and from quantum confinement[14], nanoclusters ~2.5 nm in diameter are expected to have a bandgap of 2.25-3 eV. The PL peak energies of clustered films in this work, from ~ 2.5 eV (495 nm) to ~ 2.95 eV (420 nm), fall in this region.

The origin of the unstable UV emission is not clear at this stage. The micrographs from TEM show that there are dark regions with sizes around 1 nm in diameter. It is suggested that Si-related clusters existing in the films with a size around 1 nm could be a possible species responsible for this PL. Their existence could be a result of some oxygen atoms reacting with C atoms leaving the matrices Si rich. This is in agreement with the Si-Si bond absorptions observed in Si K-edge EXAFS. Due to the strong stress between Si-Si and SiO_2, the crystalline Si-Si bonds could relax or distort to an amorphous phase or more Si-O bonds could be involved in the ultra-small clusters, which finally would lose their radiative transition function. However, the resolution of the TEM employed in this work is not high enough to estimate the density and size distribution for cluster sizes around and smaller than 1 nm. Further studies on these systems are planned which will include high resolution TEM to help clarify this.

Summary

We have presented a study of the stable blue and unstable UV photoluminescence observed from N_2-annealed C nanoclusters embedded in SiO_2 matrices. The size distributions of the clusters suggest that the quantum size effect can apply to blue emission. The local structure of the clusters, in particular the π-bonded carbon, and

crystallisation is important for efficient emission. These higher energy emissions do not directly involve the SiO_2 band transition, as there is no PL observed from as-sputtered films under albeit low (3-38 μWcm^{-2}) excitation power densities.

We acknowledge the EPSRC, BESSY (EU-HCM) and CCLRC Daresbury Laboratory for financial support, and Dr. J. Bates for assistance.

[1] D. J. Dimaria, J. R. Kirtley, E. J. Parkulis, D. W. Dong, T. S. Kuan, F. L. Pesavento, T. N. Theis and J. A. Cutro, J. Appl. Phys. **56**, 401(1984).

[2] T. Ito, T. Ohta and A. Hiraki, Jpn. J. Appl. Phys. **31**, L1(1992).

[3] S. Hayashi, M. Kataoka and K. Yamamoto, Jpn. J. Appl. Phys. **32**, l274(1993).

[4] Y. Maeda, N. Tsukamot, Y. Yazawa, Y. Kanemitsu and Y. Masumoto, Appl. Phys. Lett. **59**, 3168(1991).

[5] Y. Kanemitsu, H. Uto, Y. Masumoto and Y. Maeda, Appl. Phys. Lett. **61**, 2187(1992).

[6] Y. Maeda, Phys. Rev. B **51**, 1658(1995).

[7] Q. Zhang, S. C. Bayliss, and D. A. Hutt, Appl. Phys. Lett. **66**, 1977(1995).

[8] Q. Zhang, S. C. Bayliss, A. Al-Ajili, D. A. Hutt, Nucl. Instr. and Meth. in Phys. Res. B **97**, 329(1994).

[9] S.C. Bayliss, Q. Zhang and D.A. Hutt, Phys. Stat. Sol. B **190**, 85(1995).

[10] Q. Zhang, S.C. Bayliss, Chelsea Amorphous And Organic semiconductors Meeting, 1995 (London).

[11] T. Schedel-Niedrig, et.al., BESSY- Jahresberidht 196(1993).

[12] A.J. Kontkiewicz, et.al., Appl. Phys. Lett. **65**, 1436(1994).

[13] T. Tahagahara and K. Takeda, Phys. Rev. B **46**, 15578(1992).

[14] C. Delerue, M. Lannoo and G. Allan, J. of Luminescence **57**, 247(1993).

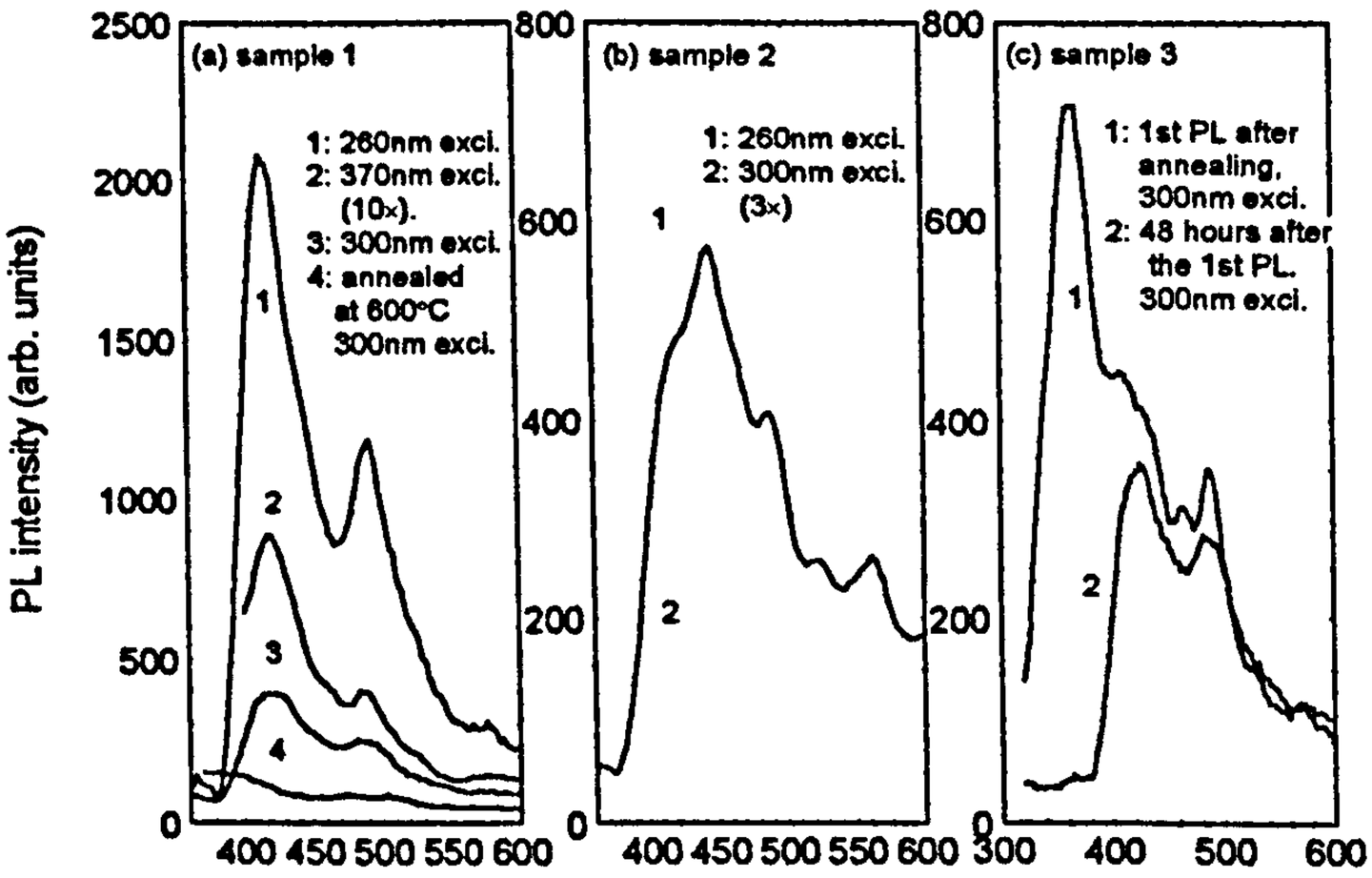

Figure 1. Photoluminescence from C clustered films showing (a) and (b): blue PL only; (c): both UV and blue PL. The films were annealed at 800°C, except where indicated. The excitation wavelengths are given.

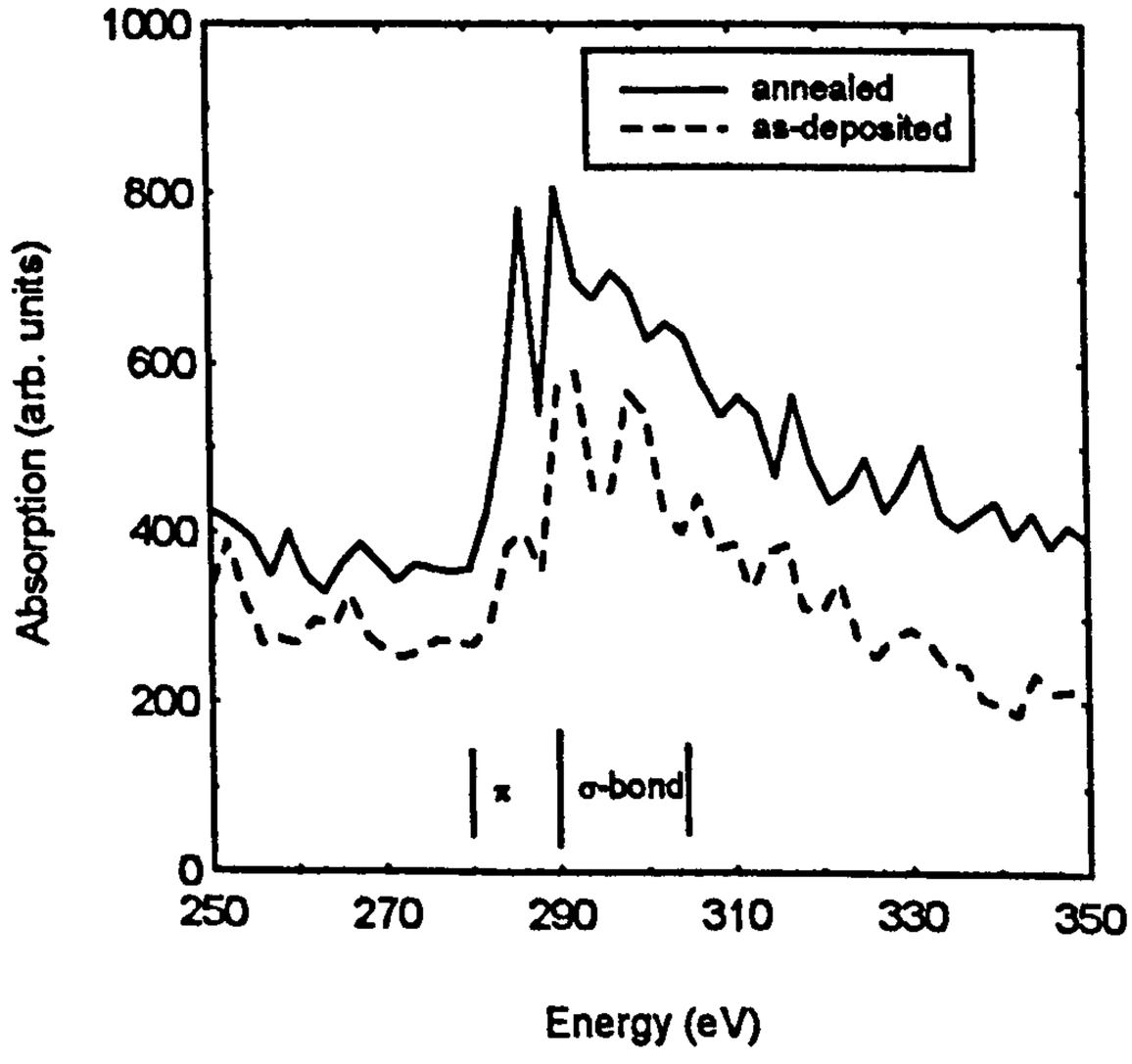

Figure 2. Near edge x-ray absorption of a group of C clustered films - as-deposited and annealed.

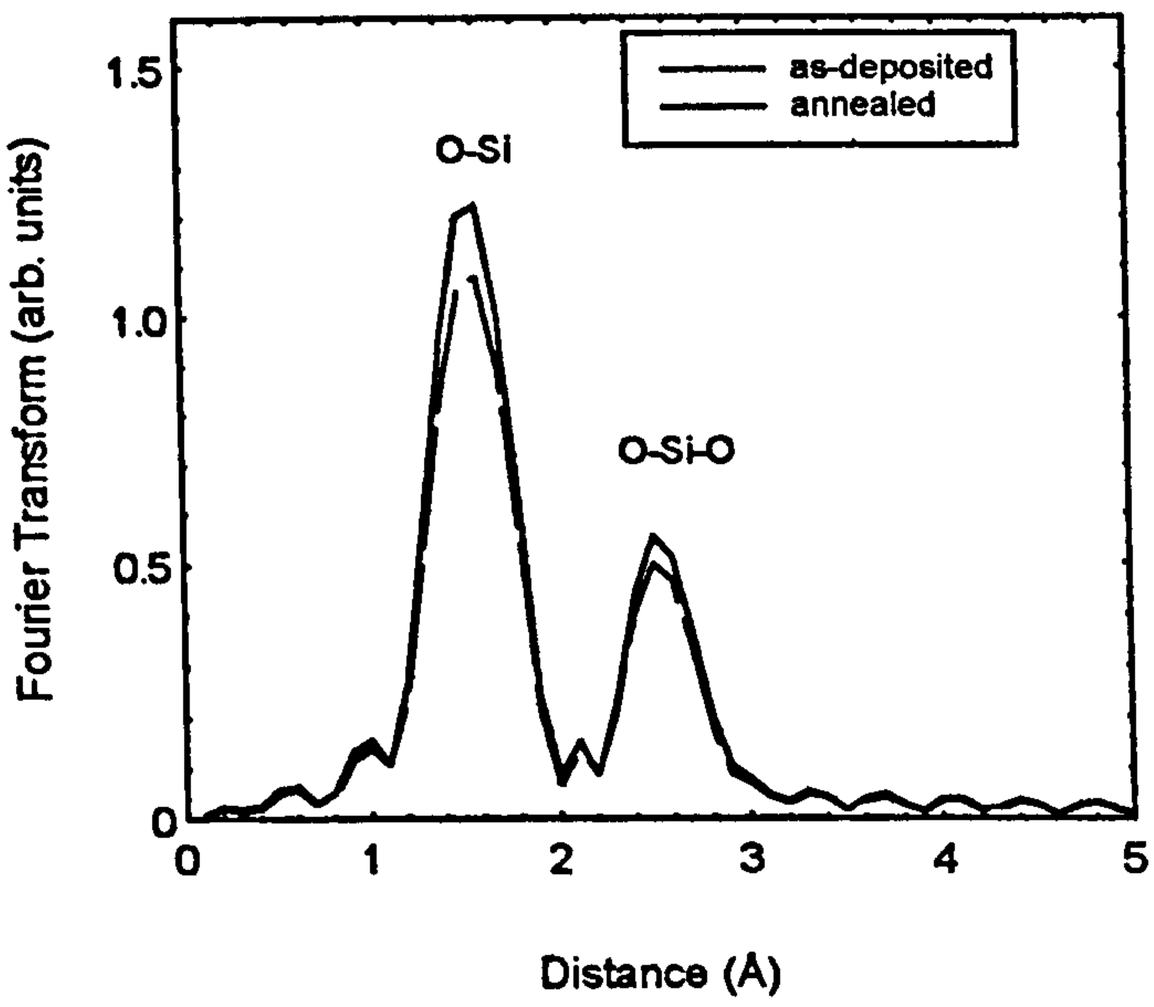

Figure 3. Fourier transforms of O K-edge EXAFS from as-deposited and annealed C cluster samples. For clarity only theoretical fits are given here.

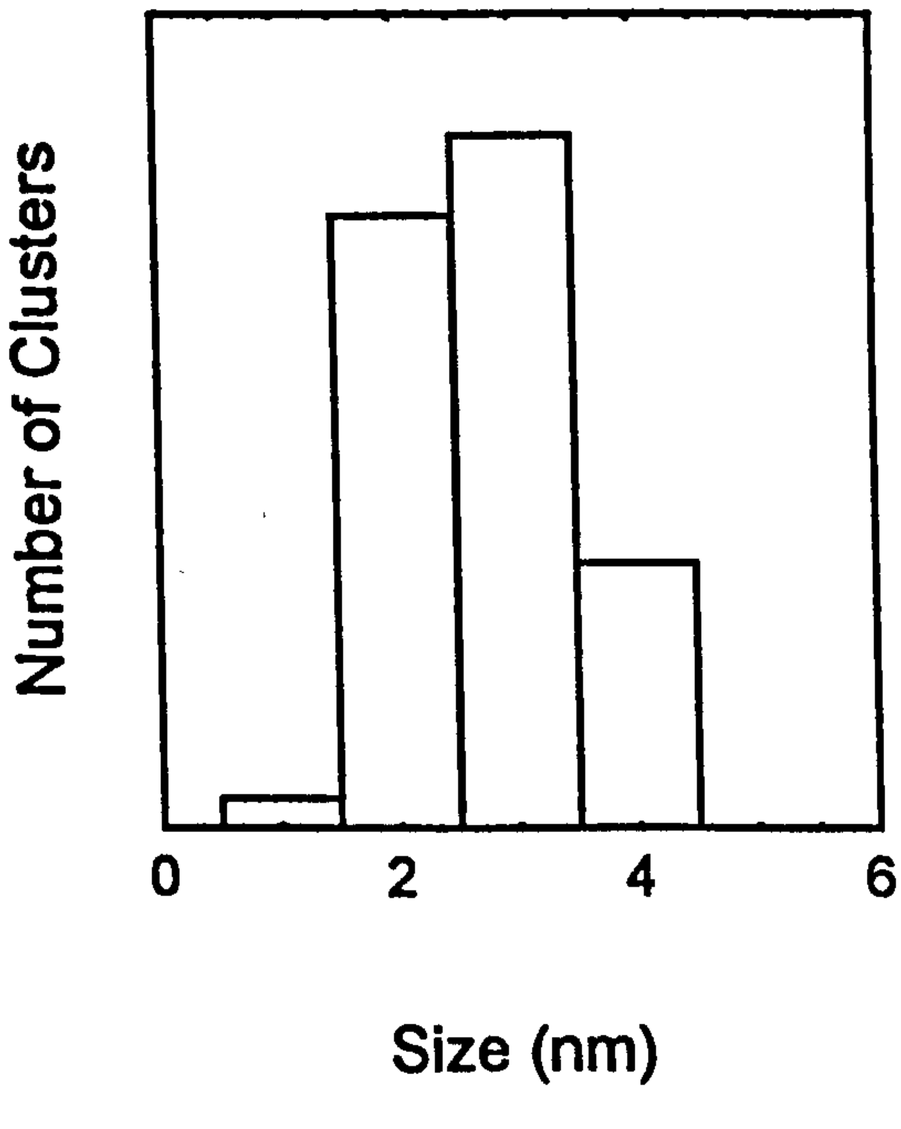

Figure 4. Size distribution of the blue PL-related carbon clusters in SiO_2 matrices.

The correlation of dimensionality with emitted wavelength and ordering of freshly produced porous silicon

Qi Zhang and S. C. Bayliss
Department of Applied Physics, School of Applied Science, De Montfort University, Leicester LE1 9BH, United Kingdom

(Received 23 June 1995; accepted for publication 16 October 1995)

Freshly produced red, yellow and green emitting porous Si specimens have been studied by NEXAFS and EXAFS (near edge and extended x-ray absorption fine structure). The emission peaks are at 690, 580, and 520 nm, which almost covers the full visible range that direct anodization can achieve. The correlation between the co-ordination numbers of the first, second and third Si neighbor shells from Fourier transform fitting of EXAFS and both emission peak energies and optical band gaps estimated by PLE (photoluminescence excitation dependence) suggests that the nanostructures of the PS are nanowires, rather than nanocrystalline. Two types of quantum nanowire with one and one-plus-a-fraction dimensionality are proposed to interpret the correlation. The order factors of the theoretical fits suggest the nanowires of the freshly produced PS have crystalline cores. © *1996 American Institute of Physics.* [S0021-8979(96)02403-1]

I. INTRODUCTION

It was suggested in the very first reports on porous silicon (PS)[1,2] that the strong blue shift of the photoluminescence (PL) was caused by a quantum size effect, mainly due to the presence of quantum wires. This strong blue shift results in the originally infrared band gap material emitting at room temperature over the entire visible region from red to blue.[3] Much research has supported the model of band gap widening by confinement, such as details of the PL,[4] soft x-ray absorption,[5] x-ray small-angle scattering,[6] conventional optical-absorption,[7] high resolution TEM,[8] extended x-ray absorption fine structure,[9,10] and our previous work on blue photoluminescence (PL) from ~2.5 nm Si clusters.[11,12] In addition other species could also cause the band gap widening depending on the sample preparation condition and post-preparation treatments, e.g., the existence of amorphous or disordered phases,[13–15] siloxene or similar complexes.[16]

Two models have been proposed to interpret the transition behavior based on the confinement effect: firstly the band-to-band transition model[1] and secondly the recombination-center-related transition model, involving surface states and disorder (tail) states.[15,17] Although it is not clear which transition type takes the major part in luminescence it is more likely to be via recombination centers.[15] Our recent study[18] on PL excitation dependence (PLE) agrees with the latter model.

Although the cores of PS are generally described as crystalline Si wires[1,2] or particles[19] and both of the individual nanostructures have been shown to exist by high resolution TEM, there remains a basic lack of knowledge regarding the ordering and the mean dimensionality and size dependence of these cores of freshly produced PS responsible for visible radiation from red to green (blue emission from PS can only be obtained by post-anodization treatments). The radiation occurs within a considerable sampling depth, typically hundreds of nm. The ordering of the cores of freshly produced PS can also help us to understand at what stage other mechanisms, rather than quantum confinement, start to take part in the band gap widening. This is mainly because (i) the size and shape of the PS framework is inhomogeneous, (ii) little structural information can be obtained by standard microscopy or diffraction techniques within the depth of the photo-exciting radiation, (iii) the average size of the cores from as-anodized PS is beyond practical detection limits. The technique of extended x-ray absorption fine structure (EXAFS) provides a useful way to estimate the mean dimensions and size, and even the ordering, on a scale of a few nanometers, within a reasonable effective sample depth (~2500 Å for 80% porosity Si[20]).

A previous report[10] on deducing core effective dimensionality and sizes by EXAFS, where only orange to deep red PS (PL peaks at ~640–840 nm) was measured, suggested a figure of three-dimensional confined nanodots with sizes from 1.5–8 nm in diameter, and two dimensional confined nanowires were ruled out. This conclusion of the structure of PS is quite negative to the applications of PS, such as in electroluminescence (EL), as lower carrier transportation between nanodots rather than nanowires would strongly affect the efficiency of EL. EL from PS however claim lower voltage and higher current. Moreover, this EXAFS study only dealt with a small visible range of emission color (from about 700 nm to 640 nm).

We present a study of PS nanostructure from a series of as-anodized PS emitting in the red, yellow and green (PL peaks at 690, 580, and 520 nm respectively). This almost covers all of the visible luminescence region that has so far been obtained from as-anodized material: blue luminescence is only observed after further processing such as rapid thermal oxidation (RTO) or boiling in water.[21] The resistance of the wafers used in this study was 1–3 Ω cm (about 40% reports quote use of 1–5 Ω cm wafers in both PL and EL research, whereas a few percent use >50 Ω cm as for example in Ref. 10). We emphasize the resistance here because it plays an important part in the PL peak energy of PS as well as the nanostructure: it is very difficult to make very efficient green PL from high resistance wafers by the processes used in this work. NEXAFS shows the near *K*-edge absorption of

 0021-8979/96/79(3)/1351/6/$6.00

Si-Si and Si-O bonds. From the fits to the Fourier transforms of the EXAFS data, combined with the widening of the band gap from both PL peak energy (suitable for the band-to-band model) and estimated optical band gap from PLE (suitable for the transition center model), the nanostructure shape has been deduced. The dependencies of structural dimensionality and sizes are predicted for differently emitting PS. The cause of the difference between nanowire and nanodot shapes of freshly produced PS is suggested to be related to wafer resistance.

II. EXPERIMENT

A. Sample preparation

Porous silicon was prepared by electrochemical anodization of (100) p-type, boron-doped, 1–3Ω cm Si wafers in a solution of HF(48%):H_2O:ethanol=1:1:2, resulting in PS film thicknesses of $>1\,\mu$m. The anodizing conditions for red, yellow and green samples are: (i) 8 min, current density 30 mA/cm^2, (ii) 20 min, 20 mA/cm^2, + 5 min without current, (iii) 20 min, 20 mA/cm^2, + 30 min without current, respectively. The wafers for yellow and green PL were coated on the back with aluminum and wax to produce a very uniform emission area. After rinsing in de-ionized water and blow-drying with N_2, the samples were put in a vacuum storage chamber and kept at 10^{-6} torr to keep them "fresh," as native oxidization would further oxidize the top layer and affect the mean nanostructure under study.

Further blue shifts can be made to the green PS, for example the PL peak can be at 510 nm by keeping the PS in the solution longer. However, this process affects the PL intensity strongly due to the great reduction of nanostructure quantity. Because detailed structural information is required here we chose to study 520 nm green PS.

B. PL and EXAFS

The PL and Si K-edge NEXAFS and EXAFS were carried out at DRAL Daresbury Laboratory of the National Synchrotron Source, beamlines 12.1 and 3.4 respectively. For EXAFS the x-rays were incident on the samples normally, and the absorption was measured as the current required to neutralize the samples as a result of photoelectron emission.[22,23] The EXAFS was determined by the total-yield technique, and taken around the Si K-edge at about 1840 eV. Scans were made from 1800 to 2500 eV (k range up to 15 Å^{-1}), with 742 independent points. The k range used in the Fourier transform fitting procedures described was 3–12.5 Å^{-1}, with ~600 independent points. For comparison EXAFS data were also taken from a c-Si wafer, a-Si and a-SiO_2 films, which were also used to calibrate the system. Both the optical and structural measurements were carried out at room temperature. The PL spectra have been normalized by the excitation intensities, and calibrated by the response efficiencies of the analyzing Minimate monochromator and detector system. All of the raw experimental data have been shifted by −0.5 eV, based on reference data from a bulk c-Si wafer, due to the error in monochromator calibration. There has not been any further shift applied to the data, to either near edge EXAFS or Fourier transformed data.

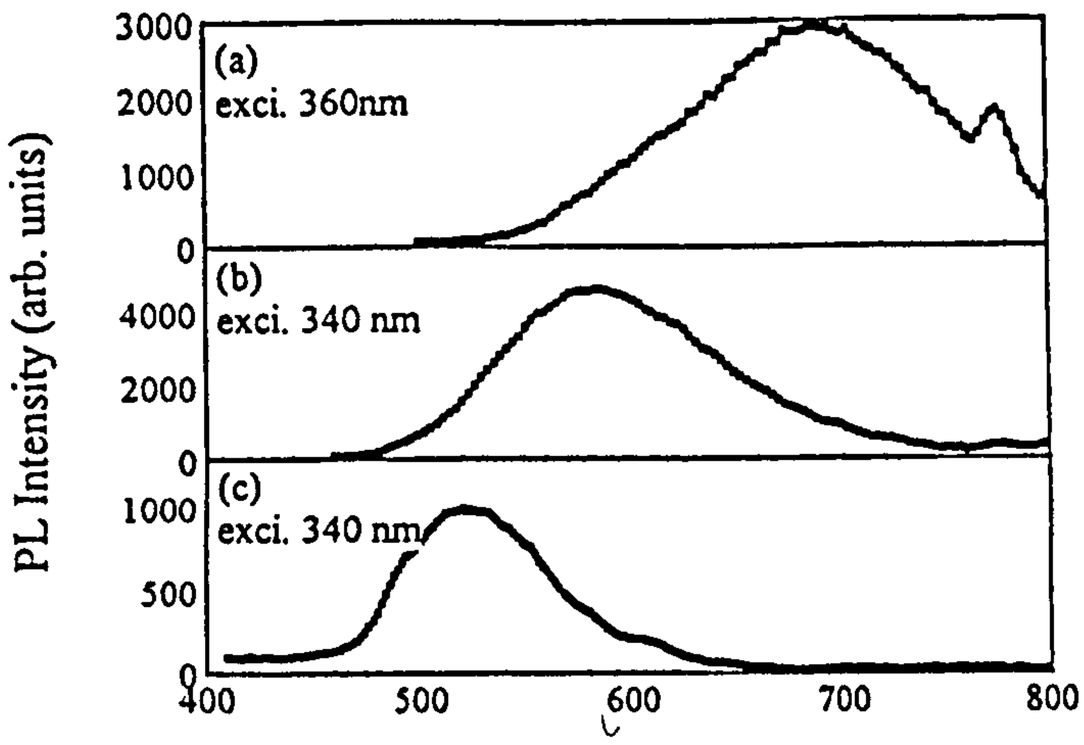

FIG. 1. Photoluminescence from (a) red, (b) yellow and (c) green porous silicon. The excitation wavelength is shown.

III. RESULTS AND DISCUSSION

A. PL and PLE

Figure 1 shows the PL of the red, yellow and green PS, with peaks located at 690, 580 and 520 nm (1.8, 2.14 and 2.38 eV), respectively, under the excitations given in the figure. These spectra are typical of PS, the energy-width of the main feature (~0.8 eV) frequently believed to be caused by the broad size-distribution of the nanostructures, and different transitions between bands and within the band gap.[15] On the contrary, the energies, E_{g1} = 2.3, 2.6 and 3 eV, are the estimated optical band gaps for the red, yellow and green emitting PS, respectively. These energies were obtained from our photoluminescence excitation dependence (PLE) measurements at room temperature for the same PS samples.[18]

B. NEXAFS and EXAFS

As the penetration depth of photo-exciting radiation is on a scale of hundreds of nanometers, measurement of EXAFS is quite suitable to detect the details of the structure within this effective radiative layer of PS. Figure 2 shows the normalized photon absorption of Si-K-edge NEXAFS from PS, c-Si, a-Si and a-SiO_2. The absorption peaks of the features of Si-Si and Si-O bonds are indicated at 1840 and 1847 eV. A further feature at ~1844 eV has previously been assigned to the presence of SiOH-related bonding.[9,22,23] It can be seen that firstly the absorption behavior of c-Si includes the 1847 eV feature, probably due to the presence of a surface native oxide. Secondly, the PS Si-Si bond absorption gradually decreases and Si-O bond absorption increases with PL blue-shift: less Si-O absorption in NEXAFS implies the samples are "fresh," similar to some of the work in Ref. 10, but unlike the data of Ref. 9 and some of our previous studies on other types of PS,[22,23] where NEXAFS shows stronger Si-O absorption. One explanation for the trends is that the average surface:volume ratio of Si cores increases with blue-shift. Moreover, this increasing ratio suggests the average volume of the nanocores decreases.

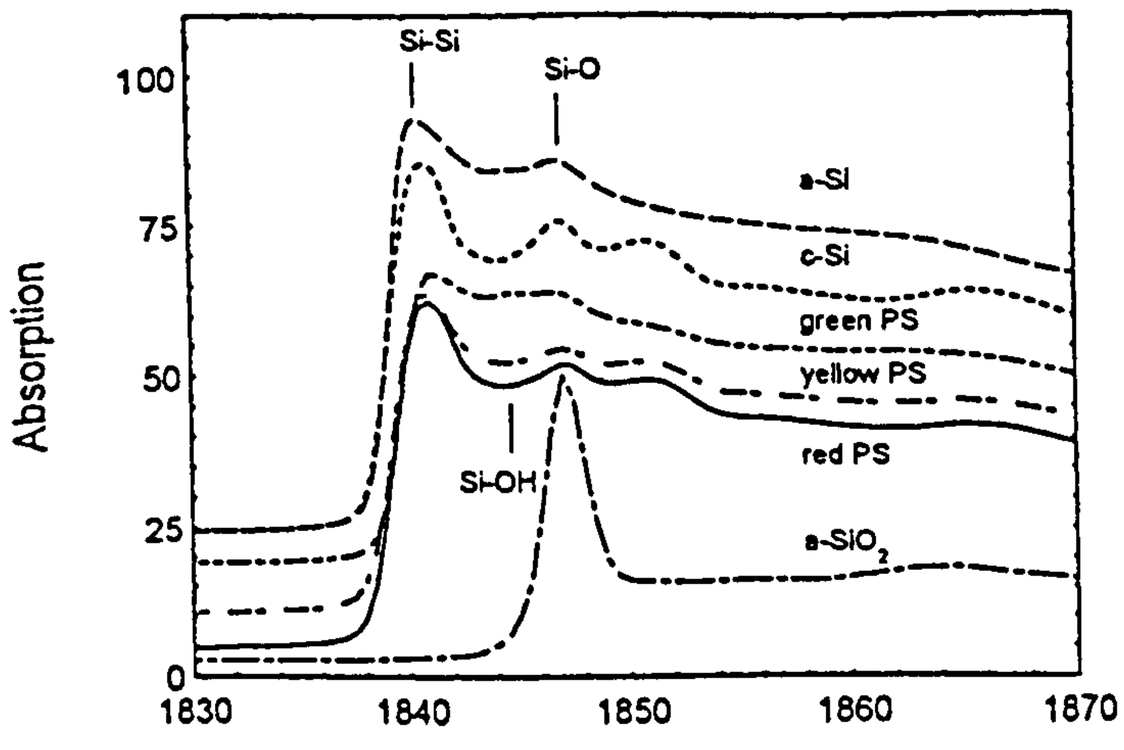

FIG. 2. NEXAFS of c-Si, a-Si, a-SiO_2, green, yellow and red PS. Si-Si, Si-O and Si-OH absorption peaks are indicated.

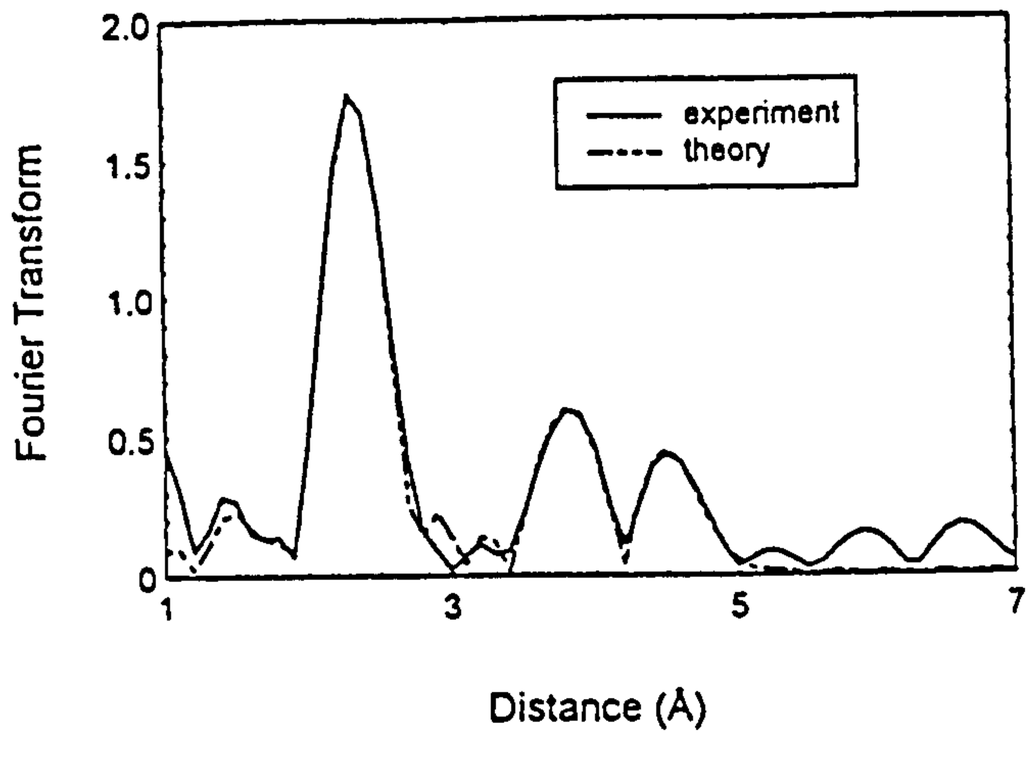

FIG. 4. Fourier transforms of both experimental data and theoretical fitting of EXAFS from the yellow emitting PS. The two curves completely overlap on the Si-Si 1st, 2nd and 3rd shells.

More information on the nanostructure has been obtained from the analysis of the EXAFS data using EXCURV92.[24] During the analysis with EXCURV92, the relaxed approximation was selected for the excited K-shell. Three phaseshifted files were set as Si (center)-Si, Si-Si (center) and O-Si, to which the amplitude and backscattering phase shift were calculated within EXCURV92. And, all spectra were phase-shift corrected within EXCURV92 so that the peaks appear at their true positions. Figure 3 shows the Fourier transform (FT) of the k^3-weighted EXAFS. For clarity, only theoretical FTs are given here. That the fits were good could be seen from error maps, the fit indexes ($\sim$0.00014), and residuals ($\sim$13).[25] Such fits almost completely overlap the experimental curves for the first, second and third Si-Si shells; as an example both experimental and nonfiltered fitted data for the yellow PS are shown in Figure 4. For this material the Si-Si shells occur at 2.34, 3.81 and 4.50 Å, respectively. All distances are ±0.02 Å. Including multiple scattering was found not to increase the quality of the fit in any of the shells.

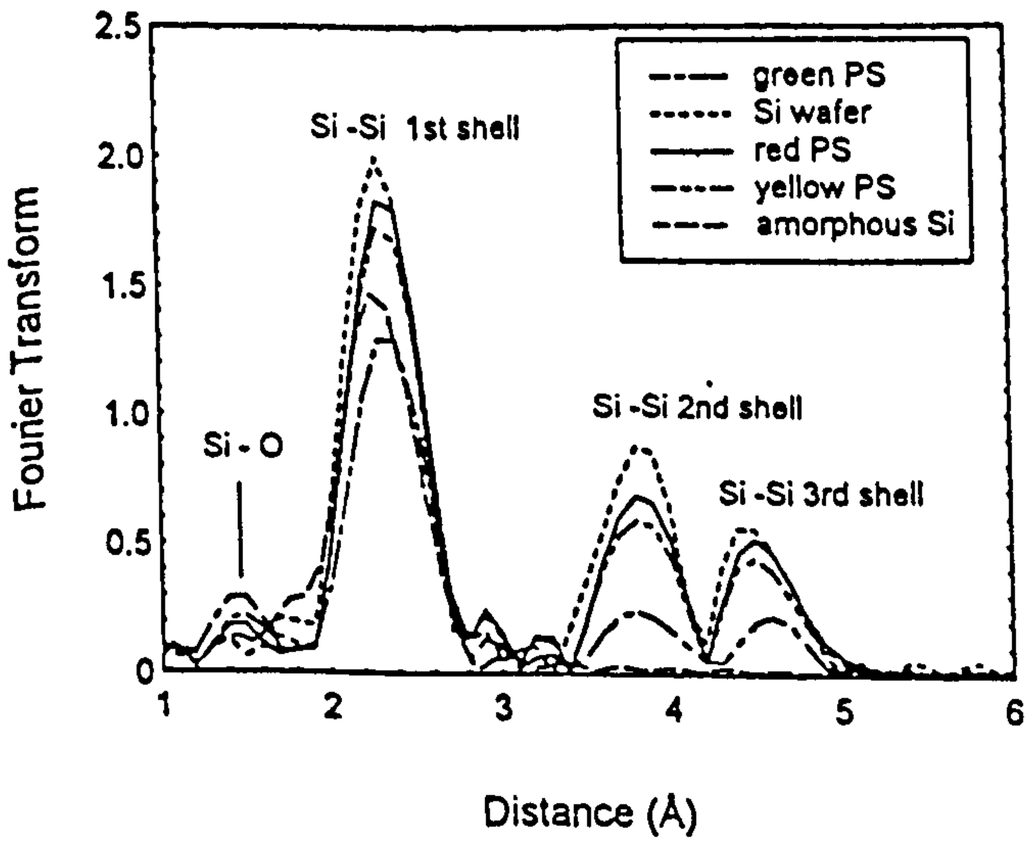

FIG. 3. k^3-weighted Fourier transform of EXAFS from c-Si, a-Si, red, yellow and green PS. 1st, 2nd and 3rd shell Si-Si and 1st shell Si-O bonds are indicated.

The fitted Si-Si nearest-neighbor partial coordination numbers $N_{Si\text{-}Si}$ for the PS, *c*-Si and *a*-Si are given in Table I, in which all the relevant errors are given. While the first shell $N_{Si\text{-}Si}$ of red and yellow PS, 3.8±0.15 and 3.65±0.13, are close to 4, that of bulk *c*-Si, those for the 2nd and 3rd shell dramatically drop to 7.4 and 8.2 respectively for red PS, and 5.7 and 6.5, respectively for yellow PS, compared with 12 in both shells for bulk Si. The rapid fall off for the 2nd and 3rd shells means that a significant part of the medium-range order has been lost. For the green PS $N_{Si\text{-}Si}$ of all of the shells drops significantly, to 3.0±0.2, 3 and 4, implying the size decreases further. This agrees with sample preparation processes. In addition, the first shell $N_{Si\text{-}O}$ increases with PL blue-shift, agreeing with the implication from NEXAFS of the increasing surface:volume ratio. However, this shell is not well-fitted by theory, as shown in Figure 4, possibly because of the involvement of O, OH and H, the possible passive species of P_b centers.[26] As a technique EXAFS is relatively insensitive to the presence of H, since H atoms are such weak scatterers. Anyway, the modelling described below only takes into account the average number of Si-Si bonds.

Table II gives the fitted 1st, 2nd and 3rd shell distances from the PS samples. All distances are ± 0.02 Å.

C. Debye–Waller order factors

As the presence of an amorphous phase could also reduce the 2nd and 3rd coordination numbers, it is necessary to know the ordering of the freshly produced PS before any modelling of nanostructure. Table III gives the Debye–

TABLE I. The coordination numbers of Si-Si shells.

	1st $N_{Si\text{-}Si}$	2nd $N_{Si\text{-}Si}$	3rd $N_{Si\text{-}Si}$
red PS	3.8±0.15	7.4±0.44	8.2±0.75
yellow PS	3.65±0.13	5.7±0.38	6.5±0.67
green PS	3.0±0.2	3±0.49	4±0.73
c-Si	4±0.1	12±0.35	12±0.58
a-Si	4±0.1	0	0

TABLE II. The distances of Si-Si shells of PS.

	1st R	2nd R	3rd R
red PS	2.34	3.81	4.49
yellow PS	2.34	3.81	4.50
green PS	2.34	3.79	4.55

Waller order factors, A(k), of the first, second and third Si-Si shells for the PS, c-Si, a-Si. The A(k) of the 1st, 2nd and 3rd are quite close to that of crystal Si, but far from *a*-Si, especially for the first shell for which the errors are given. Such values for A(k) suggest as expected that the core of the fresh PS is nanosized crystalline silicon, in agreement with Refs. 6 and 27, while Ref. 10 did not give these factors. The small difference between the A(k) of green PS and c-Si can be explained since the high surface:volume ratio of this nanostructure effects a detectable x-ray absorption due to the surface passive layer. Figure 5 shows both experimental and back transformed, nonfiltered data with k^3-weighing from the yellow PS. It can clearly be seen that both the curves have the characteristics of crystalline Si even with quite reduced coordination numbers. These fitted ordering factors suggest an important characteristic of PS before degradation and both further and native oxidization, i.e., anodization only produce a nanostructure, consequently, quantum size effect would be the first choice for the reason of the band gap-widening.

D. Dimensionality and modelling

Obtaining accurate $N_{Si\text{-}Si}$ for the red, yellow and green PS, and ordering factors, allows us to estimate the possible average sizes present, as well as the relevant structural dimensionality, and to confirm if quantum confinement is responsible. To achieve this aim, several other values are required: (i) PS band gaps; (ii) theoretical calculation of variation of band gap with size of nanowire and nanodot; and (iii) the correlation between coordination number and average nanosize with different dimensionality. In most published works the nanosizes have been compared only with the PL peak energy, i.e., the peak energy is used as an estimate for the band gap energy in order to estimate the size distribution, assuming a band-to-band transition model. Following this, our peak energies E_{g2} are 1.8, 2.14 and 2.38 eV, respectively for red, yellow and green PS, as shown in Figure 6(a). The band gaps E_{g1} obtained from our PLE measurements at room temperature[18] are also given in Figure 6(a), assuming a recombination center model. The theoretical calculation of confined band gap with nanosize of PS by the linear combination of atomic orbitals (LCAO) technique is cited in Figure 6(b) after,[28] where both nanodots and wire band gaps were given. In Figure 6(c), the coordination numbers of the first Si-Si shell of the PS are shown with errors of fits.

The average size dependence with partial coordination numbers of two types of nanowire for both (100) and (111) orientations have been calculated to match the experimental

TABLE III. The Debye–Waller order factors of Si-Si shells.

	$A_1(k)/Å^2$	$A_2(k)/Å^2$	$A_3(k)/Å^2$
red PS	0.0042±0.0008	0.011	0.01
yellow PS	0.0038±0.0008	0.011	0.012
green PS	0.0048±0.001	0.013	0.013
c-Si	0.004±0.0007	0.01	0.011
a-Si	0.007±0.0006		

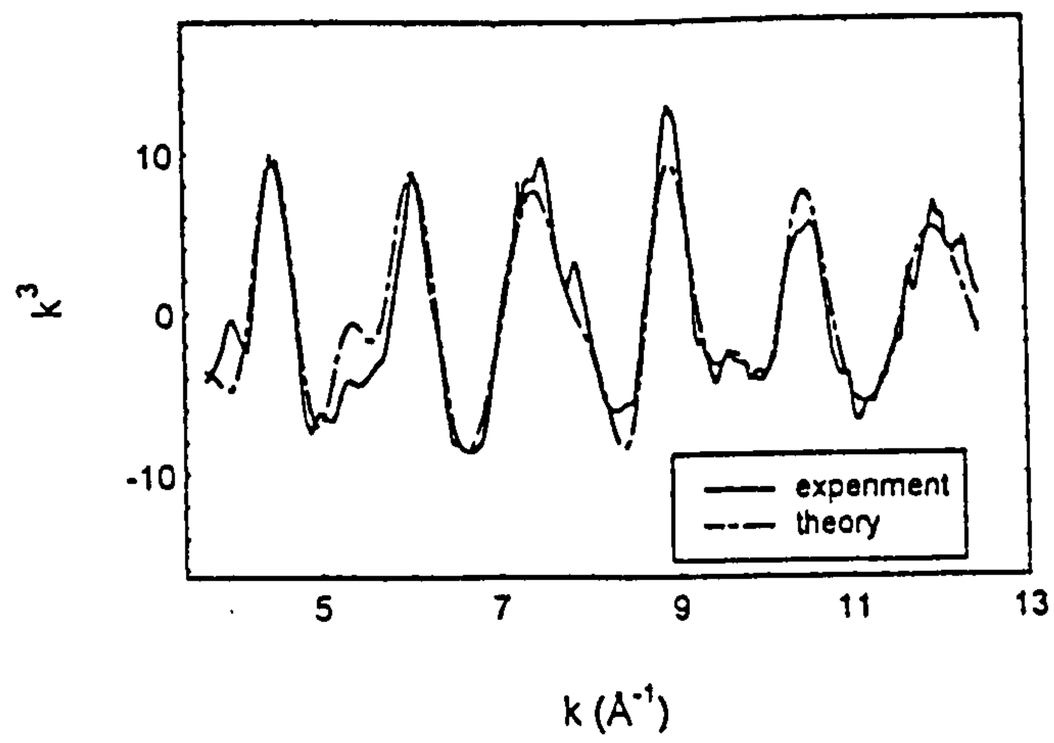

FIG. 5. k^3-weighted EXAFS of both experimental and nonfiltered theoretical fit for the yellow PS.

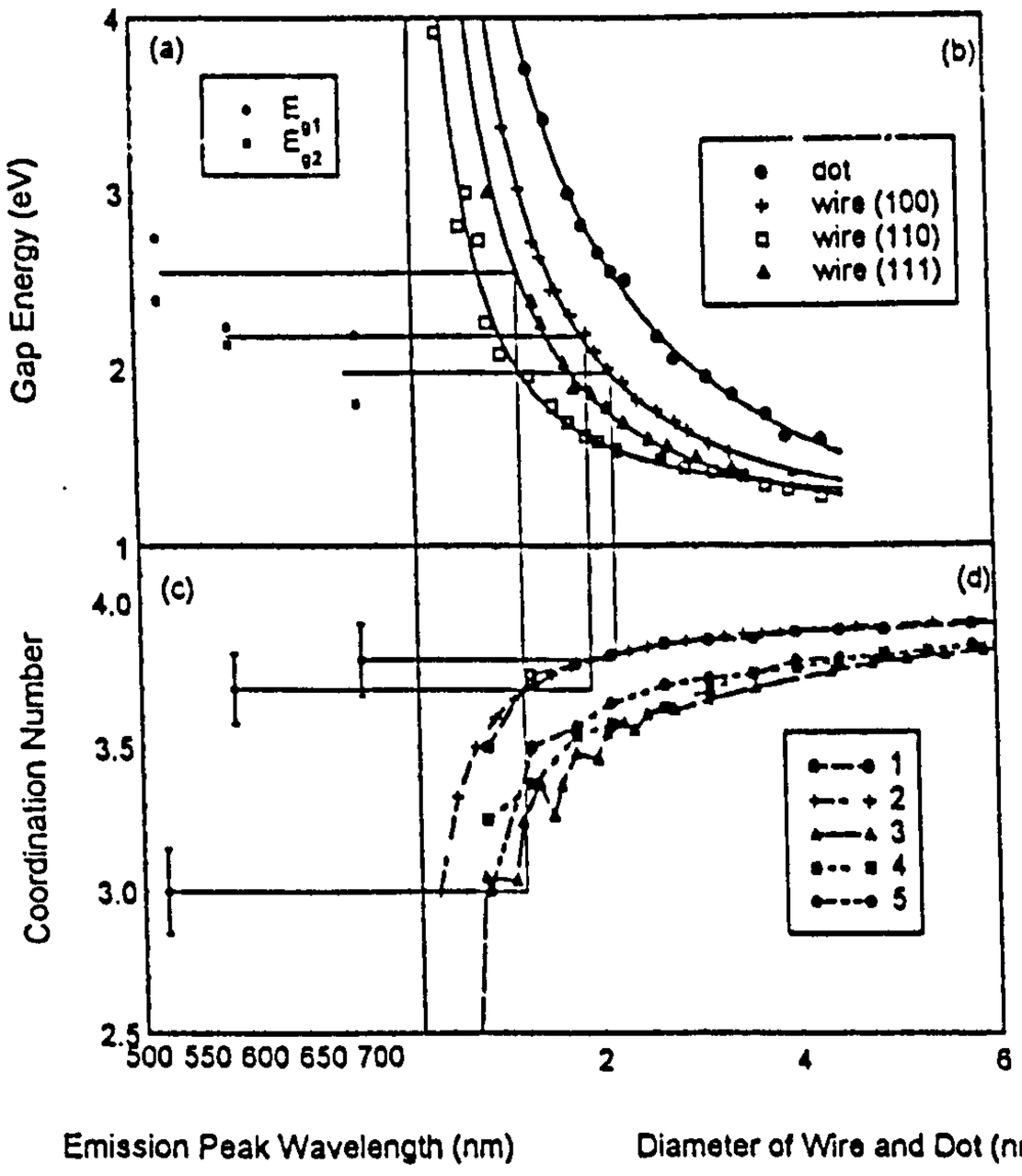

FIG. 6. Dependence of dimensionality and size with PS color. (a) Band gaps of the three types of emitting PS: E_{g1} from PLE and E_{g2} from PL peaks. (b) Theoretical calculation of confined band gap energy of PS of wires and dot by LCAO after Ref. 28. (c) 1st shell $N_{Si\text{-}Si}$ of red, yellow and green PS from EXAFS fits. (d) Dimensionality and size dependence with the $N_{Si\text{-}Si}$ from (i) bare wire: curves 3-cylinder (100), 4 and 5—two types of hexagonal columns (111); (ii) wire network (one-plus-a-fraction dimension): curves 1—(111) and 2—(100), details see Figure 7. As shown by the guiding lines, the PS in this study favor the nanowire network and wire structures, with average diameters of 2.2, 1.9 and 1.3 nm, respectively for red, yellow and green PS.

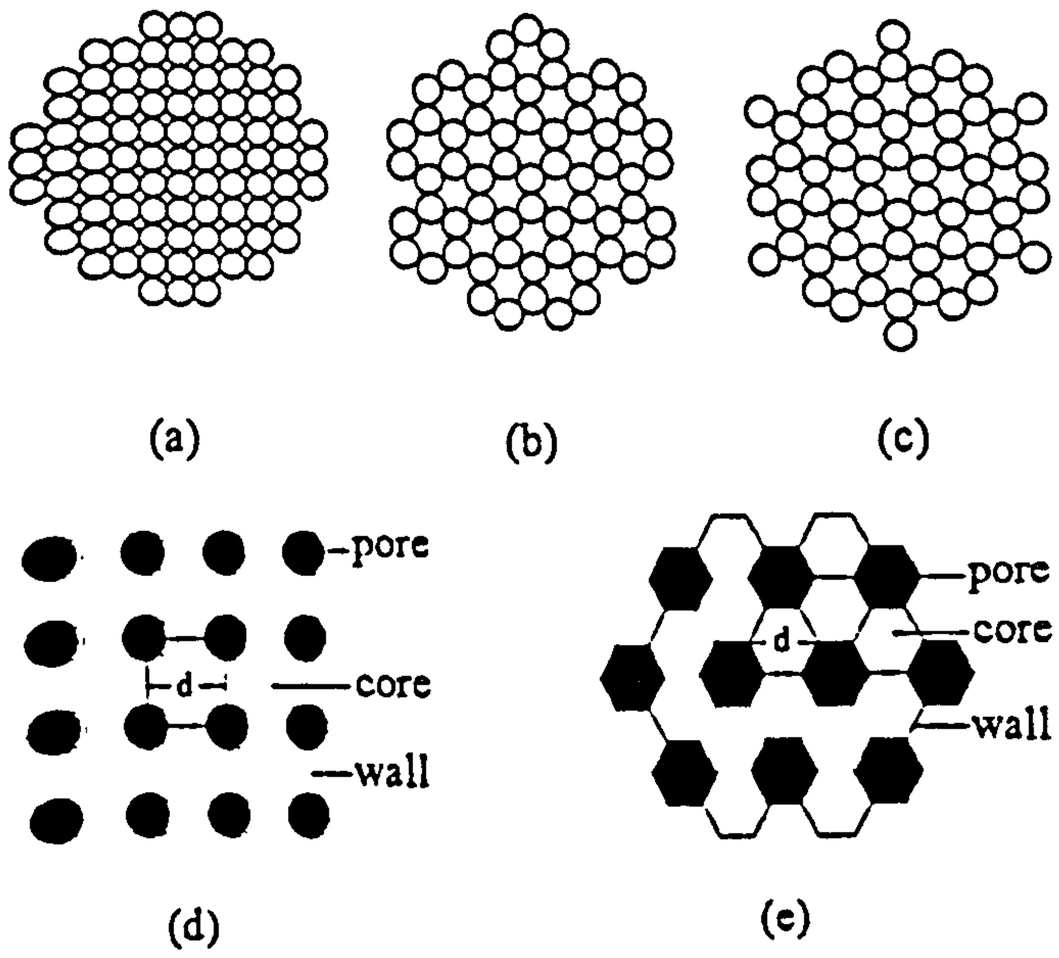

FIG. 7. The idealized atomic plan views of the bare wires and plan views of the wire networks. (a) bare wire (100), (b) bare wire (111) (type 1) and (c) bare wire (111) (type 2), appropriate for curves 3, 4 and 5 in Figure 6(d), respectively. Also shown are (d) cylinder-like structure in (100) and (e) hexagonal column-like structure in (111), appropriate for curves 2 and 1 in Figure 6(d) respectively, in which the number of surface Si atoms is only half that of bare wires of diameter d.

1st shell $N_{Si\text{-}Si}$. The results are shown in Figure 6(d): (i) one-dimensional wires of cylinder-like (100) (curve 3), and hexagonal-column-like (111) orientation (curves 4 and 5, details see Figure 7); (ii) "wire network" (curves 1 (111) and 2 (100)) with one-plus-a-fraction structural dimensionality, in which the number of surface Si atoms is only half that of bare wires of diameter d, based on the concept that the carriers within a wire network could also be confined in two dimensions.[1,2]

In the model, it is supposed that the wires are ideally one dimensional, and the wire networks are ideal one dimension plus a fractional dimension. Consequently, only the non-bonded Si atoms around the cylinder or column surface were calculated, however bonded with O, H and OH, but Si. In other words, the dangling-bonded Si atoms on tops of the two sides were ignored. For the cylinder-like wire (100), there is a Si atom at the center of the cylinder of radius $r=d/2$. If the center points of the surface Si atoms are at or within the circle of radius r, the bonds to these atoms were counted based on the bonding conditions. For the (111) orientation, two types of hexagonal columns have been used, one is with an atom at the center (curve 4 in Figure 6(d)), the other has no atom at the center (curve 5 in Figure 6(d)). The diameter, d, was the mean of the maximum and minimum distances (center point to center point of the surface atoms) across the hexagon, with step-increases of a full atomic layer all round. The details of the model are shown in Figures 7(a), (b) and (c) for the bare wires, with idealized atomic plan views appropriate for curves 3, 4 and 5 in Figure 6(d), respectively. The idealized plan views of the wire network are also shown in Figures 7(d) and (e) superimposed on the cylinder-like (100) (curve 2 in Figure 6(d)) orientation with 25% porosity and on the hexagonal column-like (111) (curve 1 in Figure 6(d)) orientation with 33% porosity, respectively. This is based on the constraint that the number of surface Si atoms is only half that of bare wires of diameter d, the other half forming bonds with the neighboring wires. One should note that the porosity of the idealized plan should be smaller than that obtained experimentally for the same nanosize, as there are a large number of bigger pores with diameters in the tens or hundreds of nm which have not been considered in the idealized calculation. The larger pores have been observed by many researchers with TEM, however, they do not make a direct contribution to the nanostructure.

Comparing Fig. 6(a), (b), (c) and (d), and knowing both band gap energies E_{g1} and E_{g2}, we can estimate the mean dimensionality and the sizes of PS in the radiative wavelength range from 690 nm to 520 nm within a sampling depth of hundreds of nm. As indicated by lines in Figure 4, it is can be seen that the nanostructure of red and yellow PS is predicted to consist of a one-plus-a-fraction dimensionality wire network and, green PS is consist of nanowire. The mean core diameter of red PS is about 2.2 nm with a larger fractional dimensionality and, that for yellow PS is about 1.9 nm with a smaller fraction. Furthermore, the mean size of green PS is much smaller, only about 1.3 nm with a dimensionality of one or less than one. On the other hand it is not suitable to predict a nanodot model for both energy and partial coordination number as it would lie outside the experimental data plus error. The characteristic structure and mean size of green PS is different from that of red and yellow because of both $N_{si\text{-}si}$ and E_{g1}. The $N_{si\text{-}si}$ has the characteristic that the difference between red and yellow PS is smaller that between yellow and green PS. The E_{g1} varies similarly, although N_{si-si} and E_{g1} are obtained by very different means—EXAFS and PLE respectively (see Fig. 6). This implies that the transition behavior varies with peak energy, the details of this are discussed in Ref. 18.

This type of nanowire with a dimensionality greater than one was proposed in very early work for PS porosity up to ~50%–80%.[1,2] Because the necks between the pores are thinner than the cores (or the quasi-rods), a stronger confinement effect results in potential barriers keeping the carriers in lower energy cores. This kind of nanoquantum-wire, the carrier being mainly confined to two dimensions but with structural dimensionality greater than one, could be called a 'wire network.'

We have tried on a range of Si wafer resistance from 1 to 30 Ω cm to make green and yellow emitting PS by the same process described in this work. The general result is that it is very difficult to produce green PS from higher resistance wafer. It lead us to conclude that the starting distance between nanopores plays an important part in producing differently emitting PS. The resistance would be one of the key factors controlling the distance: it is suggested that the distance between pores are much longer in higher resistance material by the same processes as in this work and the resulting PS has thicker wires (and bigger dots as in Ref. 10, when the wires were etched until they formed separate 'dots') and only emits red and orange PL. Since the same radiative color is obtained both from a nanowire network (suggested in this work for red PS) and nanodots in Ref. 10

which give rise to similar PL, the different nanostructures may well depend on wafer resistance or starting distance between pores. However, the wire shape is more common than the dot shape, as about 60% of published data on the resistance of Si wafers used for PS fall in the 1 to 10 Ω cm range, instead of a few % ≥ 50 Ω cm. Also the average wire shape is more suitable for EL applications, demanding lower voltage and higher current, and delivering higher EL efficiency.

The wall between the cores of the nanowire network could allow more indirect carrier-transition behavior with longer lifetimes as in bulk Si, and more direct behavior with shorter or even much shorter lifetime within bare wire or dots respectively. For PS with red, orange or yellow emitting peaks, a size distribution (related to the broad PL spectrum) implies a distribution of dimensionality or a fraction dimension. This fraction therefore would lead to a lifetime increasing with increasing PL wavelength, that is the wavelength is fraction-dimension-related. This behavior has been found present in the so-called slow PL band which is related to an emitting energy about ≤2 eV, and where the lifetime continuously increases from 60 to 220μs with increase in PL wavelength from 620 nm to 800 nm.[13,29–31] After the as-anodized PS is oxidized by dry-oxidization at 800°C, this lifetime dependence on wavelength decreases to about 60–80 μs in the same energy range.[32] This cannot be explained by the tunnelling model alone,[32] but can be explained by the fraction dimension: most of the fraction dimension in the distribution has been consumed by further oxidization, so the indirect behavior is reduced to that of bare nanowire because the carriers only have one-dimensional mobility.

IV. CONCLUSION

Although more than one mechanism is likely to be involved in the luminescence of PS, EXAFS and theoretical fits show a relatively simple picture for freshly produced PS with PL peaks from 690 nm to 520 nm, which is nearly the full range we can obtain using only anodization processes. (1) The nanocores of the PS are crystalline and quantum confinement is the only mechanism widening the band gap at this stage. Obviously disorder from degraded PS by x-ray and long time native oxidization has been observed in our other studies. (2) A nanowire network (one-plus a fraction dimensionality) for red and yellow PS, and nanowire (one dimensional or less) for green PS, are suggested. The mean core sizes are 2.2, 1.9 and 1.3 nm, respectively for red, yellow and green PS. This nanostructure shape of quantum wire is much more positive for PS application in EL than are quantum dots. (3) The fractional dimension could be one of the causes of the slow band and lifetime variety in this band, as the fraction dimension can let carriers act more indirectly.

ACKNOWLEDGMENTS

We acknowledge the support of DRAL and CVCP. We also thank D.A. Hutt for assistance with EXAFS experiments.

[1] L. T. Canham, Appl. Phys. Lett. 57, 1046 (1990).
[2] V. Lehmann and U. Gösele, Appl. Phys. Lett. 58, 856 (1991).
[3] H. Mimura, T. Futagi, T. Matsumoto, T. Nakamura, and Y. Kanemitsu, Jpn. J. Appl. Phys. 33, 586 (1994).
[4] R. Behrensmeier, F. Namavar, G. B. Amisola, F. A. Otter, and J. M. Galigan, Appl. Phys. Lett. 62, 2408 (1993).
[5] T. V. Buuren, Y. Gao, T. Tiedje, J. R. Dahn, and B. M. Way, Appl. Phys. Lett. 60, 3013 (1992).
[6] A. Naudon, P. Goudeau, A. Halimaoui, B. Lambert, and G. Bomchil, Appl. Phys. Lett. 75, 780 (1994).
[7] Y. Kanemitsu, H. Uto, Y. Masumoto, T. Matsumoto, T. Futagi, and H. Mimura, Phys. Rev. B 48, 2827 (1993).
[8] I. Berbezier and A. Halimaoui, J. Appl. Phys. 74, 5421 (1993).
[9] T. K. Sham, D. T. Jiang, I. Coulthard, J. W. Lorimer, X. H. Feng, K. H. Tan, S. P. Frigo, R. A. Rosenberg, D. C. Houghton, and B. Bryskiewicz, Nature 367, 331 (1993).
[10] S. Scuppler, S. L. Friedman, M. A. Marcus, D. L. Adler, Y. H. Xie, F. M. Ross, T. D. Harris, W. L. Brown, Y. J. Chabal, L. E. Brus, and P. H. Citrin, Phys. Rev. Lett. 72, 2648 (1994).
[11] Q. Zhang, S. C. Bayliss, and D. A. Hutt, Appl. Phys. Lett. 66, 1977 (1995).
[12] Q. Zhang, S. C. Bayliss, A. Al-Ajili, and D. A. Hutt, Nucl. Instr. Methods in Phys. Res. B 97, 329 (1994).
[13] L. R. Tessler, F. Alvarez, and O. Teschke, Appl. Phys. Lett. 62, 2381 (1993).
[14] T. Matsumoto, M. Daimon, T. Futagi, and H. Mimura, Jpn. J. Appl. Phys. 31, 619 (1992).
[15] F. Koch, V. Petrova-Koch, and T. Muschik, J. Lumin. 57, 271 (1993).
[16] M. S. Brandt, H. D. Fuchs, M. Stutzmann, J. Weber, and M. Cardona, Solid State Commun. 81, 307 (1992).
[17] J. M. Lavine, S. P. Sawan, Y. T. Shieh, and A. J. Bellezza, Appl. Phys. Lett. 62, 1099 (1993).
[18] Q. Zhang and S. C. Bayliss, 1995 (unpublished).
[19] J. C. Vial, A. Bsiesy, F. Gaspard, R. Herino, M. Legeon, F. Muller, R. Romestain, and R. M. MacFarlane, Phys. Rev. B 45, 14171 (1992).
[20] A. Eroil, G. S. Cargill, R. Frahm, and R. F. Boehme, Phys. Rev. B 37, 2450 (1988).
[21] X. Y. Hou, G. Shi, W. Wang, F. L. Zhang, P. H. Hao, D. M. Huang, and X. Wang, Appl. Phys. Lett. 62, 1097 (1993).
[22] S. C. Bayliss, D. A. Hutt, Q. Zhang, N. Danson, J. Bates, and A. Waddilove, J. Appl. Phys. 76, 9 (1994).
[23] S. C. Bayliss, D. A. Hutt, Q. Zhang, N. Danson, and A. Smith, Solid State Commun. 91, 371 (1994).
[24] N. Binsted, S. J. Gurman, and J. W. Campbell, SERC Daresbury Lab. EXCUV92 (1992).
[25] R. W. Joyer, K. J. Martin, and P. Meehan, J. Phys. C 20, 4005 (1987).
[26] B. K. Meyer, V. Petrova-Koch, T. Muschik, H. Linke, P. Omling, and V. Lehmann, Appl. Phys. Lett. 63, 1930 (1993).
[27] Y. Uchida, N. Koshida, H. Koyada, and Y. Yamamoto, Appl. Phys. Lett. 63, 961 (1993).
[28] C. Delerue, M. Lannoo, and G. Allan, J. Lumin. 57, 249 (1993).
[29] A. Takazawa, T. Tamura, and M. Yamada, J. Appl. Phys. 75, 2489 (1994).
[30] D. I. Kovalev, I. D. Yaroshetzkii, T. Muschik, V. Petrova-Koch, and F. Koch, Appl. Phys. Lett. 64, 214 (1994).
[31] L. Pavesi, M. Ceschini, and F. Rossi, J. Lumin. 57, 131 (1993).
[32] A. Takazawa, T. Tamura and M. Yamada, Appl. Phys. Lett. 63, 940 (1993).

APPENDIX C Proceeding Volume of 3rd International Symposium of Quantum Confinement: Quantum Wires and Dots, The 188th Meeting of The Electrochemical Society, Inc. Chicago, USA, October, 1995.

THE BLUE AND UV PHOTOLUMINESCENCE OF SI AND C NANOCLUSTERS EMBEDDED IN SIO_2 MATRICES

Qi Zhang, S. C. Bayliss and R.G. Pritchard

Department of Applied Physics, School of Applied Science, De Montfort University, Leicester. LE1 9BH. UK

Abstract

Silicon and carbon nanoclusters embedded in SiO_2 were deposited by rf-sputtering followed by N_2 annealing at 600 and 800°C. Stable blue photoluminescence (PL) from both types of cluster samples were recorded and observed by naked eye under the excitation power of μ W scale. UV PL from C clustered films was also recorded but not stable decaying with time. The size distributions (from 1 to 4.5nm) of the nanoclusters in the clustered films suggest that quantum confined size effect still can apply on blue PL range. Si K-edge and C K-edge EXAFS suggest that both the two types of clusters are respectively Si and C related materials.

INTRODUCTION

Visible light emission from elemental semiconductor nanostructures, such as, Si, C, Ge, especially porous silicon, has attracted significant attention in the past few years because the photoluminescence (PL) is strong and lies in the visible region, and could be useful for optoelectronics applications. Apart from the intensively studied porous silicon[1,2] and Si nanopowder[3], work on nanoclusters of group IV elements embedded in SiO_2 is one important area of the study. Previous reports on Si[4,5], C[6], and Ge[7,8] clusters embedded in SiO_2 matrices suggested that optical transitions associated with the fundamental absorption edge of the nanostructured material had direct rather than indirect character, and there were evidences for the presence of nanocrystals in high-resolution TEM real-space images. Recently, a study on Ge doped SiO_2 films shows a large visible range of PL, peaks from 500 to 800nm, observed from annealed Ge nanocrystallines (the mean size varies from 2-6nm), while weak UV and blue PL

were recorded from as-deposited samples.[9] From all of the nanocluster studies, quantum-confinement model has been concluded as suitable mechanism for the strong blue shift.

We present a study on the blue emission from annealed Si and C clusters embedded in SiO_2, and unstable UV emission from annealed C clustered films following our previous work[10-11]. With the information from TEM and both Si and C k-edge EXAFS, the origin of the blue photoluminescence is concluded as quantum size effect, while the origin of the UV emission is unknown.

EXPERIMENTAL

The semiconductor-doped glasses were deposited in one process by rf co-sputtering in a system with base pressure of 3×10^{-6} mbar. On the pure SiO_2 8" target between 3 and 20 pieces of Si wafer ($10\times10\times0.3$ mm^3) were placed in an area of ~4" in diameter to produce Si-cluster samples and, between 5 and 16 pieces of pore graphite rod of 6mm diameter were used to produce C clustered films of various PL response. The deposition conditions were: (1) for Si clustered films - 3×10^{-4} - 6×10^{-3} mbar Ar, 400W rf power; (2) for C clustered films - 6×10^{-4} - 1×10^{-2} mbar Ar, 500 - 1250W rf power. The films were deposited on Si wafer substrates with a film thickness of >1 μm. The samples were subsequently annealed at 800°C for 20 min in a N_2 atmosphere flowing at a rate of 3 *l* min^{-1}. The PL and Si k-edge and near edge x-ray absorption fine structure (EXAFS and NEXAFS) measurements were performed at DRAL Daresbury Laboratory using stations 12.1 and 3.4 respectively. And, the C k-edge EXAFS were obtained at HE - PGM2 station of BESSY Laboratory. The data from the clustered film does not contain any contribution from the Si substrate, as the film thickness is >> the EXAFS sampling depth. For PL the tuneable UV source provided excitation at 260nm, 300nm and 370nm, using a bandwidth of 10nm and a power of 0.12 -2.7μW on the samples. To all of the samples, the PL were only observed from annealed films. The PL data has been normalised to take into account the spectral sensitivity of the system and variations due to beam decay. The EXAFS were determined by the total-yield technique[12]. The cluster size distribution was obtained from TEM real-space images from the edges of tilted samples using a Jeol JEM 100CX. The resolution of this instrument is ~0.5 nm.

RESULT AND DISCUSSION

Figure 1(a) and (b), show the PL of two Si-cluster samples *1* and *2*. Peaks are located from ~420 to 495nm, and from ~450 to 490nm, depending on the

sample preparation conditions. On the contrary no emission was detected for as-deposited samples. Although many samples have been made in very different conditions, data from only two samples, those with highest PL intensities, are shown here. In Figure 1 (c) and (d), the PL from C clustered films, sample 3 and 4, are given. As shown in (d), both UV and blue PL were recorded from the sample when it was measured at the first time after annealing. However, two days after the first measurement, the UV emission disappeared and, only blue emission remained in the second measurement. About half of carbon

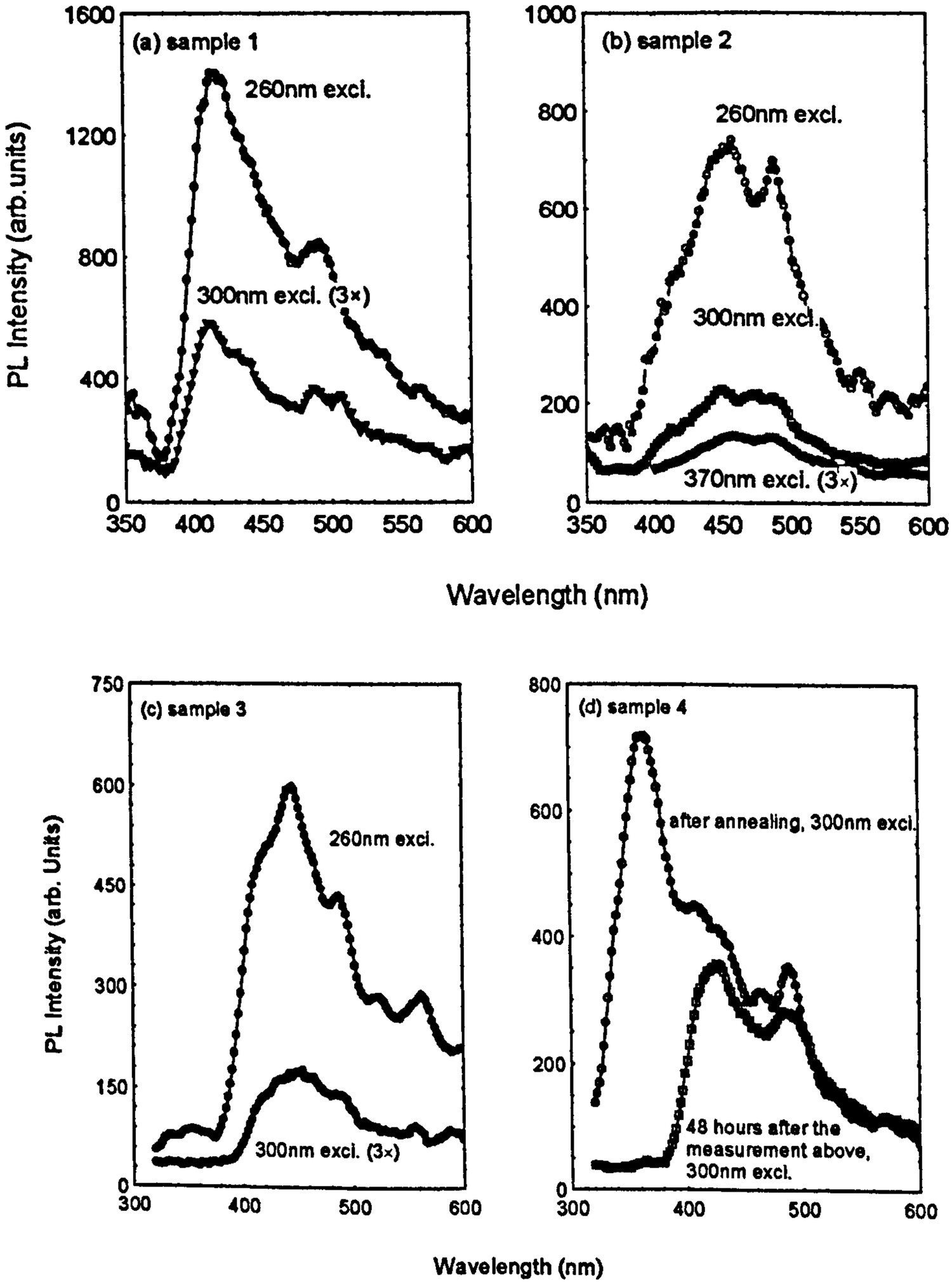

Figure 1. PL from Si ((a) and (b)) and C ((c) and (d)) clustered SiO_2 films.

clustered films we made have this characteristics of unstable UV PL, although, the UV PL intensities varied compared with blue peaks. On the contrary, the blue emissions almost kept same at the first, second and third measurements. The PL spectra of our samples consist of mainly of one, two or three strong peaks, and also some smaller peaks from different deposition conditions.

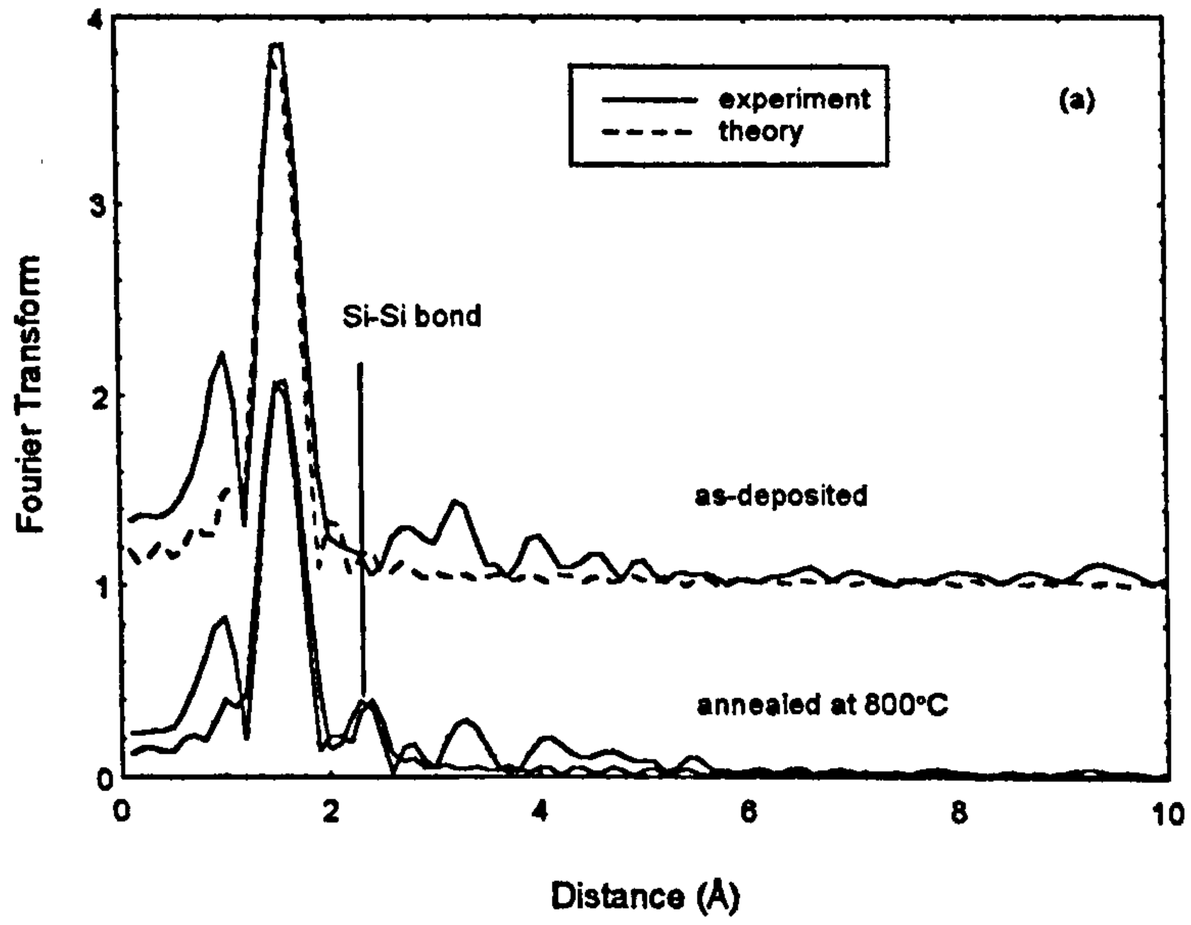

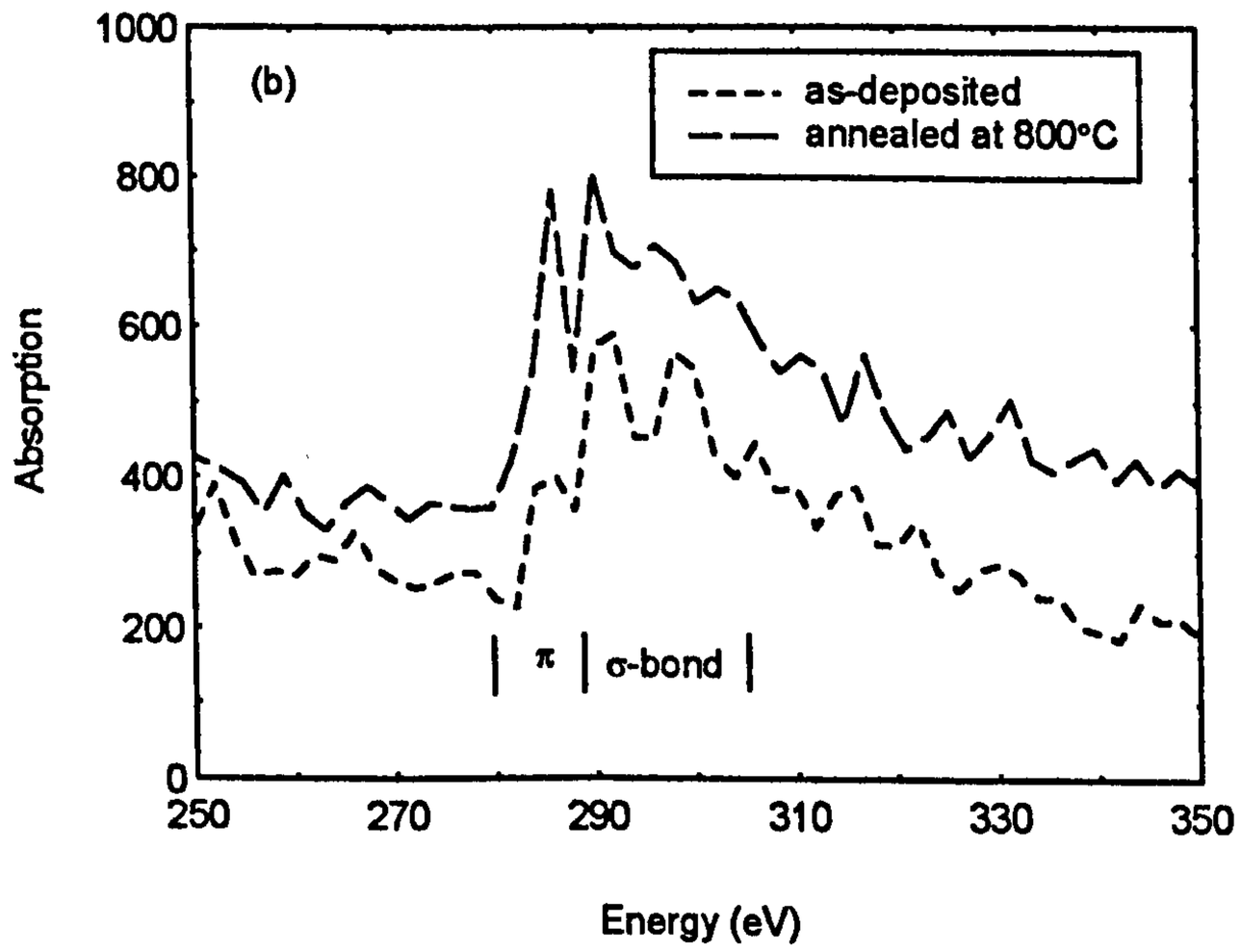

Figure 2. (a) Fourier transformed EXAFS of Si clustered film - sample 1 in Figure 1. (b) NXAFS of C clustered film - sample 3 in figure 1.

The Fourier transform from the EXAFS data shows details of the local structure of the nanosized Si clusters. In Figure 2(a), both experimental and theoretically-fitted Fourier transforms of as-deposited and annealed Si/SiO_2

(sample *1* as shown in Figure 1(a))are shown. In the unannealed material the Fourier transforms are very similar to those of SiO_2[12], with a Si-O bond-length at 1.58Å, a second shell corresponding to Si-O-Si at ~3.2Å. After annealing, the nearest neighbour partial coordination number of Si-Si bonds increases from zero, for the as-deposited material, to 0.6 for the material with the highest contribution from Si-Si bonds. On the contrary, the Si-O bond peak of the Fourier transform decreases significantly. The second shell corresponding to Si-O-Si is still present, and, a third shell corresponding to Si-O-Si-O at ~4Å emerges. As with most EXAFS data fits, however, the 4σ error in the partial coordination numbers obtained by statistical analysis of the fit is rather high : ± 0.5, but still clearly shows the existence of Si-Si bonds. Since the total coordination number is 4, and silicon oxide is chemically ordered both throughout understoichiometry and at stoichiometry[12], more than one eighth of the Si atoms are potentially bonded in elemental Si regions. The Si-Si bond length in the annealed sample is 2.35 ± 0.02Å, as expected, whereas the Si-O distance is a little short, at 1.58 ± 0.02Å instead of the expected 1.62Å. Although crystalline lattice regions have been observed by others in high resolution TEM images[7,9] in similarly-prepared materials, our EXAFS data do not show direct evidence for crystallinity : the fitted Debye-Waller factors of the first shell Si-Si bonds at about 0.006±0.003 Å² suggest a structure in between amorphous and crystalline for which the factors are 0.004 and 0.007 Å² respectively. The EXAFS suggests that the structure is composed of clusters which have crystalline cores surrounded by disordered bonds. Either way the absence of any features corresponding to second shell Si-Si-Si is not surprising considering the small first shell Si-Si contribution and the rapid fall off of EXAFS with distance.

For the carbon doped SiO_2 films, C K-edge near edge EXAFS is shown in Figure 2(b) from one of the carbon clustered films. Because the quantity of carbon atoms is quite small comparing with Si and O atoms in the films, and because of lower system sensitivity to carbon element, the NEXAFS of C k-edge is fairly noisy. However, the near edge absorption still presents certain important information about the states of carbon bonding of the clustered films. The clear increase of the absorption peak (π bond state) blow 290 eV from annealed film, compared with as-deposited film, indicates that the carbon clusters (graphite structure) has formed from oxygen rich-carbon clusters (strong σ bond absorption could be of C-O reaction/bonding[13]), while only annealed clustered film can give off strong luminescence. This discussion agrees with the imply from O K-edge EXAFS of the carbon doped films (not shown here).

After knowing the materials that are related to the clusters, we can discuss the origin of the blue emission, while the origin about the unstable UV emission is still not clear at this stage. The size distributions of the Si clusters observed by TEM are shown in Figure 3(a) for the Si clusters of sample 1 and (b) for the

C clusters of the sample 3 in Figure 1, respectively. Note that the resolution of the TEM makes estimation of cluster densities more difficult for diameters < 1nm. As expected, based on a quantum confinement model for blue emission, the cluster size is very small and there are no clusters of size >4.5nm. Crystalline regions have been observed in the diffraction patterns from the samples composed of large clusters (about 15-20 nm diameter) which show

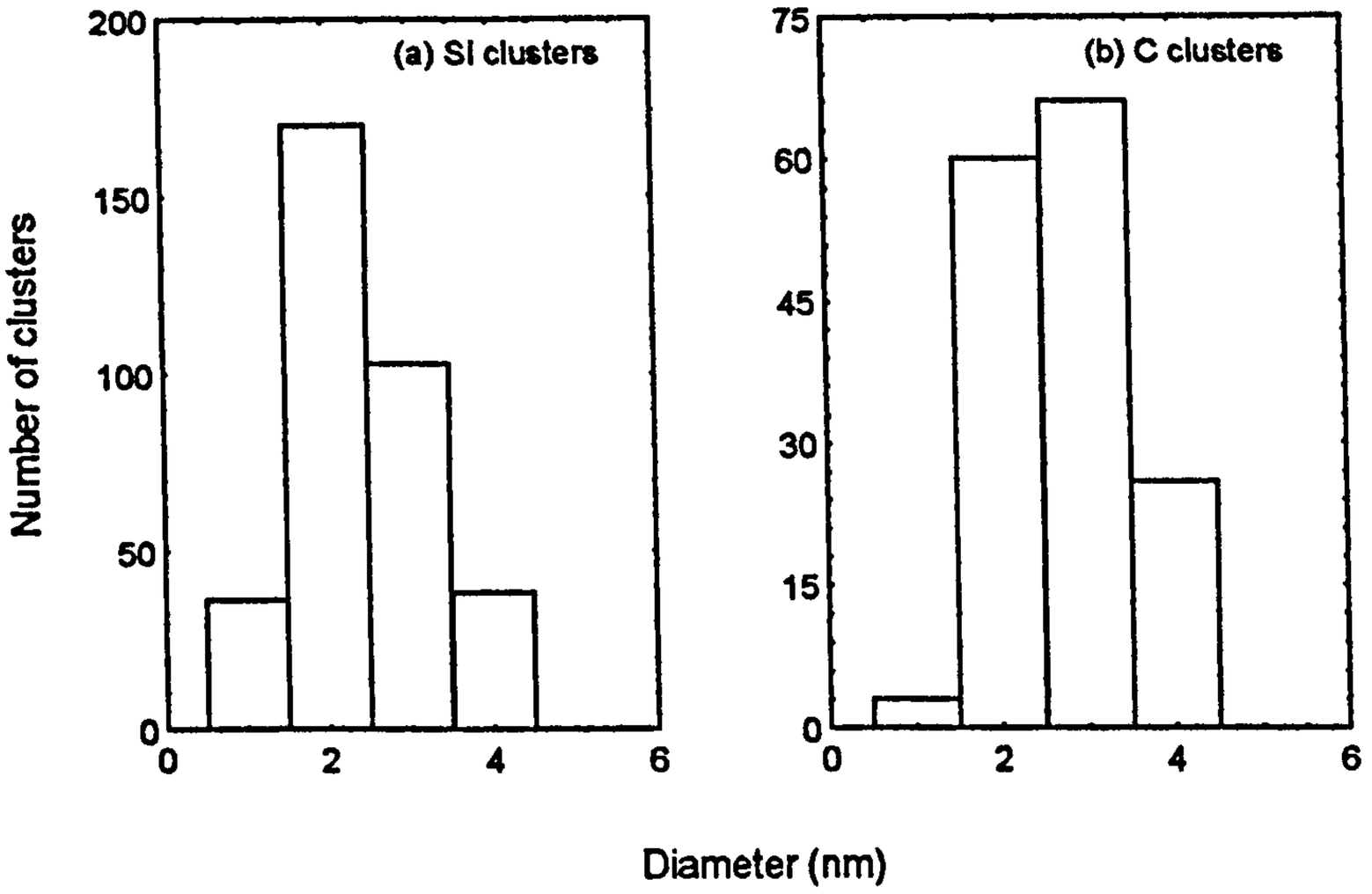

Figure 3. The size distribution of Si (a) and C (b) clusters in SiO_2 matrix.

emission at longer wavelengths. Since the blue-emitting material contained very small clusters and the resolution of the instrument was not very higher, we could not obtain evidence for crystallinity in these samples by TEM. However, the ordering factor from the EXAFS FT of Si clusters suggests that the structure is composed of clusters which have crystalline cores surrounded by disordered bonds. Furthermore, the bonding states knowing from C NXAFS suggests that the C clusters have crystalline graphite structure. According to the theoretical calculation of the electronic structure of silicon nanocrystallites by an effective-mass approximation[14] and from quantum confinement[15], nanoclusters ~2.5nm in diameter are expected to have a bandgap of 2.25-3 eV. The PL peak energies of clustered films in this work, from ~ 2.5 eV (495 nm) to ~ 2.95 eV (420 nm), fall in this region.

A relation between the density of clusters by TEM and intensity of PL, that stronger PL only comes from the films with more clusters, i.e. higher PL efficiency comes from the samples which have much more clusters as observed.

Thus we have an indication that the existence of small elemental Si clusters provides one correct environment for greater PL efficiency in the blue.

In summary, we present the work of stable blue and unstable UV photoluminescence from N_2 annealed Si and C nanoclusters embedded in SiO_2 matrices. The clusters are likely to have a crystalline core, however there is evidence for some disorder surrounding the cores. The intensity of blue PL is directly related with the density of clusters. the size distributions suggest the quantum size effect still can apply to blue emission, however, the origin of the UV emission is unknown at this stage. As the suggest from local structures, e.g. π bonded carbon, crystallisation is considerable important to the emission efficiency base on size effect.

Thanks to EPSRC, DRAL Daresbury and BESSY for financial support.

References

[1] L. T. Canham, Appl. Phys. Lett. 57, 1046(1990).
[2] S. C. Bayliss, D. A. Hutt, Q. Zhang, N. Danson, J. Bates, and A. Waddilove, J. Appl. Phys. 76, 9 (1994).
[3] T. Kawaguchi and S. Miyszima, Jpn. J. Appl. Pyhs. 32, L215(1993).
[4] D. J. Dimaria, J. R. Kirtley, E. J. Parkulis, D. W. Dong, T. S. Kuan, F. L. Pesavento, T. N. Theis and J. A. Cutro, J. Appl. Phys. 56, 401(1984).
[5] T. Ito, T. Ohta and A. Hiraki, Jpn. J. Appl. Phys. 31, L1(1992).
[6] S. Hayashi, M. Kataoka and K. Yamamoto, Jpn. J. Appl. Phys. 32, l274(1993).
[7] Y. Maeda, N. Tsukamot, Y. Yazawa, Y. Kanemitsu and Y. Masumoto. Appl. Phys. Lett. 59, 3168(1991).
[8] Y. Kanemitsu, H. Uto, Y. Masumoto and Y. Maeda. Appl. Phys. Lett. 61, 2187(1992).
[9] Y. Maeda, Phys. Rev. B 51, 1658(1995).
[10] Q. Zhang, S. C. Bayliss, and D. A. Hutt, Appl. Phys. Lett. 66, 1977(1995).
[11] Q. Zhang, S. C. Bayliss, A. Al-Ajili, D. A. Hutt, Nucl. Instr. and Meth. in Phys. Res. B 97, 329(1994).
[12] S. C. Bayliss and S. J. Gurman, J. Non-Cryst. Sol. 127, 174(1991).
[13] Th. Schedel-Niedrig, H. Werner, M. Wohlers, D. Herein, J. Blöcker, R. Schlögl, M. Keil, A. M. Bradshaw, BESSY-Jahresberidht 1993, 196.
[14] T. Tahagahara and K. Takeda, Phys. Rev. B 46, 15578(1992).
[15] C. Delerue, M. Lannoo and G. Allan, J. of Luminescence 57, 247(1993).

APPENDIX D Proceeding Volume of 1st International Symposium of Advanced Luminescent Materials, 188th Meeting of The Electrochemical Society, Chicago, USA, 10/1995.

THE DIMENSIONS AND SIZES OF AS-ANODISED RED, YELLOW AND GREEN-EMITTING POROUS SILICON AND BLUE-EMITTING CLUSTERS

Q. Zhang and S. C. Bayliss

Department of Applied Physics, School of Applied Science, De Montfort University, Leicester LE1 9BH, UK

Abstract

Freshly produced red, yellow and green emitting porous Si have been studied by NEXAFS and EXAFS (near-edge and extended x-ray absorption fine structure). The correlation between the co-ordination numbers of the first, second and third Si neighbour shells (from Fourier transform fitting of EXAFS) and both emission peak energies and optical bandgaps (estimated from photoluminescence excitation dependence) suggests that the nanostructures of the PS are nanowires, rather than nanoparticles. Two types of quantum nanowire with one and one-plus-a-fraction dimensionality are proposed to interpret the correlation. The order factors of the theoretical fits suggest the nanowires of the freshly produced PS are crystalline. Similarly, the mean sizes, 2-2.5 nm, estimated for Si and C clusters in annealed sputtered films with blue PL, suggest that size effect can apply also to blue-emitting materials.

INTRODUCTION

It was suggested in the very first reports on porous silicon (PS)[1,2] that the strong blue shift of the photoluminescence (PL) was caused by a quantum size effect, mainly due to the presence of quantum wires. This strong blue shift results in the originally infrared band-gap material emitting at room temperature over the entire visible region from red to blue. Much research has supported the model of band-gap widening by confinement, such as details of the PL, soft x-ray absorption, x-ray small-angle scattering,[3] conventional optical-absorption, high resolution TEM, extended x-ray absorption fine structure,[4,5] and our previous work on blue photoluminescence (PL) from ~2.5nm Si clusters.[6] In addition other species could also cause the bandgap widening depending on the sample preparation condition and post-preparation treatments, e.g. the existence of amorphous or disordered phases,[7] siloxene or similar complexes.

The cores of PS are generally described as crystalline Si wires[1,2] or particles[8] and both of the individual nanostructures have been shown to exist by high resolution TEM. There remains, however, a basic lack of knowledge regarding the dependence of the emission 'colour', which can be red to green for fresh PS on the ordering, the mean dimensionality and the core size. The technique of extended x-ray absorption fine structure (EXAFS) provides a useful way to estimate these on a scale of a few nanometers, within a reasonable effective sample depth (~2500Å for 80% porosity Si[9]). A previous report[5] on deducing core effective dimensionality and sizes by EXAFS, where only red to infrared PS (PL peaks at ~640-840nm) was measured, suggested a figure of three-dimensional confined nanodots with sizes from 1.5-8nm in diameter, and two dimensional confined nanowires were ruled out. This conclusion of the structure of PS is quite negative to the applications of PS, such as in optoelectronics, as lower carrier transportation between nanodots rather than nanowires would strongly affect the efficiency of electroluminescence (EL).

We present here a study on two types of nanostructure : (i) porous Si and (ii) clustered Si and C. (i) Structural information has been determined from EXAFS for a series of as-anodised PS emitting in the red, yellow and green (PL peaks at 690, 580 and 520nm respectively). From the fits to the Fourier transforms of the EXAFS data, combined with the widening of the bandgap from both PL peak energy (suitable for the band-to-band model[1]) and estimated optical bandgap from PLE (suitable for the transition centre model[7]), the nanostructure shape has been deduced. Thus the structural dimensionality and core size are predicted for PS emitting from red to green. The cause of the difference between the nanowire (this work) and nanodot[5] shapes of freshly produced PS is suggested to be related to wafer resistance. (ii) Stable blue PL has been observed under excitation powers of only a few μW from Si and C clustered films. The size distribution and mean size of the clusters measured by TEM suggest that the blue emission can also be described by quantum confinement of carriers, in this case by three-dimensional confinement in quantum dots.

EXPERIMENT

The red, yellow and green emitting porous silicon was prepared by electrochemical anodisation of (100) p-type, boron-doped, 1-3Ωcm Si wafers in a solution of HF(48%):H_2O:ethanol=1:1:2. Full details are given in reference 10. After rinsing in de-ionised water and blow-drying with N_2, the samples were put in a vacuum storage chamber and kept at 10^{-6} torr to keep them fresh. The Si and C clustered films were deposited by rf co-sputtering onto Si wafer substrates from Si/SiO_2 or C/SiO_2 targets, followed by annealing at 800°C for 20 min in a N_2 atmosphere. The thicknesses of both the PS and clustered films were > 1μm.

PL and Si K-edge EXAFS were carried out at DRAL Daresbury Laboratory for both PS and clustered films. EXAFS was determined by the total-yield technique, taken around the Si K-edge from 1800 to 2500 eV. For comparison EXAFS data were also taken from a c-Si wafer, a-Si and a-SiO_2 films, which were also used to

calibrate the system. The PL spectra have been normalised by the excitation intensities, and by the response efficiencies of the analysing Minimate monochromator and detector system. Both the optical and structural measurements were carried out at room temperature. The size distributions of the clusters in the sputtered films were obtained by TEM with a resolution 0.5 nm.

RESULTS AND DISCUSSION

Photoluminescence (PL)

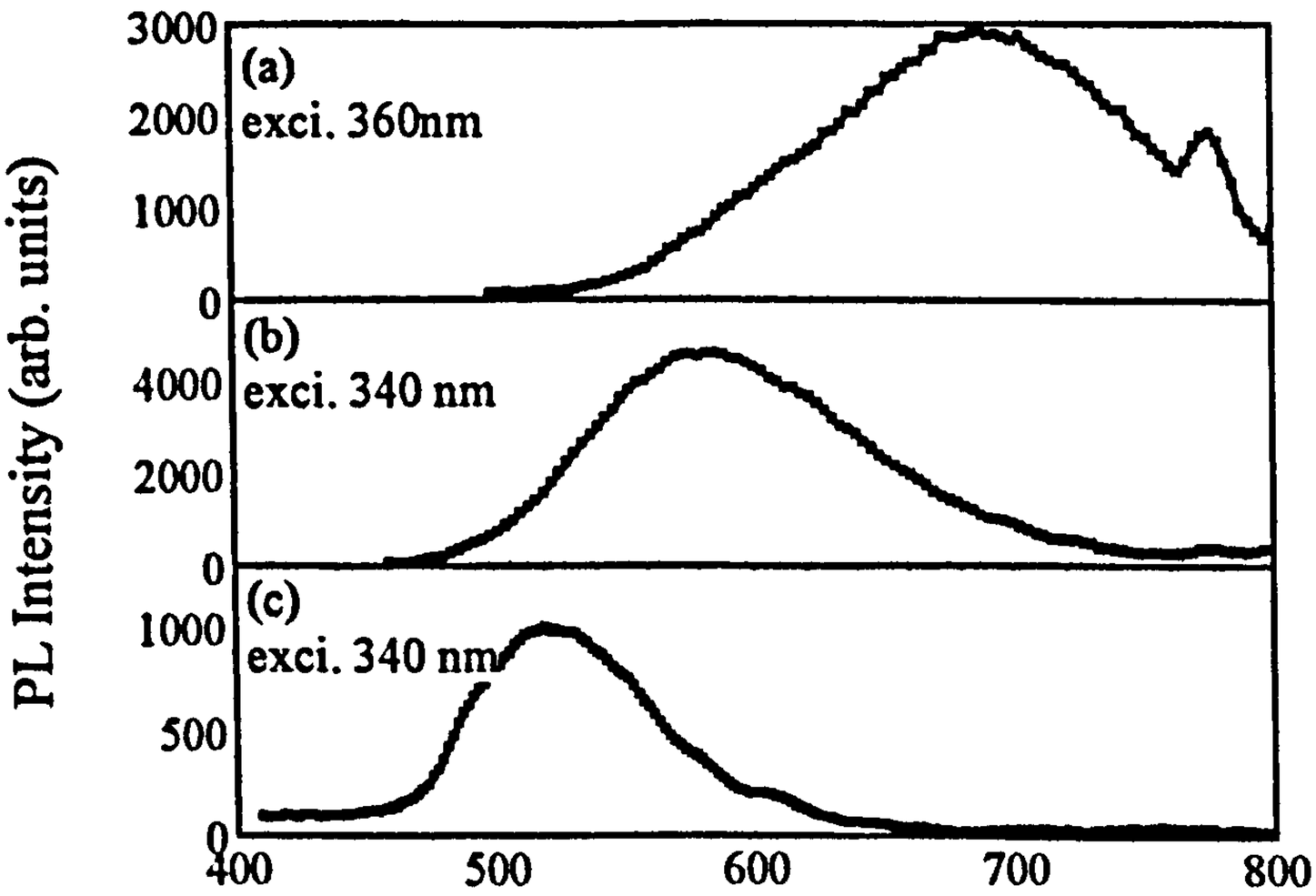

FIG.1. Photoluminescence from (a) red, (b) yellow and (c) green porous silicon. The excitation wavelength is shown.

Figure 1 shows the PL of the red, yellow and green PS, with peaks located at 690, 580 and 520nm (1.8, 2.14 and 2.38eV) respectively, under the excitations given in the Figure. These spectra are typical of PS, the energy-width of the main feature (~0.8eV) frequently believed to be caused by the broad size-distribution of the nanostructures, and different transitions between bands and within the band-gap.[7] The blue PL from both Si and C clustered films are shown in Figure 2. There was virtually no PL recorded from as-deposited samples, due to both the low excitation powers used and poor transition efficiencies before annealing.

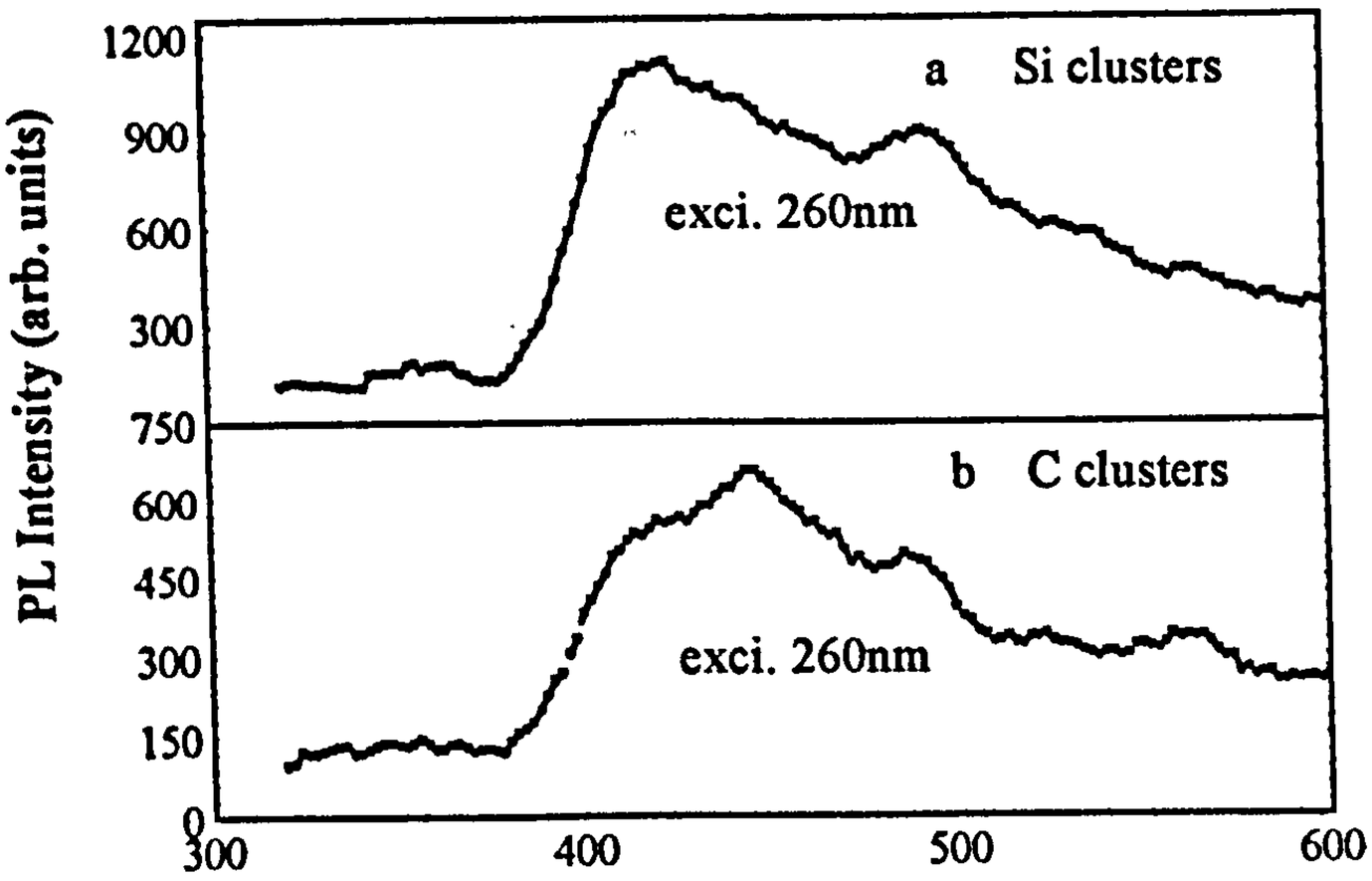

FIG.2. Photoluminescence from (a) Si clusters and (b) C clusters.

NEXAFS and EXAFS

As the penetration depth of photo-exciting radiation is on a scale of hundreds of nanometers, measurement of EXAFS is quite suitable for probing the details of the structure within the effective radiative layer of PS. Figure 3 shows the normalised photon absorption of Si-K-edge NEXAFS from PS, c-Si, a-Si and a-SiO_2. All of the raw experimental data have been shifted by -0.5 eV based on the reference data from bulk c-Si, and no further shifts have been applied. The absorption peaks due to Si-Si and Si-O bonded environments are indicated at 1840 and 1847 eV respectively. A further feature at ~1844eV has previously been assigned to the presence of SiOH-related bonding.[4,10] It can be seen that firstly the absorption behaviour of c-Si includes the 1847 eV feature, probably due to the presence of a surface native oxide. Secondly, the PS Si-Si bond absorption gradually decreases and Si-O bond absorption increases with PL blue-shift : less Si-O absorption in NEXAFS implies the samples are 'fresh', similar to some of the work in Ref. 5, but unlike the data of Ref. 4 and some of our previous studies on other types of PS,[10] where some of the NEXAFS shows stronger Si-O absorption. One explanation for the trends is that the average surface:volume ratio of Si cores increases with blue-shift. Moreover, this increasing ratio suggests the average volume of the nanocores decreases.

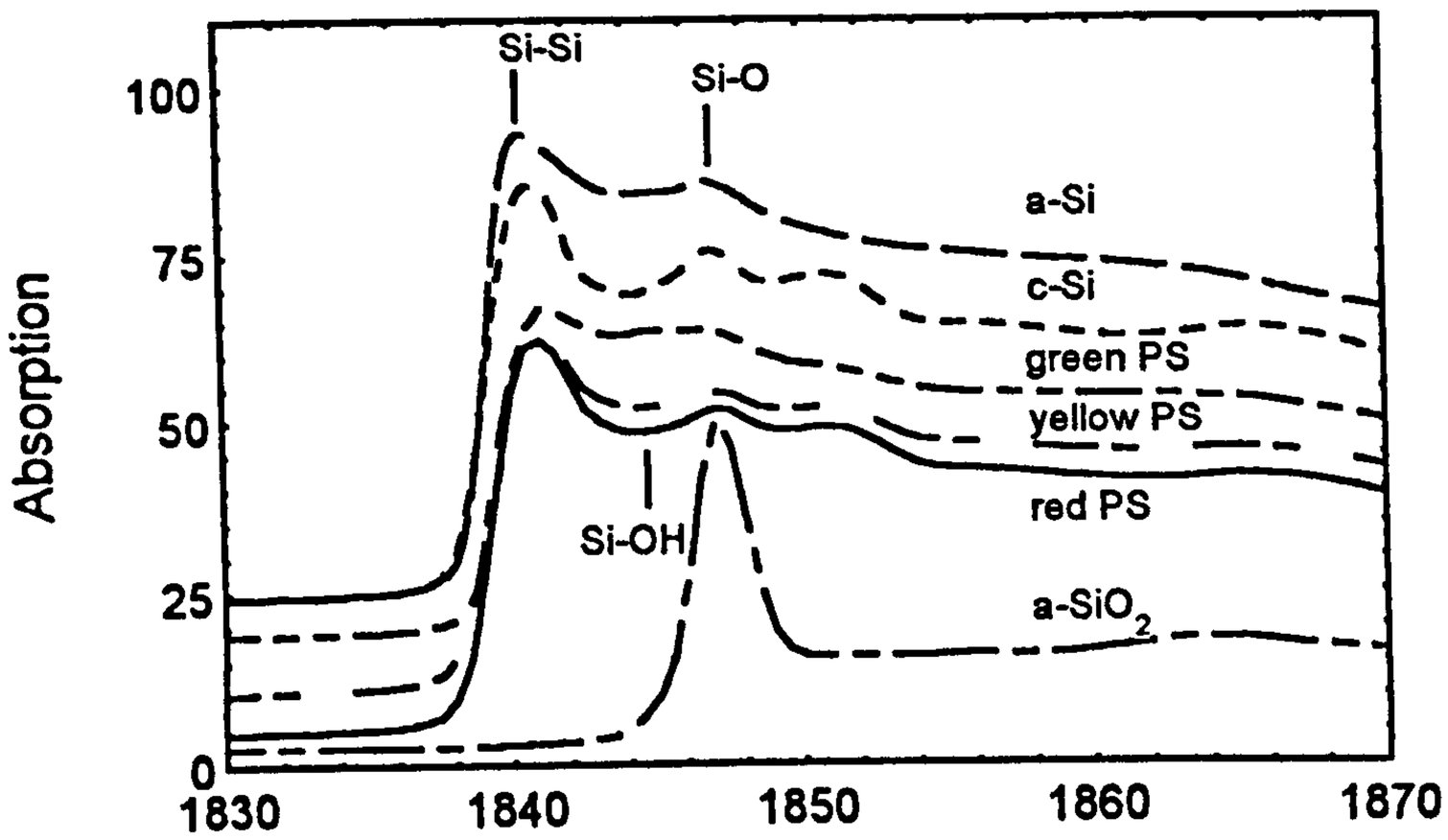

FIG. 3. NEXAFS of c-Si, a-Si, a-SiO_2, green, yellow and red PS. Si-Si, Si-O and Si-OH absorption peaks are indicated.

More information on the nanostructure has been obtained from the analysis of the EXAFS data using EXCURV92. Figure 4 shows the Fourier transform (FT) of the k^3-weighted EXAFS. For clarity, only theoretical FTs are given here. That the fits were good could be seen from error maps, the fit indexes (~0.00014), and residuals (~13). Such fits almost completely overlap the experimental curves for the first, second and third Si-Si shells, at 2.34, 3.81 and 4.50Å, respectively.

The fitted Si-Si nearest-neighbour partial coordination numbers $N_{Si\text{-}Si}$ for the 1st shell of red yellow and green PS are 3.8 ± 0.15, 3.65 ± 0.13 and 3.0 ± 0.2 respectively. 2nd and 3rd shells $N_{Si\text{-}Si}$ are 7.4 and 8.2 (red), 5.7 and 6.5 (yellow), of red and yellow PS, 3.0 and 4.0 (green). The first shell $N_{Si\text{-}O}$, however, increases with PL blue-shift. This agrees with the implication from NEXAFS of the increasing surface:volume ratio. However, this shell is not well-fitted by theory, possibly because of the involvement of O, OH and H, the possible passive species of P_b centres.

As the presence of an amorphous phase could also reduce the 2nd and 3rd coordination numbers, it is necessary to know the ordering of the freshly produced PS before any modelling of nanostructure. The fitted Debye-Waller order factors are 0.0042 ± 0.0008, 0.0038 ± 0.0008 and 0.0048 ± 0.001 for the red, yellow and green PS, respectively. These values are quite close to that of crystal Si (0.004) but far from that for a-Si (0.007). Such values for A(k) suggest as expected that the core of the fresh PS is nanosized crystalline silicon, in agreement with.[3,11] The small difference between the A(k) of green PS and c-Si can be explained since the high surface:volume ratio of this nanostructure effects a detectable x-ray absorption due to

the surface passive layer. These fitted ordering factors suggest an important characteristic of PS before degradation and both further and native oxidisation, i.e. anodisation only produces a nanostructure, and the widened bandgap is caused by quantum confinement.

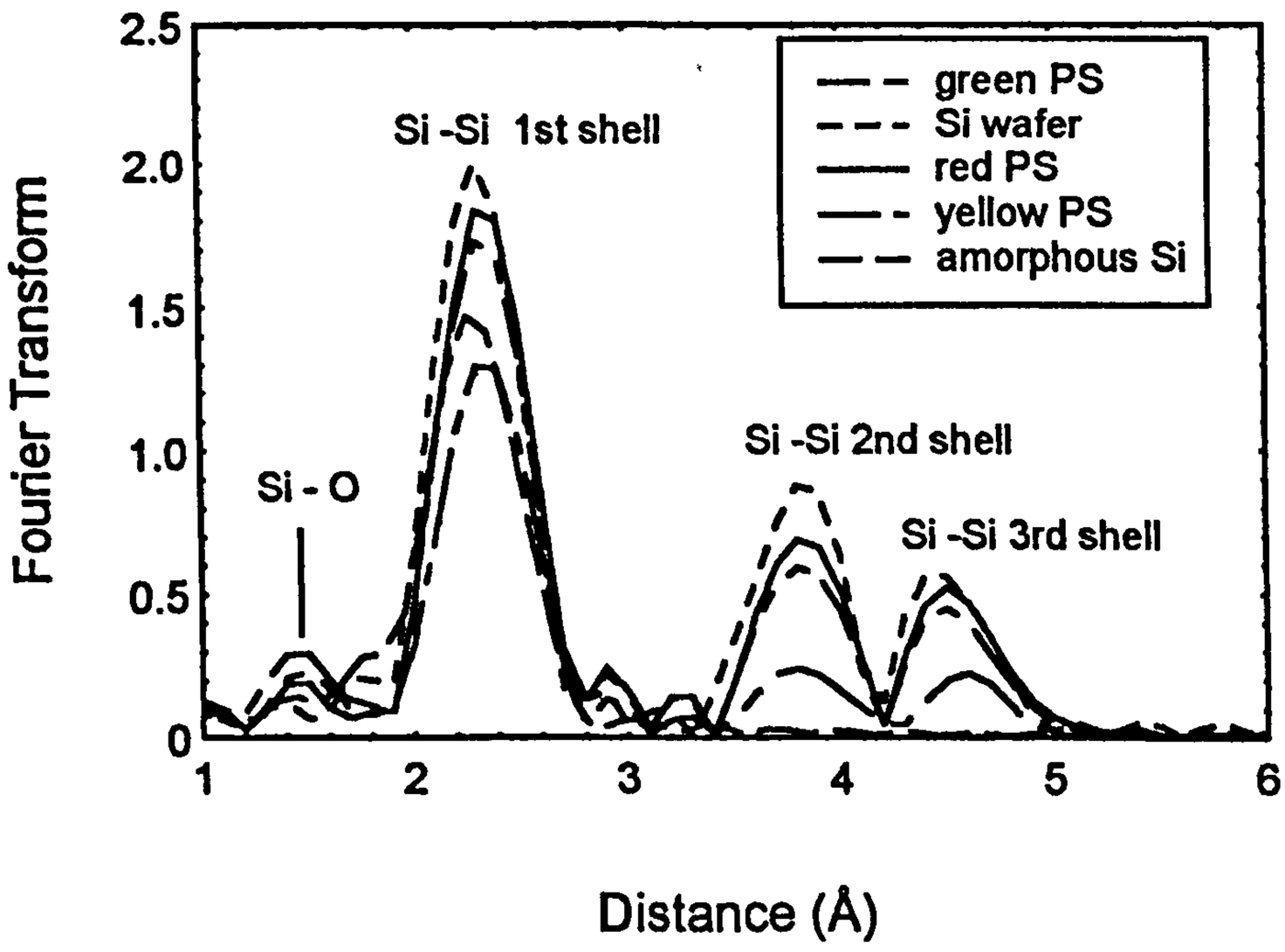

FIG.4. k^3-weighted Fourier Transform of EXAFS from c-Si, a-Si, red, yellow and green PS. 1st, 2nd and 3rd shell Si-Si and 1st shell Si-O bonds are indicated.

Dimensionality and Modelling

Obtaining accurate $N_{Si\text{-}Si}$ and ordering factors for the red, yellow and green PS allows us to estimate the possible mean sizes present, as well as the relevant structural dimensionality, and to predict if quantum confinement is responsible for the blue-shifted emission. To achieve this aim, several other values are required : (i) PS band-gaps; (ii) theoretical calculation of variation of band-gap with size of nanowire and nanodot; and (iii) the correlation between coordination number and average nanosize with different dimensionality. In most published works the nanosizes determined by TEM have been compared only with the PL peak energy, i.e. the peak energy is used as an estimate for the bandgap energy in order to estimate the size distribution, assuming a band-to-band transition model. Following this approach, our peak energies (denoted E_{g2}) are 1.8, 2.14 and 2.38 eV, respectively for red, yellow and green PS. The bandgaps (denoted E_{g1}) obtained from our PLE measurements at room temperature[12] are 2.3, 2.6 and 3 eV, respectively. One should note that the bandgap was directly obtained by PLE, without further approximation, would be a little bit bigger than that by other means. The theoretical calculation of confined bandgap with nanosize of PS by the linear combination of atomic orbitals (LCAO)

technique is employed in this work after Ref [13] where both nanodots and wire bandgaps were given.

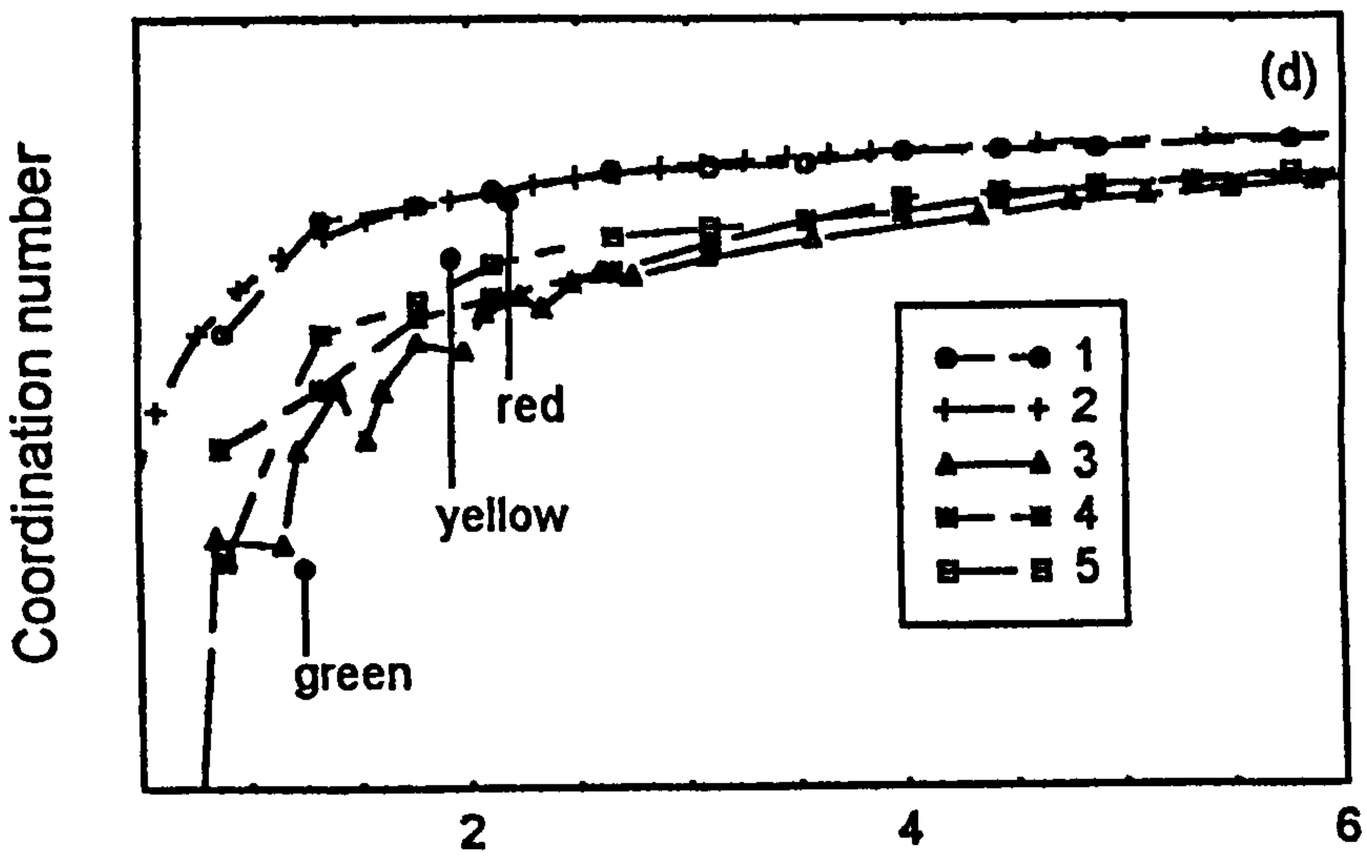

FIG. 5. Dependence of dimensionality and size with PS emission colour. As shown by the guiding lines, the PS in this study favours the nanowire network and wire structures, with average diameters of 2.2, 1.9 and 1.3 nm, respectively.

The average size dependence with partial coordination numbers of two types of nanowire for both (100) and (111) orientations have been calculated to match the experimental 1st shell $N_{Si\text{-}Si}$. The results are shown in Figure 5 : (i) bare wire: curves 3 -cylinder (100), 4 and 5 - two types of hexagonal columns (111); (ii) wire network (one-plus-a-fraction dimension) : curves 1 - (111) and 2 - (100), in which the number of surface Si atoms is only half that of bare wires of diameter d, based on the concept that the carriers within wire network could also be confined in two dimensions.[1,2]

In the model, it is assumed that the wires are perfectly one-dimensional, and the wire networks are perfectly one dimensional plus a fractional dimension. Consequently, as far as the non-bonded Si atoms are concerned, only those around the cylinder or column surface were considered in the calculation. In other words, in the model there were no undercoordinated Si atoms on the top or at the bottom of the cores.

After comparing the model calculation with bandgap energies E_{g1} and E_{g2}, with the experimental coordination numbers and with theoretical predictions of the EMA, we can estimate the mean dimensionality and the sizes of the PS within a sampling depth of hundreds of nm. As indicated by lines in Figure 5, it is can be seen that the nanostructure of red and yellow PS is predicted to consist of one-plus-a-fraction dimensionality wire networks, and green PS is predicted to consist of nanowire. The mean core diameter of red PS is about 2.2nm with a larger fractional dimensionality, that for yellow PS is about 1.9nm with a smaller fraction. Furthermore, the mean

size of green PS is much smaller, only about 1.3nm, with a dimensionality of one or less than one. A nanodot model for both energy and partial coordination number is not appropriate for any of this PS as it would lie outside the experimental data plus error. The characteristic structure and mean size of green PS is different from that of red and yellow because of both $N_{si\text{-}si}$ and E_{g1}. The $N_{si\text{-}si}$ has the characteristic that the difference between red and yellow PS is smaller than between yellow and green PS. The E_{g1} varies similarly, although $N_{si\text{-}si}$ and E_{g1} are obtained by very different means - EXAFS and PLE respectively. This implies that the transition behaviour varies with peak energy, the details of this are discussed in Ref. 12.

The presence of a wall between the cores of the nanowire network could allow more indirect carrier-transition behaviour with longer lifetimes as in bulk Si. More direct behaviour with shorter or much shorter lifetimes would be expected to occur within bare wire or dots respectively. For PS with red, orange or yellow emitting peaks, a size distribution (related to the broad PL spectrum) implies a distribution of dimensionality or a fraction dimension. This fraction therefore would lead to a lifetime increasing with increasing PL wavelength, that is the wavelength is fraction-dimension-related. This behaviour has been found present in the so-called 'slow' PL band which is related to an emitting energy about $\leq$ 2eV, and where the lifetime continuously increases from 60 to 220μs with increase in PL wavelength from 620nm to 800nm.[8,14] After the as-anodised PS is oxidised by dry-oxidisation at 800°C, this lifetime dependence on wavelength decreases to about 60 - 80μs in the same energy range.[15] This can not be explained by the tunnelling model alone as Takazawa et al. indicated,[15] but can be explained by the fraction dimension : most of the fraction dimension in the distribution has been consumed by further oxidation, so the indirect behaviour is reduced to that of bare nanowire because the carriers only have one-dimensional mobility.

The size distributions from TEM of Si and C clusters embedded in SiO_2 films are narrow, normally from 1.5 to 4.5nm in diameter. There is no information on the number-density of cluster sizes below 1.5 nm due to the resolution of the TEM used. Most of the Si clusters in the blue-emitting samples have sizes from 2 to 2.5nm. The size of crystalline core is probably smaller than this, as the fitted order parameters from EXAFS suggest that the cores are surrounded by a disordered phase. From the distributions we have also calculated that the mean size of carbon clusters is a little bigger than that of silicon clusters, about ~ 0.2nm. Compared with the three dimensional confined calculation,[13] it can be concluded that the quantum confinement is still responsible for the blue emission, agree with previous work on green-emitting Ge clusters embedded in SiO_2,[16] where the main size of clusters was about 2-3nm for green emitting Ge clusters.

CONCLUSION

Although more than one mechanism is likely to be involved in the luminescence of PS, theoretical fits to EXAFS show a relatively simple picture for freshly produced PS with PL peaks from 690nm to 520nm. (1) The nanocores of the PS are crystalline

and quantum confinement is the only mechanism widening the bandgap at this stage. Obviously surface disorder from degraded PS by x-ray and long time native oxidisation has been observed in our other studies. (2) A nanowire network (one-plus-a-fraction dimensionality) for red and yellow PS, and nanowire (one dimensional or less) for green PS, are suggested. The mean core sizes are 2.2, 1.9 and 1.3nm respectively for red, yellow and green PS. This quantum wire type of nanostructure is much more positive for PS application in EL than are quantum dots. (3) The fractional dimension could be one of the causes of the slow band and lifetime variety in this band, as the fraction dimension can let carriers act more indirectly. Moreover, the sizes of clusters in the blue-emitting sputtered films suggests that quantum confinement still can apply to emission of blue light.

References

[1] L. T. Canham, Appl. Phys. Lett. 57, 1046 (1990).
[2] V. Lehmann, and U. Gösele, Appl. Phys. Lett. 58, 856 (1991).
[3] A. Naudon, P. Goudeau, A. Halimaoui, B. Lambert, and G. Bomchil, Appl. Phys. Lett. 75, 780 (1994).
[4] T. K. Sham, D. T. Jiang, I. Coulthard, J. W. Lorimer, X. H. Feng, K. H. Tan, S. P. Frigo, R. A. Rosenberg, D. C. Houghton, and B. Bryskiewicz, Nature 367, 331 (1993).
[5] S. Scuppler, S. L. Friedman, M. A. Marcus, D. L. Adler,Y. H. Xie, F. M. Ross, T. D. Harris, W. L. Brown, Y. J. Chabal, L. E. Brus, and P. H. Citrin, Phys. Rev. Lett. 72, 2648 (1994).
[6] Q. Zhang, S. C. Bayliss, and D. A. Hutt, Appl. Phys. Lett. 66, 1977(1995).
[7] F. Koch, V. Petrova-Koch, and T. Muschik, J. Luminescence 57, 271 (1993).
[8] J. C. Vial, A. Bsiesy, F. Gaspard, R. Herino, M. Legeon, F. Muller, R. Romestain, and R. M. Macfarlane, Phys. Rev. B 45, 14171 (1992).
[9] A. Eroil, G. S. Cargill, R. Frahm, and R. F. Boehme, Phys. Rev. B 37, 2450 (1988).
[10] S. C. Bayliss, D. A. Hutt, Q. Zhang, N. Danson, J. Bates, and A. Waddilove, J. Appl. Phys. 76, 9 (1994). Q. Zhang, S. C. Bayliss, A. Al-Ajili, D. A. Hutt, Nucl. Inst. and Meth. in Phys. Res. B 97, 326(1995).
[11] Y. Uchida, N. Koshida, H. Koyada, and Y. Yamamoto, Appl. Phys. Lett. 63, 961 (1993).
[12] Q. Zhang, S. C. Bayliss, 1995 (unpublished).
[13] C. Delerue, M. Lannoo, and G. Allan, J. Luminescence 57, 249 (1993).
[14] A. Takazawa, T. Tamura, and M. Yamada, J. Appl. Phys. 75, 2489 (1994).
[15] A. Takazawa, T. Tamura and M. Yamada, Appl. Phys. Lett. 63, 940 (1993).
[16] Y. Maeda, Phys. Rev. B 51, 1658(1995).

Blue photoluminescence and local structure of Si nanostructures embedded in SiO_2 matrices

Qi Zhang,[a] S. C. Bayliss, and D. A. Hutt
Department of Applied Physics, De Montfort University, Leicester LE1 9BH, United Kingdom

(Received 21 September 1994; accepted for publication 24 January 1995)

Strong and stable blue photoluminescence (PL), visible to the naked eye under 0.4 μW of 300 nm and 2.7 μW of 370 nm excitation, has been observed for samples of Si clusters embedded in SiO_2 matrices, prepared by rf co-sputtering followed by N_2 annealing at 800 °C. Si K-edge extended x-ray absorption fine structure (EXAFS) and near-edge x-ray absorption fine structure (NEXAFS) strongly suggest the existence of Si nanoclusters with crystalline cores in the efficient emitting material. The PL excitation dependence is explained by an increase in the conduction band density of states deep in the band, and the formation of a band tail. © *1995 American Institute of Physics.*

Visible light emission from elemental semiconductor nanostructures, such as Si, C, Ge and especially porous Si, has attracted significant attention in the past few years because the photoluminescence (PL) is strong and lies in the visible region, and could be useful for optoelectronic applications. Apart from the intensively studied porous silicon[1-3] and Si nanopowder,[4-6] work on nanoclusters of group IV elements embedded in SiO_2 is one important area of study. Previous reports on Si,[7,8] C,[9] and Ge[10,11] clusters embedded in SiO_2 matrices suggested that optical transitions associated with the fundamental absorption edge of the nanostructured material had direct rather than indirect character, and there was evidence for the presence of nanocrystals in high-resolution TEM real-space images. The reported PL peak wavelengths are >800 nm for Si clusters excited by 325 nm, and ~540–570 nm for C and Ge clusters when excited by 514 nm. In this letter we report the blue emission from Si clusters embedded in SiO_2. The PL is strong enough to be visible to the naked eye observed under the excitation of 300 and 370 nm with powers of only 0.4 and 2.7 μW respectively. The blue PL from these clusters is quite stable : still visible to the naked eye after the samples had been kept in air for more than 2 months.

The semiconductor-doped glasses were deposited in one process by rf co-sputtering in a system with base pressure of 3×10^{-6} mbar. On the pure SiO_2 8 in. target between 3 and 20 pieces of Si wafer ($10\times10\times0.3$ mm^3) were placed in an area of ~4 in. in diameter to produce Si-cluster samples of various PL response. The deposition conditions were 3×10^{-4}–6×10^{-3} mbar Ar, 400 W rf power. The films were deposited on Si wafer substrates with a film thickness of >1 μm. The samples were subsequently annealed at 800 °C for 20 min in a N_2 atmosphere flowing at a rate of 3 ℓ min^{-1}. The PL and Si K-edge and near edge x-ray absorption fine structure (EXAFS and NEXAFS) measurements were performed at DRAL Daresbury Laboratory using stations 12.1 and 3.4 respectively. For PL the tuneable UV source provided excitation at 260 nm, 300 nm and 370 nm, using a bandwidth of 10 nm and a power of 0.12–2.7 μW on the samples. The PL data have been normalized to take into account the spectral sensitivity of the system and variations due to beam decay. The EXAFS were determined by the total-yield technique.[12] The cluster size distribution was obtained from TEM real-space images from the edges of tilted samples using a Jeol JEM 100CX. The resolution of this instrument is ~0.5 nm.

In Figure 1(a) we show Si K-edge NEXAFS for Si/SiO_2 films as-deposited on Si substrates and after annealing at 800 °C (sample 1, preparation conditions given in caption to Figure 2). Data from a Si wafer and SiO_2 are also shown for comparison. Note that the data from the SiO_2 film do not show a contribution from the Si substrate: as both the Si/SiO_2 sample 1 and the SiO_2 films were deposited under the same conditions and have similar thicknesses, the Si substrate does not therefore contribute to the EXAFS from the Si/SiO_2 films. The data thus represent the properties of the film alone. The absorption spectrum from as-deposited Si/SiO_2 in Figure 1(a) shows only one absorption peak at ~1847 eV which is the signature of Si bonded to O atoms.

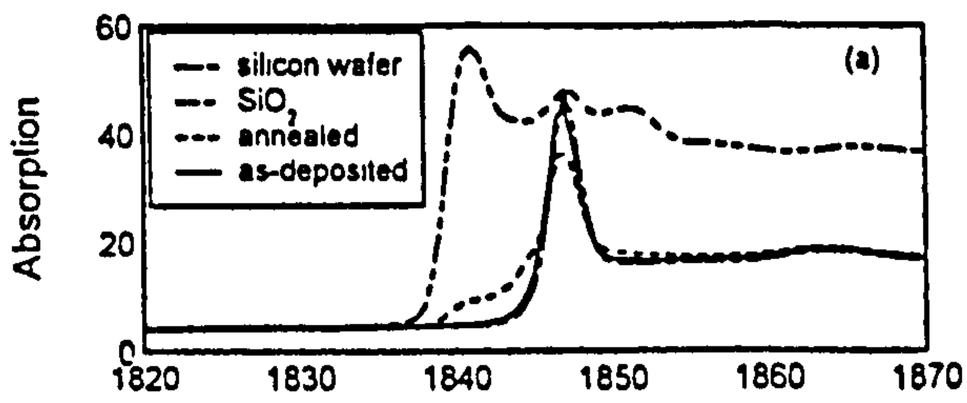

FIG. 1 (a) NEXAFS spectrum of Si/SiO_2 matrix sample 1, SiO_2 (both on Si substrates) and Si wafer; (b) Fourier transforms of EXAFS of the as-deposited and annealed sample 1.

[a]Electronic mail: qzhang@dmu.ac.uk

 0003-6951/95/66(15)/1977/3/$6.00

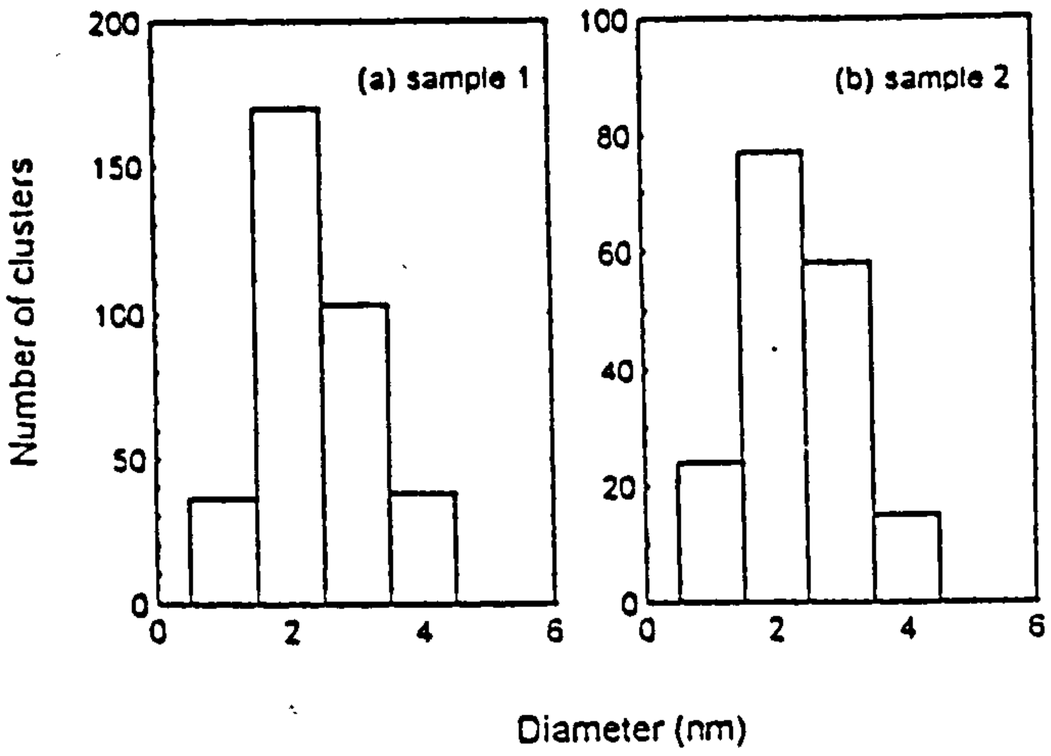

FIG. 2. The size distribution of Si clusters in SiO_2 matrix, counted within the same area size: (a) sample 1, prepared using 12 pieces of small Si wafers, 3×10^{-3} mbar Ar, 400 W rf power, 20 min deposition time. (b) sample 2, prepared using 8 pieces of small Si wafers, 3×10^{-4} mbar Ar, 400 W rf power and 35 min deposition time. Both annealed for 20 min at 800 °C in N_2.

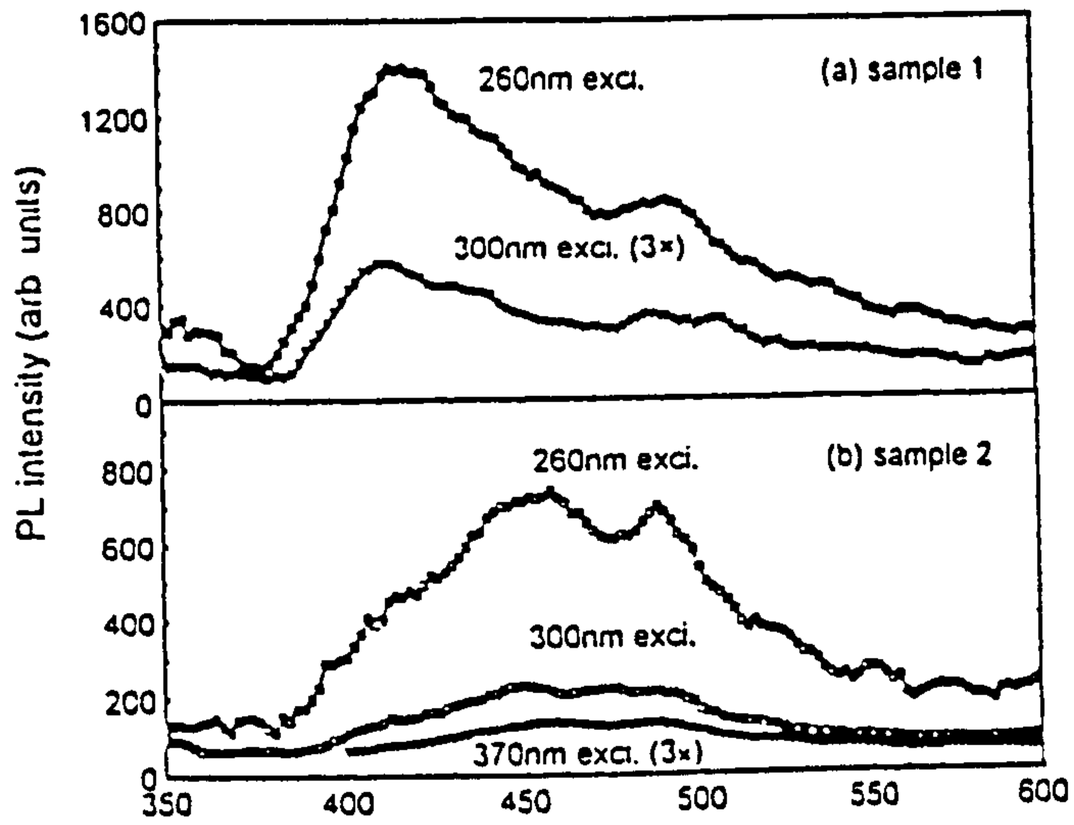

FIG. 3. PL of rf-sputtered Si/SiO_2 matrices: (a) sample 1 (b) sample 2.

After annealing at 800 °C, however, this peak decreases and characteristic absorption by Si atoms in a Si environment can be seen at ~1841 eV. This implies that Si "clusters" have formed from the amorphous as-deposited SiO_x ($x<2$) sample during the annealing process.

The Fourier transforms from the EXAFS data show details of the local structure of the nanosize clusters. In Figure 1(b), both experimental and theoretically-fitted Fourier transforms of as-deposited and annealed Si/SiO_2 sample 1 are shown.[13] In the unannealed material the Fourier transforms are very similar to those of SiO_2,[14] with a Si–O bondlength at 1.58 Å, a second shell corresponding to Si–O–Si at ~3.2 Å. After annealing, the nearest neighbor partial coordination number of Si–Si bonds increases from zero, for the as-deposited material, to 0.6 for the material with the highest contribution from Si–Si bonds. On the contrary, the Si–O bond peak of the Fourier transform decreases significantly. The second shell corresponding to Si–O–Si is still present, and, a third shell corresponding to Si–O–Si–O at ~4 Å emerges. As with most EXAFS data fits, however, the 4σ error in the partial coordination numbers obtained by statistical analysis of the fit is rather high: ±0.5, but still clearly shows the existence of Si–Si bonds. Since the total coordination number is 4, and silicon oxide is chemically ordered both throughout understoichiometry and at stoichiometry,[14] more than one eighth of the Si atoms are potentially bonded in elemental Si regions. The Si–Si bond length in the annealed sample is 2.35±0.02 Å, as expected,[14] whereas the Si–O distance is a little short, at 1.58±0.02 Å instead of the expected 1.62 Å. Although crystalline lattice regions have been observed by others in high resolution TEM images[5,6,10] in similarly prepared materials, our EXAFS data do not show direct evidence for crystallinity: the fitted Debye–Waller factors of the first shell Si–Si bonds at about 0.006±0.003 Å^2 suggest a structure in between amorphous and crystalline for which the factors are 0.004 and 0.007 Å^2 respectively. Alternatively, and the explanation which is consistent with the PL and TEM data shown below, the EXAFS suggests that the structure is composed of clusters which have crystalline cores surrounded by disordered bonds. Either way the absence of any features corresponding to second shell Si–Si–Si is not surprising considering the small first shell Si–Si contribution and the rapid fall off of EXAFS with distance.

Evidence for the presence of clusters has been obtained from TEM, crystalline regions have been observed in the diffraction patterns from the samples composed of large clusters (about 15–20 nm diameter) which show emission at longer wavelengths. The blue-emitting material however contained very small clusters, and we could not obtain evidence for crystallinity in these samples, possibly because of the resolution of the instrument, or because of the volume of material studied. The size distribution of the Si clusters observed is shown in Figures 2(a) and 2(b) for two representative blue-emitting samples (1 and 2), whose PL is shown in Figures 3(a) and (b) respectively. Note that the resolution of the TEM makes estimation of cluster densities more difficult for diameters <1 nm. As expected, based on a quantum confinement model for blue emission, the cluster size is very small and there are no clusters of size >4.5 nm.

In Figure 3, the PL of the two Si-cluster samples 1 and 2 are shown for 3 different excitations. Peaks are located from ~420 to 495 nm, and from ~450 to 490 nm, depending on the sample preparation conditions. On the contrary no emission was detected for as-deposited samples. Although many samples have been made in very different conditions, data from only two samples, those with highest PL intensities, are shown in this report. For all the samples made there is a dependence of the PL intensity on the number of small Si wafers on the SiO_2 target: the intensity increases as the number changes from 3 to 12 and rapidly decreases as the number changes from 14 to 20. This implies that the emission is cluster-related, rather than SiO_2-related. According to the theoretical calculation of the electronic structure of silicon nanocrystallites by an effective-mass approximation[15] and from quantum confinement,[16] nanoclusters ~2.5 nm in diameter are expected to have a band gap of 2.25–3 eV. The PL

peak energies of clustered films in this work, from ~2.5 eV (495 nm) to ~2.95 eV (420 nm), fall in this region.

Compared with the reported longer-wavelength photoluminescence[7–11] from clusters of Si, C and Ge which show broad single peaks, our films show PL spectra consisting mainly of two or three strong peaks, and also some smaller peaks. The multiple-peak PL spectra could be caused by a non-uniform and highly asymmetric size distribution, as Kanemitsu *et al.* suggested[11] for situations when the average cluster size is very small. Alternatively it could be due to a "size step" effect (one single atomic layer step), used to explain the multiple peaks of porous silicon PL. In this case low energy (perfect) surfaces are made more stable against further etching during anodization.[17] The PL intensity shown in Figure 3 increases rapidly with excitation photon energy and this suggests that there is a continuous increase in the density of states in the conduction band above the band minimum. Additionally, since there is some PL intensity, although very weak, for excitation photon energies very close to the PL emission energy, there could be a band tail attached to the conduction band. This tail could be due to the disorder of the clusters found by EXAFS.

From EXAFS it appears that the formation of more Si–Si bonds in the Si-clustered samples increases PL efficiency. Furthermore, higher PL efficiency comes from the samples which have much more clusters as observed by TEM. Thus we have an indication that the existence of small elemental Si clusters provides one correct environment for greater PL efficiency in the blue.

Comparing our data to published reports, the biggest difference in sample preparation is annealing in N_2 atmosphere instead of in Ar. We thus believe that nitrogen atoms play an important part in keeping the cluster size small. It was found by XPS that the Ar (from the sputtering process) in the as-deposited film was removed after the sample was annealed at 800 °C in N_2, and a peak due to nitrogen appeared, with a relative contribution to the composition of 0.8 atomic %. It is possible that nitrogen atoms stay in the voids of SiO_x, preventing construction of larger clusters. Additional evidence for the importance of nitrogen in producing a large blue-shift is from reported PL data of spark-eroded silicon nanostructure.[18] For material produced by this method, the strongest PL and biggest blue shift was made in an atmosphere of N_2, rather than Ar, He or H_2. In addition, TEM shows that clusters, presumed to be a-SiO_x ($x<2$), are present in as-deposited films (i.e., before annealing) with an average size ~1.5 times larger than that after annealing. It is likely that these regions provide the basis for crystallisation of Si clusters on annealing. So we suggest that (i) co-sputtering forms the basis of the clusters, (ii) nitrogen annealing keeps the clusters from aggregating.

In summary, we report strong and stable blue photoluminescence from N_2 annealed Si clusters embedded in SiO_2 matrices. The clusters are likely to have a crystalline core, however there is evidence for some disorder and the size and role of the interface regions are not known. Our data agree with the widely held quantum confinement mechanism for nanosized-semiconductor emission. It appears that both size control at the sputtering stage and annealing atmosphere are of great importance in producing the large blue-shift in the PL.

The authors thank D. Bazeley and A. Al-Ajili for sample processing, J. Bates for TEM, EPSRC and DRAL Daresbury for financial support.

[1] L. T. Canham, Appl. Phys. Lett. 57, 1046 (1990).
[2] G. Fishman, I. Mihalcescu, and R. Romestain, Phys. Rev. B 48, 1464 (1993).
[3] S. C. Bayliss, D. A. Hutt, Q. Zhang, N. Danson, and A. Smith, Solid State Commun. 91, 237 (1994).
[4] T. Kawaguchi and S. Miyszima, Jpn. J. Appl. Phys. 32, L215 (1993).
[5] H. Morisaki, H. Hashimoto, F. W. Ping, H. Nozawa, and H. Ono, J. Appl. Phys. 74, 2977 (1993).
[6] Y. Kanemitsu, T. Ogawa, K. Shiraishi, and K. Takeda, Phys. Rev. B 48, 4883 (1993).
[7] D. J. Dimaria, J. R. Kirtley, E. J. Parkulis, D. W. Dong, T. S. Kuan, F. L. Pesavento, T. N. Theis, and J. A. Cutro, J. Appl. Phys. 56, 401 (1984).
[8] T. Ito, T. Ohta, and A. Hiraki, Jpn. J. Appl. Phys. 31, L1 (1992).
[9] S. Hayashi, M. Kataoka, and K. Yamamoto, Jpn. J. Appl. Phys. 32, 1274 (1993).
[10] Y. Maeda, N. Tsukamot, Y. Yazawa, Y. Kanemitsu, and Y. Masumoto, Appl. Phys. Lett. 59, 3168 (1991).
[11] Y. Kanemitsu, H. Uto, Y. Masumoto, and Y. Maeda, Appl. Phys. Lett. 61, 2187 (1992).
[12] S. C. Bayliss, D. A. Hutt, Q. Zhang, J. Bates, and A. Waddilove, J. Appl. Phys. 76, 9 (1994).
[13] Q. Zhang, S. C. Bayliss, A. Al-Ajili, D. A. Hutt and P. Harris, Nucl. Instrum. Methods B (in press).
[14] S. C. Bayliss and S. J. Gurman, J. Non-Cryst. Solids 127, 174 (1991).
[15] T. Tahagahara and K. Takeda, Phys. Rev. B 46, 15 578 (1992).
[16] C. Delerue, M. Lannoo, and G. Allan, J. Lumin. 57, 247 (1993).
[17] R. Behrensmeier, G. B. Amisda, F. A. Otter, and J. M. Galligan, Appl. Phys. Lett. 62, 2048 (1993).
[18] E. F. Steigmeier, H. Anderset, B. Delley, and R. Mort, J. Lumin. 57, 9 (1993).

Nuclear Instruments and Methods in Physics Research B 97 (1995) 329–332

NIM B
Beam Interactions with Materials & Atoms

ELSEVIER

The blue photoluminescence and nanostructure of Si and C clusters embedded in SiO_2 matrices

Q. Zhang [a,*], S.C. Bayliss [a], A. Al-Ajili [b], D.A. Hutt [a], P. Harris [a]

[a] *Department of Applied Physics, De Montfort University, Leicester, LE1 9BH, UK*
[b] *Department of Physics, Loughborough University of Technology, Loughborough, LE11 3TU, UK*

Abstract

Carbon and silicon clustered films have been prepared by rf sputtering using a SiO_2 target on which were placed lumps of C or Si, respectively, followed by annealing at 800°C or 600°C for 20–30 min in a N_2 atmosphere. Information about the nanostructure of the films has been determined from photoluminescence (PL) and extended X-ray absorption fine structure (EXAFS). Blue PL from these films has been observed and reported for the first time, with peak wavelengths in the range from 420–500 nm, when excited by 260, 300 and 370 nm light produced by the tuneable synchrotron at DRAL Daresbury. The blue PL is visible to the naked eye when illuminated by ~2.7 μW UV beam.

1. Introduction

The investigation of strong electroluminescence (EL) and photoluminescence (PL) in the visible range from nanostructures containing Si, C and Ge is currently an intensive research area. This follows on from the report of Canham [1] on porous silicon which opened up the possibility for Group IV semiconductors, and in particular indirect bandgap semiconductors, to be new materials for optoelectronic applications. The research on clusters of group IV elements embedded in SiO_2 matrices (called semiconductor-doped glasses) is one of the important directions of this effort.

Apart from the hundreds of papers on porous silicon, made by electrochemical anodisation of single crystal silicon, there are some reports on nanostructures made by other methods. These include preparation of (i) silicon clusters by ion-beam irradiation [2], (ii) a-SiN nanostructure by CVD [3], (iii) Si nanoparticles by laser breakdown of SiH_4 gas [4], (iv) a-Si nanopowder by PECVD, (v) C clusters by arc discharge [5] and Ge clusters by H_2 reduction of $Si_{0.6}Ge_{0.4}O_2$ [6]. Strong visible photoluminescence has also been observed from Si [7], C [8] and Ge [9,10] clusters, produced by sputtering or co-sputtering (and partial oxidation of porous silicon), which are embedded in SiO_2 matrices.

Previous reports on C, Si and Ge clusters embedded in SiO_2 show evidence for the presence of nanocrystallites in HREM images, and the dependence of the emission wavelength on cluster size is in accord with the quantum confinement model. The reported peak wavelengths are ~540 nm (yellowish-green) and 570 nm (yellow) for Ge clusters, ~540 nm for C clusters when the 514 nm line from an Ar-ion laser is employed to excite the sample, and from dark red to yellow for silicon clusters excited by a He–Cd laser (325 nm line) [7–10]. However, our samples of C and Si clusters embedded in SiO_2 actually glowed blue, with the peak wavelength positions at ~420–500 nm, when wavelengths of 260, 300 and 370 nm from the tuneable UV source were used to excite samples. The extended X-ray absorption fine structure (EXAFS) have been measured for matrices containing Si clusters to gain information on both the possible glow mechanism and the nanostructure. Transmission electron microscopy (TEM) was used to investigate the nanostructure of the matrices, and scanning tunnelling microscope (STM) and atomic force microscope (AFM) images were used to obtain the nanosize surface morphology.

2. Experimental

The semiconductor-doped glasses were deposited by rf-sputtering from an 8 in. SiO_2 target in a CVC system with base pressure of 3×10^{-6} mbar. To obtain clustered films with strong PL, a great number of different sample preparation conditions were tested. To obtain the required compositions elemental Si or C pieces were placed on the pure SiO_2 target: between 3 and 20 pieces of Si wafer ($10 \times 10 \times 0.3$ mm^3) were used for Si-cluster samples,

* Corresponding author, tel. +44 533 551551, ext. 8113, fax +44 533 577135.

0168-583X/95/$09.50
SSDI 0168-583X(94)00727-6

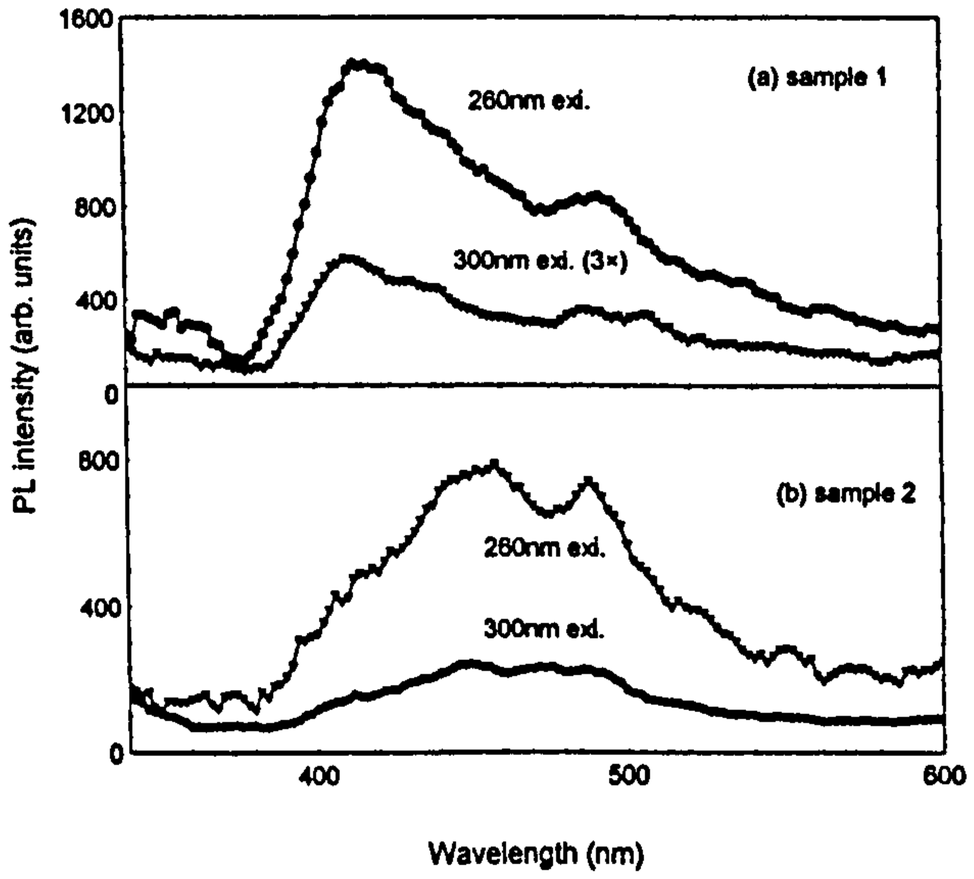

Fig. 1. PLE of rf-sputtered Si/SiO_2 matrices: (a) prepared using 3×10^{-3} mbar Ar, 400 W rf power, 20 min deposition time; (b) prepared using 3×10^{-4} mbar Ar, 400 W rf power and 35 min deposition time. Both annealed for 20 min at 800°C.

and between 5 and 16 pieces of pure graphite rod of 6 mm diameter were used for C-cluster samples. The deposition conditions were: (1) for C/SiO_2 matrices – rf power: 500–1250 W; Ar pressure: from 6×10^{-4} to 1×10^{-2} mbar; (2) for Si/SiO_2 matrices – rf power: 400 W; Ar pressure: from 3×10^{-4} to 6×10^{-3} mbar. The films were deposited on Si wafer substrates with a film thickness of 0.5–1 μm. After deposition, the samples were annealed at 600 or 800°C for 20 min in an atmosphere of N_2 flowing at a rate of 3 l min^{-1}. Data shown in Figs. 1 and 2 are from samples exhibiting the strongest PL: the respective preparation conditions are given in the captions.

The PL was measured at room temperature using station 12.1 of DRAL Daresbury Laboratory. The tuneable UV source was used for excitation at 260, 300 and 370 nm with a 10 nm bandwidth, and with a power on the samples ranging from 0.12 to 2.7 μW. The PL was analysed using a Spex Minimate monochromator and photon counting detection system. The PL data was normalised using calibrated filters to take account of the spectral sensitivity of the system, and corrections were also made for beam decay. Si K-edge EXAFS data from Si-cluster samples were obtained using station 3.4 of DRAL Daresbury Laboratory: details of the experimental procedure are given in Ref. [11]. TEM images were obtained from the edges of tilted gold-coated samples using a Jeol JEM 100CX. The resolution of the real-space images from this instrument was ~0.7 nm. AFM and STM images were taken from C-cluster specimens using a Topometrix Nanoscope II. The STM images were of superior quality, and although from gold-coated samples, showed similar features to the AFM images from uncoated samples. We have thus concentrated on interpreting the STM data.

3. Results and discussion

Instead of previously reported PL of clusters embedded in SiO_2 [7,8] in which the shortest wavelengths of emission peaks are at ~540–600 nm, the PL peaks from our samples containing either Si or C clusters are in the blue region of the visible spectral range. Figs. 1a, 1b, 2a and 2b show room temperature PL for two differently-prepared samples of silicon and carbon clustered matrices, respectively. There is evidence for the presence of clusters in the oxide matrices from the TEM real-space images: the Si/SiO_2 samples annealed at 800°C showed a high density of darker regions of ~1–4 nm diameter which we interpret as being due to the presence of Si clusters.

Similar to the reported behaviour [10], our results show that an annealing temperature of 800°C produces much more efficient PL compared to a 600°C annealing (Fig. 2a). This is consistent with our work on amorphous silicon thin films, which have been prepared and processed using the same annealing programs. In that study [12] we find that the 800°C anneal produces a decrease in bond angle disorder corresponding to the production of polycrystalline films, whereas an anneal at 600°C produces a much smaller decrease in bond angle disorder. There are, however, no large differences in the resulting PL when annealing is carried out for either 20 or 30 min at 800°C. For each of the two Si-cluster samples it appears that there are at least two, and often three, main emission bands present in the PL spectra. In general the peak of one band is localized at ~500 nm, the others at ~420 and 450 nm, and the intensity of each band depends on preparation conditions. The increase in PL intensity as the wavelength of the

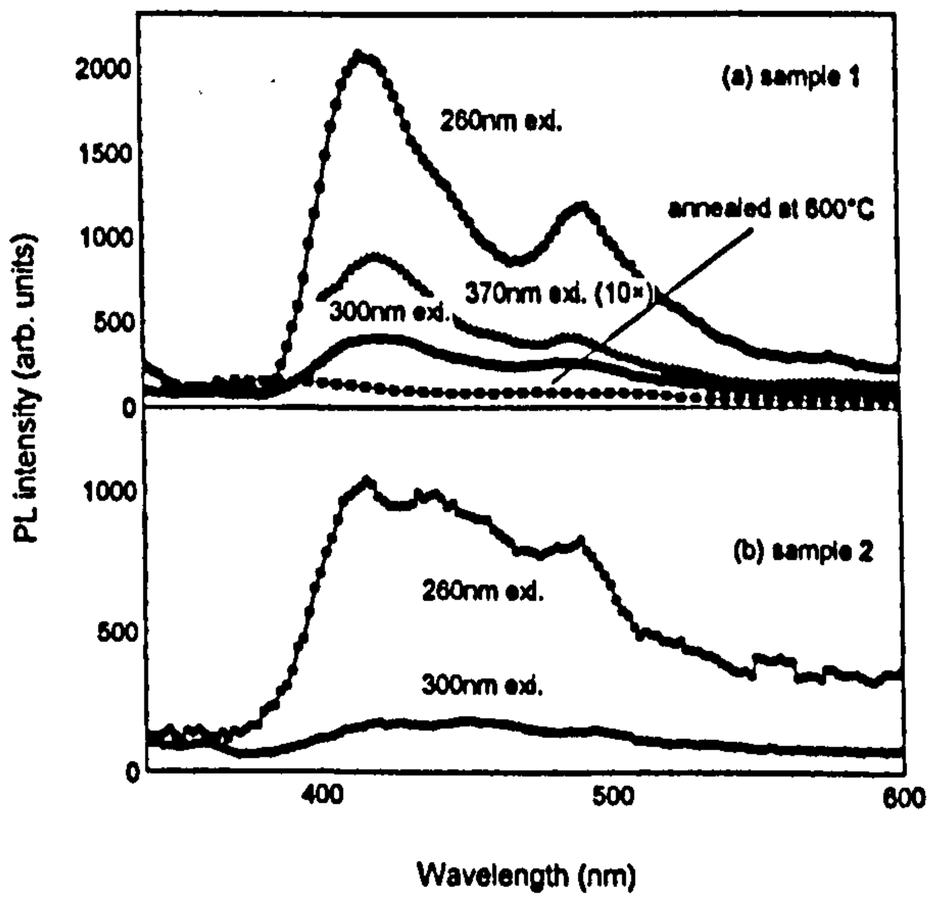

Fig. 2. PLE of rf-sputtered C/SiO_2 matrices: (a) prepared using 8×10^{-3} mbar Ar, 1200 W rf power, 30 min deposition time; (b) prepared using 8×10^{-3} mbar Ar, 850 W rf power, 40 min deposition time. Except where marked, annealing was for 20 min at 800°C.

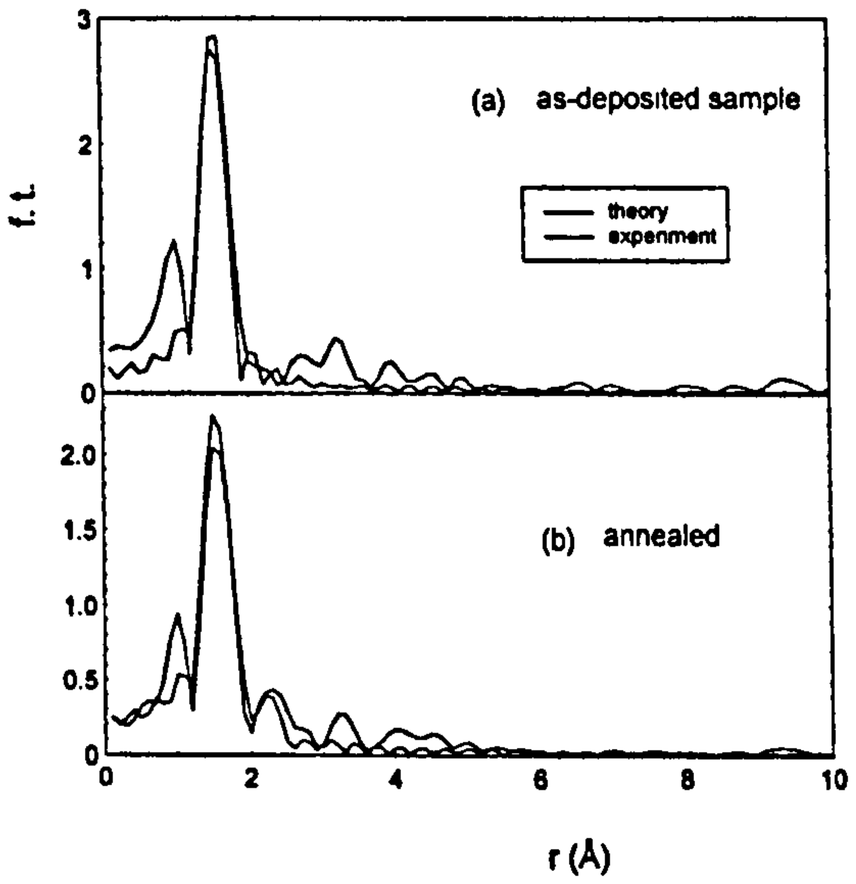

Fig. 3. Fourier transform of EXAFS of (a) as-deposited, and (b) annealed Si doped glasses.

excitation decreases from 370 nm to 260 nm implies that the efficiency of electron-pumping from the valence band to the conduction band increases. This is consistent with the size of the clusters responsible for emission being in the quantum confinement limit: since there will be a size distribution of clusters, the PL intensity varies accordingly. There is an alternative explanation for the PLE data in terms of the band structure: exciting high into the conduction band allows access to a greater density of states, and hence higher PL efficiency. The PL from C-clustered matrices (Fig. 2) also shows two or three emission peaks, at similar positions to those in the Si-clustered material.

The PL of nanostructures other than semiconductor-doped glasses, such as porous silicon and silicon nanopowder, also shows multiple-peak characteristics, and this behaviour has been explained as a "step effect" in the size distribution [13] and thus in the density of states. It is plausible that the multiple-peak features of the cluster samples is caused by the same effect. However, the step effect from our sample is greater than that from the longer-wavelength PL of clustered material [10] and that from porous silicon [13]. Kanemitsu et al. have shown a higher asymmetry of the size distribution of clustered film when the average size of cluster is in a few nanometer scale [10]. Hence, the strong multiple-peak features from our samples can be explained as the convolution of strong step and asymmetric effects.

For both silicon and carbon clustered material, a strong blue-shift has enabled a glow colour localized in the blue. Comparing the published results [7,8] for green and yellow PL with our observations, the biggest difference in sample preparation is annealing in N_2 instead of in Ar. We thus believe that nitrogen atoms play an important part in controlling the cluster size: nitrogen is the most active element in the inert gases and its atomic size is smaller than oxygen. If, during the annealing, nitrogen atoms remained in the voids of the matrices this would prevent the oxide of Si and C constructing a large cluster, and the average size of the annealed cluster would then be smaller than for samples annealed in Ar. As expected, a nitrogen peak has been found by XPS for our sample which was annealed at 800°C in N_2 [14] with the relative amount of 0.8 at.%. On the contrary, the large Ar component observed in the as-deposited sample, disappeared after annealing in N_2. Additional proof for the importance of the

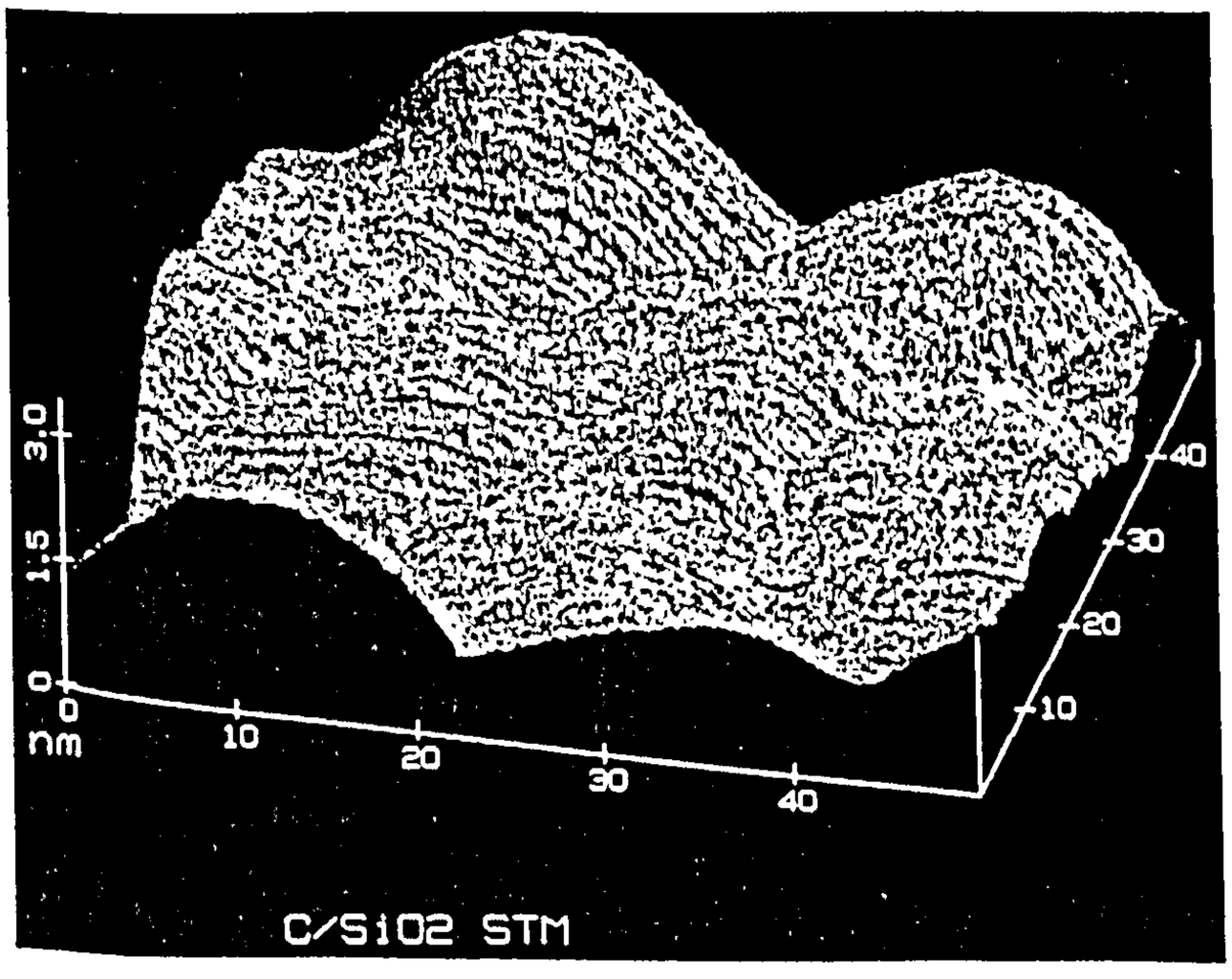

Fig. 4. STM image of gold-coated C-clusters/SiO_2.

presence of nitrogen for producing strong blue-shifted PL is from the report on spark-eroded silicon nanostructures [15]. Using this method, the strongest PL and biggest blue shift was made by using an atmosphere of N_2, rather than Ar, He or H_2.

Fourier transforms of fits to Si K-edge EXAFS data have been calculated for (a) unannealed and (b) annealed Si-clustered samples (Fig. 3). The EXAFS were obtained out to a k of 13 $Å^{-1}$. Within experimental error the data in Fig. 3a are well-fitted by Si atoms having 4 ± 0.5 oxygen nearest-neighbour atoms, whereas only 3.1 ± 0.5 oxygens are required to fit the data from the annealed sample. In both samples the Si–O bondlengths are 1.59 ± 0.02 Å. There is some evidence for the presence of higher shells, however less than expected for a crystalline material. Of particular interest to this work is a very small but significant increase in contribution from Si–Si nearest-neighbours at 2.34 Å in the annealed material, indicating the onset of Si-based regions. The Si–Si coordination number fitted in Fig. 3b is 0.8 ± 0.5, consistent with the reduction in the Si–O coordination number described above.

A STM image of a C-clustered sample, which has been annealed and gold coated, is shown in Fig. 4. It can be seen that the features are on a scale of ~ 20 nm, much larger than expected for confinement resulting in the large blue shifts observed. Obviously the gold coating of the sample broaden the features to some extent, but as described earlier the features are of a similar size to those in AFM images where the samples are uncoated. We thus infer that the main contribution to the size of the features is from the surrounding oxide, and we have presented the image merely to show evidence for the existence of regular features on a scale of nanometres: the low density of clusters is in agreement with composition from EXAFS step heights and XPS, and with the (very small) density of Si–Si bonding found in the XANES and EXAFS fits.

4. Summary

We report for the first time blue photoluminescence from Si and C clusters embedded in SiO_2 matrices. The PL is strong enough to be seen by naked eye under only 2.7 μW of beam power of 370 nm excitation. There are two or three main emission bands in the PL spectra, localised in the range 420 to 500 nm for different samples. The peaks can be interpreted as recombination processes: one is related to the full band-gap and the others are via deeper levels in the gap. The PL emission efficiency rises up rapidly with excitation energy increase, but the PL spectral dependence did not change appreciably with different excitation energies. Comparing the sample preparation conditions with published results we believe that the blue emission or the big blue shift is a result of N_2 annealing which helps to construct smaller nanosize Si and C clusters.

Acknowledgements

EPSRC and DRAL Daresbury for grants to support this work; DRAL Daresbury for Student Bursary for Q. Zhang; D. Bazeley for help in sample processing.

References

[1] L.T. Canham, Appl. Phys. Lett. 57 (1990) 1046.
[2] Y. Ochiai, N. Ookubo, H. Watanabe, S. Matsui, Y. Mochizuki, H. Ono, S. Kimura and T. Ichihashi, Jpn. J. Appl. Phys. 31 (1992) L560.
[3] C.M. Mo, J. Appl. Phys. 73 (1993) 5185.
[4] T. Kawaguchi and S. Miyszima, Jpn. J. Appl. Phys. 32 (1993) L215.
[5] S. Scraphin, D. Zhou, J. Jiao, J.C. Withers and R. Loutfy, Appl. Phys. Lett. 63 (1993) 2073.
[6] D.C. Paine, C. Caragianis, T.Y. Kim, Y. Shigesato and T. Ishahara, Appl. Phys. Lett. 62 (1993) 2842.
[7] T. Ito, T. Ohta and A. Hiraki, Jpn. J. Appl Phys. 31 (1992) L1.
[8] S. Hayashi, M. Kataoka and K. Yamamoto, Jpn. J. Appl. Phys. 32 (1993) L274.
[9] Y. Maeda, N. Tsukamoto, Y. Yazawa, Y. Kanemitsu and Y. Masumoto, Appl. Phys. Lett. 59 (1991) 3168.
[10] Y. Kanemitsu, H. Uto, Y. Masumoto and Y. Maede, Appl. Phys. Lett. 61 (1992) 2187.
[11] S.C. Bayliss, D.A. Hutt, Q. Zhang, N. Danson and A. Smith, S. S. Comm. 91 (1994) 371.
[12] S.C. Bayliss, D.A. Hutt, A. Al-Ajili, Q. Zhang, unpublished data.
[13] R. Behrensmeier, F. Namavar, G.B. Amisda, F.A. Otter and J.M. Galligan, Appl. Phys. Lett. 62 (1993) 2048.
[14] Q. Zhang, S.C. Bayliss and A. Al-Ajili, Appl. Phys. Lett., in press.
[15] E.F. Steigmeier, H. Anderset, B. Delley and R. Mort, J. Luminescence, 57 (1993) 9.

ELSEVIER

Nuclear Instruments and Methods in Physics Research B 97 (1995) 326–328

NIM B
Beam Interactions with Materials & Atoms

The optical response of porous silicon under different excitation energies

Q. Zhang [a,*], S.C. Bayliss [a], A. Al-Ajili [b], D.A. Hutt [a]

[a] *Department of Applied Physics, De Montfort University, Leicester, UK*
[b] *Department of Physics, Loughborough University of Technology, Loughborough, UK*

Abstract

The tuneable UV synchrotron source of the DRAL Daresbury Laboratory has been employed to determine the exciting-energy dependence of the photoluminescence (PLE) from porous silicon (PS). A group of samples have been studied covering a range of PL emission wavelength from red to green. We find that (1) the exciting wavelength which gives the most efficient emission shifts monotonically with the main glow "colour" of PS, which agrees with the quantum confinement model for PS; (2) the shift is non-linear. The optical properties have been correlated with structural information from Si K-edge EXAFS.

1. Introduction

Since the discovery of strong visible photoluminescence (PL) from porous silicon (PS) reported by Canham [1], porous silicon has attracted much attention and increasing interest from the points of view of the origin of the luminescence and the possible application in optoelectronics. A great number of studies have been carried out in very different aspects of research (for example measurement of PL, microscopy, effect of treatments and modelling) on the quasi-direct-gap semiconductor nanostructure obtained from the bulk indirect-gap semiconductor, in order to understand the observed optical and structural properties [2,3] and hence determine the emission mechanism. However, only a few studies have been made on the excitation wavelength dependence of the photoluminescence (PLE) of porous silicon [4–7]. Furthermore, these reported works are based on red or orange PL of porous silicon only, and/or the PLE data were restricted by the presence of second order diffraction from spectrometer gratings. There is, therefore, still a lack of knowledge about how the PS emission depends on the exciting wavelength of light: this dependence is not only one of the important properties of PS, but also is required to demonstrate the mechanism of photoluminescence in porous silicon.

Using the tuneable UV (synchrotron) source of the DRAL Daresbury Laboratory, we have measured the PL excitation dependence in an emission wavelength range of 490–700 nm (that is for samples emitting in the green to red spectral range). Interesting correlations have been obtained, involving for example: (1) the "best" exciting wavelength for efficient emission and, (2) the energy difference between the exciting wavelength and PL peak position. Moreover, this dependence could be new proof for the mechanism of PS emission, supporting an increase in bandgap due to quantum confinement.

2. Experimental

The porous silicon samples were prepared by anodisation of (100) p-type, B-doped Si wafers with a resistivity of 1–10 Ω cm in a 1:1:2 solution of HF(48%) :H_2O:ethanol; the anodising time was 5–60 min, and current density 10–30 mA cm^{-2}. Some samples were coated on one side with aluminium and wax to produce a more uniform emission, but in general the wafers were anodised uncoated. After rinsing in de-ionised water and blow-drying with N_2, the fresh samples were put in a vacuum storage chamber and kept at 10^{-6} Torr. Photoluminescence and EXAFS were carried out on stations 12.1 (excitation intensity was about 0.2–4.4 μW) and 3.4 respectively at the DRAL Daresbury Laboratory. The PL described in this paper was measured at room temperature. The bandwidth of the tuneable UV source exiting from the excitation monochromator (Spex), plus following bandpass filter, was about 10 nm. In order to compare the PL data, all the PL spectra have been normalised by assuming a linear increase of emission intensity with excitation inten-

* Corresponding author. Tel. +44 0533 551551×8113, fax +44 0533 577135.

SSDI 0168-583X(94)00372-6

sity [8]. Since all of the PL data for each sample were taken within a short time, the intensity variation of the decaying irradiating beam could be ignored. For EXAFS the X-ray source was incident on the sample normally, and the absorption was measured as the current required to neutralize the sample as a result of photoelectron emission [2,3]. Data were taken around the Si K-edge at about 1840 eV.

3. Results and discussion

Fig. 1 shows full spectral-range PL responses to various excitation wavelengths of (a) green-, (b) yellow- and (c) red-emitting PS samples respectively. As can be seen in the plots, the best exciting wavelength (i.e. leading to maximum PL intensity) shifts with the glow colours. This shift is about 100 nm, from 400 to 300 nm, the corresponding emission peak moving from ~700 nm to 500 nm for different samples. However the excitation shifts are non-linear. The reason for the non-linearity appears to be that the emission wavelength from these three kinds of sample covers not one but two emission bands, i.e. the "red" band and the "blue" band [8]. The requirement of a higher excitation energy to produce a higher emission energy strongly suggests that the cause of the enlarged bandgap, assuming band-to-band PL, comes from quantum confinement. This is in accord with our sample preparation methods: green-emitting samples were prepared simply by keeping the yellow-emitting sample in the same etching solution for a further 20 min. under zero current. We therefore believe that the nanosize of the silicon core of green-emitting PS is smaller than that of yellow-emitting material. It can be seen in Fig. 1 that the width of emission distribution becomes narrower with increasing blue shift from yellow to green. This is possibly because the etching of the larger nano-cores results in smaller cores, whilst the smaller ones are progressively etched away.

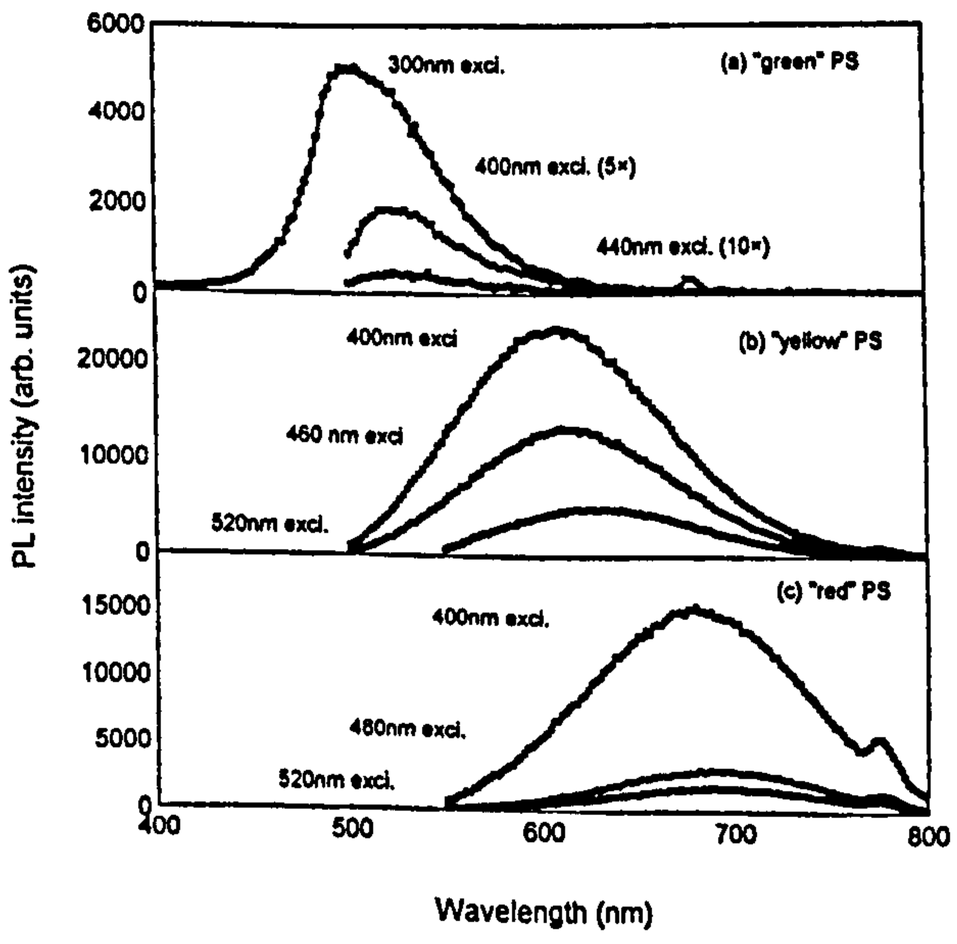

Fig. 1. The PL response under different excitation energies of (a) green-, (b) yellow-, and (c) red-emitting porous silicon respectively.

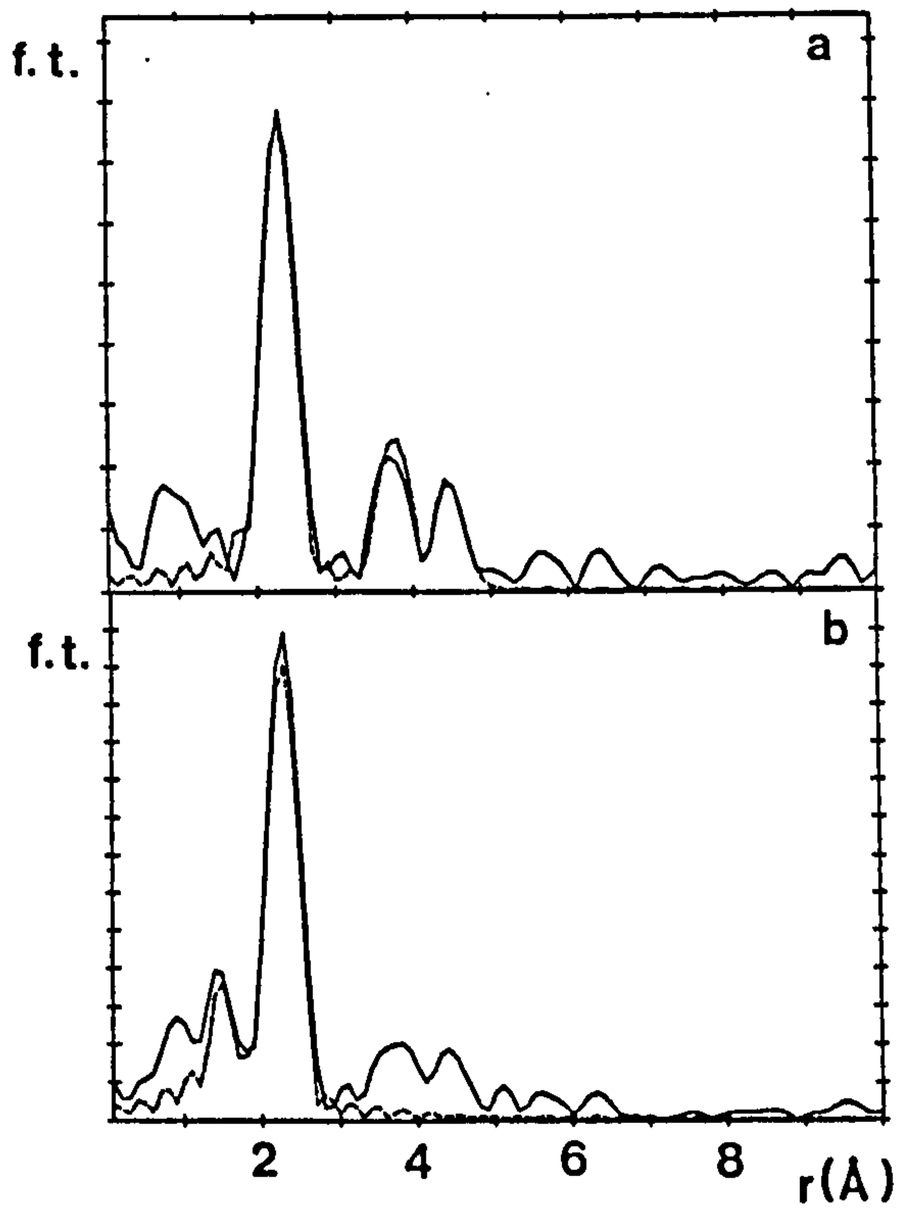

Fig. 2. Fourier transforms of $k^3\chi(k)$ for (a) red emitting and (b) green-emitting porous silicon. Solid line – experimental; dashed line – theory.

In addition, a common feature is that the peak position of PL shifts to higher energy by about 20–30 nm when the excitation energy is increased. The spectra for each sample however are all covered by the maximum spectra, thus the shifts may simply represent the variation of absorption and emission efficiencies under different excitation energies. This agrees with the main conclusions of Ref. [7] (although not in all details), in contrast to the literature report [9] (in which the maximum peak has not been given).

Experimental data and fits to the Fourier transforms of the k^3-weighted EXAFS function $\chi(k)$ are shown in Fig. 2 for (a) red and (b) green-emitting PS. The noise level of the data was such that fits could be obtained out to a k of 12 $Å^{-1}$. As found previously [2,3] the local structure of porous silicon is broadly similar to that of bulk crystalline silicon, with $N_{Si-Si} = 4$ (± 0.5) however there are some important differences. Firstly, although the Si–Si nearest neighbour bondlengths are very similar: 2.35 Å for c-Si, 2.33 Å for red-emitting PS, 2.31 Å for green-emitting (all distances accurate to ± 0.02 Å), there is evidence for Si–Si–Si bond-angle disorder in these samples, which we have attempted to quantify in the red-emitting sample.

Fitting 12 atoms in the second and third shells leads to greatly increased Debye–Waller factors for these shells, which cannot be accounted for by the (possible) error in the nearest-neighbour coordination numbers. (The green-emitting sample cannot be so-treated since there is evidence for the presence of ~ 0.5 oxygen atoms in the nearest neighbours). Using simple trigonometrical considerations we estimate that the bond angle disorder is $\sim \pm 7$ $(\pm 1)^\circ$. Additionally, the green-emitter shows less contribution from all higher shells, and hence is more (configurationally) disordered. These results are in agreement with our earlier statement that the green-emitter is simply a more oxidised red-emitter, however it also appears to be more disordered (through bond-angle disorder).

4. Summary

We have investigated the optical response of porous silicon under different excitation (from 300 nm to 520 nm) to produce a glow colour ranging from green to red. We find that (1) the "best" excitation wavelength shifts monotonically with the main glow colour of PS, but does so non-linearly. This supports the model of an increase in bandgap due to quantum confinement, and implies different bands are involved in emission; (2) for each sample the PL peak wavelength shifts along with excitation wavelength. As all of these shifted PL spectra are covered by the maximum PL spectrum excited, the shifts are interpreted in terms of absorption and emission efficiency; (3) structural trends from EXAFS support the model described above, and also provides evidence for increasing disorder in the samples as the cores are progressively oxidized.

Acknowledgements

DRAL Daresbury Laboratory for (i) award of a Student Bursary to Q. Zhang, and (ii) for Minor Grants to support this work.

References

[1] L. Canham, Appl. Phys. lett. 57 (1990) 1046.
[2] S.C. Bayliss, D.A. Hutt, Q. Zhang, P. Harris, N.J. Phillips and A. Smith, Thin Solid Films (in press).
[3] S.C. Bayliss, D.A. Hutt, Q. Zhang, N. Danson and A. Smith, Solid State Commun. 91 (1994) 237.
[4] H. Nishitani, H. Nakata, Y. Fujiwara and T. Ohyama, Jpn. J. Appl. Phys. 31 (1992) L1577.
[5] I.M. Chang, S.C. Pan and Y.F. Chen, Phys. Rev. B 48 (1993) 8747.
[6] R. Laiho, A. Pavlov, O. Hovi and T. Tsuboi, Appl. Phys. Lett. 63 (1993) 275.
[7] E.F. Steigmeier, H. Anderset, B. Delley and R. Morf, J. Lumin. 57 (1993) 9.
[8] C. Delarue, M. Lannoo and G. Allan, J. Lumin. 57 (1993) 247.
[9] M.S. Brandt, H.D. Fuchs, M. Stutzmann, J. Weber and M. Cardona, Solid State Commun. 81 (1992) 307.